Two-dimensional (2D) Functional Molecular Networks

By

Ya Hu

Thesis submitted to University College London

for the degree of

Doctor of Philosophy

Supervised by

Dr. Matthew Blunt

Department of Chemistry

University College London (UCL)

August 2016

Declaration

I, Ya Hu confirm that the work presented in this thesis is my own. Where information has been derived from other sources, I confirm that this has been indicated in the thesis.

Ya Hu

August 2016

Abstract

This thesis aims to investigate the formation of complex two-dimensional (2D) on solid surfaces. Investigations have been carried out to synthesise and characterise novel 2D functional molecular networks with controllable morphologies and properties on highly oriented pyrolytic graphite (HOPG) surfaces. Two molecular systems that undergo non-covalent 2D self-assembly and one molecular system that demonstrates the formation of 2D covalent-organic frameworks (2D-COFs) have been studied.

Following an introduction in chapter 1, chapter 2 provides a background to the doctoral research. Chapter 3 presents the experimental and theoretical methodology used during the thesis.

Chapter 4 details scanning tunnelling microscopy (STM) investigations of the interfacial self-assembly of a tetra-carboxylic acid derivative, 5, 5'-(anthracene-2,6-diyl) diisophthalic acid (ATC). This prochiral molecule forms chiral domains when it self-assembles into 2D molecular network at a liquid-solid interface. The morphology of the ATC networks is tuneable by changing the concentration of ATC in solution. Three distinct structural arrangements of ATC have been observed within the same 2D self-assembled network.

Chapter 5 describes STM investigations of self-assembled porphyrin networks organised by selective hydrogen bonding between DNA nucleobases at a liquid-solid interface. Driven by homo-molecular thymine-thymine and hetero-molecular thymine-adenine interactions, both mono-component and bi-component self-assembled structures have been formed using freebase and metal containing thymine functionalised porphyrins.

Finally, in chapter 6, a Schiff-base condensation reaction has been utilised to grow highly ordered 2D-COFs using tetra-amine functionalised porphyrin and benzene-1,4-dicarboxaldehyde (BDA) at a vapour-solid interface. These structures have been investigated experimentally using STM, atomic force microscopy (AFM) and X-ray photoelectron spectroscopy (XPS). The chemical composition of the 2D-COFs

was found to be closely related to the environmental conditions during growth. Our results demonstrate that complementary experimental techniques that probe both the structure and the chemical composition of 2D materials are necessary when investigating 2D-COF materials.

List of publications

G.. Slater#, Y. Hu#, L. Yang, S. P. Argent, W. Lewis, M. O. Blunt and N. R. Champness, Thymine functionalised porphyrins, synthesis and heteromolecular surface-based self-assembly**, *Chem. Sci.***, 2015,**6**, 1562-1569
# These authors contributed equally to this work.

Y. Hu, N. Goodeal, Y. Chen, A. M. Ganose, R. G. Palgrave, H. Bronstein and M. O. Blunt, Probing the chemical structure of monolayer covalent-organic frameworks grown *via* Schiff-base condensation reactions, ***Chem. Commun.***, 2016, **52**, 9941-9944

Acknowledgement

Looking back on the past three and a half years, I would like to express my sincere gratitude to those who offered me help, advice and encouragement throughout my PhD.

First of all, I would like to thank my PhD supervisor, Dr. Matthew Blunt. His helpful guidance, curiosity for knowledge, in-depth expertise, enthusiasm for science, and insight to scientific questions have always impressed me and made my PhD enjoyable. As we came to UCL almost at the same time, I have witnessed how Matt established the lab from zero. His devotion to the research career has inspired me to be brave to take on new challenges. I think my ability to interpret experimental results and provide novel research ideas has improved a lot – thanks to Matt's supervision. Matt, as an excellent scientist and approachable PhD supervisor, is really an invaluable asset to my PhD study at UCL Chemistry Department. Thank you, Matt.

Many thanks should go to those who participated in research projects with me, particularly my team members - Niall Goodeal and Yin Chen, and our collaborators in synthetic chemistry – Prof. Neil Champness (University of Nottingham) and Dr. Hugo Bronstein (UCL). Dr. Giovanni Costantini and Dr. Luís Perdigão should be acknowledged for their warm welcome to my visit to the University of Warwick. I also thank Martin Rosillo-Lopez and Dr. Sanjay Sathasivam for friendship and technical assistance.

I would like to thank my officemates and friends in London –Jane Yates, Yi Shi, Oliver Yim, Yu Zhang, George Harrison, Daniel Paynes, Qiang Gang, Jin Si, Lixun Liu, Xi Ji, Xingwei Zhao and Bao-luen Chang. The experience of fighting for the PhD together with you seemed to be daunting, but finally turned out to be unforgettable and precious.

My six-year higher education in Europe was financially supported by an Erasmus Mundus Scholarship awarded by the European Commission and a UCL Overseas Research Scholarship. All these would never have been possible without support from Prof. Nora de Leeuw (UCL), Prof. Richard Palmer (University of Birmingham), Dr.

Brigitte Prevel (University Lyon 1), Prof. Alfonso San-Miguel (University Lyon 1), and Prof. Xiaofang Bi (Beijing University of Aeronautics and Astronautics).

A special and big thank you must go to my parents, Chengguo Hu and Xiaoxia Han. Their love and support helped me go through this “luxury” PhD in the UK. I will try to pay back my parents by being a better person. Although being so far away from home, I highly cherish the memory of staying in London with my cousins Yan Liu and Dr. Ning Guo. I would like also to say thank you to my boyfriend, Yunlong Meng, for helping me through the long thesis writing. I love you.

Table of contents

Chapter 1

Introduction

1.1 From non-covalent supramolecular self-assembly to covalent on-surface synthesis

Supramolecular self-assembly is the spontaneous process by which simple molecular components organise themselves into complex structures through non-covalent intermolecular interactions. As an equilibrium process, self-assembly occurs via nucleation and growth, and proceeds towards the minimization of free energy. During the formation of a self-assembled structure, the molecular components of a system have the possibility to adopt a large number of different configurations. When the interactions between the components are weak and reversible, the individual molecules can easily attach and detach from a growing molecular structure. Consequently, the molecular system can adjust the packing arrangement of the molecules until reaching the configuration with the lowest free energy.

Self-assembly has attracted huge research interest for several reasons. Because of the ability to sample numerous different structural configurations as mentioned above, self-assembly of molecular components can lead to the formation of nanostructures with high levels of spatial order. Due to the abundance of biological and synthetic molecular components, self-assembly is a versatile bottom-up method that can be used to fabricate complex, functional structures. Moreover, the self-assembly of molecules can be carried out in a wide array of different environments such as in solution, on solid surface or at the liquid-solid interface. Despite these advantages, applications of supramolecular self-assembly are still often limited by the inherent weakness of the individual non-covalent bonds that are used to stabilise these structures.

Examples of supramolecular self-assembly are commonplace in biological systems,

including: the assembly of lipids to form membranes, the formation of multiple folded proteins and the double helical structure of deoxyribonucleic acid (DNA). Based on the recognition and highly selective binding found in these biological structures, researchers have explored similar methods to design synthetic nanostructures. In one example based on this approach, Y. He *et al*. proposed a method to assemble large three-dimensional structures by copying basic DNA units as demonstrated in Figure 1.1 [1]. For this strategy, three different types of DNA single strands (S, M and L/L') are first assembled into three-point-star motifs which can act as unit building blocks for the further assembly of DNA polyhedra.

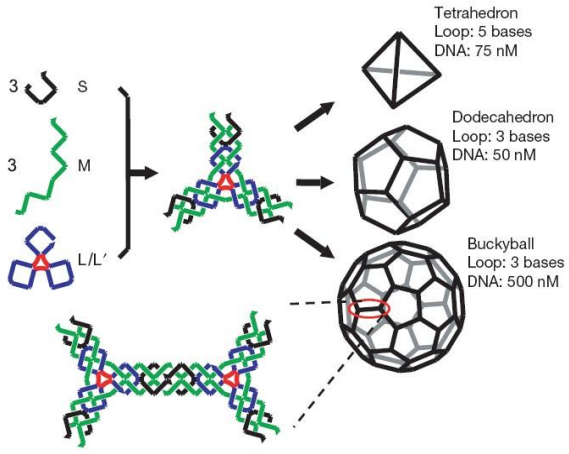

Figure 1.1 Schematic representation of the self-assembly of DNA polyhedral [1].

An important sub-division of research into supramolecular self-assembly is the formation of two-dimensional (2D) molecular networks on solid surfaces. Surface-based self-assembly has been shown to occur under various different environmental conditions including ultra-high vacuum (UHV) and liquid-solid interfaces. One important example of 2D self-assembly under UHV conditions is that of perylene tetra-carboxylic di-imide (PTCDI) and melamine. The self-assembly of PTCDI and melamine forms a 2D hexagonal network (see Figure 1.2) stabilised by a triple hydrogen bond between adjacent PTCDI and melamine molecules [2]. The PTCDI and melamine molecules form a porous hexagonal network when these molecules are

deposited on a Ag/Si(111)-$\sqrt{3} \times \sqrt{3}$ R30^0 surface under UHV conditions. The molecular network formed by PTCDI and melamine has well-defined pores that can act as 'nanoscale containers'. These pores offer space to accommodate fullerene guest molecules that are deposited on-top of the pre-formed self-assembled network.

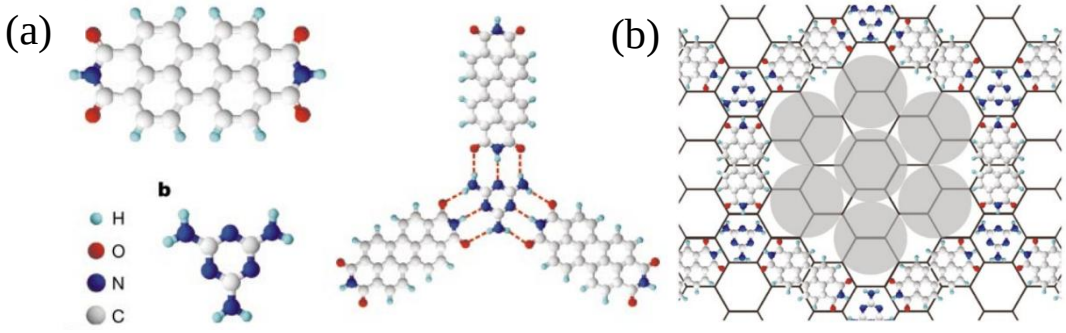

Figure 1.2 (a) Chemical structures of PTCDI and melamine. Schematic diagram of a PTCDI-melamine hydrogen bonded junction. (b). Schematic of a C_{60} heptamer trapped within a pore of the PTCDI-melamine open hexagonal network. [2]

Supramolecular 2D self-assembly allows the quick and easy formation of highly ordered structures over large surface areas. In contrast to some top-down methods of nanostructure formation, e.g., lithographic processes, which have limited spatial resolution and strict requirements for instrumentation and surface preparation, supramolecular self-assembly provides an economical and rapid bottom-up approach to the fabrication of ordered structures with nanometre precision.

One promising future research trend in supramolecular self-assembly is the application of molecular networks as templates which can accurately direct the assembly of other nano-sized components. For example, the formation of the previously described PTCDI-melamine network has also been reported on a gold surface using a solution-based fabrication strategy [3]. The utilisation of solution-based deposition allows a wider range of molecular components to be used than would be possible under UHV and opens the possibility of more complex modification of the self-assembled structures. The results on the PTCDI-melamine self-assembly on gold demonstrate that the network exhibits sufficient stability to be used as a template to assemble three types

of thiol molecules. Moreover, a more recent study has shown that gold nanoparticles which exhibit useful electronic and optical properties can also be incorporated into self-assembled mono-layers at the phenyloctane-graphite interface [4].These types of hybrid molecular-nanoparticle systems not only open up novel possibilities to increase network functionality for technological applications, but also help enhance scientific understanding of the unique properties of these materials at the nanometre scale.

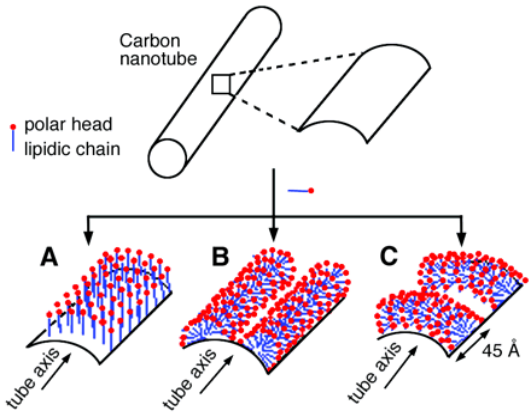

Figure 1.3. Schematic diagram showing the different possible arrangements of sodium dodecyl sulphate molecules physisorbed onto a CNT surface [5].

The development of 2D supramolecular self-assembly is of considerable importance to a number of other relevant disciplines as well. Firstly, in the field of surface functionalisation, the assembly of surfactants and synthetic lipids has been employed to decorate the surface of carbon nanotubes (CNTs) for the purpose of developing new bio-sensor and bioelectronic nanomaterials (Figure 1.3) [5]. In contrast to other covalent chemistry strategies, supramolecular self-assembly is more attractive as it functionalises the surface without altering the inherent physical properties of the CNTs. Detailed investigations have been carried out on the acquisition of stable supramolecular assemblies at the CNT-liquid interface. Secondly, supramolecular self-assembly plays an important part in the design of optical sensor devices. Due to the ability to combine the properties of organic and inorganic components, supramolecular metal-organic assemblies can potentially be applied for the sensing of molecules and ions. A supramolecular chromatic sensor, which is able to rapidly detect Ni^{2+}, Cd^{2+} and

Cr^{2+} at micro-molar concentrations has been constructed via self-assembly [6]. Lanthanide ions, which exhibit particularly desirable photo-physical properties, have been reported to be used in supramolecular luminescent sensors in various ways [7]. Thirdly, self-assembled structures have been found to have an impact on the development of molecular electronics. A key example includes the application of self-assembled guanosine derivatives in the fabrication of electronic nano-devices [8]. Self-assembly enables the realisation of these devices in a cheap and easy to implement approach. However, self-assembled structures do lack control over the material orientation between electrodes.

The sample preparation methods used for the majority of self-assembled molecular networks can be classified into two main sub-groups: sublimation and solution-based deposition [9]. In sublimation processes, molecular materials are thermally evaporated onto solid surfaces under UHV conditions. Sublimation achieves high versatility at the expense of time, effort and applicability for large molecular species. In solution-based deposition approaches, a drop of solution containing the target molecules is deposited directly onto a substrate. Self-assembled networks can then form either directly at the liquid-solid interface, or at the air-solid interface following solvent evaporation. When using volatile solvents, the final surface coverage can vary between sub-monolayer and multi-layer films. In contrast, solution-based deposition techniques using non-volatile solvents offer more intriguing possibilities for the investigation of self-assembled systems: the structure of solvent molecules and the concentration of solutions can have an important influence on the morphology of self-assembled structures.

One obstacle to the application of 2D supramolecular networks in real-world applications is their poor chemical and thermal stability. A promising solution to help overcome this weakness of 2D self-assembled structures is to link together molecular building blocks using covalent bonds. The idea of covalently bonded molecular networks has opened up a multidisciplinary area of research, known as two-dimensional covalent-organic frameworks (2D-COFs). 2D-COFs have attracted significant interest from diverse research communities including: supramolecular chemistry, nanoscience, organic synthesis and materials science. The covalent interlinking of molecular

components within 2D-COFs provides these materials with enhanced stability and the potential to form new, fully conjugated 2D structures. The wide variety of molecular building blocks made available by organic synthesis means that the properties of 2D-COFs can be tuned by careful selection of the component molecules. The ability to design and control the physical properties of 2D-COFs means that 2D-COFs are emerging as novel 2D materials for applications in areas such as sensing, molecular electronics and catalysis.

1.2 Thesis outline

This PhD thesis addresses some of the research questions at the forefront of the field of 2D organic molecular networks, including self-assembled structures organised by hydrogen bonding between carboxylic acid groups, and porphyrin arrays linked by non-covalent and covalent bonds. Both 2D molecular self-assembly and on-surface synthesis are studied using a combination of scanning probe microscopy, spectroscopic experimental techniques, and theoretical simulations. The results presented in this thesis focus on three molecular systems and help to provide a deeper understanding of the driving forces behind the self-assembly of 2D molecular networks and the growth routes and properties of high-quality 2D-COFs. The doctoral research has contributed to advances in the design, and growth of novel 2D functional molecular networks with controllable morphologies and chemical properties.

Chapter 2:

This chapter gives a background to the doctoral research by presenting an outline of the current state-of-the-art in research into 2D supramolecular self-assembly and on-surface synthesis of 2D-COFs. The discussions will be mainly focused on 2D self-assembled networks at liquid-solid interfaces and single-layered 2D-COFs formed under ambient conditions.

Chapter 3:

All the significant experimental techniques and simulation methods employed in the thesis are described, including scanning tunnelling microscopy (STM), atomic force

microscopy (AFM), X-ray photoelectron spectroscopy (XPS) and molecular mechanics (MM) simulations.

Chapter 4:

The interfacial self-assembly behaviour of a tetra-carboxylic acid derivative, 5,5´-(anthracene-2,6-diyl) diisophthalic acid (ATC) is studied using STM operating at a liquid-solid interface between a graphite surface and an organic solvent. This work includes a study of the dependence of the morphology of the self-assembled network on the concentration of molecules in solution, and the co-adsorption of ATC with guest molecules.

Chapter 5:

This chapter focuses on the 2D self-assembly of thymine-functionalised porphyrin molecules, including freebase and Zn-containing tetra-(phenyl-thymine) porphyrin. This research investigates the possibility of forming hetero-molecular structures driven by the hydrogen bonding interactions between thymine and adenine functional groups. In addition, multi-component self-assembly of thymine-functionalised porphyrins with melamine molecules is also discussed.

Chapter 6:

This chapter presents a systematic investigation of the formation of porphyrin 2D-COFs on graphite surfaces via Schiff-base condensation reaction between benzene-1,4-dicarboxaldehyde and freebase or zinc-containing tetra-amine functionalised porphyrins. Both the morphology and chemical structure of the porphyrin 2D-COFs was studied using a combination of scanning probe microscopy (SPM) and X-ray photoelectron spectroscopy (XPS).

Chapter 7:

In the last chapter, all the findings and conclusions of the research carried out in the chapters 4, 5 and 6 will be summarised. Based on these results, future directions for this work will be suggested.

Chapter 2

2D self-assembly and on-surface synthesis

This chapter is a review of the state of current research into 2D functional molecular networks formed either via non-covalent self-assembly or via on-surface chemical reactions. Relevant work in the literature will be discussed to give an overview of the background knowledge, important research questions and possible future trends in the area of 2D organic molecular nano-architectures. A particular focus will be given to 2D molecular networks fabricated under ambient temperature and pressure conditions.

2.1 Thermodynamics and kinetics of 2D self-assembly

Numerous different 2D self-assembled structures have been formed under environmental conditions ranging from UHV to liquid-solid interfaces. The growth processes of 2D self-assembled structures are influenced by both thermodynamic and kinetic effects.

Figure 2.1 illustrates how molecules or atoms that are deposited from the vapour phase grow into nanostructures on a surface [10]. The atoms or molecules are assumed to be deposited onto the surface at a constant deposition rate *F*. Activated by thermal energy, these adsorbed species can overcome surface diffusion barriers and move laterally on the surface. This lateral motion continues until adsorbates are trapped by fixed nucleation sites, such as surface defects or steps edges, or until sufficient binding to other adsorbates occurs to allow the formation of a stable nucleus. At low diffusivity to deposition rate ratio (*D*/*F*), the adsorbates do not have enough time to find the lowest energy configuration on the surface before meeting other adsorbed molecules or atoms. Thus the system is not at a minimum energy configuration and the growth process is controlled by kinetics. In comparison, structure growth at large *D*/*F*, where adsorbates are highly mobile and can sample many different configurations on the surface before

forming a nucleus, can be termed as thermodynamically controlled. For supramolecular self-assembly at liquid-solid interfaces, adsorbed molecules have the possibility to desorb back to solution and solvent molecules may also adsorb back onto the surface, rendering the growth mechanism more complicated.

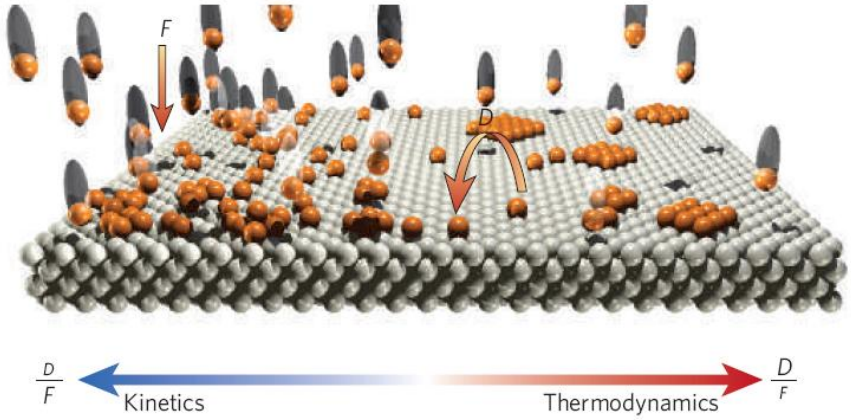

Figure 2.1. Schematic diagram showing growth processes for atoms or molecules deposited at surfaces. *D* = diffusivity, the mean square distance by which an adsorbate travels per unit time; *F* = deposition rate. The ratio *D*/*F* characterises the growth regime: kinetically or thermodynamically controlled. [10]

In order to rationalise the experimentally observed formation of different 2D self-assembled structures, the respective roles played by kinetics and thermodynamics in controlling 2D self-assembly processes have been investigated extensively [11].

As an equilibrium process, self-assembly in 2D leads to a minimisation of the free energy of a molecular system. The free energy of the system can be represented by the Gibbs free energy as written below:

$$\Delta G = \Delta H - T\Delta S \tag{2.1}$$

where ΔG is the change in Gibbs free energy, ΔH is the change in enthalpy, ΔS is the change in entropy and T is the absolute temperature of the molecular system.

During the self-assembly of extended ordered structures on a solid surface, the entropy of the molecular system decreases. This decrease in entropy should be

compensated by an increase in enthalpy so that ΔG is negative. The increase in enthalpy can be achieved by the formation of intermolecular interactions between molecular components. In the case of 2D self-assembly at a liquid-solid interface, the morphology of self-assembled molecular networks is related to several factors, including molecular structure; solvent type; surface structure; concentration; and temperature.

Similar to other self-assembly processes, individual molecules in 2D can also attach or detach from a growing structure until an arrangement with the lowest free energy is reached. In addition to this equilibrium aspect, non-equilibrium processes are also involved in the growth of 2D self-assembled structures. Therefore, kinetic effects play an important role in determining the morphology of the resulting 2D molecular networks. At a liquid-solid interface, enthalpy gains for a molecular systems are associated with both the adsorption of solute and solvent molecules and the formation of intermolecular interactions.

As described previously for Figure 2.1, the self-assembly process for extended, ordered 2D molecular networks occurs via two steps: nucleation and growth. During a nucleation process, a region of stable self-assembled network with a size larger than the critical nucleus size is formed. After the nucleation, the network continues to grow by the addition of individual molecules at the periphery. Non-equilibrium arrangements can form because they have a faster nucleation or growth rate than the equilibrium structure. If the system does not have sufficient energy to overcome the energy barrier for the transition from the as grown arrangement to the free energy minimum structure, the non-equilibrium arrangements will persist on the surface. In this case, the molecular system is kinetically trapped. The formation of defects and disordered molecular arrangements also results from kinetic trapping. When the concentration of target molecules is high or the temperature is low, individual molecules will add to the growing nucleus at a rapid rate. Under this condition, a molecule that attaches to the periphery of the nucleus into a defective arrangement may be trapped by further molecules adding to the structure. Consequently, the configuration of the molecule cannot be adjusted to reach the minimum free energy arrangement.

The formation of domains and domain boundaries in surface-based 2D self-assembled networks also results from kinetic effects. When molecules are deposited on a surface multiple nucleation points occur across the surface. Growth of each nucleation point leads to the formation of an individual domains. Domain boundaries are formed when domains with different orientations or alignment meet each other. The domain boundaries consist of molecules in energetically unfavourable packing arrangements. If sufficient energy is provided to the molecular system, the domain boundaries can be eliminated via a process known as Ostwald ripening [12]. In Ostwald ripening, larger domains grow at the expense of smaller domains, reducing the amount of domain boundaries..

At a liquid-solid interface, the formation of stable and highly ordered self-assembled monolayers with structures that do not evolve with time can be thermodynamically controlled. In this case, the adsorbed molecules are in equilibrium with molecules in solution and the entire system which includes surface, solution and self-assembled monolayer, is at a minimum Gibbs free energy state. However, currently there is no generalised thermodynamic model that describes 2D supramolecular self-assembly at liquid-solid interfaces [13]. Effects of thermodynamic factors such as solute concentration, solvent type and temperature have been explored in numerous different publications. However, to determine the exact roles of these parameters in the thermodynamics and kinetics of interfacial self-assembly and to develop a general thermodynamic model that is applicable across a range of different molecular systems, further investigations are still required.

2.2 Factors controlling interfacial 2D self-assembly

As mentioned previously, the morphology of 2D molecular networks self-assembled at liquid-solid interfaces can be influenced by a range of factors, such as molecular structure, surface structure, solvent type, concentration and temperature. In this section, our current understanding of these factors will be introduced. Firstly, we will present the role that molecule-molecule and molecule-substrate interactions play in 2D

self-assembly. Secondly, the influence of solvent structure, concentration and temperature on the morphology of 2D self-assembled networks will be discussed. Gaining a deeper understanding of these factors will help to realise the prediction and systematic design of self-assembled networks either through tailoring the functional groups of component molecules, or by controlling experimental conditions.

2.2.1 Molecule-molecule and molecule-surface interactions

In the field of surface-confined molecular self-assembly, molecule-molecule and molecule-substrate interactions play a combined role in the stabilisation of molecular networks. The morphology and dimensionality of self-assembled structures can be tuned by adding functionalising molecular building blocks with suitable chemical groups at different positions [14]. These functional groups can be chosen to promote specific types of directional, non-covalent interactions.

Non-covalent interactions between molecular building blocks have an important impact on the creation of self-assembled structures. The formation of complex, functional supramolecular systems is often a result of more than one type of non-covalent interactions working in a cooperative way [15].

Among various non-covalent interactions, hydrogen bonding, van der Waals interactions and π-π stacking are non-covalent interactions that are closely related to the molecular self-assembly systems studied in this PhD thesis.

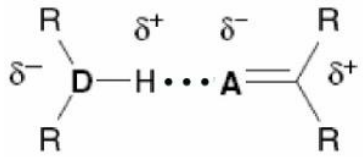

Figure 2.2. Hydrogen bond donor and acceptor atoms.

Figure 2.2 is the standard expression of a hydrogen bond which is an electromagnetic attractive interaction between the hydrogen bond donor and acceptor atoms. The hydrogen bond donor consists of a hydrogen atom attached to an

electronegative atom (D), thus forming a dipole in which the hydrogen atom is slightly positively charged. The hydrogen bond acceptor is a highly electron-withdrawing atom (A), for example, oxygen, fluorine or nitrogen.

In terms of strength, hydrogen bonds can be categorized as very strong, strong and weak. Among these hydrogen bonds, strong hydrogen bonds, which are much stronger than van der Waals interactions, are able to control and direct supramolecular structures because the interactions are highly directional and sufficiently strong. Typical examples of strong hydrogen bonds include O-H ··O=C (7.4 kcal/mol) [16], N-H ··O=C (5.19 – 5.73 kcal/mol) [17] and O-H ··O-H (5.0 kcal/mol) [18, 19].

An extensively reported example of hydrogen bonding stabilised 2D self-assembly are molecular networks formed using carboxylic acid functionalised molecules. The reason that carboxylic acid groups readily facilitate the self-assembly of ordered and stable structures is that each group contains both a hydrogen bond donor (the hydroxyl) and acceptor (the carbonyl). This allows for the formation of a hydrogen bond dimer between two carboxylic acid groups. Figure 2.3 shows three different hydrogen bonding arrangements common to carboxylic acid functionalised molecules in 2D self-assembled network structures [9].

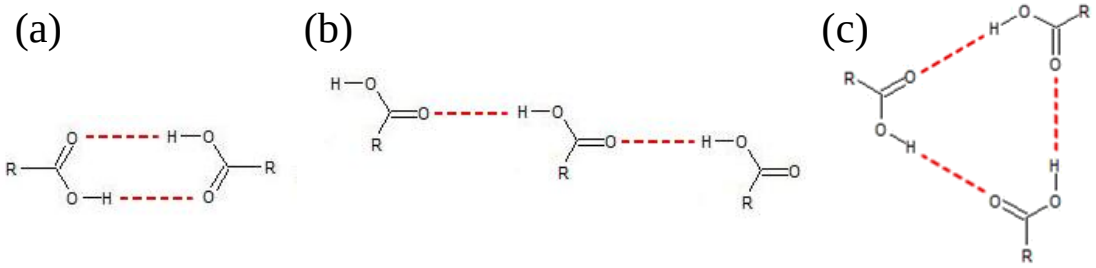

Figure 2.3. Modes of interlinking carboxylic acid groups via hydrogen bonds (marked as red dots) in molecular crystals. (a) Cyclic hydrogen-bonded dimer, the most commonly observed hydrogen bonding arrangement in 2D self-assembled networks. (b) Catemer motif. (c) cyclic trimer [9, 20].

The self-assembly of trimesic acid (TMA), which is a benzene derivative with three symmetrically positioned carboxyl groups, is a typical example of the formation of molecular mono-layers directed by hydrogen bonding. M. Lackinger *et al.* have reported two different crystallographic phases of self-assembled TMA mono-layers: a “chicken

wire" structure formed at the saturated heptanoic acid-HOPG interface and a "flower" structure at the saturated pentanoic acid-HOPG interface [21]. As can be seen in Figure 2.4, these two arrangements are stabilised by two different hydrogen bonding schemes between the carboxylic acid groups.

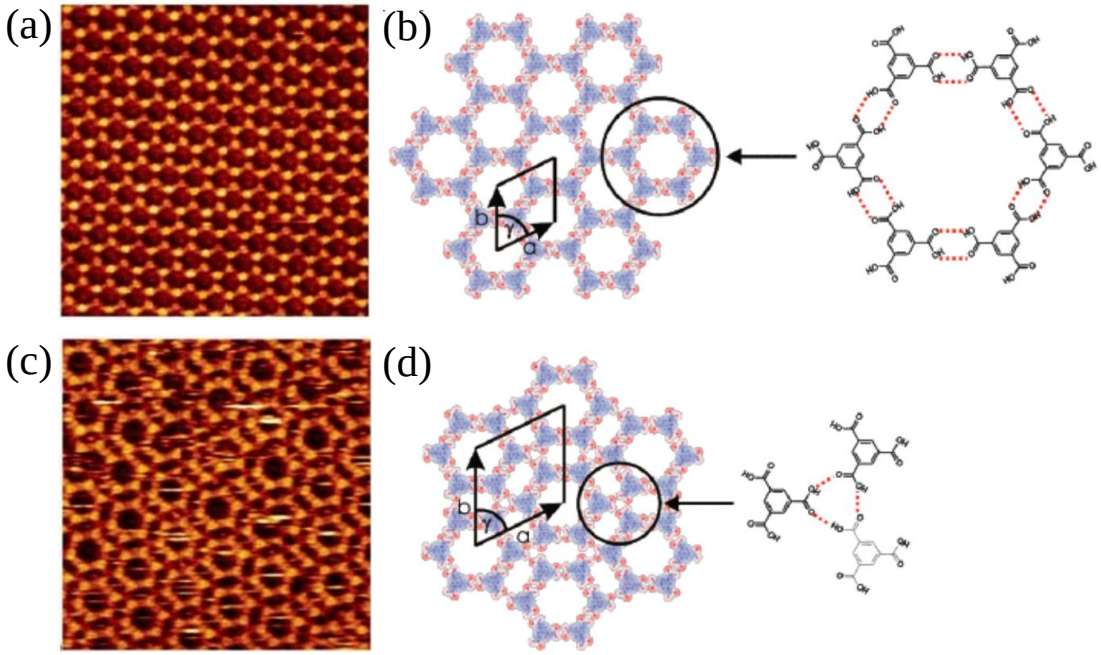

Figure 2.4. Two 15×15 nm^2 constant current STM images of TMA monolayers formed at fatty acid-HOPG interfaces. (a)-(b) STM image of the "chicken wire" structure and its corresponding molecular model; (c)-(d) STM image of the "flower" structure and its corresponding molecular model. [21]

Apart from the extensively studied carboxylic acids, researchers have also been exploring other hydrogen bonding schemes that would yield more interesting 2D functional networks. Examples include hydrogen bonding between amide groups for photosensitive self-assembled networks at liquid-solid interfaces [22], and selective hydrogen interactions between natural and artificial nucleobases [23].

In addition to hydrogen bonding, van der Waals interactions can also drive the formation of highly ordered 2D self-assembled structures. Van der Waals interactions are defined as the forces between molecules or atoms excluding covalent bonding and electrostatic interactions of ionic groups. Arising from the polarizability of atoms or molecules, van der Waals interactions exist between two instantaneous induced dipoles,

two permanent dipoles, or a permanent and an induced dipole.

Van der Waals interactions differ from hydrogen bonding in several ways. Hydrogen bonds are discrete entities associated with a specific group of atoms. A strength can be assigned to a hydrogen bond based on the energy required to break this interaction. In contrast, van der Waals interactions are cumulative and act between all the atoms of two interacting molecules. As with all non-covalent interactions, the strength of van der Waals interactions is distance dependent. The strength of the overall van der Waals interactions between two molecules depends on the contact surface areas between the atoms of the two molecules. Moreover, hydrogen bonding interactions are directional, which means the strength of a hydrogen bond can be changed significantly by changing the angle between the two hydrogen bonding groups. Unlike hydrogen bonding, the strength of van der Waals interactions does not depend on the angle between atoms. However, a specific orientation that leads to a maximum area of interaction between two molecules will be favoured by van der Waals interactions. This is caused by the fact van der Waals interactions are very short range, only operating effectively over a few Angstroms: essentially when the molecules are in direct contact. In practice, this means that the strength of van der Waals interactions between two molecules is governed by the surface area of contact between two molecules. Therefore, van der Waals interactions can drive the formation of highly ordered self-assembled structures with a specific orientation of molecules that helps achieve the maximum area of interaction.

Despite their weakness in comparison to other non-covalent interactions, van der Waals interactions have the advantage that they act cumulatively between all the atoms of two interacting molecules. For example, a combination of lateral van der Waals interactions between alkyl chains and the registry of the chains to an underlying graphite lattice makes alkyl chain interdigitation an extensively employed arrangement for network stabilisation on HOPG surfaces. As shown in Figure 2.5, the alkyl chains attached to the π-conjugated molecules are oriented along the C3 axis of the (001) plane of the underlying HOPG lattice resulting in the formation of close-packed lamellar structures [24]. The distance between two neighbouring methylene (-CH_2-) groups is

0.251 nm. This value is in good agreement with the lattice parameter of the underlying HOPG surface (0.246 nm). The registry of the alkyl chains with the HOPG surface leads to an increase in the adsorption energy of the methylene groups [25]. Additionally, the lateral interactions between the adsorbed alkyl chains also contribute to the stabilisation of the 2D self-assembled structure [26].

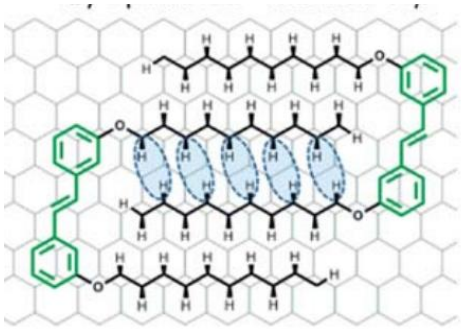

Figure 2.5. Schematic illustration showing packing interactions between interdigitated alkyl chains on a HOPG surface. [24]

π-π stacking is another non-covalent attractive interaction that plays an important role in the 2D self-assembly of molecular components containing aromatic rings. The nature of this interaction is still under investigation [27], but it has been found to be important in large aromatic molecular systems [28]. In a π system, the formation of π bonds involves the overlap of p atomic orbitals. An electron-rich π system can interact with a metal, a polar molecule or another aromatic π system. The interaction between a π electron-rich system and a π electron-deficient system is called π-π stacking [29]. As illustrated in Figure 2.6, two aromatic rings can interact with each other in a face-to-face, face-to-edge or displaced face-to-face orientation.

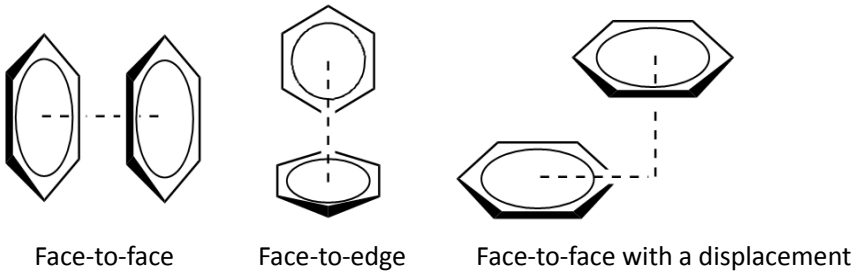

Figure 2.6. Schematic representations of benzene dimers interacting in different orientations.

Zhu *et al.* has reported the molecular arrangement of an aromatic helical polymer self-assembled both in solution and at the liquid-solid interface, as shown in Figure 2.7 [30]. From direct STM observation (Figure 2.7 (d)), the spacing distance between two adjacent double helix polymers is in good agreement with the value measured from XRD experiments (Figure 2.7 (b)). The columnar π-π stacking of the conjugated backbones leads to the formation of the helical polymers observed by STM.

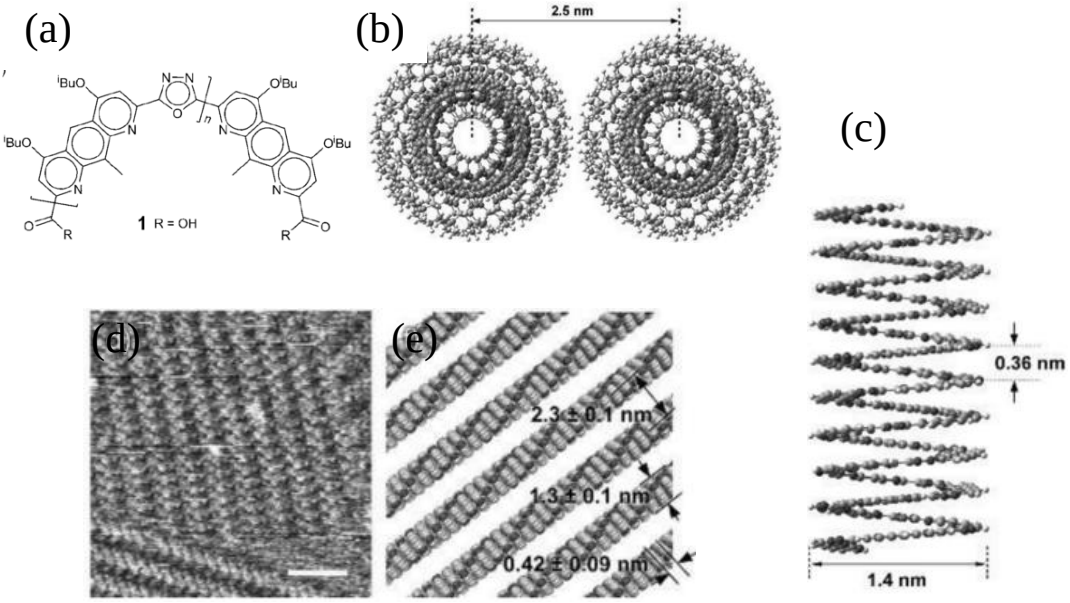

Figure 2.7. (a) Chemical structure of polymer 1. (b) Molecular model showing the distance between two adjacent polymers. (c) Molecular model presenting the columnar stacking of the inner aromatic backbone. (d) STM image of polymer 1 (scale bar: 5 nm). (e) Schematic illustration of the corresponding molecular structure in (d). [30]

In addition to intermolecular interactions, interfacial interactions also play a crucial role in 2D supramolecular self-assembly at surfaces. For studies carried out at liquid-solid interfaces, commonly used conductive substrates including highly oriented pyrolytic graphite (HOPG); Au (111); and substrate-supported graphene. These surfaces are used because they do not promote chemisorption of molecules. HOPG and Au (111) are chemically inert, thus, most organic molecules do not form covalent bonds with them: i.e. molecules adsorb onto these surfaces via physisorption. As physisorption is relatively weak compared with chemisorption, the adsorbed molecules can freely

diffuse across the surface. In the case of liquid-solid interfaces, adsorbed molecules can also desorb back into overlying solution. This free movement of molecules allows them to attach and detach from a growing self-assembled structure, and then to find the minimum free energy arrangement. Due to differences in their electronic and crystallographic structures, these surfaces interact with molecular building blocks in different ways. The predominant interactions between an organic molecule and one of the surfaces are van der Waals and electrostatic forces.

Upon the deposition of a target solution onto a surface, some of the molecules dissolved in the solution may be physisorbed on the surface driven by van der Waals interactions. Depending on factors such as the strength of the molecule-substrate adsorption interaction, solvent, concentration and temperature, these molecules may also desorb back into the solution or diffuse across the surface. Balandina *et al.* have systematically investigated the self-assembly of a multi-component system composed of alkylated dehydrobenzo[12]annulene (DBA), isophthalic acid (ISA) and coronene molecules at the liquid-Au(111) interface [31] (Figure 2.8). By comparison with the results obtained from an identical molecular system formed on HOPG, they pointed out that the substrate material affects the adsorption energy and diffusion barrier of the molecules and their ability to act as nucleation sites for further 2D crystal growth. On Au(111), the molecules experience higher diffusion barrier in comparison to HOPG. Thus, guest molecules can act as nucleation sites on Au(111) leading to the formation of achiral pores.

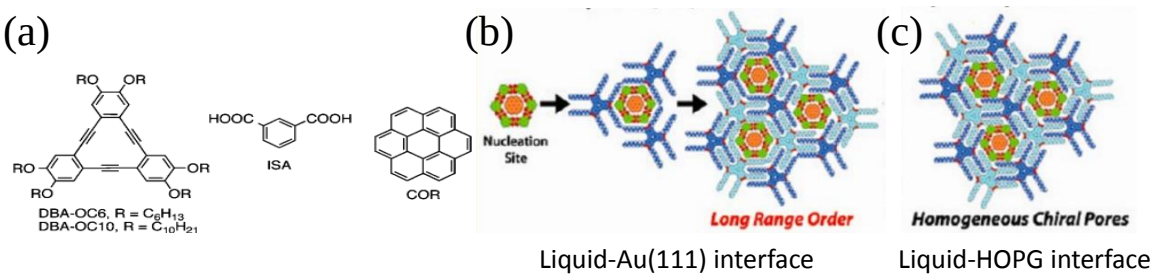

Figure 2.8. (a) Chemical formulae of DBA, ISA and coronene molecules. (b) Schematic illustrations of the formation of both chiral and achiral pores at the liquid-Au(111) interface. (c) Display of only chiral pores at the liquid-HOPG interface.[31]

2.2.2 External experimental conditions

In 2D self-assembled systems, the same molecular components have the ability to adopt different packing arrangements. This phenomenon has been observed in many molecular systems that self-assemble from a solution onto a solid surface. The self-assembly of 2D molecular networks is influenced by a combination of molecule-molecule, molecule-substrate, molecule-solvent and solvent-substrate interactions. Therefore, the morphological structures formed by 2D self-assembled networks are closely related to the formation conditions, such as temperature, the type of solvent and the concentration of target molecules.

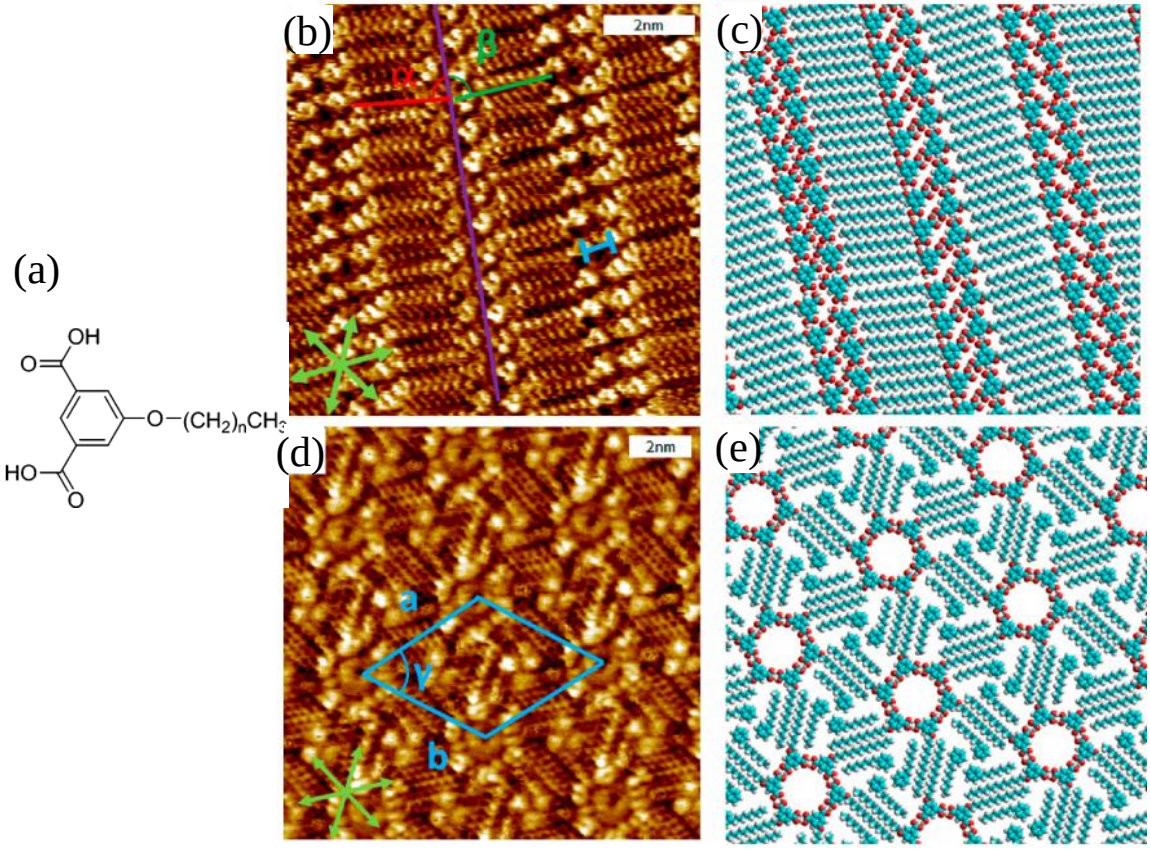

Figure 2.9. (a) Molecular structure of an alkylated isophthalic acid derivative (ISA-OC_{14}). The term *n* indicates the number of the repeating –CH_2– units (*n* = 13). (b)-(c) STM image and corresponding molecular model of the linear structure formed by ISA-OC_{14} at the interface between HOPG and 1-phenyloctane. (d)-(e) STM image and corresponding molecular model of the porous structure formed by the same molecule.[32]

The dependence of interfacial 2D self-assembly on the concentration of target molecules has been demonstrated for a number of molecular systems. The intermolecular interactions that drive the formation of concentration-dependent molecular networks include: hydrogen bonding between pyridyl containing molecules [33] and carboxylic acid groups [32]; and van der Waals interactions between interdigitated alkyl chains [34, 35]. Concentration-dependent molecular systems often consist of molecular building blocks that can have more than one packing arrangement with distinct adsorption energy, intermolecular interaction, or packing density. An example of this is the 2D self-assembly of an alkylated isophthalic acid (ISA-OC14), the molecular structure of which is shown in Figure 2.9 (a) [32]. At high concentrations, ISA-OC14 self-assembles into a mixture of a close-packed, linear structure (0.69 molecules/nm^2) and a porous structure (0.33 molecules/nm^2) in separate domains as shown in Figure 2.9 (b)-(e). In contrast, less ISA-OC14 molecules adsorb at the interface at low concentrations. This decreased presence of ISA-OC14 leads to the formation of only the porous structure. The co-adsorption of solvent molecules within the hexagonal pores and between the interdigitated alkyl chains helps compensate the energy loss raised by the formation of less densely packed structures. In a more recent study, the concentration-dependent self-assembly of a pyridyl containing molecule at the liquid-solid interface has been investigated using density functional theory (DFT) simulations [33]. This theoretical method calculates the packing density, the adsorption energy and the energy of intermolecular interactions for each of the self-assembled structures the target molecule can form. The calculation results reveal that the number of the target molecules per surface area plays an important role in determining the morphology of self-assembled structures. The number of molecules present on the surface is tuneable by changing the concentration of the solutions deposited onto the surface [36]. Thereby, the respective dominance of porous and densely packed structures at low and high concentrations can be predicted.

Solvent molecules may play a dual role in 2D molecular self-assembly. The universal function of solvent molecules is to dissolve target molecules and act as a medium for interfacial 2D self-assembly. However, in some cases, especially for porous

2D molecular networks, solvent molecules may also participate in self-assembly as a second molecular component. Solvent molecules with favourable functional groups for self-assembly, for example, carboxylic acid groups and alkyl chains, are particularly likely to co-assemble with target molecules through hydrogen bonding or van der Waals interactions [37]. Solvent co-adsorption effects lead to difficulty in determining whether the observed network structure is the most thermodynamically stable one or not. An effective method for determining if an observed structure is metastable is simply heating the network [38]. When given enough energy, metastable network structures, caused either by solvent co-adsorption or other kinetic trapping effects will re-arrange into the equilibrium structures. True phase transitions between different equilibrium structures are indicated by reversible transition between structures.

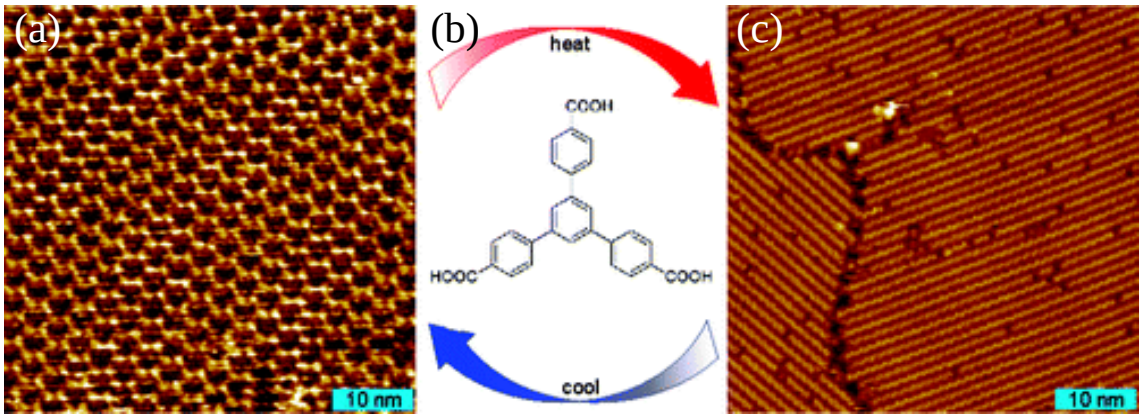

Figure 2.10. Reversible temperature-induced phase transition observed for 1,3,5-tris(4-carboxyphenyl) benzene (BTB) networks self-assembled at the nonanoic acid-HOPG interface. (a) STM image of the nanoporous phase acquired at 25 ℃. (b) Chemical structure of BTB. (c) STM image of the densely packed structure obtained at 55 ℃.[39]

Substrate temperature has a significant influence on the thermodynamics and kinetics of 2D self-assembly processes. Firstly, an elevated temperature is favourable for the removal of kinetic effects and can lead to the formation of thermodynamically stable structures [40]. Structural transitions from metastable to thermodynamically stable phases are irreversible. This means if a sample is cooled back to the initial low temperature, the structure at the equilibrium state will not change back. Secondly, changes in substrate temperature can also result in reversible transitions between two

equilibrium states. R. Gutzler *et al*. presented a system that displayed a reversible phase transition from a nanoporous low-temperature phase to a more densely packed high-temperature phase [39]. The molecular system in question was 1,3,5-tris(4-carboxyphenyl) benzene (BTB) at a fatty acid-HOPG interface as shown in Figure 2.10. The transition temperatures were found to be related to the type of solvent and the solute concentration. A thermodynamic model was employed to interpret the experimental results by means of analysing the entropic cost and enthalpy gain upon monolayer self-assembly. This study suggested that elevation of the temperature favoured desorption of weakly bound solvent molecules from the nano-porous phase. Removal of these solvent molecules from the surface led to the thermodynamic stabilisation of the densely packed polymorph over the nano-porous polymorph and resulted in the phase transition.

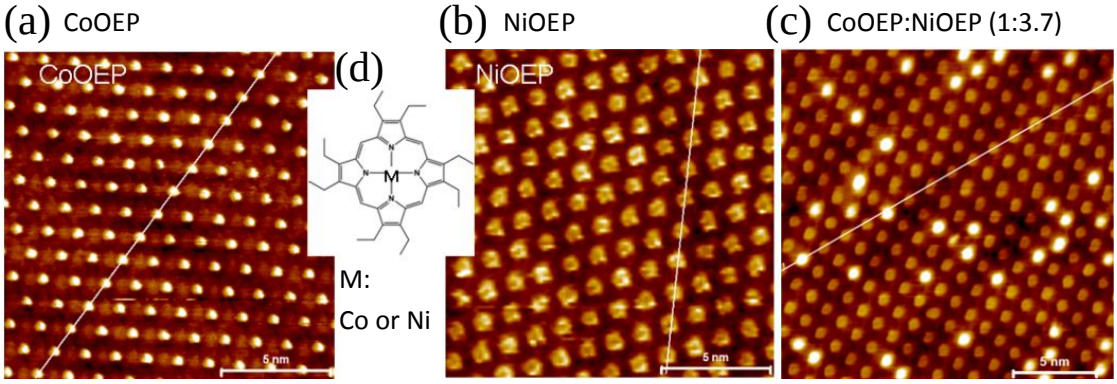

Figure 2.11. (a)-(c) STM images showing the self-assembled molecular networks formed by CoOEP, NiOFP and a mixture of CoOEP and NiOEP. (d) Molecular structure of CoOEP (NiOEP).[41]

In addition to the formation of thermodynamically stable phases, temperature is a factor that can induce adsorption and desorption of target molecules at a liquid-solid interface. The temperature-dependent kinetics of self-assembled metal porphyrin networks at the interface between Au (111) and phenyloctane has been investigated by K.W. Hipps *et al.* [41]. Figure 2.11 (a) and (b) show the STM images of the mono-component self-assembled networks formed by cobalt(II) octaethylporphyrin (CoOEP) and nickel(II) octaethylporphyrin (NiOEP), respectively. These two

porphyrin species exhibit different apparent heights in the STM images collected using the same scanning parameters. Since CoOEP appears higher NiOEP, these two porphyrin species are clearly resolved in the STM image of the bi-component molecular network formed by a mixture of porphyrins (Figure 2.11 (c)). Consequently, desorption of either CoOEP or NiOEP can be traced using STM operating at the liquid-solid interface. In order to study the desorption of CoOEP, a mono-component CoOEP network was prepared and then exposed to a solution containing both NiOEP and CoOEP. The sample was heated at a range of temperatures for different time lengths. Any exchange in composition between the molecular network and the upper solution can be observed and analysed quantitatively. The results show that a temperature as high as 135 ℃ is needed to overcome the desorption barrier for CoOEP at the interface between Au(111) and the mixture of both NiOEP and CoOEP.

2.3 Inclusion of guest molecules

Using porous molecular networks as adsorption sites for guest molecules is one potential approach to add functionality to 2D self-assembled molecular networks. In addition to adding functionality, the inclusion of guest molecules within molecular networks also provides the ability to arrange individual molecules in 2D with nanometre accuracy. A range of guest molecules have been reported to be accommodated within surface-confined nano-porous structures. The ability of various molecules to act as effective guests depends on their size and geometry and the complementarity between guest molecule and the pores of the host network.

Simple examples of guest molecules include coronene, which has been shown to fill the pores of hexagonal networks formed from trimesic acid at the liquid-solid interface [42]. As research into host-guest molecular systems has advanced, more complex and varied guest species have been investigated along with novel strategies to understand and apply host-guest self-assembly. Coronene and its derivative hexabenzocoronene (HBC) have been reported to act as guest molecules in 1,3,5-tris[(E)-2-(3,5-didecyloxyphenyl)-ethenyl]- benzene (TSB35) host matrix as

illustrated in Figure 2.12 [43], where the dynamics of these guest molecules were probed in situ using STM. When exposing the TSB35 self-assembled network to a mixture of coronene and HBC solutions, a simultaneous adsorption of the two guest molecules within the pores of the host network was observed. Compared with HBC, coronene exhibits a higher diffusion ability within the pores. Therefore, coronene appears as a striped feature in STM images while HBC appears as a solid circular shape. The results demonstrate that the trapping and diffusion of individual guest molecules can be selectively controlled by a host self-assembled molecular network with well designed pore sizes.

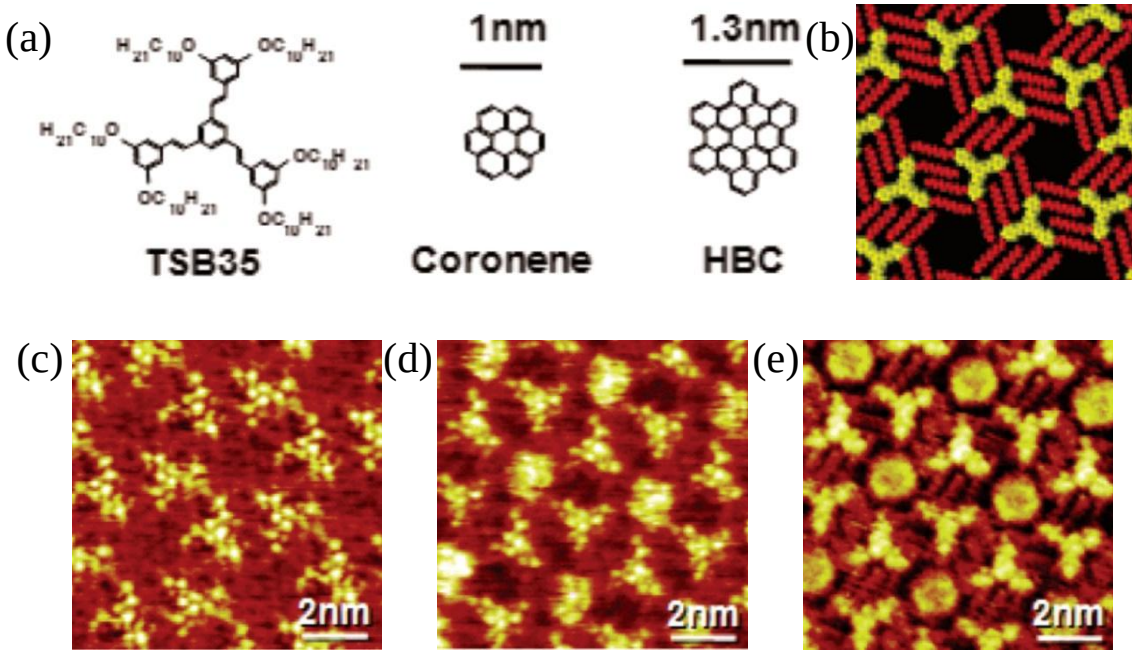

Figure 2.12. (a) Molecular structures of the host molecule TSB35 and the two guest molecules coronene and HBC. (b) A model of the porous TSB35 molecular network stabilized by van der Waals interactions arising from alkyl chain interdigitation. (c)-(e) Constant current STM images of (c) TSB35 host network on HOPG; (d) the network after the addition of coronene; and (e) the network after the addition of HBC.[43]

Studies of more complex multi-component host-guest structures have been extended to four-component molecular systems based on a DBA molecular network investigated by De Feyter *et al.* [34, 44, 45]. A DBA1 derivative with four short alkoxy chains and two longer alkoxy chains (Figure 2.13 (b)) was synthesised and used to form

a self-assembled molecular network. By changing the environmental conditions during self-assembly, such as solvent, temperature and concentration, two distinct porous structures (p6 and p2) were obtained selectively (Figure 2.13 (a)).

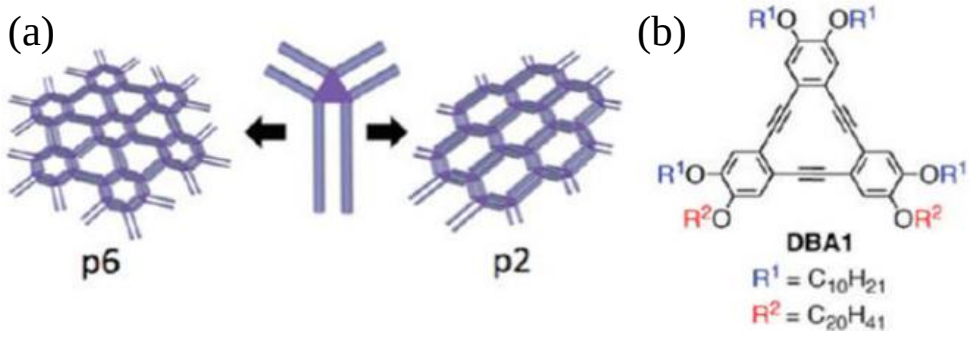

Figure 2.13. (a) Schematic diagram of the two porous structures (p6 and p2) obtained using DBA1 building block. (b) Chemical structure of the DBA1 building block with four short alkoxy chains ($C_{10}H_{21}$) on two sides of the triangular DBA core and two longer alkoxy chains ($C_{20}H_{41}$) on the third side.[34]

Both coronene-isophthalic acid (COR_1-ISA_6) heteroclusters and triangular nano-graphene (NG) species (Figure 2.14 (a)) were added into the p6 porous network. The COR1-ISA6 and NG acted as guest molecules and were observed to preferentially fill different shaped pores within the network. This selective interaction of particular guest molecules with specific pores based on shape complementarity led to the formation of a four-component self-assembled network at the interface between HOPG and 1-phenyloctane (Figure 2.14 (b)-(d)).

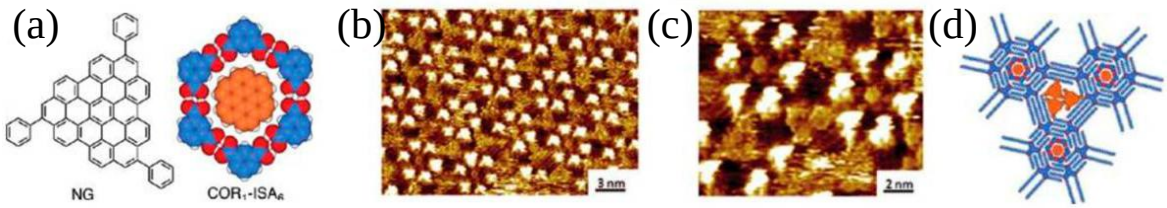

Figure 2.14. (a) Molecular structure of nano-graphene and schematic diagram of COR1-ISA6 hetero-cluster. (b), (c) STM images of a mono-layer of DBA1, coronene, ISA, and nano-graphene at the 1-phenyloctane-HOPG interface. (d) Molecular model showing the structure of the four-component network.[34]

Non-planar molecules, such as C_{60} and $C_{70,}$ are another group of guest molecules that have attracted interests from the 2D self-assembly research community. Ordered C_{60} arrays have potential technological applications in electronic devices as electron acceptors [46], and can be fabricated using 2D self-assembled networks as templates. Under UHV conditions, $C_{60,}$ $C_{70,}$ and their derivatives have been observed to organise into ordered 2D arrays on metal or semiconductor substrates, either by employing porous host networks [2, 47], or by using low temperatures to immobilise C_{60} [48]. At room temperature and pressure, the formation of ordered C_{60} arrays can be directed using porous self-assembled molecular networks at liquid-solid interfaces. Li *et al.* studied the self-assembly of a tetra-carboxylic acid functionalised molecule that forms a Kagom é pattern [49]. The 2D network self-assembled at the interface between HOPG and heptanoic acid consists of two types of pores within distinct shapes. Each of these pore types can act as adsorption sites for guest molecules: C_{60}, C_{80}, and $Sc_3N@C_{80}$. Selective adsorption of these non-planar guest molecules leads to the self-assembly of highly ordered host-guest networks. In some molecular systems, the boundaries between different domains of nano-porous networks can also act as adsorption sites for C_{60} molecules [50].

It is also worthwhile noting that the role of guest molecules is not limited to passively filling pores within self-assembled nano-porous networks. The inclusion of guest molecules can actively induce phase transitions between different structural arrangements [51] or even promote the growth of supramolecular bi-layers [52]. These results open intriguing possibilities for the control of 2D supramolecular architectures and the extension of self-assembled networks from 2D to 3D systems.

2.4 Chirality in 2D self-assembled systems

A chiral object is one that is not superimposable on its mirror image by in-plane translational or rotational motion. At the molecular level, chiral molecules demonstrate right- and left-handed appearances. The right- and left-handed mirror images of a chiral molecule are called enantiomers. Achiral molecules that can be changed into chiral

through additional interactions, e.g., adsorption on a surface, are defined as prochiral.

In 2D molecular systems, target molecules self-assembled into ordered molecular networks on a solid surface directed by molecule-molecule and molecule-surface interactions. The chiral characteristic of the resulting molecular networks is closely related to the chirality of the target molecules and the underlying surface. The interactions between chiral molecules and chiral inorganic surfaces have shown an enantio-selectivity [53]. The chiral surfaces used to study the adsorption of chiral molecules are often kink sites of single crystal metal surfaces. Examples include Pt(643) and space-inverted enantiomer surfaces created by cutting a single Pt crystal [54]. To date, the flat solid surfaces commonly used for STM investigations of 2D self-assembled molecular networks are all achiral. The achiral substrates include: HOPG and Au(111) for STM operating at ambient conditions; and Cu(100), Cu (100) and other noble metal surfaces for STM operating in ultra-high vacuum (UHV).

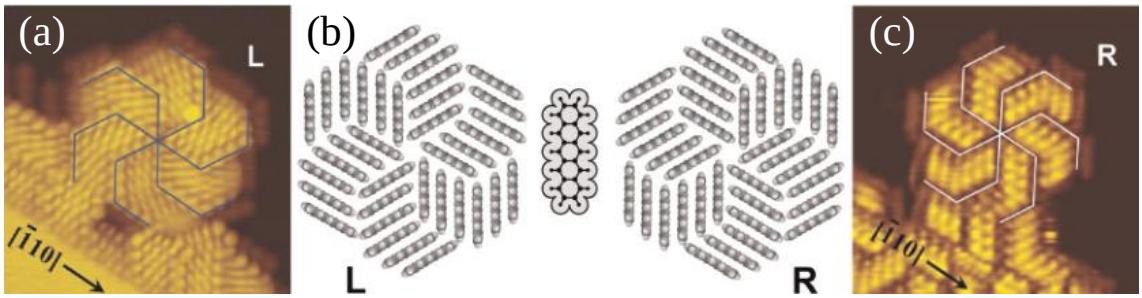

Figure 2.15. (a) and (c) STM images showing the left-handed and right-handed pinwheel structures formed by pentacene on Bi(111). (b) Molecular models of the molecular assemblies and pentacene. [55]

At achiral surfaces, chiral 2D self-assembled networks have been observed to form from molecular components that are intrinsically achiral, chiral and prochiral [56]. For achiral molecules, the chirality of the resulting self-assembled molecular networks are usually caused by molecule-surface interactions. Although no chiral feature is exhibited for the individual molecular components, the chirality of the 2D self-assembled networks may result from the oblique alignment of the molecules with respect to the underlying surface. In addition to oblique alignment, the chirality of the 2D

self-assembled networks may also arise from the interdigitation and close packing of the molecules. Figure 2.15 shows the left- and right-handed pinwheel-shaped molecular structures formed by symmetric pentacene molecules on a Bi(111) surface [55]. The chirality of the pinwheel structures is induced by the 2D self-assembly of pentacene. All of the individual pentacene molecules adsorb on the surface in a planar fashion. Each of the single pinwheel structures consists of six hexamers. In a single hexamer, six pentacene molecules are aligned parallel with each other. The close packing arrangement of the six hexamers gives rise to the chirality of the single pinwheel structure.

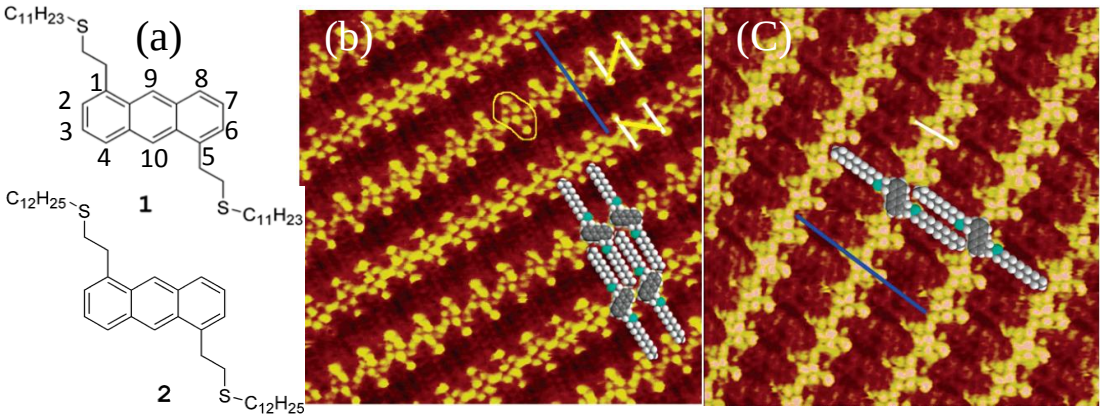

Figure 2.16. (a) Molecular structures of 1,5-bis-(3′-thia-tetradecyl) anthracene (1) and 1,5-bis-(3′-thia-pentadecyl) anthracene (2). (b) STM image showing the self-assembled network formed by the opposite enantiomers of 1 on HOPG. (c) STM image showing the self-assembled network formed by the same enantiomers of 2. [57]

In addition to 2D self-assembly induced chirality, chiral molecular networks can also result from the adsorption of prochiral molecular components. This adsorption induced chirality has been frequently observed for asymmetric planar molecules when adsorbing onto achiral solid surfaces [58]. When the opposite enantiomers of a prochiral molecule are both present on a surface, they can either form separate chiral domains or co-crystallise into a mixed domain. If the interactions between the same enantiomers are more favourable than those between the opposite enantiomers, then they form chiral domains. If the interactions between the opposite enantiomers are more favourable, they will co-assemble into mixed domains. The chain length dependent self-assembly of

alkylated anthracene derivatives is a good example showing the 2D self-assembly behaviour of a prochiral molecule on an achiral surface [57]. As illustrated in Figure 2.16 (a), the two target molecules are anthracene derivatives with alkyl chains connected to the anthracene 1 and 5 positions via sulphur atoms. For anthracene derivative 1, each of the side chains consists of ten methylene groups. Compared with anthracene derivative 1, each of the side chains of anthracene derivative 2 contains eleven methylene groups. This difference in chain length leads to the different packing arrangements of the two target molecules on HOPG surfaces as shown in Figure 2.16 (b) and (c). Both of the molecular networks self-assembled by 1 and 2 are composed of closely packed rows of a single enantiomer. For the molecular network of 1, two adjacent rows adopt a mirror-image configuration where the opposite enantiomers of 1 are present. In contrast, the energy of the molecular network formed by 2 reaches a minimum when all the molecules adopt the same enantiomer in all of the rows.

2.5 On-surface synthesis of 2D covalent molecular networks

Covalent organic frameworks (COFs) consist of extended materials, where molecular building blocks are linked by strong covalent bonds. COFs have elicited interest from a wide array of research areas including: organic synthesis; molecular nanoscience; surface science; and 2D materials. COFs can be synthesised in various forms, such as 3D-COFs, bulk 2D-COFs and mono-layer 2D-COFs. 3D-COFs consist of a single interlinked molecular crystal. In bulk 2D-COFs, 2D covalent molecular layers are stacked on top of each other driven by van der Waals interactions. Discussions in this chapter will focus on mono-layer 2D-COFs that have been grown directly onto supporting surfaces.

The structure of mono-layer 2D-COFs is analogous to that of other 2D layered materials: e.g. graphene and hexagonal boron nitride. If the periodically distributed carbon atoms in a graphene sheet were replaced with organic molecular building blocks, then a 2D molecular network is created. In this 2D layered structure, the target functional molecules are linked together via covalent bonds.

The formation of a variety of mono-layer 2D-COFs structures with potential applications in nanotechnology have been explored under UHV conditions as well as at solid-liquid and solid-vapour interfaces. One example is 1,3,5-tris(4-bromophenyl) benzene (TBPB) (Figure 2.17 (a)). TBPB assembles into ordered, close-packed mono-layers on Au(111) at room temperature under UHV. On annealing to 110 ℃, the TBPB molecules were observed to form porous 2D networks (Figure 2.17 (b)) by undergoing a surface-mediated Ullmann coupling reaction between the Br functional groups [59]. The TBPB covalently linked network was further applied as a template to direct the adsorption of thermally evaporated C_{60} molecules on the surface.

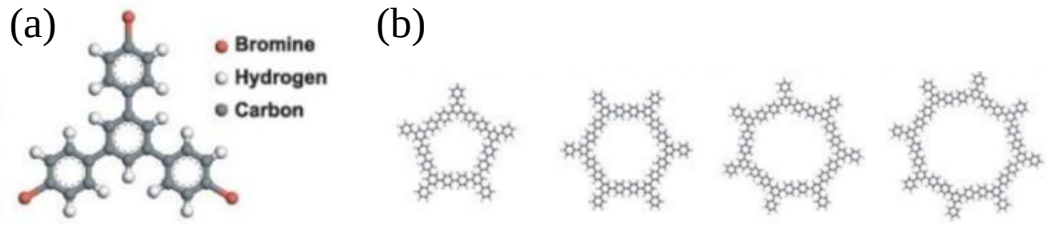

Figure 2.17. (a) Molecular structure of the TBPB molecule. (b) Schematics of different pore types formed in the TBPB 2D-COF.[59]

Since Grill *et al.* made the first mono-layer covalently linked network via an Ullmann coupling reactions [60], a large number of 2D-COF structures have been created and characterised by various innovative approaches. 2D covalently bonded polymer networks have attracted attention from experimental chemists and raised interest in the study of their electronic structures through theoretical methods [61, 62].

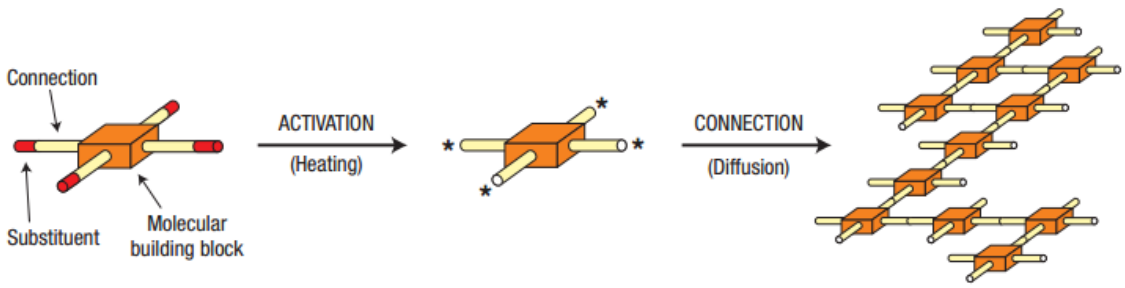

Figure 2.18. Scheme showing the method of constructing 2D-COFs proposed by Grill *et. al.* [60], in which molecular components bear chemical groups for radical addition reactions.

Strategies to synthesise mono-layer 2D-COFs include top-down exfoliation of bulk 2D-COFs [63] and direct formation of mono-layer 2D-COFs from molecular building blocks via on-surface synthesis. The on-surface synthesis approach is currently the most widely used method for the synthesis of mono-layer 2D-COF materials. The chemical structure of molecular components plays a key role in controlling the final morphology of 2D-COFs. As can be seen from Figure 2.18, Grill *et al.* employed molecular building blocks functionalised with chemical groups that can undergo radical addition reactions to form ordered covalently bonded nano-architectures [60]. The work is a good example of building up extended 2D-COFs without the need for the addition of other external molecules as linkages to connect the target functional components.

Connecting target molecular components using additional linker molecules is another effective design strategy used for the growth of 2D-COF materials. Figure 2.19 shows a schematic illustration of this construction method. The precursor molecules A with a three-fold symmetry (marked in red) are connected by the linker molecule B with a two-fold symmetry (marked in blue). Connecting A and B together allows the formation of an extended porous network with hexagonal morphology. The formation of the molecular network is driven by a chemical reaction between functional groups at the reactions sites of the two molecular species.

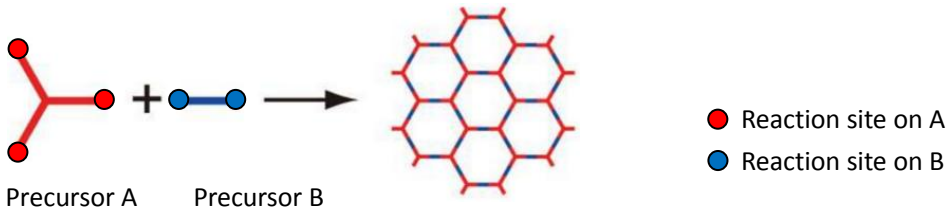

Figure 2.19. Representative 2D-COFs construction scheme using additional molecules as linkers [64].

The morphology and dimensions of the resulting 2D-COFs built from the coupling reactions shown in Figure 2.19 are highly tuneable and can be controlled by varying the size, shape and chemical structure of the molecular building blocks used. The shape of the molecular building blocks, and the properties of the chemical reaction sites also

have a significant influence on the physical and chemical properties of the final 2D-COFs mono-layers.

In order to grow high-quality mono-layer 2D-COFs with pre-designed structure and function, a better understanding of the chemical reactions used to form these systems is required. Under different reaction conditions, distinct experimental parameters are adjusted carefully to help elucidate their influence on the resulting 2D-COF structure. Performing 2D-COFs growth outside UHV conditions has proven to be an effective and easy to implement approach. A range of growth environments from ambient to high pressures have been investigated to synthesise mono-layer 2D-COFs. The applicability of these different growth environments depends on the activation conditions of the chosen reaction scheme for 2D-COF formations.

On-surface synthesis approaches to the formation of ordered mono-layer 2D-COFs involve the formation of covalent bonds between molecular building blocks via suitable chemical reactions schemes. The suitability of a reaction scheme is based on several factors. Firstly, the reaction must be selective so that covalent bonds are formed only at desired locations on the molecular building blocks and undesired side reactions are avoided. Secondly, the reaction must maintain the symmetry of the original molecular building blocks. This requirement is based on the concept of reticular synthesis [65]. In this synthesis approach, the final morphology of the 2D-COF can be tuned by controlling the structure of the individual molecular components. Thirdly, the reaction should be reversible under suitable growth conditions. This requirement allows the formation of highly ordered 2D-COF structures. To date, Ullmann coupling, boronic acid condensation and Schiff-base condensation reactions have been the most widely employed chemical reactions used to grow mono-layer 2D-COFs outside of UHV.

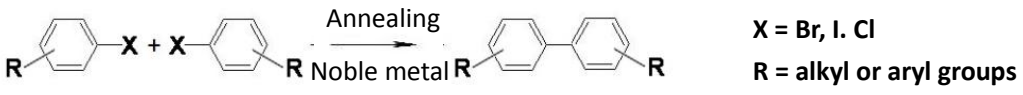

Figure 2.20. Ullmann couple reaction assisted by a noble metal surface.

The Ullmann reaction is a radical addition coupling reaction that takes place

between aryl halides in the presence of a metal catalyst, such as Cu, Ag or Au (Figure 2.20). Noble metals are widely believed to participate in the reaction by forming an intermediate metal-organic complex with C radicals following the breaking of C-X bonds.

Typical surface-assisted Ullmann coupling reactions start with the pre-organisation of target molecules on a metal surface via 2D self-assembly. Subsequently, the sample is annealed at elevated temperatures to activate covalent crosslinking. Most on-surface Ullmann coupling reactions are performed under UHV conditions. However, this reaction scheme has also been demonstrated to be applicable under ambient conditions [66, 67]. Most early work on on-surface Ullmann reactions adopted active metal surfaces which act as catalysts for the coupling reactions. The application of this reaction scheme in on-surface synthesis of 2D-COFs is limited by the irreversibility of the coupling reactions. Additionally, the activation conditions of the coupling reactions requires high temperatures and the presence of a metal substrate. This also leads to a narrow range of growth conditions that are suitable for the connection of molecular building blocks directed by Ullmann reactions.

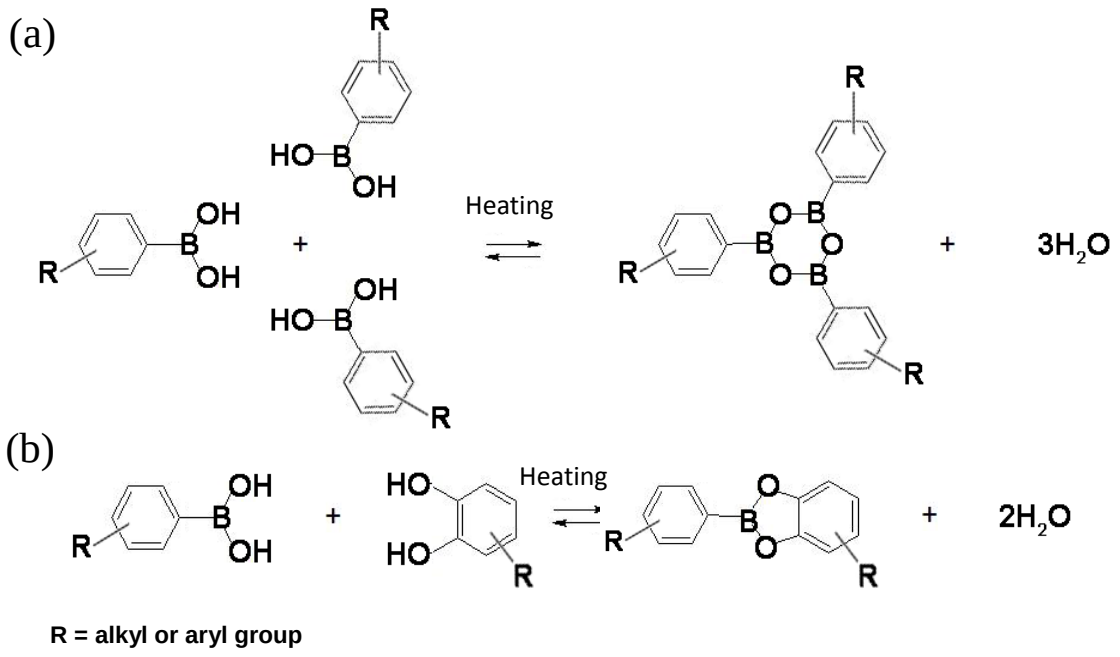

Figure 2.21. Boronic acid condensation reactions. (a) Boroxine ring formation via poly-condensation reaction between three boronic acid derivatives. (b) Boronic ester formed by the condensation reaction between a boronic acid and a diol group.

The formation of hexagonal boroxine rings and boronic esters results from condensation reactions between boronic acids and diol groups (Figure 2.21). The self-condensation of boronic derivatives was first introduced by Yaghi and co-workers in the synthesis of 3D bulk COFs using solvothermal methods [68]. Zwaneveld *et al.* later applied this synthetic scheme to form 2D networks via the co-deposition of ditopic and tritopic boronic acid derivatives onto Ag (111) in UHV [69]. Unlike radical addition reactions, boronic acid condensation reactions can be activated with no requirement for the presence of catalytic noble metals. On chemically inert surfaces, such as HOPG, boronic acid condensation has been employed to obtain extended highly ordered 2D-COFs [70]. The flexible activation conditions allow for boronic acid condensation reactions to be performed outside of UHV conditions.

Another key advantage of boronic acid condensation, and other condensation reactions, is that the equilibrium position of the reaction can be controlled via the presence of water in a closed reaction vessel. Control over the equilibrium position of the reaction allows control over the reversibility of the reaction during the growth phase. As discussed previously, having a reversible reaction favours defect eliminations during growth and leads to the formation of highly ordered 2D-COF structures with large domain sizes. Studies have shown that the thermodynamic equilibrium of the boronic acid condensation reaction can be successfully tuned by the addition of a small amount of $CuSO_4$ $5H_2O$ as an equilibrium regulator [71]. Despite these advantages, the intrinsic reversibility of the boronic acid condensation reactions lowers the chemical stability of the covalent bonds in presence of water. The 2D-COFs formed using boronic acid condensation reactions are susceptible to decomposition of the boroxine or boronic ester groups by hydrolysis.

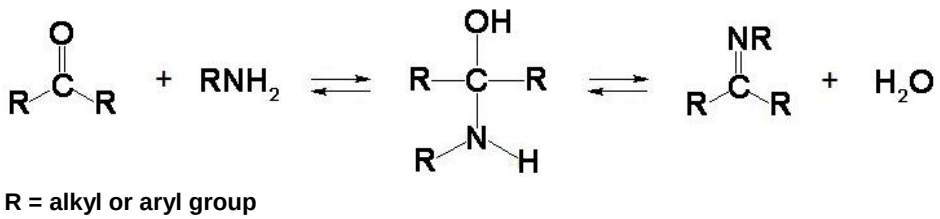

Figure 2.22. Addition and elimination steps in a Schiff base condensation reaction.

Schiff-base condensation reactions, which lead to the formation of polyimide networks, are one of the most effective reactions for the fabrication of mono-layer 2D-COFs. As shown in Figure 2.22, Schiff-base condensation involves two linked reaction steps. In the first step, an aldehyde reacts with an amine forming an unstable, intermediate product, known as a hemiaminal. In the second step, the hemiaminal group undergoes dehydration producing an imine. The reaction is reversible and can also be shifted to favour either reactants or products via the presence of water. The imine can be converted back into amine and aldehyde via a hydrolysis process.

Schiff-base condensation reactions are generally induced either by annealing or with the assistance of an acid catalyst. Amine-aldehyde covalent crosslinking has been demonstrated on an Au(111) surface under UHV conditions [72]; in aqueous solutions [73]; and at the interface between an octanoic acid solvent and a copper-supported graphene substrate [74]. Compared with the other chemical reaction schemes discussed above, Schiff-base condensation reactions exhibit the ideal combination of moderate synthesis conditions, flexibility in design of molecular building blocks and good stability of the final covalent bonds. Moreover, Schiff-base condensation reactions have the advantage over boronic acid condensation that they produce conjugated imine linkages between molecules, something that is vital for the fabrication of new fully conjugated 2D-COF materials.

The Schiff-base condensation reaction scheme has been utilised for the growth of mono-layer 2D-COFs under different conditions, including liquid-solid and vapour-solid interfaces. Liquid-solid interfaces provide a unique environment, where molecules adsorbed on a surface can be in a state of dynamic equilibrium with those in the overlying solution. The ability of molecules to easily adsorb and desorb from the surface helps to minimise kinetic effects for self-assembly at liquid-solid interfaces. In turn, this facilitates the assembly of thermodynamically stable 2D molecular structures. The dynamic environment offered by liquid-solid interfaces has been used to produce highly ordered 2D self-assembled networks and 2D-COFs. The presence of a solution layer above the growing 2D-COF is especially favourable for covalent reaction schemes where the reversibility of the reaction can be tuned by control over the solution pH.

To date, the growth of mono-layer 2D-COFs at liquid-solid interfaces has been applied for both Schiff-base condensation and boronic acid condensation reactions [70, 75]. Tanoue *et al.* [73] introduced a general surface-based solution approach for the fabrication of extended 2D porphyrin networks (Figure 2.23). In this fabrication scheme solution pH and the substrate material were carefully selected for the purpose of achieving spontaneous and selective polymerization reactions. Later, Xu *et al.* reported an in-situ STM study of an imine-based 2D-COF formed at the interface between octanoic acid and HOPG [75]. In the resulting 2D-COF molecular arrangements resulting from incomplete condensation were frequently observed.

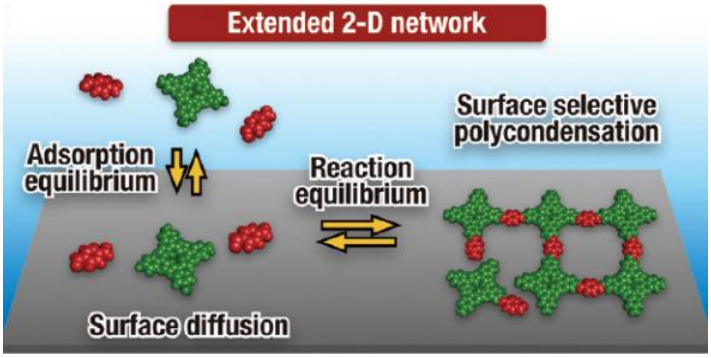

Figure 2.23. Schematic diagram showing the formation mechanism for a mono-layer Schiff-base 2D-COF, consisting of porphyrin units connected by smaller linker molecules, formed at a liquid-solid interface. [73]

Synthetic approaches to the growth of mono-layer 2D-COFs at vapour-solid interfaces are applicable to both mono-component and bi-component 2D-COFs. In mono-component systems, molecular building blocks are usually deposited on a surface followed by a reaction activation process, normally annealing. If two types of precursor molecule are used for the growth of a 2D-COF, then two distinct approaches can be adopted. Firstly, the two molecular species can be co-deposited onto the surface prior to activation [76]. Secondly, one of the precursor molecules can be deposited onto the surface while the second molecule is present in the vapour phase above the surface (see Figure 2.24) [64, 77]. In comparison, the second approach is more favourable for the growth of highly ordered mono-layer 2D-COFs. This is because the precursor molecules

deposited on the surface have more space to diffuse on the surface, thus are more likely to avoid being trapped by kinetic effects. The molecular species present in the vapour phase is able to adsorb and desorb from the interface. The increased mobility of the vapour phase component results in smaller kinetic barriers for the free energy minimisation of the molecular system. The minimisation of these barriers means that the systems can easily reorganise and defect elimination within the mono-layer 2D-COFs can proceed more quickly. Despite these advantages, a growth mode where one precursor is on the surface and the other precursor is in the vapour phase, is not suitable for linker molecules with a high boiling point.

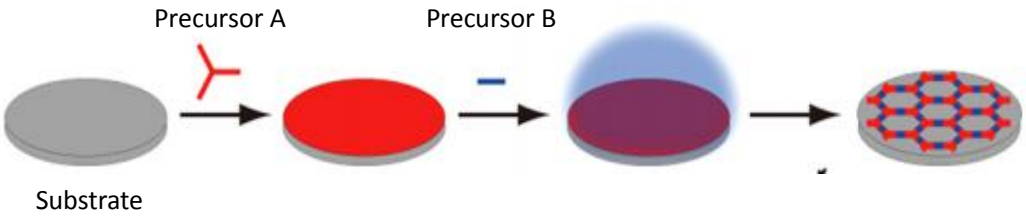

Figure 2.24. Schematic illustration of 2D-COFs synthesis between a tritopic precursor (red) that has been deposited onto a surface and a ditopic precursor (blue) that is present in the vapour phase above the surface. Growth of the 2D-COF occurs at the vapour-solid interface. [64]

For condensation reactions, during which water is released, extra water added to the vapour phase enhances the reversibility of the reactions. As a result, the reorganisation of molecules and defect elimination are promoted leading to the growth of highly ordered 2D-COFs. The concept of equilibrium manipulation has been applied to improve the synthesis of 2D COFs via boronic acid and Schiff-base condensation reactions [64, 71]. Additional water can be introduced to the reaction schemes by adding a suitable amount of $CuSO_4$ $5H_2O$ as an agent to regulate the dehydration processes.

Many interesting aspects of 2D-COFs grown at vapour-solid interfaces have been investigated, such as synthesis on copper supported graphene surfaces [74], growth of 2D-COF bi-layers [78], network structures with non-aromatic linkages [79], and side functionalisation of 2D-COFs [80]. Moreover, 2D-COFs formed at vapour-solid interfaces are accessible to further tests of their capability in technological applications, due to the absence of an overlaying solution layer. For example, both boroxine- and

imine-based 2D-COFs have been used as host templates for the adsorption of guest molecules [81, 82]. In order to study the performance of 2D-COFs as components in electrodes, electrochemical measurements have been carried out to test a porous, imine-based 2D-COFs grown on graphene layers [83].

2.6 Conclusions

In this chapter, non-covalent and covalent interactions that have been used in the formation of 2D self-assembled molecular networks and 2D-COFs have been summarised. The control over 2D self-assembled structures has been discussed with a focus on thermodynamics and kinetic effects for molecular systems formed at liquid-solid interfaces. Examples reported in the literature demonstrate how the functionality of interfacial 2D self-assembled architectures has been explored via the addition of guest molecules. 2D-COFs have been introduced as a class of novel 2D materials that are able to overcome the chemical and thermal weakness suffered by 2D self-assembled networks. The increased stability of 2D-COFs in comparison to 2D self-assembled molecular networks makes them ideal candidates for a range of technological applications. To deepen the understanding of the physical and chemical properties of 2D-COFs, further investigations into the formation of highly ordered 2D-COF mono-layers with complex multi-component structures and desired chemical functionality are required [64]. A key advance related to the fabrication of highly-ordered 2D-COFs over extended scales would be a method to pre-organise molecular precursors in a controlled manner prior to covalent bond formation.

Chapter 3

Methodology

Discussions in this chapter are focused on the main experimental techniques and simulation tools used to investigate 2D molecular networks in this thesis. The experimental techniques include scanning tunnelling microscopy (STM), atomic force microscopy (AFM), and X-ray photoelectron spectroscopy (XPS). The simulation method employed in this work was molecular mechanics (MM) simulation. Firstly, a description of the physical principles that form the basis of these experimental and theoretical methods will be given. Secondly, the specific equipment (and software packages) used for the research presented in this thesis and the current state-of-the-art for the respective techniques will be discussed. Finally, examples of the application of these techniques in the study of molecular nano-architectures on solid surfaces will be briefly described.

3.1 Introduction

Scanning probe microscopy (SPM) encompasses a large collection of different microscopy techniques that are used in surface characterisation. The thing that all SPM techniques have in common is that a sharp probe, commonly referred to as the tip, is used to map features on a surface. The tip is brought into close proximity with a surface, normally within a few nm or less, and scanned across the surface using a piezo-electric scanner. Interactions between the tip and the surface means that the tip can record a signal that is related to a certain property of the surface: e.g. height, charge, or temperature. The particular property of the surface being measured is specific to each different type of SPM. The sharpness of the tip and the distance dependence of the interactions between the tip and the surface means that the property is only measured for the local region of the surface directly underneath the tip. By scanning the tip

back-and-forth across the surface while measuring the signal in question, a map of the surface can be built up, often with a lateral resolution ranging from a few nm down to Angstroms. Among the variety of existing SPM techniques, STM and AFM are the most widely adopted imaging and manipulation tools used for the real space investigation of 2D self-assembled or covalently bonded molecular networks on solid surfaces.

Despite the high levels of spatial resolution, standard SPM techniques such as STM and AFM often only provide information on the morphology and structure of a surface molecular layer. Information such as the height, lateral size of molecular features and unit cell dimensions for ordered 2D molecular crystals are commonly obtained by these techniques. However, while providing detailed structural information, STM and AFM provide little or no information about the chemical composition of surface molecular features. Thus, the experimenter is often left to infer the exact chemical structure of molecular structures based on a prior knowledge of the molecular building blocks used. While this approach can be effective for simple systems, when structures have been formed where a covalent reaction has occurred, it is often necessary to use a technique that provides additional information on the chemical structure and composition of surface features. As a complementary approach to SPM, X-ray photoelectron Spectroscopy (XPS) is a quantitative, surface-sensitive technique that can be used to analyse the chemical state of adsorbates on a sample surface.

Molecular Mechanics (MM) simulations offer a computationally inexpensive theoretical approach to the interpretation of molecular structures resolved by STM. MM allows the easy construction and testing of a wide variety of different surface molecular structures. The results from MM simulations, most often the 2D unit cell dimensions for molecular networks, can be directly compared to results obtained from SPM. Therefore, MM helps elucidate the packing morphologies and non-covalent bonding modes adopted by molecules in surface-based 2D molecular structures.

The combined utilisation of SPM, XPS and MM simulations provides a comprehensive set of information concerning the properties of 2D molecular networks formed either via supramolecular self-assembly or via on-surface covalent synthesis.

3.2 Scanning Tunnelling Microscopy (STM)

3.2.1 Basic principles of STM

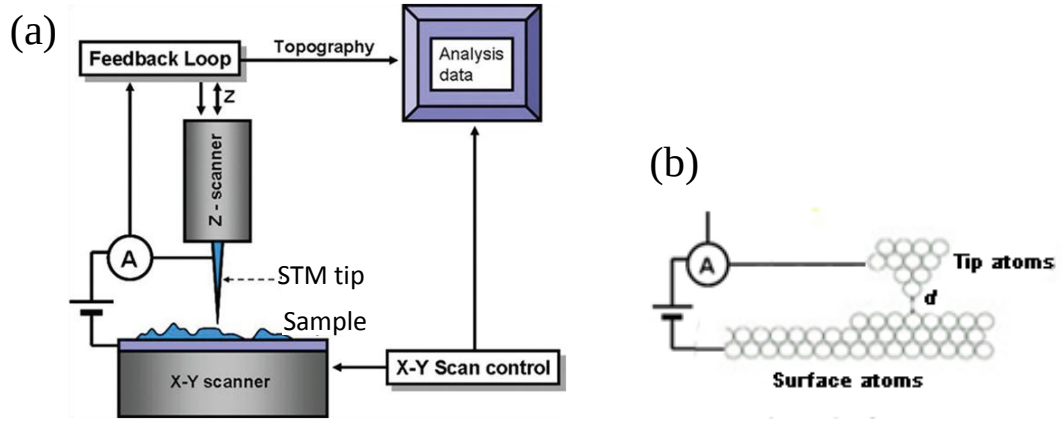

Figure 3.1. (a) Schematic representation of the basic operational principles of STM. (b) Image showing the atomic scale depiction of the tip-sample tunnel junction.

STM, invented by G. Binnig and H. Rohrer at IBM Zürich in 1982 [84], was the first SPM technique to be developed. In STM, a bias voltage is applied between a sharp metallic tip and a conductive sample as shown in Figure 3.1 (a). When the tip is positioned within a few nanometres of the sample surface, electrons can tunnel through the narrow gap between the tip and the surface forming a measurable electrical current called the tunnelling current.

The direction of the tunnelling current depends on the polarity of the bias voltage. STM commonly operates in two different imaging modes: constant current mode and constant height mode. In constant-current mode, which is the first and most widely used mode in STM operation, the tunnelling current is maintained at a set-point value by means of adjusting the height of the probe tip using a feedback loop. As the magnitude of the tunnelling current is small (a few nA or pA), it is amplified by a tunnelling current amplifier prior to entering the feedback loop. The feedback loop is essentially an electronic circuit that converts current to voltage. The tunnelling current is constantly monitored by the feedback loop. In order to maintain the tunnelling current at a constant value, the feedback loop adjusts the gap between the tip and the sample surface. The

motion of the STM probe is controlled by stepper motors and the piezo scanner. The piezo scanners are calibrated during manufacture using samples with known feature size. When a particular voltage is applied to the scanner, it is known exactly how much it will move in a particular direction. Thus, the voltage signals that are sent to the Z piezo scanner in constant current mode can be used to build a height map of the surface. The probe height recorded at each location is then used to directly reconstruct the scanned area of the surface as a real space topographic map.

3.2.2 Understanding the tunnelling current

The primary signal detected in STM experiments, the tunnelling current, results from the tunnelling of electrons between the tip and the surface, a phenomena which can only be understood from the viewpoint of quantum mechanics. The description of the dynamic properties of microscopic particles in quantum theory by the use of wavefunctions leads to several phenomena that are at odds with our classic view of the macroscale physical world. One such phenomenon is quantum mechanical (QM) tunnelling. The wave-like nature of electrons means that they are able to "tunnel" from one electronically conductive region to another through a non-conductive potential energy barrier. Importantly, this tunnelling occurs even when the height of that barrier is greater than the electron's own energy. The rate at which electrons can tunnel through such a barrier is delicately dependent on a number of factors including: the height and width of the barrier; the potential energies of the electrons before and after tunnelling; and the local density of electronic states of the two electrical contacts on either side of the barrier. In order to build a robust and accurate theory of QM tunnelling all of these factors need to be taken into account.

Electron tunnelling

The mathematical description of quantum mechanical tunnelling has been elaborated in a large number of journal papers [85-87] and book chapters [88-90]. These

descriptions adopt different levels of complexity and theoretical detail depending on what aspect of tunnelling they are attempting to explain.

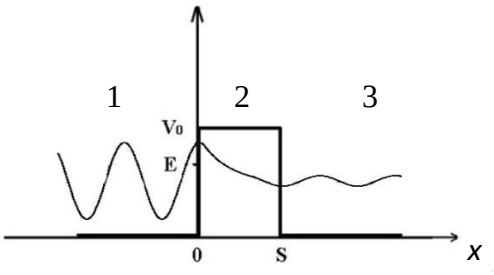

Figure 3.2. Schematic diagram of an electron traversing a 1D rectangular potential barrier which can be divided into three regions marked as 1 ($x < 0$), 2 ($0 < x <$ S), and 3 ($x >$ S). E: energy of the electron. V_0: height of the potential barrier.

Among the various theoretical treatments, elastic tunnelling through a one-dimensional (1D) rectangular potential barrier is a simple but illustrative model used to understand the electron tunnelling effect (Figure 3.2). By solving the time-independent Schrödinger equation for the regions 1, 2, and 3, respectively, the barrier transmission coefficient T, which is defined as the square of the ratio of the transmitted flux to the incident flux, is derived as:

$$T = \frac{1}{1+\left(K^2+\aleph^2\right)^2/\left(4K^2\aleph^2\right)\sinh^2(\aleph s)} \tag{3.1}$$

In equation (3.1) the decay rate is given by $\aleph = [2m(V_0 - E)]^{1/2}/\hbar$, K is the wavenumber of the tunnelling electrons, m is the mass of electrons, s and V_0 are respectively the width and height of the one-dimensional rectangular potential barrier, E is the energy of the impinging electron, and $\hbar$ is the Planck's constant divided by 2π.

If the energy barrier is strongly attenuating, $\aleph s >> 1$, then:

$$T \approx \frac{16K^2\aleph^2}{(K^2+\aleph^2)^2}\cdot e^{-2\aleph s} \tag{3.2}$$

Typically, the barrier transmission coefficient T is exponentially dependent on the

barrier width s and the square root of an effective barrier height $(V_0 - E)^{1/2}$, regardless of the exact shape of the barrier. Inspired by this fact that the barrier transmission is extremely sensitive to the barrier width, G. Binnig and H. Rohrer and coworkers developed the idea that a type of microscopy with unprecedented levels of spatial resolution could be built based on this electron tunnelling effect [88].

Tunnelling between an STM tip and the surface

In STM, electron tunnelling occurs across a tip-surface junction as illustrated in Figure 3.3. Figure 3.3 (a) shows a simplified representation of the energy levels of an STM tip and a solid surface when the tip-surface distance is infinitely large. The tip and surface can be regarded as two isolated objects with their own Fermi levels (E_F) and work functions (ϕ_{tip} or ϕ_{surface}). If the tip and surface are then brought into very close proximity (s < 10 Å), their Fermi levels align when reaching an equilibrium, leading to a shift in vacuum level (Figure 3.3 (b)). This alignment is caused by the tunnelling of transient electrons. In the case of the diagram shown in Figure 3.3 (a), the electrons tunnel from the surface to the tip, which lowers the Fermi level of the surface and raises that of the tip. This tunnelling is instantaneous and only proceeds until the Fermi levels are aligned at which point no further current flows. When reaching the state shown in Figure 3.3 (b), no tunnelling current flows between the tip and the surface across the energy barrier.

As can be seen from Figure 3.3 (c), a tunnelling current occurs if a bias voltage is applied across the tip-surface junction. When the tip is biased negatively with respect to the surface, the Fermi level of the tip is raised with respect to that of the surface. The raising of the tip Fermi level allows electrons to tunnel from filled tip states through the barrier into empty states in the surface. Similarly, if a positive bias is applied to the tip with respect to the surface the tunnel current will flow in the opposite direction. From this qualitative description of electron tunnelling effects in STM, we can clearly see that the magnitude of the tunnelling current between an STM tip and a surface will depend on the bias voltage V and the electronic structures of the tip and the surface.

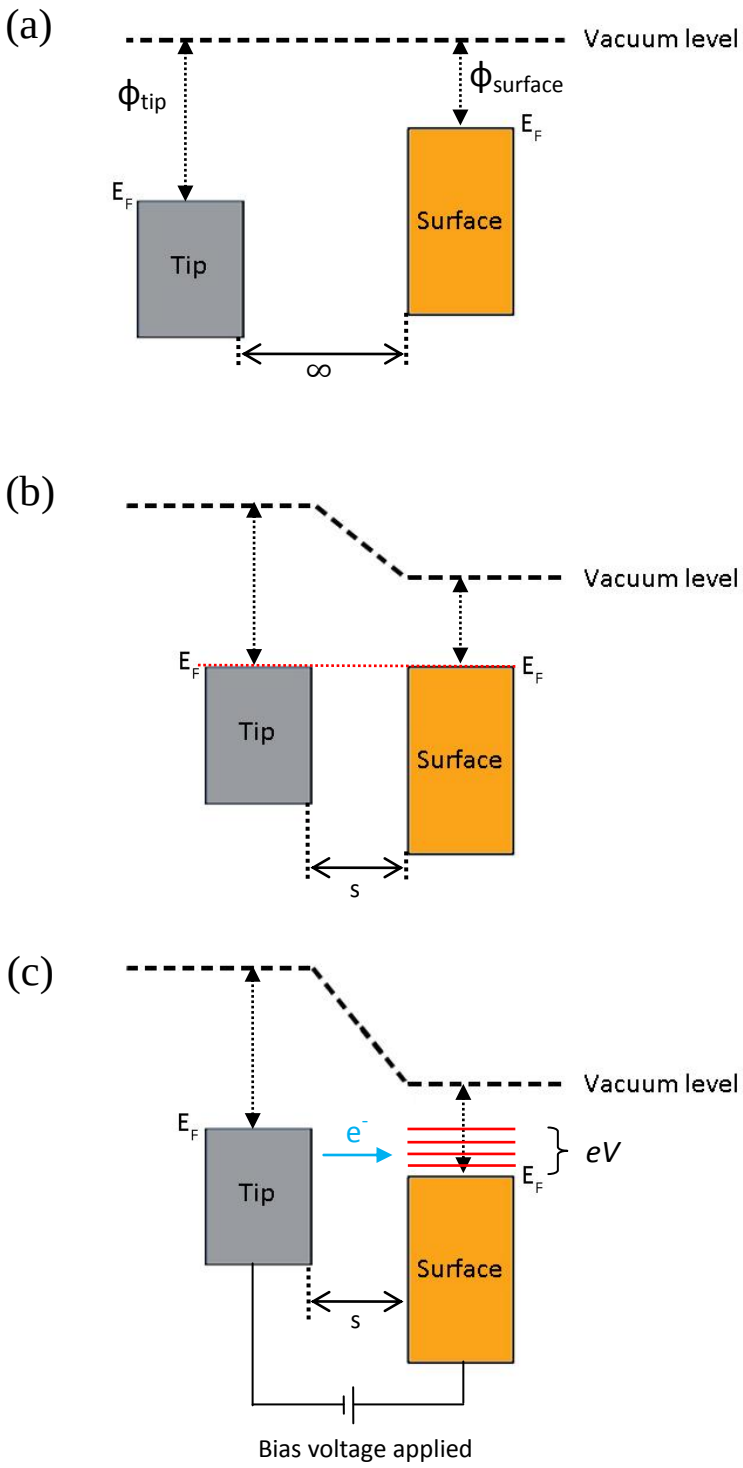

Figure 3.3. Schematic diagrams showing energy schemes of a tip-surface junction in STM under different conditions. (a) The tip and surface have infinite separation, thus can be regarded as isolated objects. (b) When the tip and surface are brought into close proximity their Fermi levels align. (c) When the tip is biased negatively with respect to the surface, the Fermi level of the tip is raised above that of the surface and electrons can tunnel from filled states in the tip to empty states in the surface. As a result, a tunnelling current is established. *eV*: increase in the Fermi level of the tip caused by the bias voltage. Red lines: empty sample states. Blue arrow: tunnel current flowing from the tip to the surface.

Tersoff-Hamann Theory

Since the invention of STM, several more complete theoretical models have been developed in an attempt to derive a general formula for elastic tunnelling between an STM tip and a surface. These description include theories established by Tersoff and Hamann [91, 92], Lang [93-95], Wentzel-Kramers-Brillouin (WKB) [96] and Chen [97]. The model suggested by Tersoff and Hamann is one of the most widely used to interpret STM images.

According to Fermi's golden rule [98], an initial expression of the total tunnel current flowing between the tip to the sample can be written as shown in equation (3.3):

$$I = I_{t\to s} - I_{s\to \mathrm{t}} = -\frac{2\pi e}{\hbar} \int |M_{ts}|^2 N_t(E - eV) N_s(E)[f_s(E) - f_t(E - eV)]dE \qquad (3.3)$$

In equation (3.3), $f(E) = [\exp((E - E_F)/k_B T) + 1]^{-1}$ is the Fermi function, k_B is the Boltzmann constant, T is the temperature, $N(E)$ is the density of states, M_{ts} is the matrix element of the perturbation potential between the tip (*t*) and the sample (*s*), and *V* is the potential applied across the tip-surface junction.

At *T* = 0 K, the Fermi function can be represented by a step function, and thus the tunnelling current can be simplified to the form shown in equation (3.4):

$$I\,(\mathrm{T} = 0) \approx -\frac{2\pi e}{\hbar} \int_{E_F}^{E_F + eV} |M_{ts}|^2 N_t(E - eV) N_s(E) dE \qquad (3.4)$$

While the polarity of the bias voltage applied between tip and surface determines the direction in which the tunnel current flows, the magnitude of the bias voltage also plays an important role in the tunnelling process. The magnitude of the bias voltage defines the energy that tunnelling electrons have with respect to the Fermi levels of the tip and surface. As the local density of states for a real sample will vary with energy, the magnitude of the bias voltage can have a significant impact on the magnitude of the tunnel current.

In order to calculate the tunnelling current I, the matrix element M_{ts} should be evaluated. Bardeen first applied time dependent perturbation theory to analyse the matrix element M_{ts}, which can be expressed using equation (3.5) [99]:

$$M_{ts} = \frac{\hbar^2}{2m}\int_S (\Psi_s \nabla \Psi_t^* - \Psi_t^* \nabla \Psi_s) \cdot d\mathbf{S} \tag{3.5}$$

In equation (3.5) the surface integral $\int_S d\mathbf{S}$ is evaluated over any arbitrary surface that separates the tip and surface regions. Ψ_t and Ψ_s, represent the wave functions of the tip and surface, respectively.

According to the approximations introduced by Bardeen, knowledge of the wave functions of the tip and the sample are required in order to evaluate M_{st} quantitatively. However, the electronic structure at the very end of the tip is usually unknown. To address this problem, Tersoff and Hamann proposed the first quantitative model in which the STM tip is represented by a single s-orbital located at the apex of the STM tip (see Figure 3.4).

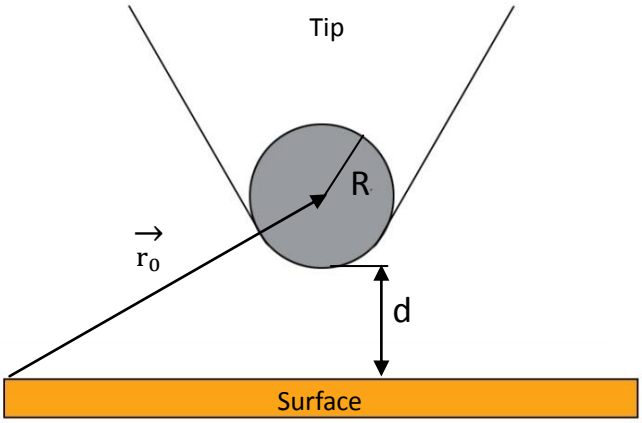

Figure 3.4. Tip-surface model built by Tersoff and Hamann [92]. The tip apex is assumed to be spherical with a tip radius of curvature R. $\mathbf{r_0}$ denotes the vector linking an arbitrary point on the surface with the centre of spherical tip. The term d is the shortest distance between the tip and the surface.

In the theory proposed by Tersoff and Hamann, the wave function used to represent

the STM tip is assumed to be a spherically symmetric s-wave function. The justification for this simplification is based on the exponential dependence of the tunnel current on the tip-sample distance. The exponential decrease in tunnel current with increasing tip-sample separation means that for a real tip geometry the vast majority of tunnel current will flow through the atom at the apex of the tip. The tunnelling current between the tip and the surface is regarded as resulting from an overlap of the s-wave function with the surface structure.

At low temperature ($\approx$ 0 K) and low bias voltages, the total tunnelling current can be simplified to the expression shown in equation (3.6):

$$I = \frac{2\pi e}{\hbar} V \sum_s |M_{ts}|^2 N_t(E_F)\delta(E_s - E_F) \tag{3.6}$$

In order to calculate the matrix element M_{ts}, the wave functions of the surface and the tip are analysed. The surface wave function Ψ_s can be written as a 2D Bloch expansion and inserted to the Schrödinger equation to obtain a new expression. The tip wave function Ψ_t can be calculated using the form of an s-wave function and then rewritten as a 2D Fourier sum. If the surface plane $\mathbf{S}$ separating the surface and tip is assumed to be parallel with the surface, the matrix element M_{ts} is found to be proportional to Ψ_s at the tip centre of curvature $\mathbf{r_0}$.

$$M_{ts} \propto \Psi_s(\mathbf{r_0}) \tag{3.7}$$

As a result, the total tunnelling current is given by equation (3.8):

$$I \propto V N_t(E_F) \sum_s |\Psi_s(\mathbf{r_0})|^2 \delta(E_s - E_F) \tag{3.8}$$

As the sum $\sum_s |\Psi_s(\mathbf{r_0})|^2 \delta(E_s - E_F)$ corresponds to the surface local density of states (LDOS) at the Fermi level evaluated at the position of the point probe, the STM tunnelling current is then given by equation (3.9):

$$I \propto VN_t\,(E_F)\mathrm{LDOS}(\mathbf{r_0}, E_F) \tag{3.9}$$

The total tunnelling current is therefore proportional to the LDOS of the surface in the Tersoff and Hamann's model. Thus, STM images acquired at low bias voltages and in constant current mode can be interpreted as a contour map of constant surface LDOS.

3.2.3 Applications of STM in studying molecules on solid surfaces

STM is a powerful experimental technique for the study of molecular nanostructures adsorbed on solid surfaces. A wide range of experiments have been performed to both visualise and manipulate atoms/molecules at surfaces using STM.

As a structural characterisation tool, STM offers the ability to produce real-space images of molecules with atomic resolution. STM has proven to be particularly effective for the study of conjugated organic adsorbates. STM images allow us to understand the morphology, molecular interactions, and quantum phenomena of low-dimensional molecular structures. In constant-current mode, conjugated moieties, such as aromatic rings, are observed to have a brighter contrast. This is related to the high density of states around the Fermi level present in conjugated systems.

When electrons tunnel through an organic molecule physisorbed on a solid surface, the resulting image is a result of the complex interaction of the surface, molecule and tip electronic states. A good understanding of all three of these systems is required in order to arrive at the correct interpretation of an STM image. Because of the involvement of the electronic density of states of the adsorbate in the tunnelling process, the tunnelling current through a tip-molecule-substrate junction depends on the energy of the highest occupied molecular orbital (HOMO) and the lowest unoccupied molecular orbital (LUMO) of the adsorbed molecule relative to the tip and surface Fermi levels [100]. Moreover, the tunnelling current also depends on the mixing of the molecular orbitals with the surface electronic states. For molecules that strongly interact with the underlying surface, the LDOS will be a mixture of the molecule and surface electronic

states: the well-defined molecular orbitals of some molecules are broadened by the interaction with the surface. Under UHV conditions, this broadening effect can be reduced by depositing a thin insulating layer on the surface prior to adsorption of the molecule. The insulating layer de-couples the adsorbed molecules from the conducting surface. Experimental and theoretical investigations of some molecular systems have been reported showing that STM image contrast is bias-dependent [101, 102]. For instance, A. J. Fisher and P. E. Blöchl [103] have simulated STM images of benzene on graphite over a range of bias voltages using electronic structure calculations. They concluded that the STM image contrast at low voltages results from weak mixing of benzene and graphite states while the images at higher voltages represent a map of only the molecular states.

Currently, STM investigations can be carried out under a range of different environmental conditions, including: ambient and ultra-high vacuum (UHV) conditions. UHV STM systems enable most of the manipulation experiments of single atoms/molecules creating artificial nano-architectures [104, 105]. Regarding thermal drift and the mobility of molecules, low temperature conditions are usually required for STM manipulation on atomic/molecular scales. At these low temperatures, any gases in the atmosphere above the surface would quickly adsorb, contaminating the surface and destroying the experiment. A careful control over the interaction between the atom at the very end of an STM tip and the single atom/molecule being manipulated is required in order to move the atom/molecule to a predesignated position [106]. Moreover, STM tips can even enable activation of on-surface chemical reactions with single-molecule precision [107].

Compared with UHV STM systems, STM operating at ambient conditions has a number of advantages and disadvantages. Apparently, STM systems operating under ambient conditions do not demand expensive UHV chambers and pumping equipment. This significantly reduces both the price and complexity of these systems. More importantly, ambient STM allows the experimenter to probe both the formation and the chemical behaviour of molecular surface structures under technologically relevant environmental conditions such as at liquid-solid interfaces. Firstly, ambient STM

systems enable studies of chemical reactions. For example, Hulsken *et al.* reported the first example of real-time single-molecule studies of oxidation catalysis at a liquid-solid interface [108]. In their work, the individual catalysts self-assembled at the interfaces were monitored using ambient STM so that the activity and stability of the catalysts could be measured. Secondly, the less strict requirements concerning the operating conditions allows adsorption and desorption occurring during physisorption processes to be revealed [109, 110]. Thirdly, reversible modification of the structural arrangement of 2D molecular networks are achievable through the adjustment of the external environment [111-113]. Despite these advantages, STM systems operating under ambient conditions have less imaging stability, higher noise levels, and the potential for contamination in comparison with UHV STM equipments.

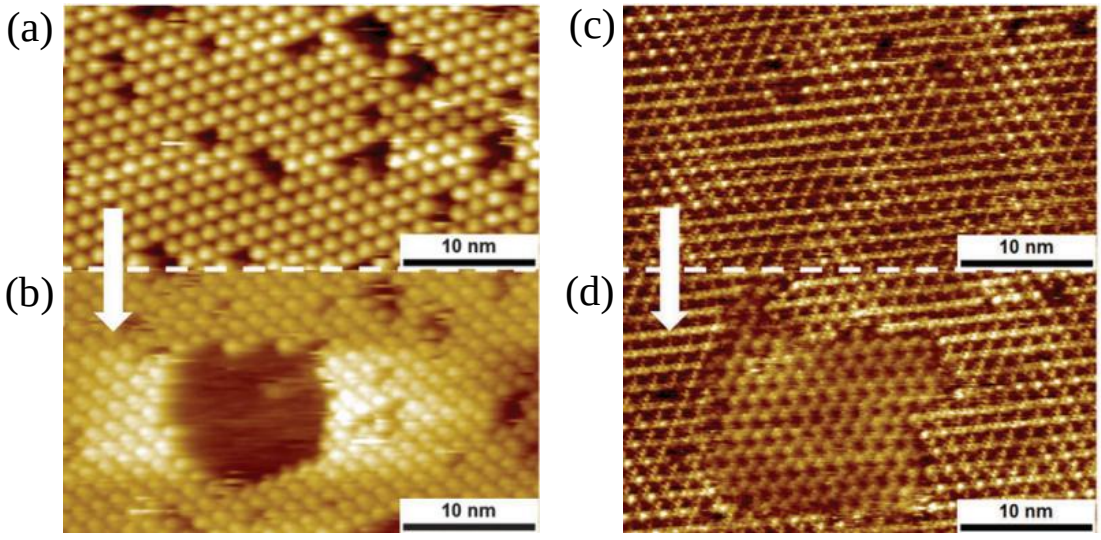

Figure 3.5. STM images showing the results of molecular patterning achieved using a STM system operating under ambient conditions. (a)-(b) show STM images of C_{60} molecules sitting within the pores of a 2D-COF sheet, while (c)-(d) show a bi-layer COF.[114]

Recently, several novel areas of application for STM operating under ambient conditions have been explored. Nirmalraj *et al.* have studied the molecular dynamics and electronic structure of C_{60} and its derivatives adsorbed at the interface between silicone oil and a spacer-coated Au(111) surfaces using *in situ* STM/STS [115]. The experimental platform designed in this work opens up opportunities to achieve

single-atom/molecule measurements at liquid-solid interfaces without requiring cumbersome UHV STM systems operating at low temperatures. Moreover, ambient STM has been used as a SPM lithography facility realising local molecular manipulation. Plas *et al.* have reported a successful case of patterning guest-host covalent organic framework (COF) structures by using ambient STM [114]. Figure 3.5 shows the removal of C_{60} molecules and bilayers of COF structures caused by carefully tuned STM scanning conditions.

3.2.4 Data acquisition and processing in ambient STM

Experimental setup

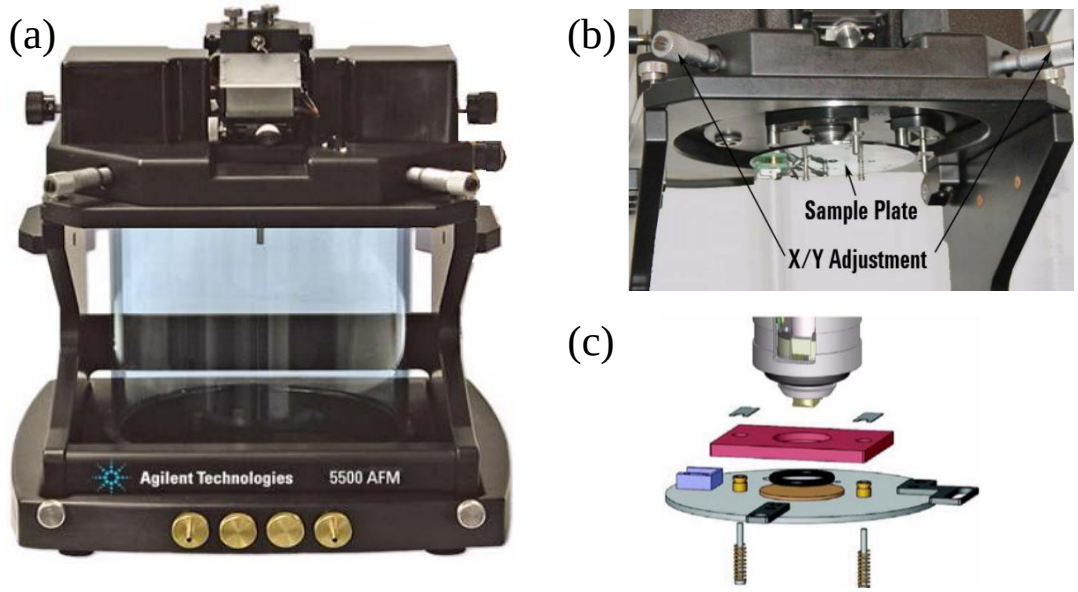

Figure 3.6. (a) Agilent 5500 series SPM microscope including glass environmental chamber for carrying out experiments under inert gas and low humidity atmospheres. (b) Sample plate magnetically attached to the microscope body. (c) Schematic illustration of the assembly of a liquid cell for STM imaging at liquid-solid interfaces [116].

An Agilent 5500 SPM system was employed for all of the STM investigations presented in this PhD thesis. Figure 3.6 (a) shows the core part of the SPM, the microscope equipped with a detachable environmental chamber. STM imaging is extremely sensitive to noise, mechanical vibration and air turbulence. This sensitivity

means that the microscope is positioned on the top of an anti-vibration device which is housed inside an acoustic isolation chamber. The anti-vibration device consists of either an air table which has a heavy table top floating on four nitrogen pistons, or an active vibration cancellation system where piezo-electric actuators are used to both sense and compensate for mechanical vibrations. The sample plate that holds the sample and makes electrical contact to it is attached to the microscope stand by three magnetic posts. These magnetic posts are connected to stepper motors that allow the coarse vertical positioning of the sample stage with respect to the tip. The lateral position of the sample plate is adjustable within ± 5 mm controlled by X and Y micrometer screws (Figure 3.6 (b)). STM measurements at liquid-solid interfaces can be achieved by fixing a liquid cell and an O-ring on the sample plate, as presented in Figure 3.6 (c). The liquid cell allows a small volume of liquid (50 – 100 μl) to be held on the sample surface for extended STM imaging.

Specimen and tip preparation

Sample surfaces used for STM experiments need to be conductive and flat. Commonly used substrates for ambient STM systems include highly oriented pyrolytic graphite (HOPG) and Au (111). HOPG substrates have the dual advantages of chemical inertness and very simple preparation procedures.

A new HOPG surface with large atomically flat areas can be easily formed by cleaving off the top layers of a HOPG sample using adhesive tape to expose a fresh HOPG surface. Commercial HOPG substrates are classified into three levels in terms of their quality: ZYH (grain size: 30 – 40 nm), ZYB (grain size: up to 1 μm), and ZYA (grain size: up to 10 μm). Figure 3.7 shows the structure and an example STM image of the HOPG surface [117, 118]. When imaged using STM, only half the atoms in the surface layer appearing as bright features because of the ABA stacking of the HOPG layers.

Gold substrates are normally made by thermal evaporation of a thin layer of gold film onto a heated mica or silicon substrate. Annealing procedures are necessary to

reconstruct the Au(111) surfaces and remove any contamination.

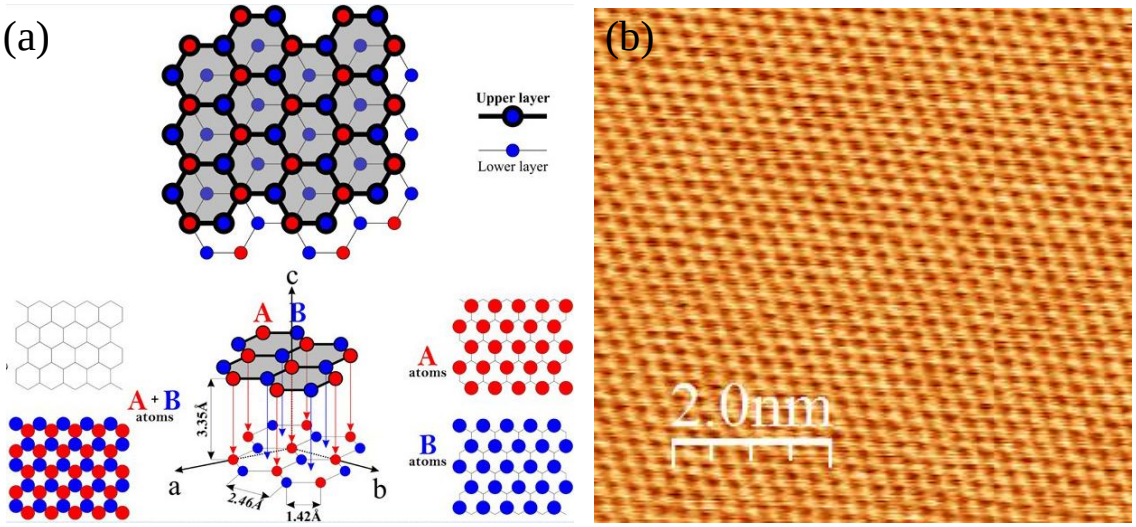

Figure 3.7. (a) Schematic representations of the crystal structure of bulk graphite. The upper section of the figure shows a top view of the graphite surface. The structure shown in the lower left corner represents an idealized STM image of the HOPG surface where both the A and B atoms are visualized. The structure shown in the lower right corner displays how the STM image would appear if only either A or B atoms are visualized [117]. (b) The most frequently observed STM contrast for HOPG. Each bright spot corresponds to an individual carbon atom. The oblique lattice shown in the STM image is in good agreement with the case in the lower right corner of (a). Image size: 5 nm × 5 nm. STM imaging parameters: V_s = 0.05 V, I_t = 1 nA.

Due to the exponential dependence of the tunnelling current on the tip-sample distance, the vast majority of tunnelling current flows through the atom at the very end of the STM tip, as demonstrated in Figure 3.1. Consequently, the fabrication of an atomically sharp STM tip is of extreme importance to the acquisition of STM images with atomic resolution. Under UHV conditions, tungsten tips are widely adopted for STM studies. However, in air, tungsten oxidises readily forming a nonconductive tungsten oxide coating on the tip surface. Thus, tungsten probes prepared for UHV STM systems by chemical etching are not applicable to ambient conditions. In place of tungsten, platinum-iridium (Pt/Ir) alloy is widely employed for STM tips used in ambient atmospheres and at liquid-solid interfaces [119]. Etching of Pt/Ir tips is possible [120], however, for most experiments simple mechanical cutting of Pt/Ir wire will produce an acceptable STM tip. Beyond these standard STM tips, scientists have

recently proposed the possibility of collecting STM images with atomic resolution for Au (111) or graphite surfaces using a variety of carbon-based tips, such as carbon fibre and diamond tips [121-124].

Drift correction

As the lateral and vertical resolution of STM is able to reach down to the atomic scale, STM is an effective experimental method for accurately measuring the lattice parameters of 2D molecular networks physisorbed at the liquid-solid interface. However, in order to interpret quantitative information from STM images precisely, various distortions arising during the image acquisition process need to be taken into consideration: the most prominent of these is image drift.

There are a number of possible reasons for STM image distortion that have been discussed in previous research [125-127]. The drift of an STM tip with respect to the scanned sample surface underneath is said to play a dominant role in causing differences between the structures that are observed in STM images and the real structure of the sample surface. Drift effects present in STM images may result from a variety of effects. One of the most common factors to induce drift into STM images is the differing rates of thermal expansion of STM components due to changes in temperature [128]. In addition to temperature effects, distortions may arise because the scanned area on the surface and the STM scanning plane are not parallel, depending on the sample installation slope [129]. Finally, in addition to the above factors, the hysteresis and creep of piezo-electric materials employed in the STM scanners can also contribute to causing distortions during STM scanning. Unlike the variable distortions associated with temperature and sample orientation, these scanner induced distortions remain constant for a specific piece of STM equipment [130, 131].

For the work presented in this thesis, a drift correction process has been applied to some high resolution STM images in order to remove the effects of drift and obtain accurate unit cell dimensions for 2D molecular layers. Drift correction of STM images is based on using the known lattice dimensions of the HOPG surface as a calibration

lattice. Drift correction is performed by first collecting an STM image of the target molecular structure. Immediately after acquisition of this image and without altering any scanning parameters that could influence the level of drift in the image (e.g. scan direction, scan speed, scan size or scan angle), an image of the underlying HOPG lattice is obtained. The HOPG surface can be selectively imaged over the molecular layer by adjusting the set-point and sample bias to values of I_t = 1 nA and V_s = 0.05 V, respectively. Changing the set-point and sample bias alters the vertical distance between the tip and the sample but leaves the lateral drift of the sample with respect to the tip unaffected. This means that the two images, that of the molecular structure and of the underlying HOPG lattice, should have the same level of lateral drift and therefore their structures should be distorted by the same amount.

A software package (SPIP software, Image Metrology, Denmark) is then used to analyse the unit cell constants of the image of the graphite surface. This process is based on calculating the two-dimensional Fourier transform of the STM image of the HOPG surface. A set of correction parameters are then calculated through the comparison of the distorted HOPG unit cell with the known unit cell values of the graphite lattice as presented in Figure 3.7. These correction parameters represent the image modification that is required to make the HOPG lattice in the drift-distorted image match the known values for the HOPG lattice. As we have assumed that the levels of drift for the image of HOPG as the same as for the image of the molecular structure, we can then apply the same correction parameters to the image of the molecular structure in order to obtain a drift-corrected image.

All large-scan STM images presented in this report have been flattened using WSxM or SPIP software [132]. All high-resolution STM images have been processed using SPIP software (Denmark, Image Metrology).

3.2.5 Advantages and drawbacks of STM

Compared with other surface characterisation tools, for example electron microscopy, STM probes the electronic properties of a sample’s surface by detecting a tunnelling

current in the near-field regime. In this case, the resolution of STM is no longer limited by diffraction and can reach atomic scales. Because no free electrons are involved in the tunnelling process, STM measurements are not limited by the environmental conditions and can be conducted in conditions ranging from ultrahigh vacuum (UHV) to liquid-solid interface. This flexibility makes STM a powerful technique for the investigation of self-assembled molecular networks in a range of different environments. Electrons that tunnel between the STM tip and sample surface have a low energy, in the order of a few electronvolts, which is smaller than the energy of typical chemical bonds. Because of this, STM is applicable for imaging samples without causing damage to the chemical structure of the samples being studied. Another significant advantage of STM is that even non-periodic structures can be directly determined in real-space, leading to its potential applications in the study of complex systems.

Despite the above advantages, one of the major limitations of STM is that insulating surfaces cannot be imaged. The requirement for a very small tunnel current often less than 1 nA to be measured for STM to operate means that only highly conductive substrates can be used. In order to overcome this drawback, other SPM techniques have been developed that probe different interactions and do not require an electrical current to flow between tip and surface. The most widely used of these SPM techniques is atomic force microscopy (AFM). Another limitation of STM is that operating under ambient conditions it provides very limited information about the chemical composition of a sample surface. Thus, complementary spectroscopic techniques need to be used in conjunction with STM in order to fully understand the structural and chemical composition of 2D molecular networks.

3.3 Atomic Force Microscopy (AFM)

3.3.1 Basic principles of AFM

In 1986, G. Binnig, C. F. Quate and C. Gerber developed the first AFM which was able to provide topographic information for both conductive and insulating surfaces [133].

The signal measured in AFM is based on the interaction forces between a sharp probe and a sample surface.

Figure 3.8 (a) presents the basic principle of the AFM technique. In AFM, a sharp tip, mounted at the free end of a cantilever beam, scans a specimen surface line by line. The interaction forces between the tip and the surface (see Figure 3.8 (b), (c)) cause the cantilever to bend. The deflection of the cantilever is detected by a laser beam which is focused to the back-side of the cantilever and reflected into a photodetector. This configuration allows the deflection of the cantilever to be monitored by observing the position change of the laser spot on the photodetector. In the majority of AFM configurations a feedback loop is then used to keep the tip-surface interaction maintained at a constant set-point value.

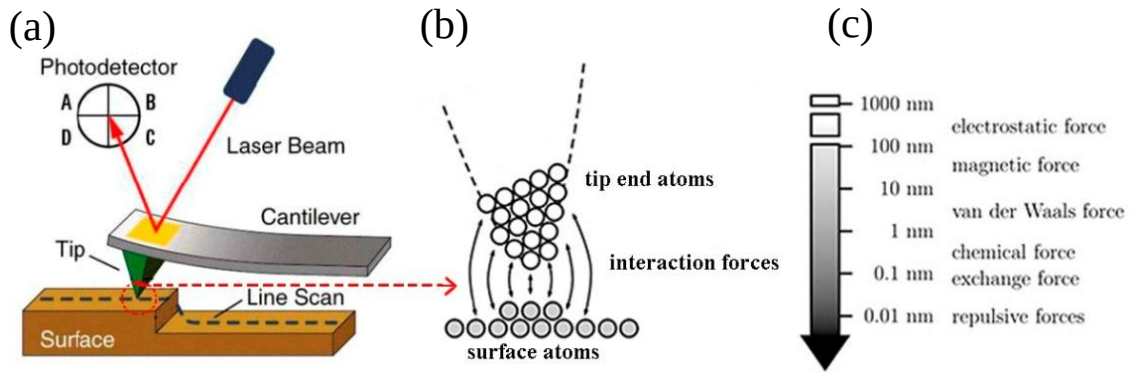

Figure 3.8. (a) Schematic diagram of a typical AFM system. (b) Enlarged image of the AFM tip-surface region. (c) General long-range and short-range interaction forces that exist during the approach of an AFM tip towards a sample surface [134].

3.3.2 Tip-surface interactions and conventional AFM imaging modes

AFM can operate in a variety of modes by means of probing different regions of the interaction potential between the tip and the surface. Generally, there are three basic imaging modes performed in AFM measurements: contact (static) mode, intermittent contact (tapping) mode and non-contact mode.

Figure 3.9 illustrates how the interaction force between an AFM tip and a surface changes as the tip approaches the surface. At large distances between the tip and the surface there is no interaction between the probe and the surface. As the tip is brought closer to the surface, long-range attractive van der Waals interactions dominate over short-range repulsive interactions resulting from the overlap of electronic orbitals. This results in an initially attractive interaction between the tip and the surface. This region of the force-distance curve is referred to as the "non-contact" region.

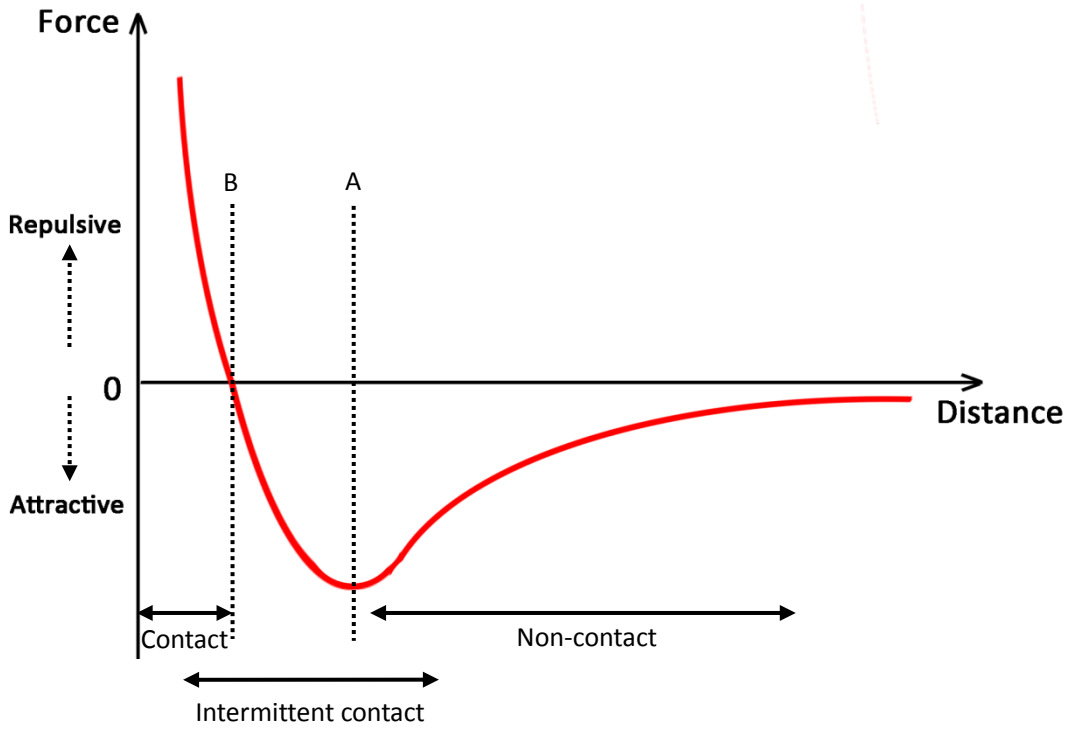

Figure 3.9. Plot showing how the force acting between an AFM tip and a surface varies as a function of the tip-surface distance. Point A corresponds to the maximum attractive force between the tip and the surface. Point B corresponds to the tip-surface distance where the attractive and repulsive forces cancel each other out.

As the tip is brought closer to the surface, the repulsive interactions begin to have a more dominant role. As the tip is brought closer and closer to the surface, it first goes through a point where the attractive interaction reaches a maximum. As the tip-surface distance is further reduced, the tip goes through an equilibrium point where the attractive and repulsive interactions cancel each other out. This equilibrium point is normally found at tip-surface separations on the order of a few Angstroms. At

tip-surface distances smaller than this, repulsive interactions dominate and the force between the tip and the surface acts to push the tip sway from the surface. This region of the force-distance curve is referred to as the “contact” region. Tip-surface distances that vary around the equilibrium point and cover regions of both attractive and repulsive interactions are termed the “intermittent contact” region.

In contact mode, a feedback loop is employed to maintain a constant cantilever deflection and therefore a constant interaction force between the tip and the surface. The surface topography is measured by measuring how much the sample position is moved in the vertical direction in order to maintain this set-point value of the cantilever deflection. The resolution of this mode can reach down to atomic dimensions because of the extremely short-range nature of the repulsive interactions between the tip and the surface. However, this sensitivity comes at a risk of the sample or the tip being damaged by the large forces that result from contact between the tip and the surface.

Non-contact mode AFM, in which the tip is not in physical contact with the surface, normally achieves good resolution under UHV conditions as opposed to ambient conditions [135]. This is primarily related to the presence of a water meniscus between the tip and the surface when imaging under ambient conditions. In non-contact mode, a piezo-electric resonator connected to the cantilever oscillates the AFM tip as it scans across the surface. The frequency of oscillation is chosen to match the resonant frequency of the AFM cantilever. Tip-surface interaction forces are detected by measuring changes in either the amplitude or the resonant frequency of the cantilever’s oscillation. To date, non-contact mode AFM operating under UHV conditions has achieved the highest spatial resolution of any SPM technique, with imaging resolution that has been able to visualise intramolecular structure including covalent bonds and even individual hydrogen bonds [136-138].

Intermittent contact (tapping) mode bridges the contact and non-contact regions of tip-surface interactions. One of the key advantages of tapping mode is that it is able to obtain high resolution images of delicate sample surface without inflicting the same level of damage associated with contact mode imaging. In tapping mode a cantilever with attached tip is oscillated at its resonant frequency while scanning across a surface.

Changes in the distance between tip and surface caused by topographic features on the surface change the force acting on the tip and thereby change the amplitude of the cantilever's oscillation. Similar to other SPM techniques, a feedback loop is used to maintain a constant oscillation amplitude by moving the tip vertically. These vertical movements of the tip are then used to construct a topographic map of the surface.

3.3.3 Applications of AFM in molecules on solid surfaces

Advanced AFM systems are able to image both atomic and molecular features with no restriction on the electrical conductivity of sample surface. Under UHV conditions technical improvements in the mechanism used to oscillate AFM tips and to record their motion along with advances in tip functionalisation have driven forward non-contact AFM as a key tool for studying molecules for surfaces. Examples of key milestones in this research area include: revelation of the chemical structure of individual molecules [135]; real-space imaging of non-covalent intermolecular interactions [138, 139]; and the visualisation of covalent bonds formed by on-surface synthesis [140].

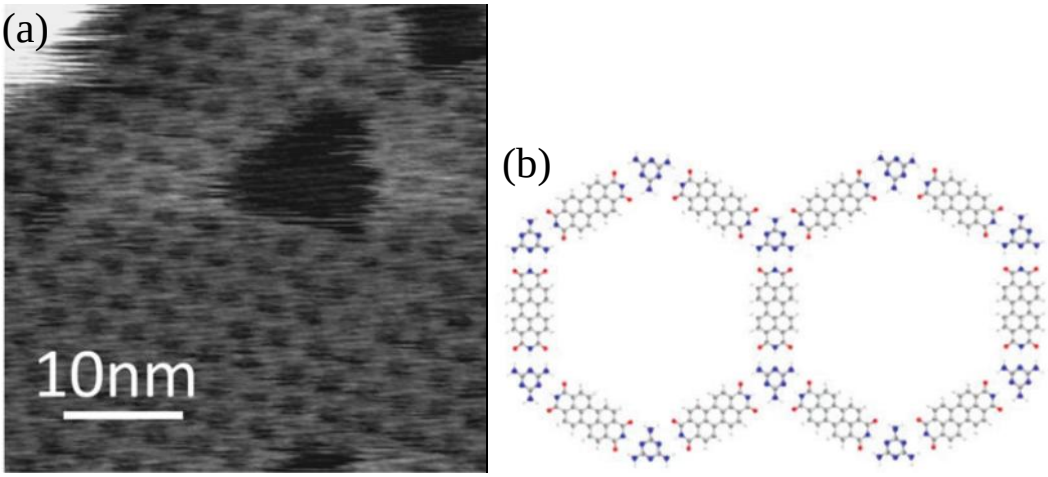

Figure 3.10. (a) PeakForce Tapping Mode AFM image of the porous PTCDI-melamine network self-assembled on a boron nitride surface. (b) Molecular model of the PTCDI-melamine network [141].

Outside of UHV environments, commercial AFM systems operating at ambient temperatures and pressures have been employed to image molecules constrained within

2D self-assembled molecular networks on various non-conductive surfaces. Examples include molecular networks formed on HOPG, Au(111), hexagonal boron nitride (hBN) and molybdenum disulphide (MoS_2) (Figure 3.10) [141-143]. The technological advances in ambient AFM have helped to extend research of self-assembled 2D molecular networks from only STM studies on graphite or gold to a wider range of insulating or semi-conductive surfaces.

3.3.4 Setup of high-resolution AFMs at ambient conditions

Without the necessity for complex UHV instrumentation, the PeakForce Tapping mode implemented on the Multimode AFM from Bruker and the Cypher™ AFM from Asylum Research are both capable of producing molecular resolution images with a versatile and easily implemented approach. Figure 3.11 shows the microscopy parts of the Bruker Multimode 8 and the Cypher AFM systems.

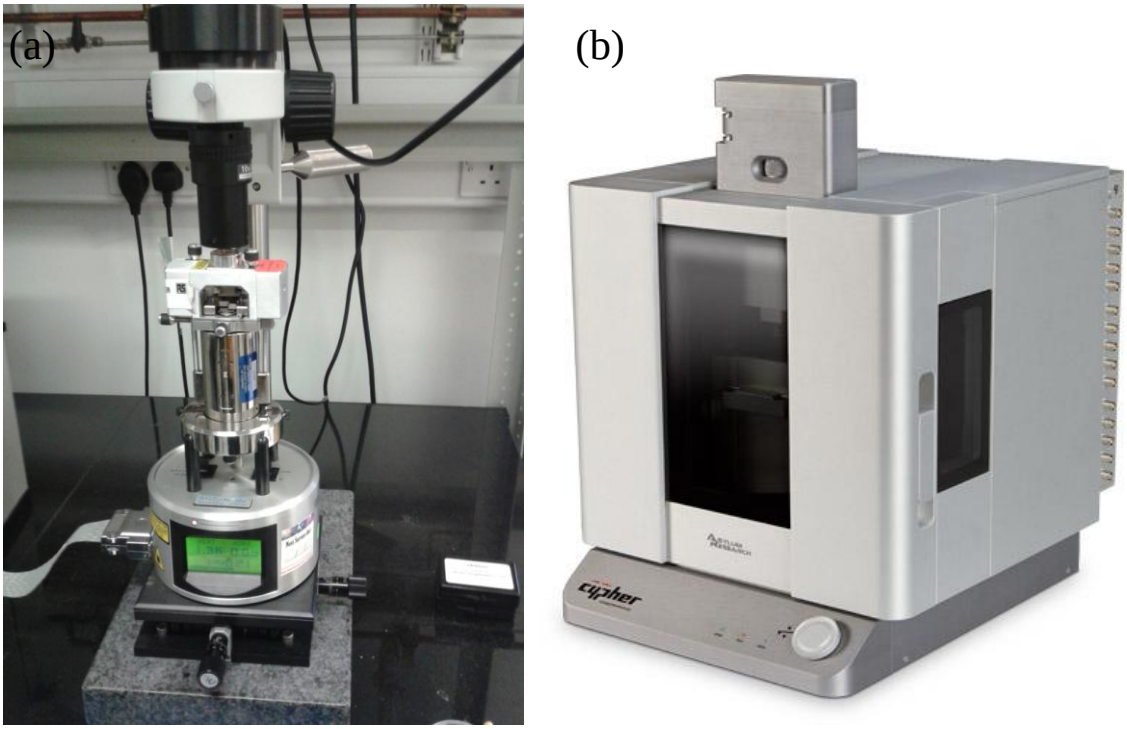

Figure 3.11. Ambient environment AFM systems with molecular resolution. (a) Bruker Multimode 8 AFM. (b) Cypher™ AFM [144].

PeakForce Tapping™ (PFT) is a new imaging technology first introduced by Bruker to improve the efficiency and controllability of AFM systems operating under conventional modes. Similar to basic tapping mode, an AFM probe also adopts an intermittent contact with the sample being measured in PFT mode. Force-distance curves are periodically obtained during scanning in PFT mode. Each force-distance curve measures how the cantilever's deflection changes as it is moved towards the surface. The exact force applied on the AFM tip can then be calculated from the cantilever's deflection if the force constant of the cantilever is known. The PFT mode uses a feedback loop to maintain the force of interaction between the tip and the surface at a constant and small value of the order of a few pN. In comparison, tip-surface forces in standard tapping mode can reach to as high as several nN. The reduced and controllable tip-surface forces in PFT mode lead to reduced tip and surface damage and to the acquisition of far more stable AFM images. All main imaging parameters for PFT can be adjusted automatically by ScanAsyst program (Bruker) rendering the manipulation acquisition of high quality AFM images significantly easier than with the ordinary Multimode AFM.

Cypher™ AFM provides fast scanning on atomic scales by utilising the patented sensor technology developed by Asylum Research. The sensors on the AFM systems are capable of reaching atomic resolution in all x, y and z axes. A number of standard scanning modes are available on Cypher, such as contact mode, intermittent contact mode, force curve mapping and nano-manipulation. In addition to these various AFM scanning modes, Cypher also supports upgrades to other characterisation tools including: STM, low-current measurements, band excitation and enhanced imaging ability in liquid by the blueDrive photothermal excitation [144].

3.3.5 Advantages and drawbacks of AFM

With the limitation to conductive substrates removed, AFM is a more versatile nano characterisation tool than STM. In addition to being able to operate on non-conductive surfaces, AFM offers several key advantages over STM. Some of the most notable

advantages of AFM are the ability to obtain mechanical information about a surface and the ability to study substrates with a significantly larger surface roughness than is possible with STM. Due to the ability to offer topographic information of non-conductive surfaces and adsorbates with high resolution, AFM has found application in a vast range of research areas. Some of the most common areas that AFM is utilised in include: surface science, the semiconductor industry; the cosmetic industry; and biomedical and life sciences. Under different scanning conditions, a number of tip-surface interactive forces can be detected by AFM, including: electrostatic; electromagnetic;and intermolecular interactions.

The invention of UHV non-contact AFM opened up fascinating opportunities to visualise and manipulate individual atoms and molecules with unprecedented levels of resolution. UHV non-contact AFM has become one of the most powerful experimental techniques to help scientists understand fundamental properties of individual molecules, and is used more commonly in academia.

Technological advances in commercial ambient AFM systems have improved their scanning performance enormously. AFM imaging can now be carried out at different temperatures and in diverse environments, including in liquids. By integrating other techniques with AFM, experimental systems are becoming more and more powerful and offering new insights into surface molecular systems. A key example of this is the combination of Raman spectroscopy with SPM in the form of tip-enhanced Raman spectroscopy (TERS) [145]. The TERS approach combines the high levels of spatial resolution obtained with SPM with the chemical information available to Raman spectroscopy. Such techniques offer a wealth of new information for surface scientists.

3.4 X-ray Photoelectron Spectroscopy (XPS)

3.4.1 Basic mechanism of XPS

XPS is a widely used surface analysis tool that provides quantitative information on the elemental composition and the chemical state of a surface region irradiated with soft

X-rays (200 – 2000 eV).

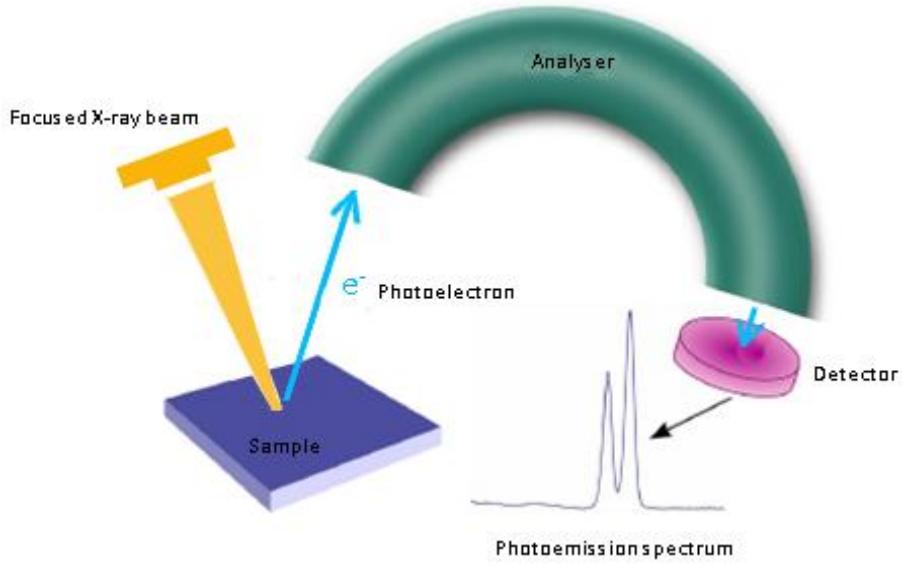

Figure 3.12. Schematic illustration of the basic mechanism of the XPS technique.

The basic mechanism that underlies XPS is illustrated in Figure 3.12. A monochromatic X-ray source is used to excite an area on the sample surface. X-ray photons are absorbed by the atoms in the irradiated surface region. The absorption of an X-ray photon can result in ionization and photoemission of core level electrons from the surface atoms: these electrons are referred to as photoelectrons. The typical analysis depth of XPS is less than 10 nm. The reason for the high surface sensitivity of the XPS signal is that photoelectrons are easily scattered and absorbed by the atoms of the sample. Thus, only the photoelectrons that originate from the top of the surface can escape from the material without either being scattered or absorbed by the sample. The kinetic energy and intensity of the photoelectrons are then measured by a hemispherical energy analyser. The energy analyser consists of two concentric hemispheres of different radius dimensions. An electrostatic field is applied across the hemispheres. The potential at the central line of the two hemispheres is known as the pass energy. When passing through the analyzer, the photoelectrons are deflected by the electrostatic field induced by the hemisphere. Photoelectrons with a range of electron energies are able to pass through the energy analyser. The range of electron energies depend on a few

parameters including: the magnitude of the pass energy; the angle with which the photoelectrons enter the analyser; and the size of the entrance. The information obtained from XPS experiments allows the elemental composition and the chemical environments of the surface atoms to be evaluated.

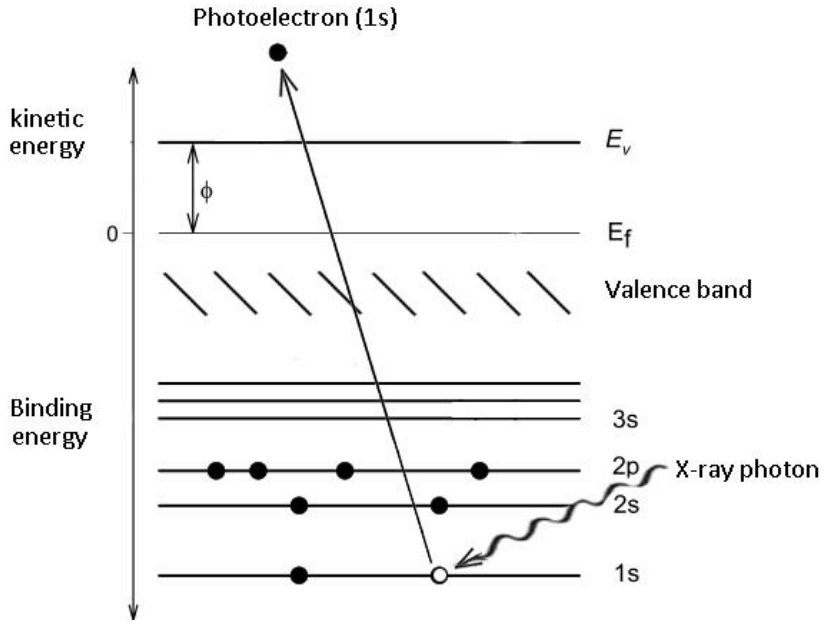

Figure 3.13. Schematic energy level diagram showing the photoemission process from the O1s oxygen core level in an XPS experiment.

Taking oxygen as an example, Figure 3.13 shows the photoemission process for a photoelectron emitted from the O1s level of oxygen. The underlying physical principle used to interpret the XPS experiment is the photoelectric effect [146], which can be expressed by equation (3.10):

$$E_{\text{kinetic}} = h\upsilon - \left(E_{\text{binding}} + \phi_{\text{sample}}\right) \tag{3.10}$$

The terms in equation (3.10) are: E_{kinetic} is the kinetic energy of the emitted photoelectron; $h\upsilon$ is the energy of the incident X-ray photon; E_{binding} is the binding energy of the core level involved in the photoemission process measured relative to the

material's Fermi level; and ϕ_{sample} is the work function of the surface material.

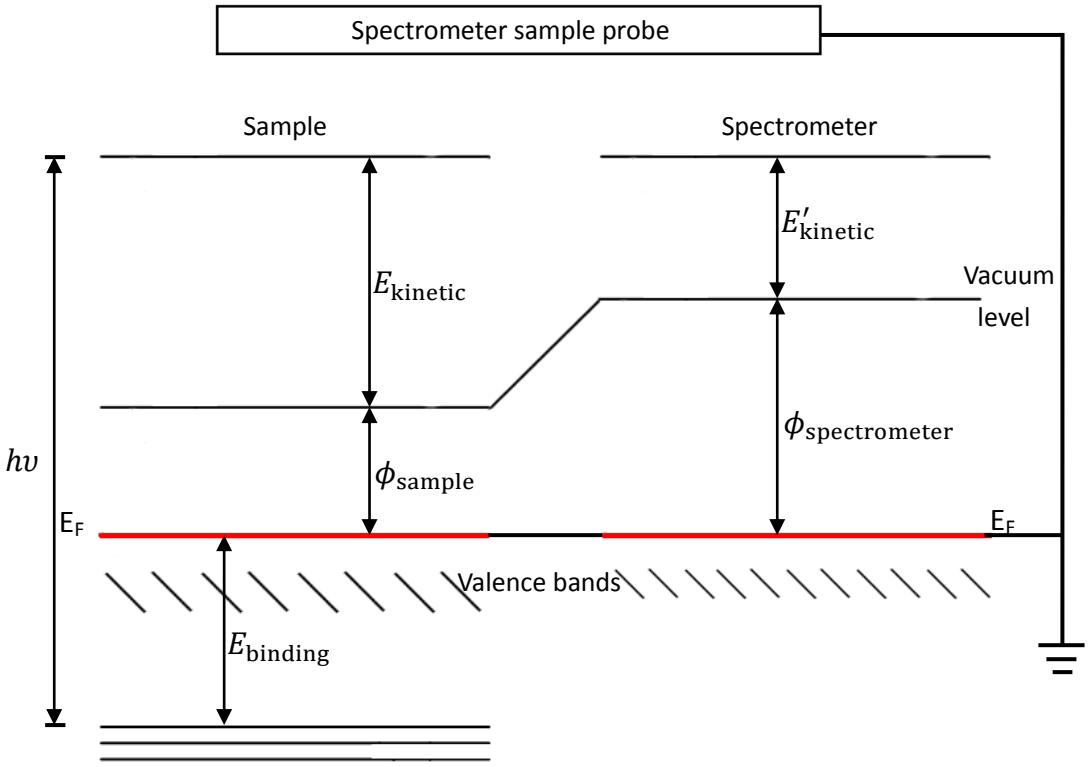

Figure 3.14. Energy level diagram showing the calibration of an XPS equipment. The Fermi levels of the sample and spectrometer are aligned by grounding the sample to the spectrometer.

In real XPS measurements, a conductive sample is grounded to the spectrometer so that the Fermi levels of the sample and spectrometer are aligned. As can be seen in Figure 3.14, the binding energy of the core level E_{binding} can be determined by measuring the work function of the spectrometer and the experimentally measured kinetic energy. The expression shown in Equation 3.10 is then reduced to that shown in equation (3.11):

$$E'_{\text{kinetic}} = h\upsilon - \left(E_{\text{binding}} + \phi_{\text{spectrometer}}\right) \tag{3.11}$$

In equation (3.11) E'_{kinetic} represents the kinetic energy of the photoelectron

measured by the XPS energy analyser and $\phi_{\text{spectrometer}}$ is the work function of the XPS spectrometer. The work function term $\phi_{\text{spectrometer}}$ can be regarded as a constant that is specific to a particular XPS machine.

Figure 3.15 shows an example XPS spectrum collected from a freshly cleaved HOPG surface. The resulting XPS spectrum is a plot of the intensity of photoelectrons versus E_{binding} of core level electrons. The background signal in the XPS spectrum correspond to emitted photoelectrons that have lost some of their energy due to inelastic scattering. The well-defined characteristic O1s and C1s peaks in the XPS spectra result from photoelectrons that have escaped the HOPG surface without undergoing any inelastic scattering. The lack of any inelastic scattering means that the kinetic energy of these photoelectrons can be linked directly back to the binding energy of the core atomic level from which they originated. The likelihood of a photoelectron undergoing an inelastic scattering process is very dependent on how much material it has to travel through in order to escape from the surface. Thus, the sharp peaks in XPS spectra are dominantly composed of photoelectrons from the top few nm of the surface.

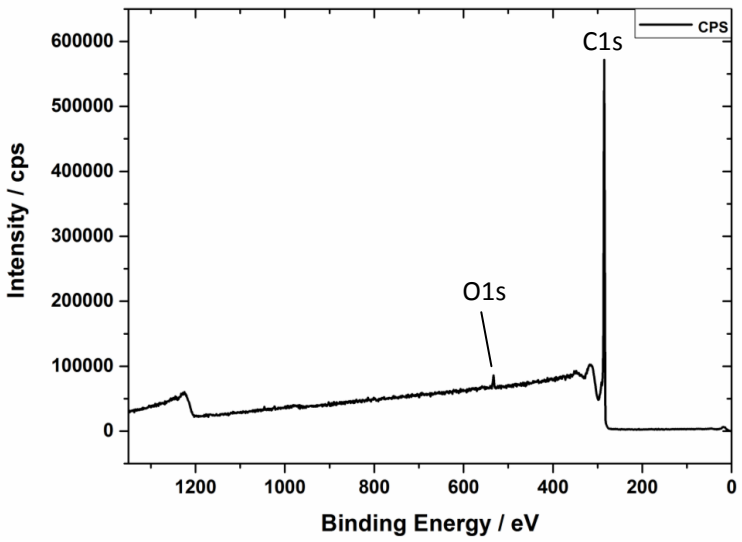

Figure 3.15. XPS survey scan of a blank HOPG sample.

The exact value of the binding energy observed for a particular core atomic level is influenced by the chemical environment of the element in question. If an element forms

covalent bonds with other elements, the binding energy of electrons in that element will change based on the electronegativity values of the elements it is bound to. Examples include C1s binding energies in organic samples. The C1s binding energy for carbon bound to four fluorine atoms is significantly higher than that of carbon bound to four hydrogen atoms. This change in binding energy values is known as chemical shift. Based on this idea of chemical shift, XPS can be used to provide information about the chemical bonding arrangement of a particular atomic species.

3.4.2 XPS setup and peak fitting

Experimental setup

Figure 3.16 presents the configuration of the Thermo Scientific K-Alpha XPS system used for XPS experiments presented in this thesis. The XPS system consists of an analysis chamber that is maintained at UHV conditions with pressures typically of 1×10^{-7} mbar or lower. The analysis chamber is connected to the outside atmosphere via the load-lock chamber. Samples for XPS analysis are placed into the load lock chamber and the chamber is pumped down until it has a pressure less than 1×10^{-6} mbar before transferring the samples into the analysis chamber. Samples such as HOPG often require extended pumping down times in the load lock chamber in order to reach suitable pressures. This is a result of outgassing by these samples resulting from small adsorbed molecular species (e.g. O_2, N_2 and H_2O) that can intercalate between the layers of HOPG. The vacuum environment ensures samples loaded into the system are free from contamination, and helps prevent losses in electron kinetic energy. The extreme surface sensitivity of XPS means that it is vitally important to minimise the presence of unwanted contamination on the sample surface. The Thermo Scientific K-Alpha XPS system is equipped with a monochomated Al Kα X-ray source (1486.6 eV), generated by electron bombardment of aluminum target. Spot sizes of the X-ray beam can be adjusted within the range of 30 to 400 μm. The application of monochromators improves the spectral resolution of XPS significantly by removing X-ray satellite peaks

and lowering background signals. Photoelectrons emitted from an illuminated area are collected by a lens system and directed into a hemispherical kinetic energy analyser. The analyser acts as an energy filter allowing electrons with a kinetic energy equal to its pass energy to reach the detector at the other end. By varying the pass energy in steps, electrons from a range of kinetic energies are detected. The detector counts the intensity of photoelectrons at a certain kinetic energy. The collected data is used to produce the final XPS spectrum.

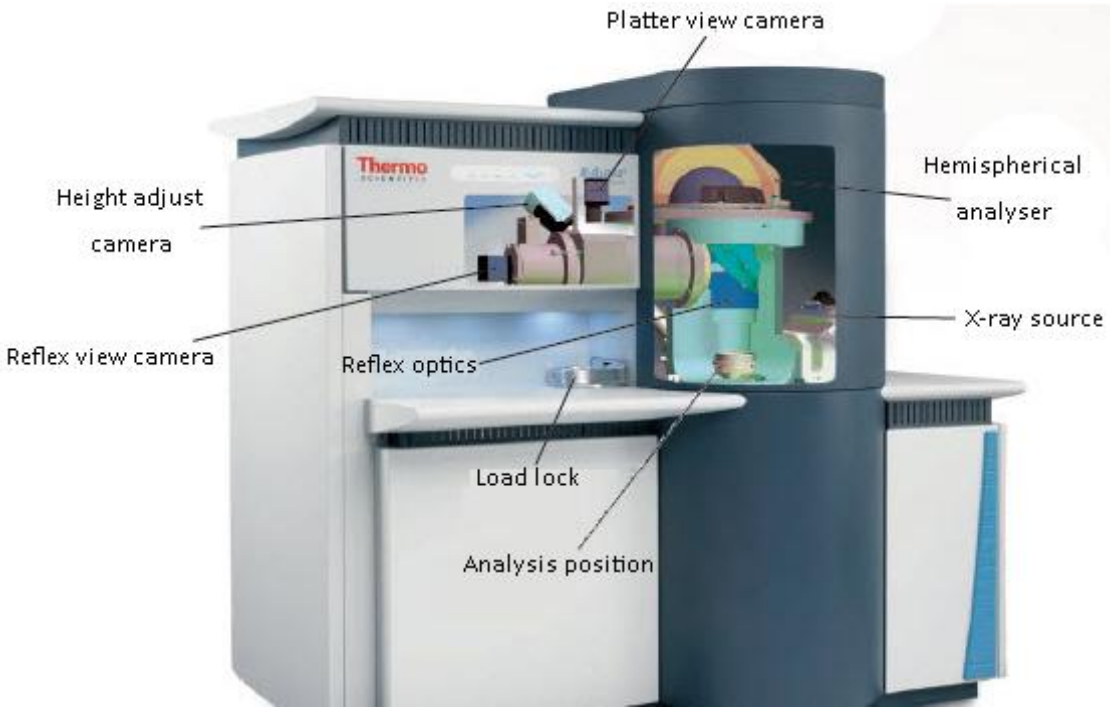

Figure 3.16. Schematic of theThermo Scientific K-Alpha XPS system [147].

A charge compensation system is implemented on the K-Alpha XPS system to solve the problem of surface charging when analysing insulating samples. For conductors, the positive charge induced by photoelectron emission can be rapidly replaced by electrons via an electrical contact between the sample and gound removing the need for charge compensation. However, on an insulating surface positive charge caused by photoelectron emission builds up and cannot be removed by the flow of electrons through an electrical contact. In this case, a flood gun, which is a beam of low energy electrons, is used to irradiate the surface and to neutralise the positive charge

caused by emitted electrons from the analysis area.

The K-Alpha XPS system can also be used to perform depth profiling experiments to study the elemental and chemical composition of sub-surface layers. In this appraoch either a monatomic or a gas cluster ion source is used to etch away material from the surface. Depth profiling allows XPS experiments to be performed on layers that were previously buried beneath the surface. Using this approach deeper layer for both organic and inorganic smaples can be investigated. The most commonly adopted approach is using an argon ion beam to remove materials from the top of a surface and collect XPS signals for each new layer sequentially.

XPS peak fitting

Fitting different peaks to a high resolution XPS spectrum is a complex process that relies on the ability of the experimenter to provide a physically sensible interpretation of the data and the mathematical model used to fit it. Several key factors should be kept in mind prior to starting the peak fitting process. These include: the expected elemental and chemical composition of the surface based on the preparation procedures; the presence of potential contaminants; the binding energies of atomic species expected on the surface. As mentioned above, the exact binding energy of a peak in an XPS spectrum can vary depending on the chemical environment of the atomic species in question. Therefore, if a sample has a structure which includes an atomic species present in several different chemical environments, such as different bonding geometries, the XPS peak shape for an atomic core level of that atomic species will be complex. For this reason, it is vital that a good knowledge of the chemical system under invesitgation is employed when analysing XPS data.

A complete peak fitting procedure consists of three main steps: subtraction of a background function from the XPS data; choosing suitable peak shapes to fit to the data; and performing a least squares fit of these peaks to the data. Least squares fitting is a mathematical method used to fit a given set of points to a curve where the sum of the squares of the offsets of the points reaches a minimum value. Different least squares

models are used to fit XPS spectra, depending on the type of data analysis software employed.

Linear, Tougaard and Shirley are the three most commonly used functions for background subtraction from XPS data. Each background subtraction function has its own advantages, drawbacks and preferred application areas. A proper selection of background function will result in a fitting outcome that is closest to the real situation of a XPS spectrum. For the CasaXPS software, the Shirley background is the most generally applicable function for XPS peak fitting.

After subtracting a suitable background function from the XPS spectrum, peaks are added based on the prior understanding of the physical and chemical properties of the samples. The number of peaks used to model the data depends on the expected number of different chemical environments for the element in question. The starting positions of the peaks are usually decided according to binding energy values reported in literature. Another factor that needs to be taken into consideration is the peak shape. Peak shapes commonly used for XPS peak fitting are: Doniach – Sunjic, Gelius, Gaussian – Lorentzian, and Voigt and pseudo-Voigt line shapes. The choice of which peak shape to use should be made by considering the composition of the materials being analysed and the computational ability of the software package used for peak fitting.

To optimise the fitting results, constraints, such as peak position, full width at half maximum (FWHM) and line shape parameters (Gaussian/Lorentzian ratio and asymmetry factors), are adjusted in a step-by-step process. In order to obtain an accurate fit to an XPS peak, the fit needs to be both mathematically valid, and chemically and physcially meaningful.

3.4.3 Applications of XPS

XPS has a wide range of applications in research areas related to solid surfaces. These include: catalysis; polymers; and microelectronics. As a complementary tool to other surface analysis methods, for example, STM and AFM, XPS offers chemically specific information for molecular surface structures, information that is inaccessible with SPM

techniques.

XPS is a powerful technique that allows the quantitative identification of different elemental and chemical species on surfaces The chemical analysis is achieved by measuring the binding energy values for core level electrons. Moreover, XPS is also able to determine quantitatively the relative concentration of each chemical state that an element has in the surface region.

In addition to detection of core levels, XPS is able to help understand the valence band (VB) structures of metals and semiconductors. Compared with core atomic levels, the VB no longer consists of well specified individual energies but rather a region of closely spaced electronic states close to the Fermi level. This band of densely packed electronic states arise from the combination of atomic orbitals (AOs) in the material structure. Thus, VB peak shapes can reflect how AOs overlap and can be used to study the arrangement of atoms in crystal structures.

3.5 Molecular Mechanics (MM) simulation

Molecular mechanics (MM) simulations, also called force field modeling, is a theoretical method used to predict molecular structures by classical mechanics treatment of molecular structure.

In a MM simulation, a molecule is assumed to be made of atoms linked by elastic bonds. Similar to springs, the chemical bonds can undergo a range of deformation, such as stretching, compression, bending (bond angles) and torsion (dihedral angles). The force field of the molecule is defined as the total energy of the deformed “springs” and interactions between atoms that are not chemically bonded.

A number of molecular mechanics force fields have been developed by computational chemists. Each of the force fields contains a set of functions and parameters used to calculate the potential energy of systems made up of different atomic species combined in different ways. A force field model is verified by comparing the outcome it produces with a large range of molecules of known atomic arrangements. Once established, a force field can be used to simulate other molecular structures. In the

HyperChem package used for the MM simulations in this thesis, four types of MM force fields are available, the application areas of which are tabulated in Table 3.1.

To run a MM simulation, a suitable force field should be chosen for the target molecules and interaction types that are being investigated. After building the starting geometry of the molecular structure, a geometry optimization process is carried out. Geometry optimization adjusts the molecular structure in a step-by-step process that aims to lower the overall strain energy of the molecular structure. Once the strain energy of the molecular system drops below a pre-defined level chosen prior to starting the simulation, the MM system is said to be geometry optimized.

One of the main advantages of MM over quantum mechanical simulation approaches such as density functional theory (DFT) is that MM simulations are much less computationally intensive. This means that smaller molecular systems can be simulated much more quickly or larger molecular system that cannot be simulated using DFT can potentially be investigated. However, the applications of MM simulations are limited to molecules with known structures due to the restrictions of the force fields used to model the structures. Moreover, since classical mechanics does not provide any information on the electronic structures of atoms, MM calculations cannot be used to simulate electronic properties of molecules, such as molecular orbital (MO) energies or shapes.

Force fields	Preferred molecular systems
MM+	A wide range of molecules [148]
AMBER	Proteins and DNA [149]
BIO+(CHARMM)	Small molecules and macromolecules [150]
OPLS	Molecules in liquids [151]

Table 3.1. The various molecular mechanics (MM) force fields implemented in the HyperChem software simulation package and their application areas [152].

Chapter 4

2D supramolecular self-assembly of a tetra-carboxylic acid derivative

Carboxylic acid functionalised molecules have attracted extensive research interest as molecular building blocks for 2D supramolecular self-assembly. The strong and highly directional hydrogen bonding interaction between carboxylic acid groups provides a reliable, and to some extent, predictable interaction between molecular building blocks. In this chapter, the interfacial self-assembly of a tetra-carboxylic acid derivative with an anthracene backbone, 5, 5'-(anthracene-2,6-diyl) diisophthalic acid (ATC), has been investigated using STM, combined with MM simulations. Compared with other tetra-carboxylic acid building blocks, the two interesting properties that this material exhibits upon adsorption from long chain fatty acids solutions onto HOPG are: (ⅰ) the ATC molecule is prochiral and following adsorption self-assembles into chiral domains; (ⅱ) ATC displays 2D polymorphism with three distinct structural arrangements being resolved within the same 2D self-assembled interfacial layer. Additionally, ATC can also co-assemble with coronene forming a bi-component network. The self-assembly of ATC provides another model system to deepen our understanding of the formation of 2D molecular networks at liquid-solid interfaces.

4.1 Introduction

Directional hydrogen bonding interactions between carboxyl groups are reliable driving forces for the 2D supramolecular self-assembly of molecular networks [9, 153-156]. Extended 2D self-assembled networks have been realised using organic molecules functionalised with one [157],two [158, 159], three [160-162] or four [51, 163] carboxyl groups. As a model molecular building block, the self-assembly of trimesic acid (TMA)

at liquid-HOPG interfaces has shown dependency on the deposition temperature and solvent used to dissolve the molecule [21, 164]. Analogous to TMA and its derivatives, tetra-carboxylic acid functionalised molecules are a group of extensively investigated molecular building blocks that have been used for obtaining predesigned 2D molecular crystals.

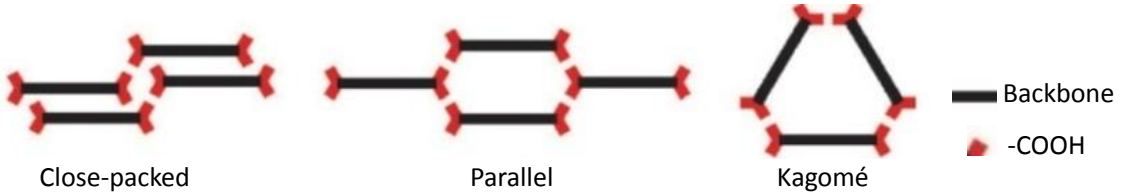

Figure 4.1. Schematic diagram showing three example molecular arrangements of planar tetra-carboxylic acid molecules. Each tetra-carboxylic acid derivative is represented as a back bar with the carboxylic acid groups shown as red arrows at either end of the bar. [51]

As discussed in section 2.2.1, carboxyl groups very often form a standard hydrogen arrangement consisting of a hydrogen bond dimer, but can also form a cyclic trimer of hydrogen bonds (Figure 2.4 (c) and (d)). Linked by inter-molecular hydrogen bonding dimers between carboxyl groups, planar tetra-carboxylic acid derivatives form a few commonly observed molecular patterns as presented in Figure 4.1 [51].

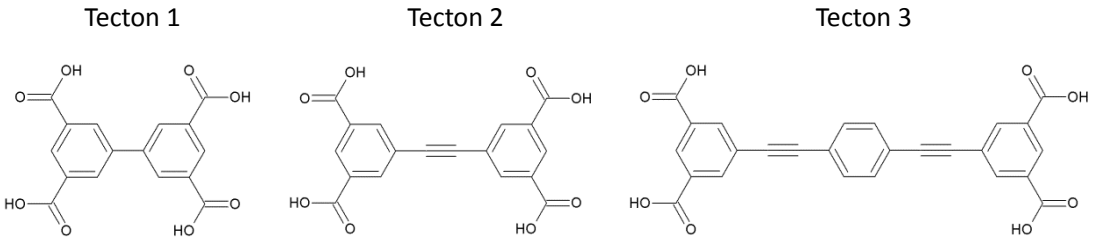

Figure 4.2. Molecular structures of three tetra-carboxylic acid derivatives formed by grafting isophthalic acid groups to either end of linear connectors. [165].

Wuest and co-workers have studied a series of tetra-acid derivatives, as shown in Figure 4.2 [165]. For each of the molecules, two isophthalic acid groups are linked directly or grafted onto either end of a linear conjugated core forming a planar structure. Their study demonstrated that tecton 1 self-assembles into an open parallel network, and

tecton 3 forms a Kagomé structure at the HOPG-heptanoic acid interface. In contrast to tecton 1 and tecton 3, tecton 2, however, fails to produce any large periodic domains. The frustrated crystallisation of tecton 2 was attributed to the smooth, defect-free transition between its two packing arrangements. This result shows the conjugated backbone of a tetra-carboxylic acid derivative plays an important role in determining the morphology of the resulting self-assembled network structure.

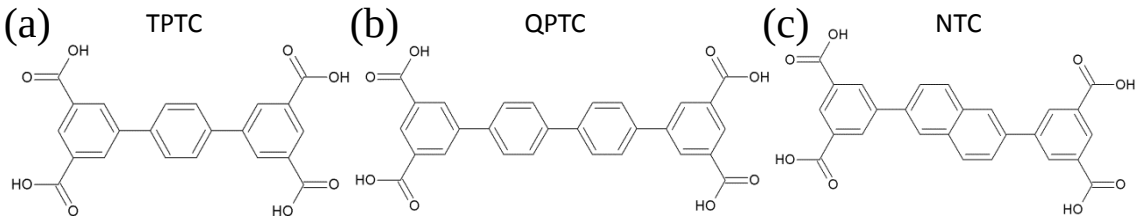

Figure 4.3. Molecular structures of (a) TPTC [51, 52, 163, 166]; (b) QPTC [51, 163]; (c) NTC [51].

Figure 4.3 presents a range of tetra-carboxylic acid derivatives that have been investigated by Beton and co-workers [51, 52, 163, 166]. The morphology of 2D self-assembled networks constructed from these molecules were initially studied systematically by depositing them from organic solutions onto a HOPG surface. Terphenyl-3,5,3″,5″-tetra-carboxylic acid (TPTC) molecules have been found to self-assemble into a hexagonally ordered network with no extended translational symmetry [166]. By contrast, quaterphenyl 3,5,3‴,5‴-tetra-carboxylic acid (QPTC) or 5,5′-naphthalene- 2,6-diyldibenzene-1,3-dicarboxylic acid (NTC) molecules do not exhibit such diverse self-assembly properties. As far as previous results have shown, QPTC and NTC molecules assemble exclusively into parallel and close-packed networks, respectively, at the liquid-HOPG interfaces [51]. In order to study the influence of the underlying HOPG surfaces and presence of fatty acids, dried TPTC and QPTC networks were formed by dipping Au(111) substrates in aqueous solutions followed by N_2 blowing. Instead of forming the standard inter-molecular hydrogen bonding dimers, TPTC and QPTC in the resulting dried films were packed in a "head-to-edge" arrangement, as shown in Figure 4.4. The results illustrate that the

combination of solvent and substrates plays an important role in determining the self-assembled structures formed by the tetra-carboxylic acid derivatives.

Highly ordered 2D self-assembled networks formed by tetra-carboxylic acid molecules can be used as host structures for the inclusion of guest molecules. Both of the closely packed QPTC and NTC networks at liquid-HOPG interfaces can be directed to form stable Kagomé structures by the inclusion of the planar molecule coronene as a guest [51]. Because of its planar, conjugated core with a six-fold symmetry, coronene exhibits strong surface adsorption and can fit into the hexagonal pores formed by carboxyl groups. Thus, coronene is a suitable guest molecule for 2D self-assembled networks stabilised by hydrogen bonding between carboxylic acid groups [32, 167].

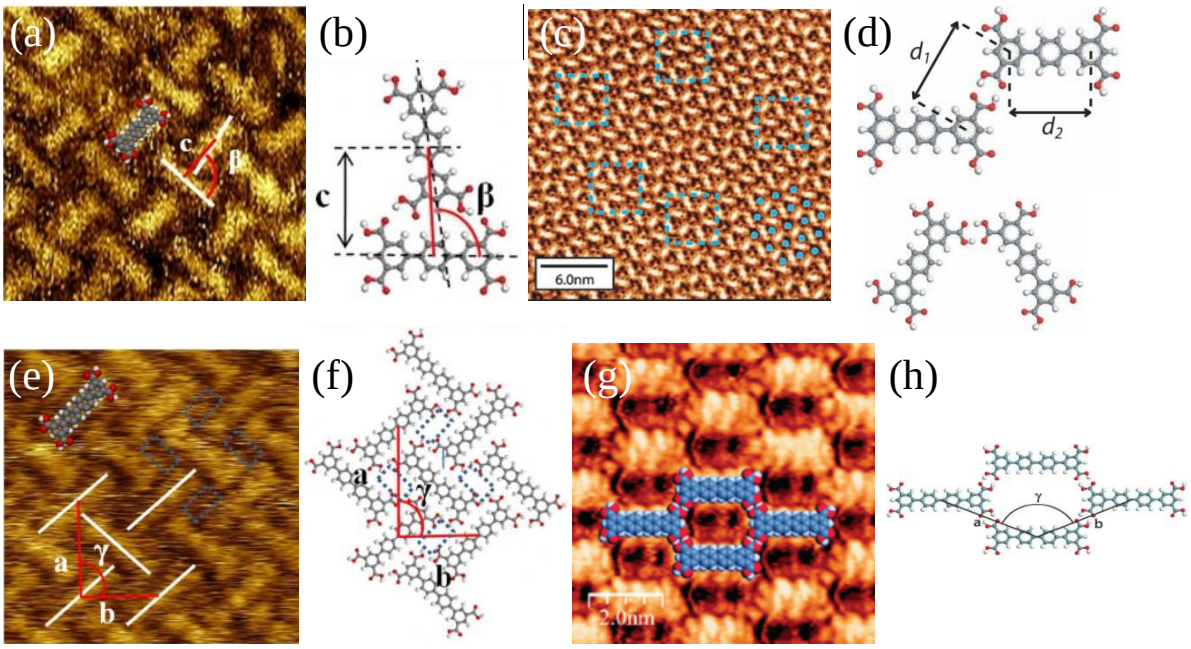

Figure 4.4. STM images and schematic representations showing molecular packing arrangements of TPTC and QPTC within dried films on Au(111) surfaces, and the liquid-HOPG interfaces.(a)-(b) STM image and schematic representation of TPTC on Au(111). (c)-(d) TPTC on HOPG. (e)-(f) QPTC on Au(111). (g)-(h) QPTC on HOPG [51, 163, 166].

Despite the wide range of carboxylic acid functionalised molecular species that have been investigated as tectons in 2D molecular self-assembly, very few examples of the self-assembly of prochiral tetra-carboxylic acid derivatives have been reported. In this chapter, we use an anthracene tetra-carboxylic acid derivative, 5,

5'-(anthracene-2,6-diyl) diisophthalic acid (ATC) (Figure 4.5 (a)) as a model building block to further probe the interfacial self-assembly behaviour of tetra-carboxylic acid derivatives. The chirality, formation conditions and guest adsorption characterisations of the ATC self-assembled structures at the liquid-HOPG interfaces will be discussed.

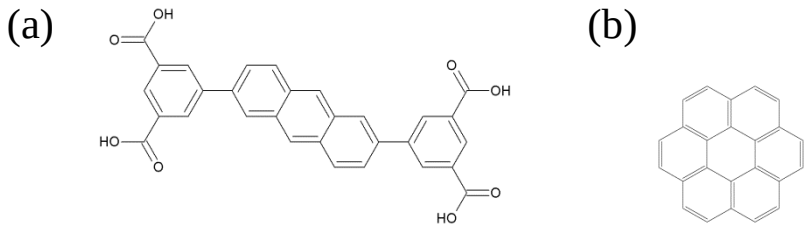

Figure 4.5. Chemical formulae of (a) ATC; (b) coronene.

4.2 Experimental details

Acid	Formula	Molecular weight (g/mol)	Boiling point (℃)	Melting point (℃)	Density (g/cm^3)	Dielectric constant at 20 ℃	Viscosity (mPa•s)	Vapour pressure (mmHg at 410 K)
Heptanoic	$C_7H_{14}O_2$	130.2	223	-7.5	0.9200	3.04	4.3371 (20 ℃)	39.0
Octanoic	$C_8H_{16}O_2$	144.2	237	16.5	0.9088	2.83	5.105 (25 ℃)	17.3
Nonanoic	$C_9H_{18}O_2$	158.2	254	10	0.9057	2.49	7.25 (24 ℃)	9.90

Table 4.1. Physical and chemical properties of the fatty acids used as solvents for the self-assembly experiments of ATCmolecules [9]

To prepare samples for STM imaging, the target compound, ATC, was dissolved in a suitable solvent which should be non-conductive, non-volatile and able to dissolve the molecule of interest. In this work, a series of fatty acids were tested as solvents to

dissolve ATC molecules: nonanoic acid (Grade Ⅰ, ≥.97 %, Sigma Aldrich), octanoic acid (≥.99.0 %, Sigma Aldrich) and heptanoic acid (≥.99.0 % (GC), Sigma Aldrich). The physical and chemical properties of these solvents are tabulated in Table 4.1 [9].

For each of the solvents, a saturated solution of ATC was first obtained as a stock solution. After this stock solution had been allowed to settle, the supernatant was taken and diluted to make up a range of solutions with different concentrations relative to the saturated solution concentration. A 10 μl droplet of prepared ATC solution was then deposited onto a freshly cleaved HOPG surface under ambient conditions. The ATC molecules physisorbed from the solution onto the HOPG surface. The adsorbed molecules then diffuse across the HOPG surface interacting with each other to nucleate and grow ordered domains of various self-assembled structures. These self-assembled interfacial molecular layers are stabilised via hydrogen bonding interactions between the carboxylic acid groups. In experiments where coronene was also included in the self-assembly process, coronene was added to heptanoic acid solutions of ATC prior to the mixture being deposited onto the HOPG surface.

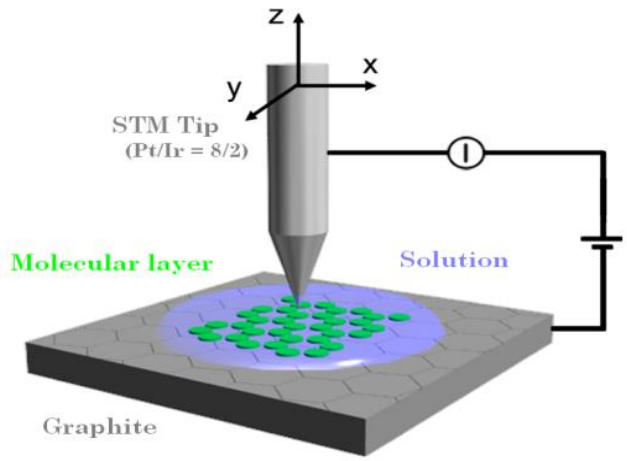

Figure 4.6. Schematic representation of the experimental setup for the acquisition of STM images at liquid-solid interfaces.

The self-assembled molecular networks were imaged using an Agilent 5500 series STM system operating at liquid-solid interfaces. As illustrated in Figure 4.6, an STM tip (Pt/Ir = 8/2) is immersed in the solution and is used to image the self-assembled

network that forms at the interface between the HOPG and the organic solvent. All STM images were obtained in constant-current mode. The quality of the mechanically cut Pt/Ir tip can be tested by imaging the bare, dry HOPG surface prior to solution deposition. All of the STM images presented in this chapter have undergone a flattening process. The flattening procedure is used to remove image artefacts that arise from the nature of STM system. The Agilent 5500 system uses a tube piezoelectric scanner arrangement [116]. The scanner is responsible for moving the tip back and forth across the surface and building up the STM image. In a tube scanner, the nature of the tip motion is not perfectly parallel to the sample surface. This can introduce image artefacts that make STM images appear as if they are bowed. Added to this, the sample surface and the scanner motion may not be perfectly aligned, leading to the image appearing to be tilted. Both of these effects can be removed using a flattening process. Flattening assumes that the overall morphology of the surface is that of a flat plane. Software then uses a 0, 1^{st}, 2^{nd} or 3^{rd} order polynomial equations to model the bowed or tilted surface and then modifies the image to remove these effects and flatten the image. This process can massively enhance the contrast of the STM images. However, care must be taken when applying the flattening procedure to ensure that it does not introduce its own artefacts into the image. For the high-resolution STM images, the influence of thermal and mechanical drift was removed by using the atomic lattice of the underlying HOPG surface as a calibration. All the image processing used on STM images presented in this thesis was performed using SPIP software (Image Metrology, Denmark).

Geometry optimised molecular models were calculated using MM simulations employing the HyperChem software package. Starting molecular structures for the MM simulations were based on unit cell dimensions and angles obtained from high resolution, drift-corrected STM images. A fixed graphene sheet was added below the molecular structure to be simulated so that the influence of the underlying HOPG substrate on the molecular arrangement could be modelled. The distance between the graphene sheet and the centres of the planar ATC molecules was initially set as 0.35 nm. The MM+ force field was chosen to apply geometry optimisation to the molecular structures.

4.3 Results and analysis

Results on three separate aspects of the self-assembly of ATC molecules will be discussed in the following sections: the choice of solvent; the concentration dependence of self-assembled patterns; and coronene-ATC bi-component self-assembly.

4.3.1 Choice of solvent

The first step for studying the self-assembly behaviour of ATC at the liquid-solid interface was to find a suitable solvent. The carboxyl groups of fatty acid readily form hydrogen bonds with other carboxylic acid functionalised molecules thereby promoting dissolution. Therefore, fatty acids have previously been widely used as solvents for carboxylic acid functionalised molecules. In this project, three fatty acid solvents were studied, including: nonanoic acid, octanoic acid and heptanoic acid. ATC molecules exhibit good solubility in all of these solvents. The difference in alkyl chain length for these three solvents will have a significant influence on the solvent's co-adsorption ability within porous structures. Consequently, it is interesting to investigate how the self-assembled structures of ATC are affected by the alkyl chain length of the solvents used to dissolve the target molecules.

Nonanoic acid

The STM image presented in Figure 4.7 shows the morphology of the ATC network self-assembled at the interface between HOPG and nonanoic acid. The concentration of the ATC/nonanoic acid was a 1/20 dilution of stock solution (sat/20). Each bright unit feature on the STM image corresponds to an individual ATC molecule. This higher contrast in the STM images results from the higher electronic density of states around the Fermi level for the central aromatic anthracene section of ATC. Anthracene represents a class of extended π conjugated systems that contain polycyclic aromatic hydrocarbons. Among the occupied and empty molecular orbitals of

anthracene, only a few of the highest-energy orbitals occupied by electrons, and a few of the lowest-energy orbitals unoccupied by electrons (frontier orbitals) are involved in electron transitions. The Fermi level (E_F) of anthracene falls within the gap between the highest occupied molecular orbital (HOMO) and the lowest unoccupied molecular orbital (LUMO). Anthracene exhibits a high density of states (DOS) at energies close to E_F and a narrow HOMO-LUMO gap [168]. Given the bias voltages applied in our STM measurements (sample negative, - 0.8 – - 0.4 V), the STM tunnelling probability is closely related to the DOS of anthracene with energy levels close to its E_F [169]. Therefore, anthracene, and other aromatic groups appear as bright features in STM images. This is in direct contrast to non-conjugated molecular features, such as alkyl chains that appear as much darker features.

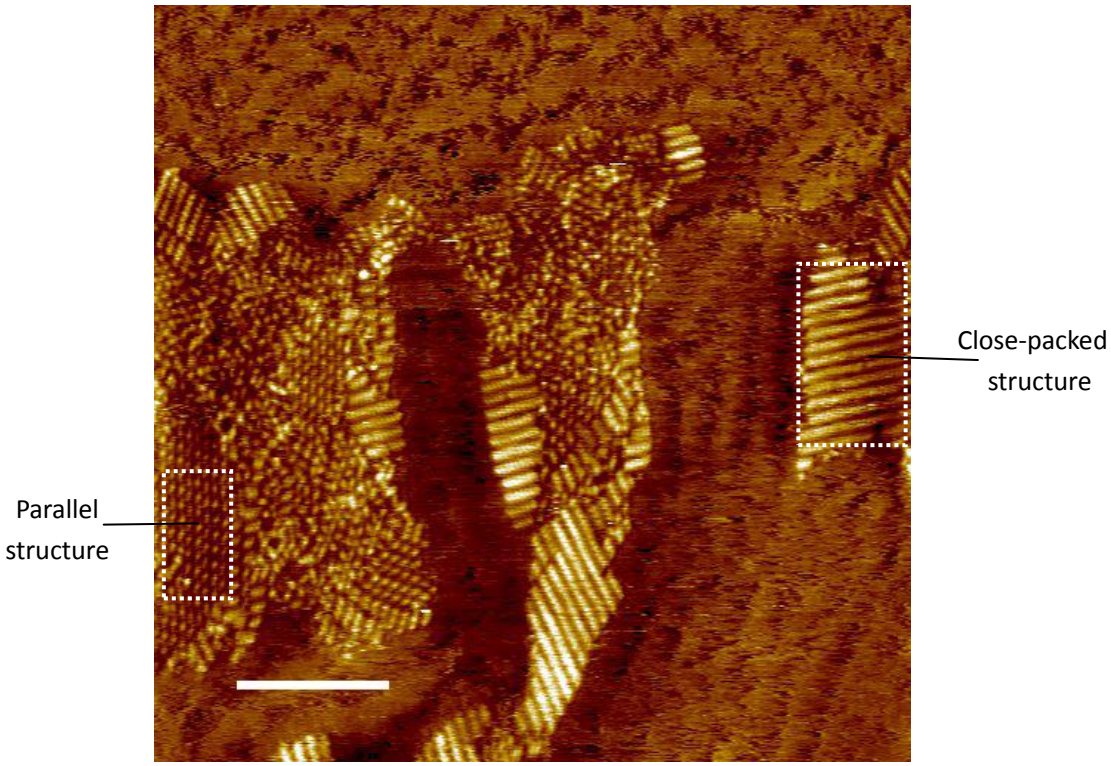

Figure 4.7. STM image of the ATC network self-assembled at the nonanoic acid-HOPG interface. Concentration of the ATC/nonanoic acid solution: sat/20. STM imaging parameters: V_s = - 0.5 V, I_t = 0.04 nA. Image size: 150 nm. Scale bar: 30 nm.

As can be seen from the STM image presented in Figure 4.7, the ATC network

adsorbed from nonanoic acid is a combination of disordered regions and ordered domains with both close-packed and porous morphologies being observed. In this STM image, approximately 60.0 % of the surface was covered with an unknown contamination that formed quasi-ordered stripe-like domains. The percentage coverages of the close-packed and parallel structures were measured to be about 16.0 % and 9.0% respectively. The rest of the surface was covered with disordered regions (15.0 %). Identical contamination patterns were detected when using freshly opened nonanoic acid. By taking the average and standard deviation of ten measurements, the average separation of the linear contamination features was measured to be 7.2 ± 1.1 nm. This value is comparable to the size of a linear contamination observed for the growth of TAPP 2D-COFs (Section 6.3.1, Figure 6.11). Thus, this stripe-like contamination is highly likely to arise from polydimethylsiloxane (PDMS) present on the disposable needles used to make these solutions.

Octanoic acid

Figure 4.8 presents an STM image showing the self-assembled structure resulting from the deposition of ATC molecules from an octanoic acid solution. The solution deposited on HOPG was produced by making a 10-fold dilution of the supernatant of a saturated ATC/octanoic acid (sat/10).

Compared with the case of nonanoic acid, the total coverage of the ATC molecular network increases and no periodic stripe-like contamination is visible in regions without ATC network. Measurements taken from the STM image in Figure 4.8 show that the surface was covered with 4.8 % of the close-packed structure, 19.0 % of the kagomé structure, 8.9 % of the parallel structure, 45.2 % of disordered regions, and 22.1 % of bare HOPG with no ATC networks. The domain sizes of the ordered close-packed, kagomé and parallel structures can also be measured from the STM image. The domain size of an ordered domain can be determined by taking the square root of the surface area occupied by the domain. For each of the ordered structures, at least five domain sizes were collected to calculate their average value and standard deviation. As a result,

the domain sizes of the close-packed, kagomé and parallel structures were measured to be 8 ± 1 nm, 18 ± 4 nm and 15 ± 4 nm, respectively. Compared with results obtained in the nonanoic acid system, the increase in molecular coverage may result from the lower adsorption of the stripe-like contamination.

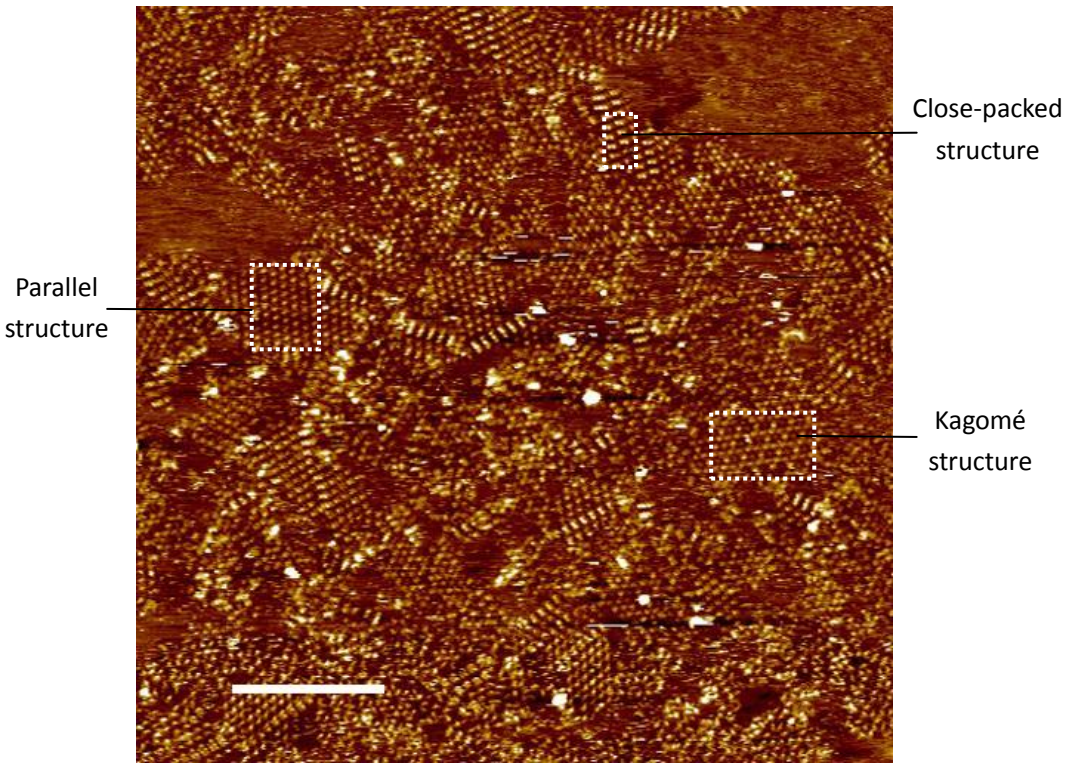

Figure 4.8. Morphology of the ATC network self-assembled from octanoic acid onto HOPG. Concentration of the ATC/octanoic acid solution: sat/10. STM imaging parameters: V_s = - 0.6 V, I_t = 0.01 nA. Image size: 150 nm. Scale bar: 30 nm.

Heptanoic acid

Further experiments were performed to investigate the effect of depositing ATC from heptanoic acid. Heptanoic acid has a shorter aliphatic chain length compared with that of nonanoic acid or octanoic acid. Figure 4.9 presents an STM image showing the HOPG surface covered by an ATC network self-assembled from heptanoic acid. The molecular system in heptanoic acid yields ATC networks with extremely high surface coverage (> 99.9 %). Three types of ordered phases in separate domains were formed

when the molecular system reached an equilibrium under ambient conditions. The surface shown in Figure 4.9 was covered with 7.2 % of the close-packed structure, 12.4 % of the kagomé structure, 23.9 % of the parallel structure and 56.5 % of disordered and unoccupied regions.

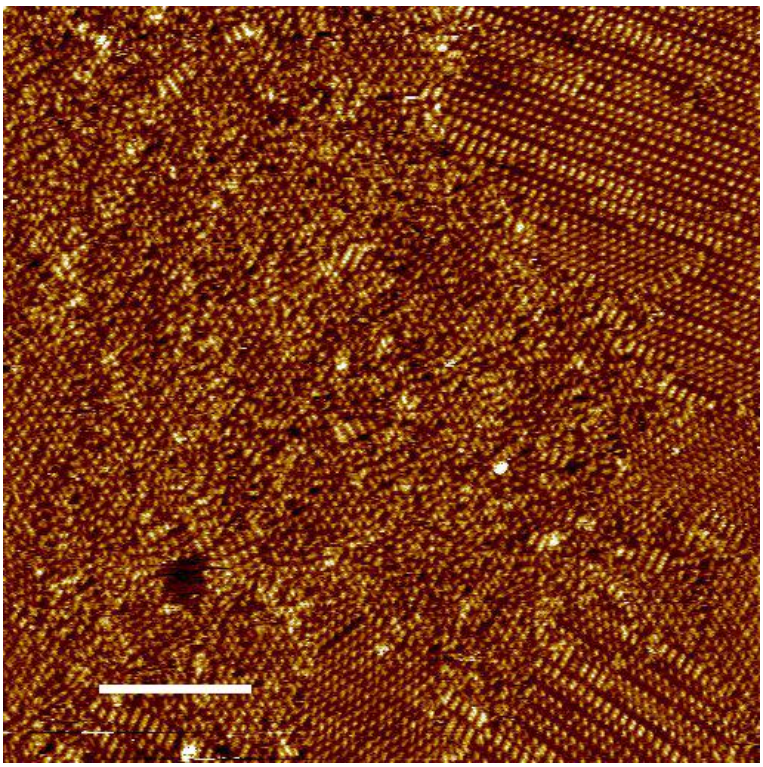

Figure 4.9. STM image of a good quality ATC network assembled at the heptanoic acid-HOPG interface. Concentration of the heptanoic/nonanoic acid solution: sat/20. STM imaging parameters: V_s = - 0.5 V, I_t = 0.05 nA. Image size: 150 nm. Scale bar: 30 nm.

With an aim to fabricate extended two-dimensional ATC molecular networks, heptanoic acid was used as a solvent in all the subsequent experiments. The high-quality ATC network structures are favourable for the acquisition of consistent STM images over extended scales. The lack of uncovered regions of the surface meant that there were fewer freely moving ATC molecules on the surface. This restriction of molecular motion allowed for both higher contrast and more consistent STM imaging.

4.3.2 Concentration-dependent self-assembly

The self-assembly behaviour of ATC at the interface between heptanoic acid and HOPG was probed using STM. In Figure 4.10, two typical STM images were recorded for ATC self-assembled networks formed via the deposition of heptanoic acid solutions with different concentrations. The solution used for the formation of the ATC network presented in Figure 4.10 (a) was a 1/20 dilution of the saturated ATC/heptanoic acid solution (sat/20). While the ATC solution corresponding to the STM image in Figure 4.10 (b) was a 1/50 dilution of the saturated ATC/heptanoic acid solution (sat/50).

At the higher concentration, ATC molecules self-assemble into three packing arrangements that coexist on the surface in separate domains. These packing arrangements include a porous wheel-like pattern, and two densely packed structures. In contrast, only the wheel-like pattern is observed in the lower concentration sample. For the STM image in Figure 4.10 (b), the end of the STM tip changed halfway through the scanning process. Despite a contrast alternation between the central area, and the lower and upper parts of the image, it is still reasonable to determine that all of the domains consist of the porous wheel-like arrangements with defects and domain boundaries.

Using the method introduced in the previous section, quantitative analysis of the percentage surface coverage and domain size was carried out for the different packing arrangements observed in Figure 4.10. At the concentration of sat/20, the surface was approximately covered with: 21 % of the close-packed structure; 11 % of the kagomé structure; 49 % of the parallel structure; and 19 % of disordered regions. By taking at least three measurements, the average domain sizes of the close-packed, kagomé and parallel structures were measured to be 14 ± 5 nm, 27 ± 6 nm, and 28 ± 11 nm, respectively. At the concentration of sat/50, the surface was covered with around 78 % of the kagomé structure and 22 % of disordered regions. In contrast to the concentration of sat/20, the domain size of the kagomé structure increased to approximately 75 ± 3 nm by taking two measurements from the STM image shown in Figure 4.10 (b).

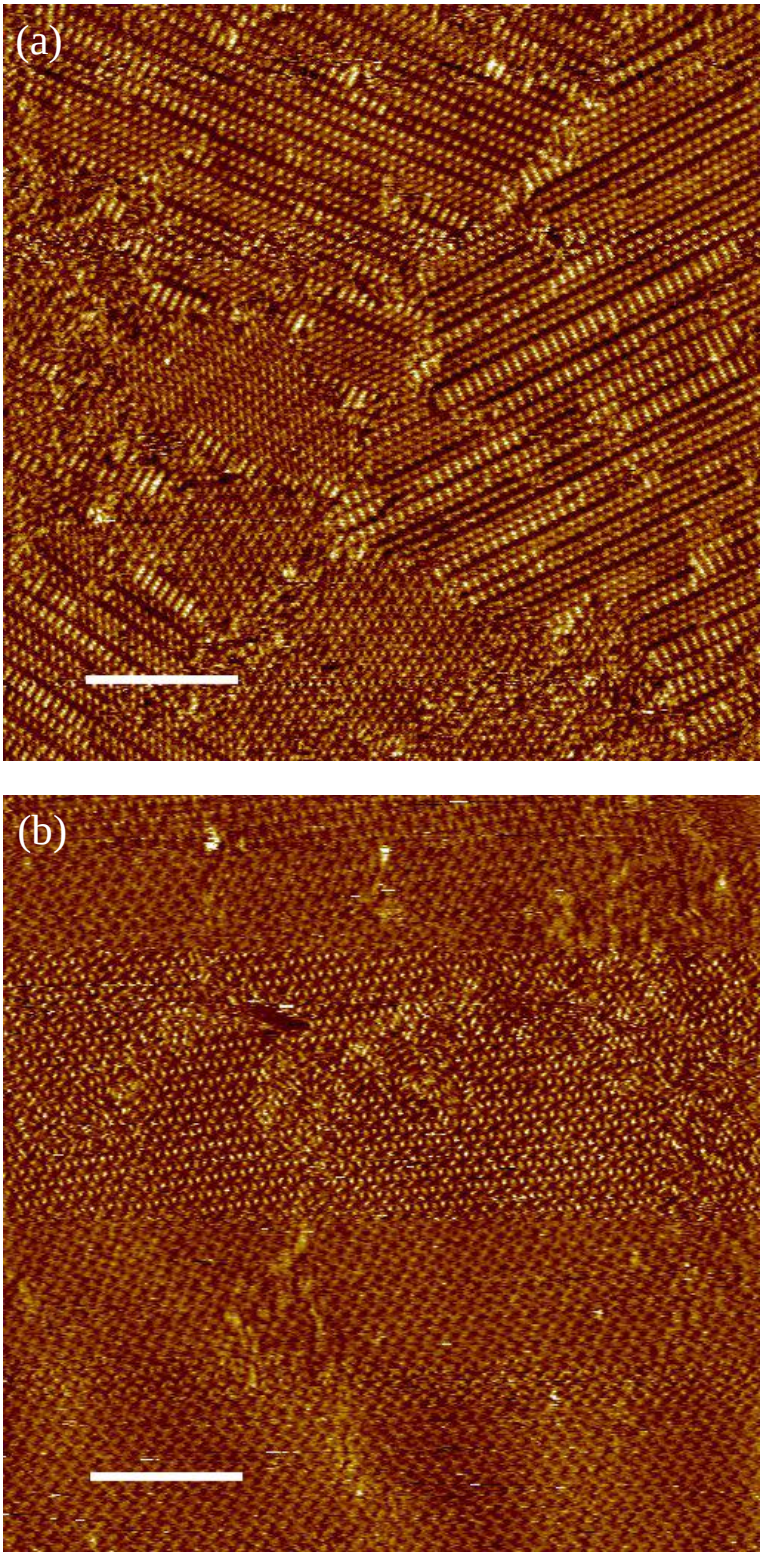

Figure 4.10. Morphology of self-assembled ATC monolayers at high and low concentrations. (a) STM image of the ATC network formed at the concentration of sat/20. (b) ATC network formed at the concentration of sat/50. STM scanning parameters: (a) V_s = - 0.5 V, I_t = 0.05 nA; (b) V_s = - 0.5 V, I_t = 0.06 nA. Both image sizes are 150 nm. Both scale bars are 30 nm.

These results clearly demonstrate that the ratio of the three coexistent 2D molecular arrangements is dependent on the concentration of ATC molecules in heptanoic acid. The parallel structure dominates at the higher concentration (sat/20), while the porous kagomé structure dominates and grows into larger domains at the lower concentration (sat/50).

Kagomé network

The term *Kagomé lattice* was first used in theoretical descriptions of magnetics phenomena [170]. The original meaning of the term Kagomé is a pattern common in woven Japanese bamboo baskets consisting of interlaced triangles and hexagons [171]. In a Kagomé lattice, each triangular lattice point has four neighbouring points. Kagomé structures have previously been observed to form in 2D self-assembled structures stabilised by hydrogen bonding [172], van der Waals interactions [173] and metal-organic coordination interactions [174]. The molecular arrangement of Kagomé lattices formed by tetra-carboxylic acid derivatives has been presented in Figure 4.1.

Figure 4.11 (a) shows a drift-corrected STM image of the ATC Kagomé structure. Each rod-like feature in the STM image corresponds to an individual ATC molecule adsorbed on the HOPG surface. The unit cell of the Kagomé structure is composed of three ATC molecules. Multiple measurements were carried out on two such high resolution, drift-corrected STM images to obtain unit cell dimensions for the ATC Kagomé network. At least ten datasets were collected to obtain an average value and its corresponding standard deviation as an error. The unit cell parameters of the Kagomé structure was experimentally determined to $a = b = (3.2 \pm 0.2)$ nm; and $\gamma = (59 \pm 3)$ °.

In the STM image presented in Figure 4.11 (a), it is even possible to discern the electronic orbital structure of the anthracene moiety within the ATC molecule. The three fused benzene rings that makes up the central anthracene group of an ATC molecule appear as six individual bright features. In striking contrast, the two isophthalic acid groups at either end of the ATC molecule appear as circular features at the ends of the fused benzene backbone and are significantly darker.

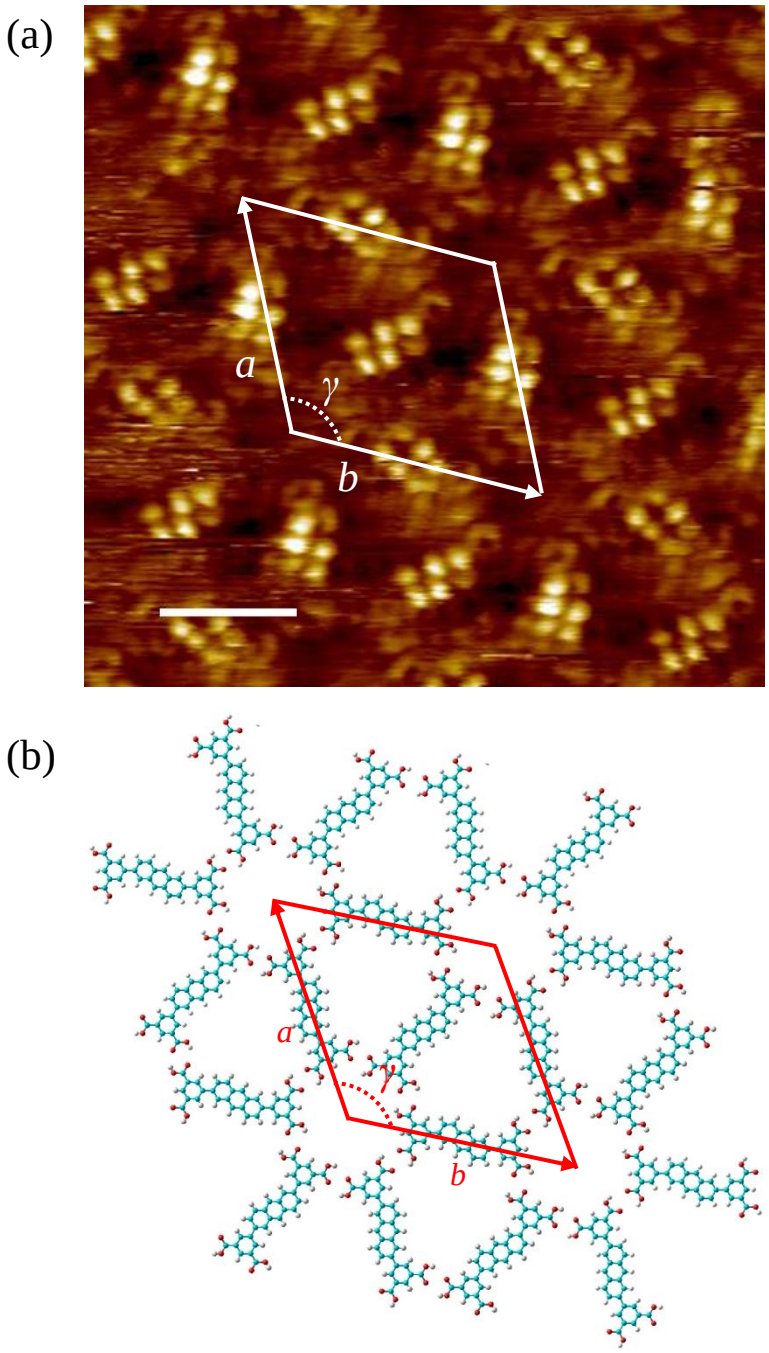

Figure 4.11. (a) High resolution, drift-corrected STM image of the ATC (sat/50) Kagomé structure with its unit cell marked in black. STM imaging parameters: *Vs* = -0.4 V, *It* = 0.05 nA. Image size: 8 nm. Scale bar: 1.6 nm. (b) Corresponding MM simulated molecular model with a unit cell marked in red.

The six-lobe anthracene feature of ATC has previously been observed for other anthracene derivatives. The alkyl chain functionalised anthracene molecule shown in Figure 4.12 (a), for example, was imaged as consisting of six lobes at the interface

between phenyloctane and an HOPG surface [57]. The six lobes shown in this STM image can be overlaid with the spatial distribution of the HOMO of the anthracene group. In comparison with the case presented in Figure 4.12, the tunnelling pattern of the anthracene shown in Figure 4.11 (a) would also be a direct result of the morphology of the HOMO of anthracene.

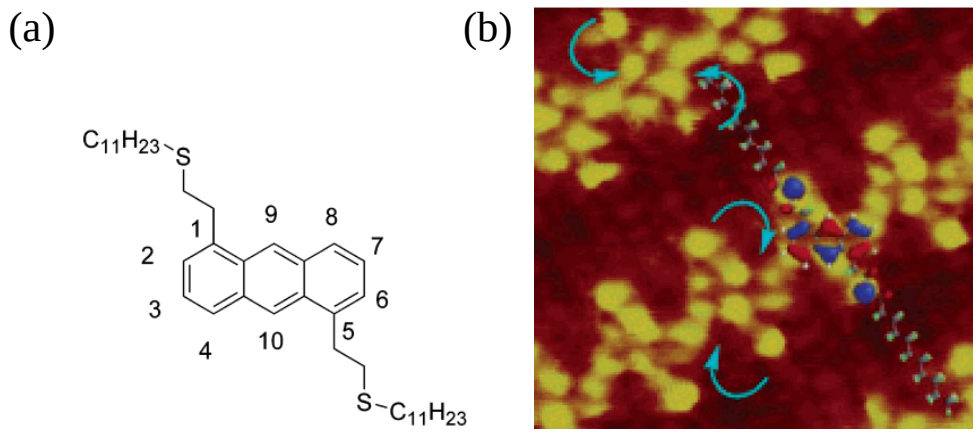

Figure 4.12 (a) Chemical structure of 1,5-bis-(3′-thia-tetradecyl) anthracene. (b) STM image of the self-assembled network of the compound shown in (a) at the interface between HOPG and phenyloctane (V_s = - 0.8 V, I_t = 0.28 nA, 12 ×12 nm^2). From reference [57].

Based on the high resolution STM image, a molecular model was built for the wheel-like porous structure using MM simulations (see Figure 4.11 (b)). The model was then geometry optimised with the influence of a fixed, single layer of underlying HOPG taken into account. As can been seen from the model, all ATC molecules adsorb on HOPG in a planar fashion. The entire network is stabilised by hydrogen bonding interactions between the carboxylic acid moieties on adjacent ATC molecules. The unit cell dimensions from the MM simulated molecular model were $a = b$ = 3.4 nm; and γ = 60 °, in excellent agreement with the STM measurements.

As the conjugated anthracene backbone of ATC is not symmetric, each ATC molecule is prochiral and can form one of two possible enantiomers upon adsorption onto the HOPG surface. A mirror-image domain of the porous network displayed in Figure 4.11 (a) was observed on a different area of the same surface. Figure 4.13 (a) shows the co-existing chiral domain formed by the opposite-handed enantiomer of ATC,

the corresponding molecular model of which is presented in Figure 4.13 (b).

(a)

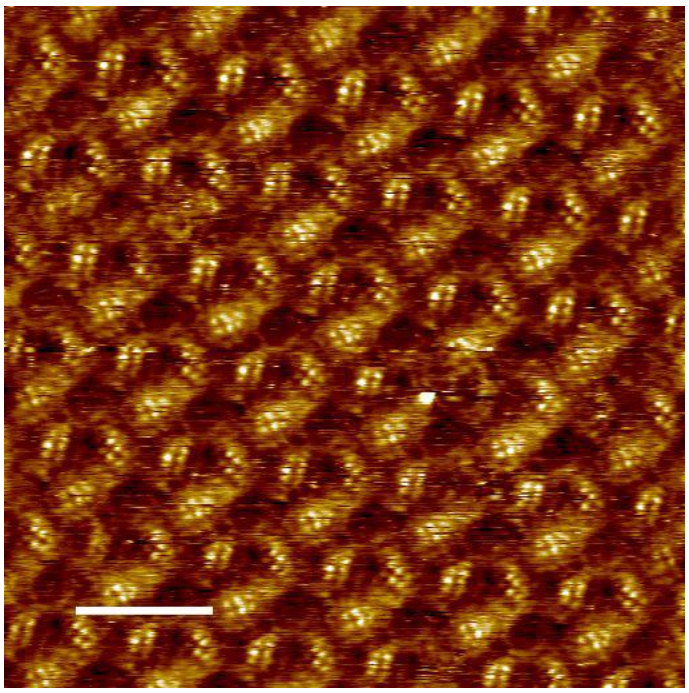

(b)

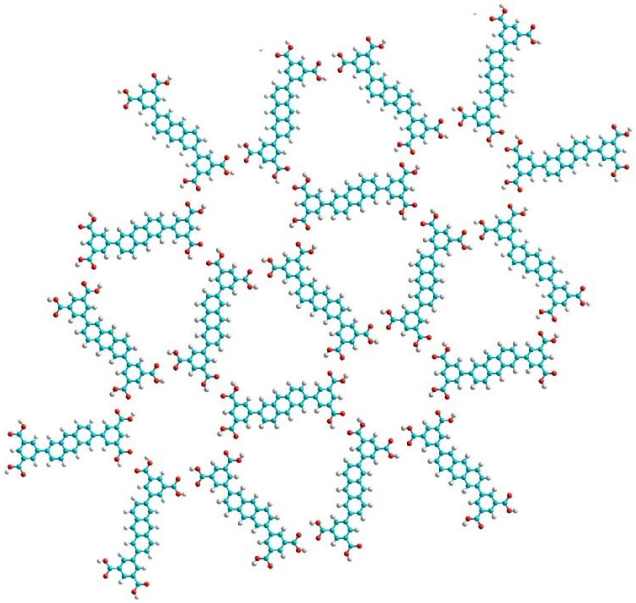

Figure 4.13. (a) STM image of the ATC mirror-image domain. This image has not been drift-corrected. STM imaging conditions: V_s = - 0.6 V, I_t = 0.04 nA. Image size: 20 nm. Scale bar: 4 nm. (b) MM molecular model of the chiral, Kagomé porous structure shown in (a).

Parallel network

At the higher concentration (sat/20), the ATC parallel phase is the dominant

configuration on the surface (49.2 %). Figure 4.14 (a) shows a high resolution, drift-corrected STM image of the parallel structure. To determine the unit cell dimensions, more than ten measurements were recorded from the STM image. The data were analysed by taking their average and standard deviation as error values. The unit cell parameters for the parallel structure were, by this way, measured to be a = (1.6 ± 0.1) nm; b = (2.3 ± 0.1) nm; and γ = (50 ± 2) °.

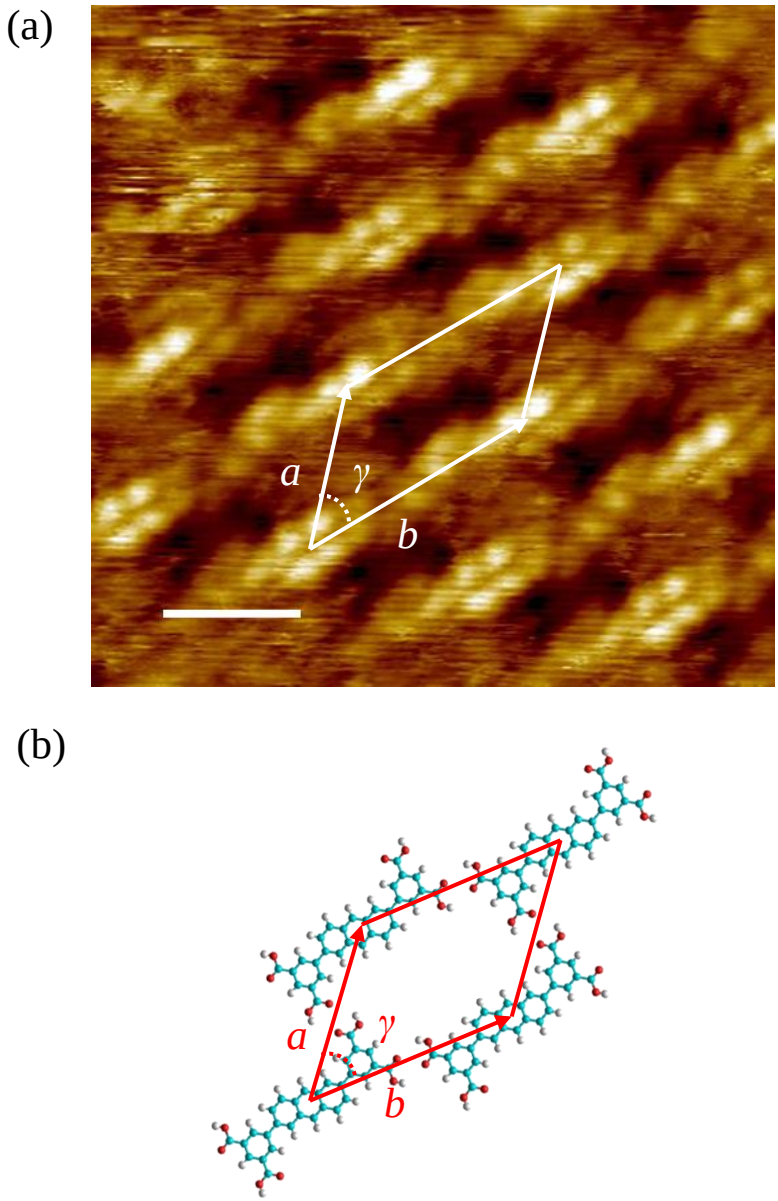

Figure 4.14. (a) Drift-corrected STM image of the ATC (sat/20) parallel structure with its unit cell marked in black. STM imaging conditions: V_s = - 0.4 V, I_t = 0.04 nA. Image size: 6.5 nm. Scale bar: 1.3 nm. (b) MM geometrically optimised molecular model (Unit cell marked in red).

Figure 4.14 (b) presents the molecular model constructed for the parallel phase using MM simulations. The unit cell dimensions determined from this model following geometry optimisation were a = 1.8 nm; b = 2.2 nm; and γ = 51 °, in good agreement with the values obtained from STM experiments. As illustrated by the molecular model, all the four carboxylic acid groups of each ATC molecule are involved in the formation of intermolecular -COOH ••• HOOC- double hydrogen bond dimers.

Close-packed network

As can be seen from Figure 4.10 (a), some ATC molecules adopt a closely packed arrangement within certain areas of the surface. Figure 4.15 (a) shows a drift-corrected, high resolution STM image of the close-packed structure. Ten line profiles were taken through this image to give different sets of unit cell dimensions. Then the average values and associated standard deviations of this data was taken to determine the experimentally measured unit cell constants: a = (0.9 ± 0.1) nm; b = (2.0 ± 0.1) nm; and γ = (69 ± 3) °.

A molecular model for the close-packed arrangement observed using STM is shown in Figure 4.15 (b). In the MM calculation, the stabilisation of the close-packed structure was assessed with molecule-surface interactions being taken into consideration. The unit cell constants obtained by the MM theoretical study were a = 1.0 nm; b = 2.2 nm; and γ = 62 °, in good agreement with values measured from STM images. In the close-packed arrangement, two carboxylic groups on individual ATC molecules adopt intermolecular -COOH ••• HOOC- double hydrogen bonding dimers. The other two carboxylic groups of the ATC molecule form weak =O •••HC- or -OH •••O= hydrogen bonding. This type of hydrogen bonding motif is also displayed in the 2D self-assembly of NTC molecules introduced in section 4.1 (Figure 4.3 (c)) [51].

Similar to the Kagomé network, the two enantiomers of ATC induced by surface adsorption can lead to the formation of mirror-image chiral domains for the parallel and close-packed networks. In the cases of the two molecular networks, the enantiomers should both be present on surfaces within different homochiral domains.

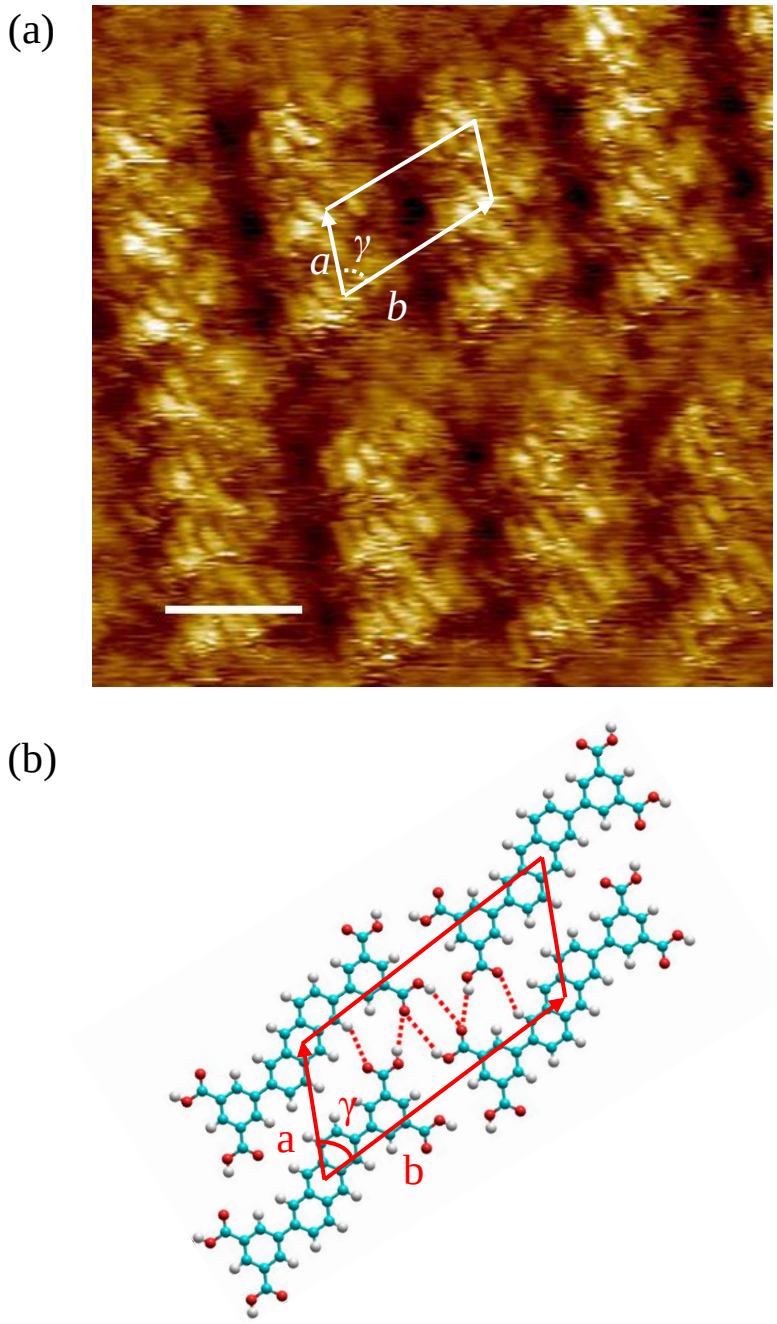

Figure 4.15. ATC (sat/20) close-packed structure. (a) Drift-corrected STM image. STM imaging conditions: V_s = - 0.4 V, I_t = 0.05 nA. Image size: 7.5 nm. Scale bar: 1.5 nm. (b) MM geometry optimised molecular model. Dashed, red lines: different hydrogen bonds involved in the close-packed structure.

4.3.3 Inclusion of coronene

Figure 4.16 presents the resulting network by depositing a mixture of ATC in heptanoic acid solutions (sat/20) and coronene 1.0 × 10^{-4} mg/ml. Compared with the ATC

mono-component network formed using the same concentration of ATC (Figure 4.10 (a)), the existence of the parallel or close-packed structures was not observed following the inclusion of coronene to the solution. The ATC Kagomé networks, which were not dominant for the mono-component system at this higher concentration, have been observed to be stabilised by the inclusion of coronene in the surface structure. Measured from the STM image shown in Figure 4.16, 75.6 % of the surface was covered with the ATC-coronene bi-component, and the remaining 24.4 % was not covered by the molecular network. Thus, the coverage of the bi-component networks was not as high as the mono-component system without coronene. Following the inclusion of coronene, the domain sizes of ATC networks reduced with numerous structural defects visible at domain boundaries.

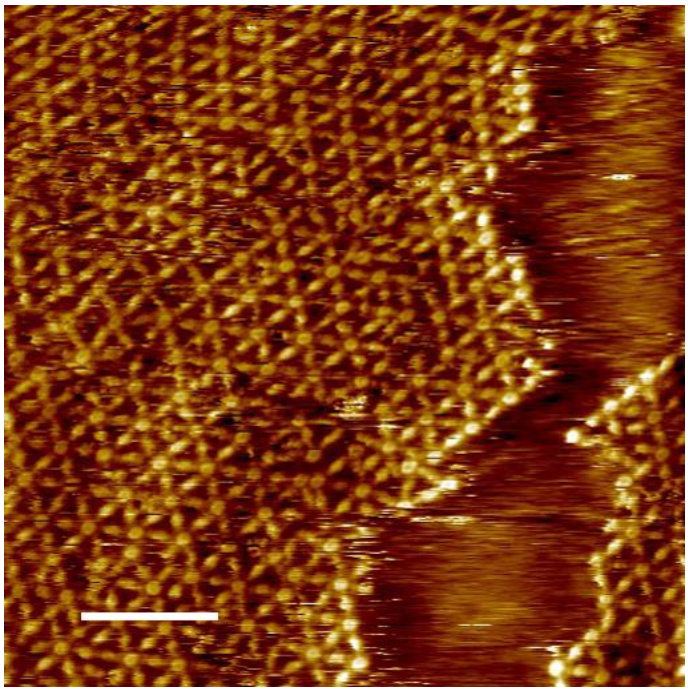

Figure 4.16. STM image of the bi-component network formed by the mixture of ATC (sat/20) and coronene 1.0 $\times 10^{-4}$ mg/ml at the heptanoic acid-HOPG interface. STM imaging conditions: V_s = - 0.6 V, I_t = 0.01 nA. Image size: 49.5 nm. Scale bar: 9.9 nm.

High resolution STM images of the Kagomé structure co-assembled with coronene were collected to resolve detailed features of the bi-component network structure. Figure 4.17 (a) is a high resolution STM image showing coronene molecules adsorbed

within the hexagonal pores formed by six isophthalic acid groups at the ends of the ATC molecules. Similar bi-component structures have been observed in the QPTC and NTC molecular systems following the inclusion of coronene at liquid-HOPG interfaces [51]. The period of this network structure, defined as distance between two adjacent coronene molecules, were measured to be 3.2 ± 0.1 nm. Ten data sets were collected to calculate their average and standard deviation as an error value. In the STM image shown in Figure 4.17 (a), the homo-chiral arrangement of ATC can be resolved from the STM image. In order to form the ordered Kagomé structure, all the ATC molecules within the bi-component domain should adopt the same handedness.

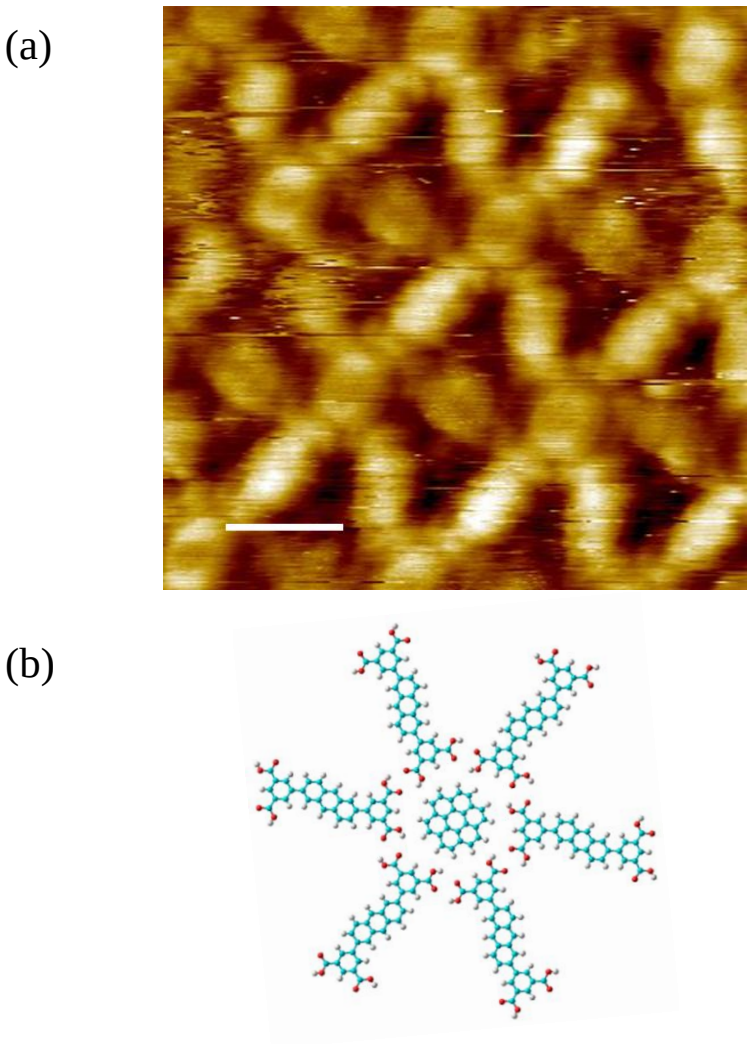

Figure 4.17. (a) Drift-corrected STM image of the ATC Kagomé structure stabilised by the co-adsorption of coronene. STM imaging conditions: V_s = -0.6 V, I_t = 0.01 nA. Image size: 8.5 nm. Scale bar: 1.7 nm. (b) Tentative molecular model of the ATC-coronene bi-component structure.

A tentative molecular model for the node of six isophthalic acid moieties stabilised by a coronene molecule was built using MM simulations (see Figure 4.17 (b)). The orientation of the coronene was placed in the centre of the pore as the starting point for the simulation. The period of the ATC-coronene network was measured to be 3.4 nm from this MM geometry optimised molecular model. The MM simulated and STM experimentally measured period values are in good agreement and remain unchanged in comparison to the mono-component Kagomé structure discussed in section 4.3.2.

4.4 Conclusions

In conclusion, it has been shown that ATC molecules self-assemble into extended 2D networks at the interface between heptanoic acid and HOPG. The morphology displayed by the ATC self-assembled networks depends on the concentration of the heptanoic acid solutions of ATC. At higher concentrations (sat/20), the parallel and close-packed structures dominate on the surface. At the lower concentrations (sat/50), the porous Kagomé structure dominates and grows into larger domains as compared with the network formed at the higher concentration. The inclusion of coronene in the self-assembly process significantly enhances the formation of the ATC-coronene bi-component Kagomé structure.

Compared with other tetra-carboxylic acid derivatives, ATC exhibits two interesting properties upon adsorption from the heptanoic acid solutions onto HOPG surfaces. Firstly, the prochiral nature of ATC means that it can adopt two different enantiomers upon adsorption to the surface, leading to the formation of homo-chiral self-assembled domains. Secondly, ATC displays 2D polymorphism with three structurally distinct patterns being resolved within the same two-dimensional self-assembled interfacial layer.

4.5 Future work

Based on the current results concerning the concentration-dependent self-assembly of ATC, a more detailed range of concentration experiments are suggested to be performed

to demonstrate how self-assembled structures of ATC vary with changes in concentration. Kinetic effects most probably play a very important role in determining the final morphology of the ATC network. The influence of kinetic effects will be removed or minimised by using an annealing and cooling procedure during network preparation. More specifically, ATC molecules will be deposited on preheated HOPG substrates. The heating may provide ATC molecules with enough energy to overcome any kinetic barriers and hopefully form structures with minimum Gibbs free energy. The sample will then be allowed to cool down naturally prior to STM imaging at the liquid-solid interface.

A set of STM experiments studying the temperature dependence of the ATC networks will also be conducted. In these experiments, ATC will be deposited onto substrates that are being maintained at elevated temperatures. In-situ STM images will then be recorded at a range of such elevated temperatures. The substrate will be allowed to cool back down to room temperature in a controlled fashion.

All of the experiments suggested above would help us gain control over the 2D self-assembly of prochiral ATC molecules by tuning concentration and temperature. These experiments would also provide new insights into the thermodynamic and kinetic factors that influence carboxylic acid drived 2D self-assembly. This would provide another model molecular system to study guest adsorption, chirality selection and other interesting phenomena during the formation of 2D self-assembled networks at the liquid-solid interfaces.

Chapter 5

Surface-based self-assembly of thymine functionalised porphyrins

Hydrogen bonding between DNA nucleobases has been shown to be an effective intermolecular interaction to drive the formation of two-dimensional (2D) molecular self-assemblies. This project aims to utilise selective hydrogen bonding between DNA nucleobases as a driving interaction to help organise more complex molecular structures. In order to achieve this goal, the 2D self-assembly of thymine functionalised porphyrins including tetra-(phenylthymine)porphyrin (tetra-TP) and its metal coordinated derivative, tetra-(phenylthymine)porphyrin-Zn(Ⅱ) (Zn-tetra-TP), was investigated at the interface between HOPG and organic solvents. The resulting self-assembled networks were studied using STM and MM simulations. In mono-component porphyrin systems, hydrogen bonding between the thymine groups of tetra-TP or Zn-tetra-TP leads to the growth of an extended, highly ordred network that is part of the p2 plane symmetry group. By careful selection of additional molecular components that can form complementary hydrogen bonds with thymine, it has been possible to form bi-component self-assembled networks with the functionalised porphyrin molecules. Thermodynamic aspects and concentration dependence of the self-assembly of these diverse molecular networks will also be discussed.

5.1 Introduction

The interaction between carboxylic acid groups is just one of a range of different hydrogen bonding motifs that have been used to drive the self-assembly of 2D molecular networks. Taking inspiration from nature, the hydrogen interactions between DNA nucleobases are potential candidates for the generation of highly ordered 2D

molecular structures.

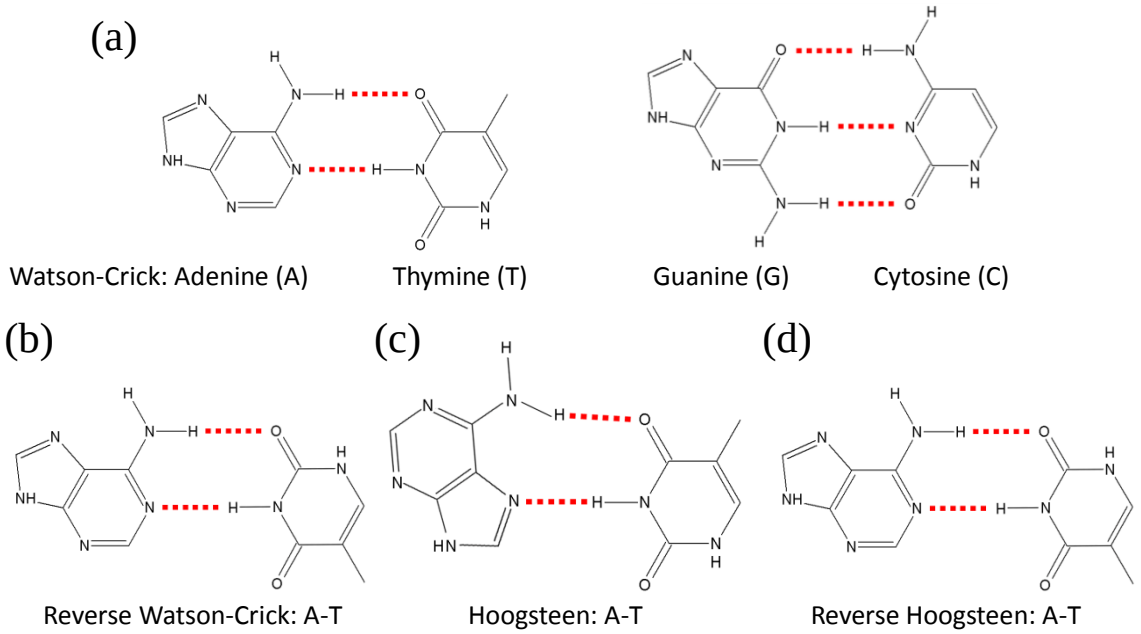

Figure 5.1. Chemical structures and hydrogen bonding interactions between DNA nucleobase pairs: (a) Watson-Crick DNA nucleobase pair; (b) Reverse Watson-Crick A-T base pair; (c) Hoogsteen A-T base pair; (d) Reverse Hoogsteen A-T base pair [175-178]. Red, dashed lines: hydrogen bonds.

The selective and directional hydrogen bonding between Watson-Crick base pairs is an important noncovalent interaction that contributes to the formation of the fascinating DNA double helix structure [175]. Figure 5.1 (a) describes the hydrogen bonding schemes formed between guanine (G)-cytosine (C) and adenine (A)-thymine (T) nucleobase pairs in DNA. In addition to the Watson-Crick base pairing, a number of other possible DNA nucleobase bonding modes exist such as reverse Watson-Crick; Hoogsteen; and reverse Hoogsteen base pairing (Figure 5.1 (b) - (d)) [176-178]. This variety of possible hydrogen bonding arrangements makes DNA nucleobases powerful groups for driving 2D self-assembly.

In addition to DNA nucleobases, other nucleobases that play important roles in biology have also been used as molecular recognition groups to form 2D supramolecular structures. Examples include uracil (U) in RNA [179], unnatural xanthine (X) [180], and isocytosine [181]. The versatile hydrogen bonding interactions between these natural and unnatural nucleobases have been used to drive the

self-assembly of a large number of 2D supramolecular structures at solid surfaces and interfaces [182]. While the recognition process during the self-assembly can be obtained by visualising adsorbed molecules directly, more experimental and theoretical attempts are still needed to allow the pre-programmed self-assembly of nucleobase functionalised molecules [23].

At the liquid-solid interface, highly ordered 2D self-assembled networks formed by mixing adenine and thymine molecules were first observed by Besenbacher *et al.* [183]. As the molecules were too small to be clearly resolved by STM under ambient conditions, orientations of the individual thymine or adenine could not be identified. Theoretical calculations were carried out to interpret the structures observed using STM. In order to illustrate the molecular recognition features between DNA nucleobase pairs at liquid-solid interfaces using STM, efforts can be devoted to functionalising larger molecular building blocks with DNA nucleobase. Porphyrins make an ideal candidate for such a molecule because of the ease with which they can be functionalised via synthetic routes, and the high contrast that their conjugated molecular core displays in STM images. If the orientation and geometrical size of the resulting self-assembled porphyrin arrays can be determined exactly, then from this information, the hydrogen bonding scheme adopted by the nucleobase functional groups can be decuced.

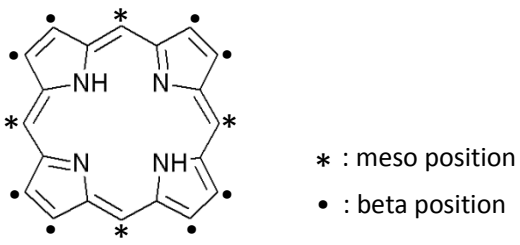

Figure 5.2. Molecular structure of porphyrin and possible positions for functionalisation.

As molecular building blocks for surface-based self-assembly, porphyrins (Figure 5.2) exhibit several advantages: (i) each *meso*- / *beta*-position of a four-fold symmetric porphyrin core can act as a site for functionalisation with a target chemical group; (ii) the four nitrogen atoms at the porphyrin core can coordinate a metal atom which can then act as a reactive site; and (iii) the conjugated nature of the macrocycle

core gives porphyrins favourable optical and electronic properties [184, 185]. The adsorption of porphyrins on solid surfaces has also been demonstrated to be visualised clearly by STM. A wide range of porphyrin derivatives have so far been used as molecular building blocks to grow 2D molecular structures. These include: covalently linked networks [60, 186]; and self-assembled patterns driven by hydrogen bonding between carboxylic acid groups [187, 188]; and 2D networks stabilised by metal-ligand coordination bonds [174, 189, 190]. However very few studies have been conducted on the self-assembly of porphyrins arrays directed by hetero-molecular hydrogen bonding interactions [191, 192].

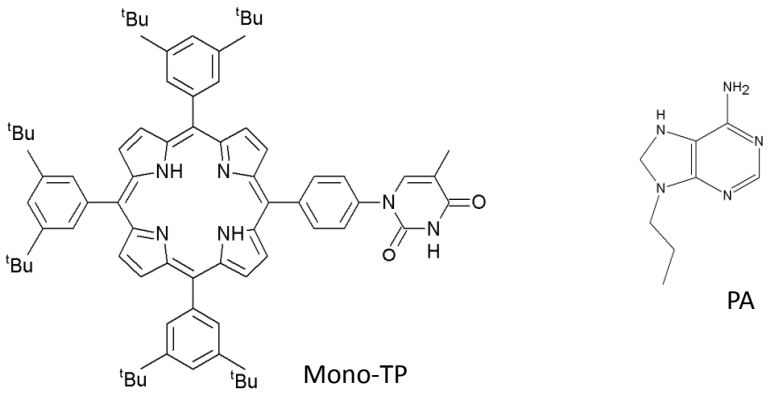

Figure 5.3. Chemical structure of the molecules used to probe thymine-adenine interactions in solution phases: mono-thymine-tri-(3,5-di-*tert*-butylphenyl)porphyrin (Mono-TP) and 9-propyladenine (PA).

Prior to studying the intermolecular interactions of DNA nucleobases on surfaces, our collaborators at the University of Nottingham first probed the property of hydrogen bonding between thymine functionalised porphyrins and adenine in solution by investigating a model molecular system consisting of mono-thymine-tri-(3,5-di-*tert*-butylphenyl)porphyrin (mono-TP) and 9-propyladenine (PA) (Figure 5.3) [193]. The bulky tertiary butyl groups of mono-TP act as obstacles to prevent π–π stacking between porphyrins in solution phase [194]. A phenyl group was synthetically inserted between the porphyrin core and the thymine to act as a spacer in order to minimise steric effects between the thymine group and the porphyrin core.

Planar groups attaching to the *meso* positions directly may experience steric interactions with the porphyrin core. The molecular design shown here allows the thymine functional group and the porphyrin macrocycle to be coplanar, a vital condition for 2D self-assembly [195].

Our collaborator in synthetic chemistry at the University of Nottingham, Prof. Neil Champness conducted structural studies on mono-TP and PA [193]. Single crystal X-ray diffraction was used to characterise the 3D crystal structure formed by mono-TP molecules. The single crystal was produced by diffusing CH_3OH into a mono-TP in CH_2Cl_2 solution. A synchrotron X-ray source was then used to collect single crystal diffraction data for the mono-TP sample [196]. As a result of this diffraction experiment, the relative arrangement of the thymine group with respect with the porphyrin plane was determined. Based on the crystal structure of the mono-TP, an $R_2^2(8)$ double hydrogen bonding interaction [197] as illustrated in Figure 5.4 was identified between thymine groups of adjacent mono-TPs.

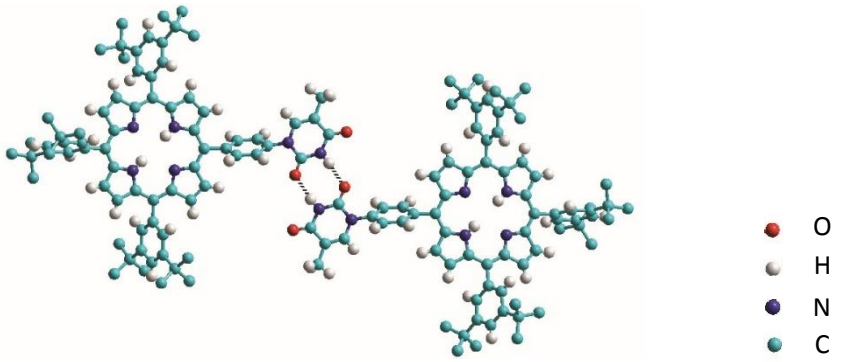

Figure 5.4. Single crystal X-ray structure for mono-TP showing the $R_2^2(8)$ double hydrogen bonding interaction (see the two black, dashed lines) between two adjacent thymine groups in 3D mono-TP cystals [193].

With the aim to evaluate hetero-molecular adenine-thymine interactions, NMR measurements were performed for mono-TP in deuterated chloroform solution with defined amounts of PA added into the solution gradually. Figure 5.5 (a) presents ^1H NMR spectra collected at each increasing concentration of PA in the mixture of mono-TP and PA.

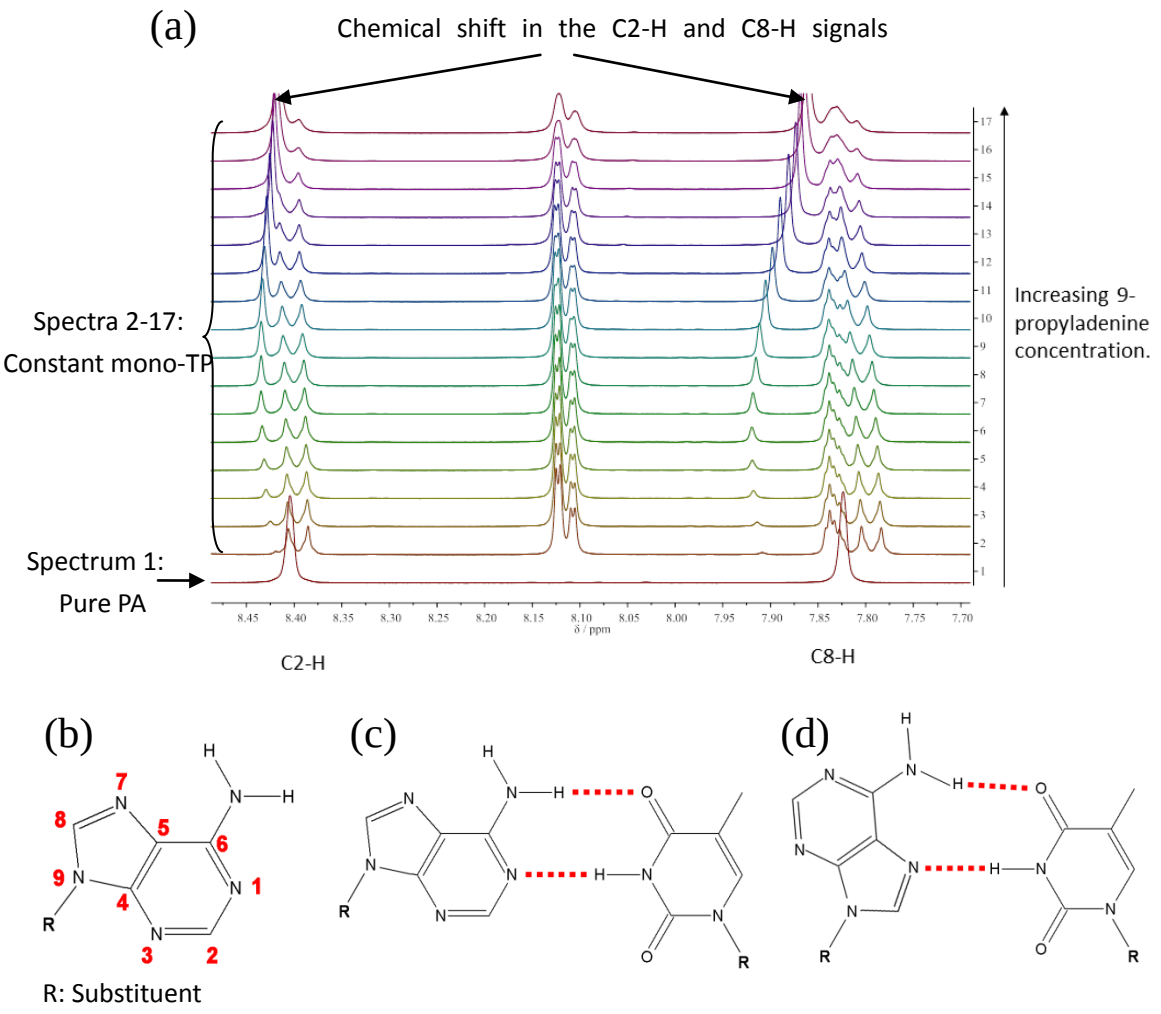

Figure 5.5. (a) ^{1}H NMR spectra of mono-TP in deuterated chloroform solutions with PA being titrated into the system gradually. Spectrum 1 is recorded in pure PA. Spectra 2-17 correspond to mixtures with an increasing concentration of PA [193]. (b) Structural illustration of PA with numbering of positions. (c) Schematic representation of Watson-Crick A-T hydrogen bonding between PA and Mono-TP. (d) Schematic representation of Hoogsteen A-T hydrogen bonding between 9-propyladenine and Mono-TP.

In spectrum 1 at the bottom of the graph, the two peaks can be attributed to the H atoms located at the C2 and C8 positions of the adenine group (Figure 5.5 (b)). The amine ^{1}H of the adenine group was not detected at this range. In the host Mono-TP solution with an increasing ratio of PA (Spectra 2-17), the two peaks corresponding to the C8-H and C2-H of the PA adenine demonstrate chemical shifts. The shifts were reported to be caused by the change in the electronegativity of the neighbouring nitrogen species when forming hydrogen bonds with the mono-TP thymine groups. As two shift directions of the C2-H and C8-H signals were observed, the electronegativity

of the neighbouring C7-N and C1-N changed in two ways. This suggests that the binding interactions between the thymine and adenine groups consist of both Hoogsteen [198] and Watson-Crick [175] hydrogen bonding modes as illustrated in Figure 5.5 (c) and (d).

Prior to analysing the hetero-molecular adenine-thymine interactions, the homo-molecular adenine-adenine interactions were also analysed by recording the chemical shift in adenine N*H*^{1}H when increasing the concentration of mono-component PA solutions. The same method was also applied to the measurement of homo-molecular thymine-thymine interactions for mono-TP. The magnitude of the increase in N*H*^{1}H shift for the mono-TP thymine in the mixture of mono-TP and PA was larger than the shifts observed in the mono-component systems. Thus, the hetero-molecular interactions between mono-TP and PA were shown to be stronger in comparison with homo-molecular interactions for mono-TP or PA.

In order to expand the structural studies that had been carried out in the solution phases to solid surfaces, the self-assembly of tetra thymine functionalised porphyrins, including freebase tetra-TP and Zn-tetra-TP, have been investigated. As shown in Figure 5.6, the *meso*-positions of the optically active porphyrin cores were functionalised with phenylthymine groups. The selective hydrogen bonding formed between the DNA nucleobases should result in more versatile 2D self-assembled networks compared with those directed by other less complex hydrogen bonding schemes such as carboxylic acid hydrogen bonding dimers. Moreover, the Zn metal atoms coordinated at the centre of Zn-tetra-TP molecular system has the potential to act as a site for forming further ligand coordination bonds with pyridine derivatives. Due to the axial nature of the coordination interaction, the on-surface self-assembly of Zn-tetra-TP could then potentially be extended from 2D to 3D. The extension of porphyrin self-assembled structures from 2D to 3D has potential applications in catalysis, molecular motors and gas storage [199]. Our experimental results show that both mono-component and multi-component networks can be formed at liquid-solid interfaces by utilising these thymine functionalised porphyrins and other small organic molecules with suitable hydrogen bonding groups as molecular building blocks.

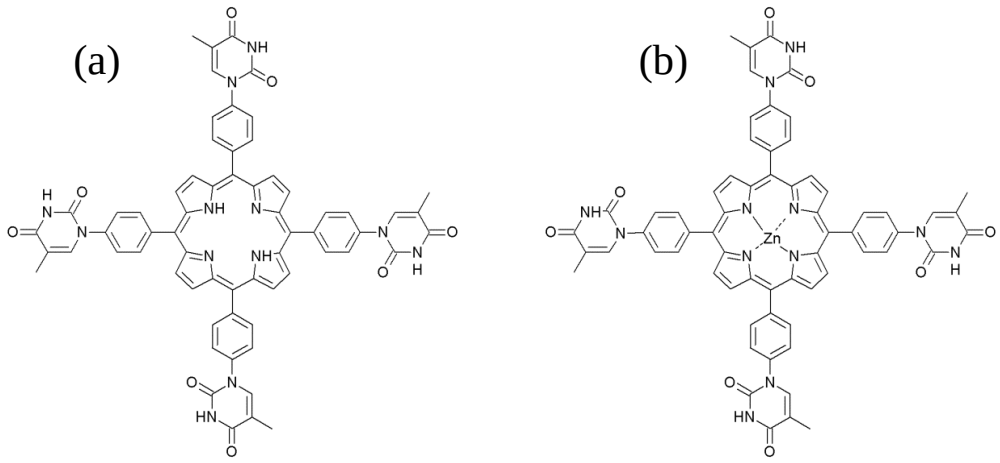

Figure 5.6. Chemical formulae of (a) tetra-(phenylthymine)porphyrin (tetra-TP); and (b) tetra-(phenylthymine)porphyrin-Zn(Ⅱ) (Zn-tetra-TP).

5.2 Details of experiments and simulations

For investigations of the self-assembly of porphyrin networks, tetra-TP (or Zn-tetra-TP) were dissolved in a mixture of tetrahydrofuran (THF) (anhydrous, > 99.9%, Sigma Aldrich) and 1,2,4-trichlorobenzene (TCB) (anhydrous, > 99.9%, Sigma Aldrich) with a 1:9 volume ratio. Stock solution of tetra-TP (or Zn-tetra-TP) with a concentration of 0.056 mg/ml (0.059 mg/ml for Zn-tetra-TP) were made and diluted successively to produce several tetra-TP (or Zn-tetra-TP) solutions with concentrations ranging between 0.0056 mg/ml and 0.056 mg/ml (0.0059 mg/ml to 0.059 mg/ml for Zn-tetra-TP). .

In order to mix PA with tetra-TP (or Zn-tetra-TP) PA was also dissolved in a mixture of THF and TCB with a 1:9 volume ratio. The nucleobase functionalised porphyrin molecules exhibit good solubility in THF. However, THF was too volatile for successful STM measurements, non-volatile TCB was needed to be used to allow STM experiments to be carried out at the liquid-solid interface. PA solutions with concentrations ranging between 0.0016 mg/ml and 0.20 mg/ml were prepared by diluting a stock solution with a concentration of 0.45 mg/ml. This large range of PA concentrations was used in order to investigate how the bi-component structures formed by tetra-TP (or Zn-tetra-TP) and PA are modified by the amount of PA. PA solutions were then mixed with tetra-TP (or Zn-tetra-TP) solutions to produce a range of mixed of

tetra-TP (or Zn-tetra-TP) and PA solutions with different overall concentrations and molar ratios.

In the studies of melamine self-assembly, both tetra-TP and melamine were dissolved in a mixed solvent of dimethyl sulfoxide (DMSO) (anhydrous, > 99.9%, Sigma Aldrich) and TCB with a 1:9 volume ratio. DMSO was used as a solvent as THF proved to be unsuitable to dissolve melamine. Since DMSO is a highly polar solvent, a measurable leakage current was observed during STM experiments. Thus, TCB was mixed with DMSO to reduce the leakage current of the melamine and tetra-TP solutions. The STM sample preparation procedures were the same as used for the tetra-TP and 9-propyladenine networks.

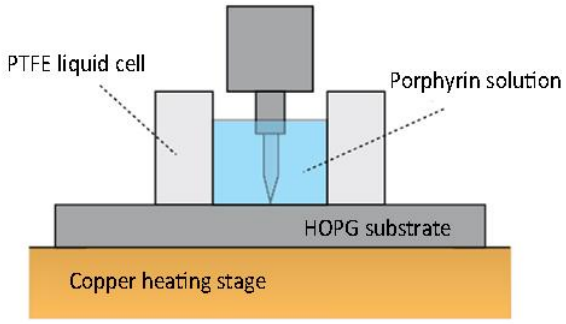

Figure 5.7. Illustration of an STM tip scanning at the liquid-HOPG interface mounted inside the temperature control liquid cell.

Self-assembled networks were prepared by depositing ~ 50 µl of the target solution onto a freshly cleaved HOPG substrate (Agar Scientific) mounted in a PTFE liquid cell (Figure 5.7). If no special explanation is provided, HOPG substrates were preheated to 60 ℃, held at this temperature for 5 ~ 10 minutes and then left to cool down to room temperature (~ 25 ℃) naturally prior to STM imaging. All STM images were collected in constant-current mode using an Agilent 5500 series STM system operating at the liquid-HOPG interface at ambient conditions. Mechanically cut Pt/Ir (80:20) tips (Advent Research Materials Ltd) were used for STM imaging. Flattening processes have been applied to all of the STM images presented in this chapter. For the high resolution STM images, drift-correction was implemented using the SPIP software

(Image Metrology, Denmark) by using the underlying HOPG lattice as a calibration.

The HyperChem software package was used to produce MM simulations of the mono-component and bi-component self-assembled porphyrin structures. The MM simulations were carried out with no repeat boundary conditions. Thus, the calculations were performed on individual clusters of molecules, instead of systems representing by a repeating lattice. The influence of the underlying HOPG surfaces was taken into consideration by including a fixed graphene sheet as a substrate below the molecular clusters of 2D network structures. Molecular structures derived from high resolution STM images after drift-correction used to guide the starting morphology of the MM simulations. The initial positions of the planar porphyrin macrocycles, adenine cores and melamine centres were set to be 0.35 nm above the underlying graphene sheet. The MM+ force field was used in order to geometry optimise the starting unit cell of the network structures. When reaching an energy gradient < 0.01 kcal $Å^{-1}$ mol^{-1}, the geometry optimisation process was deemed complete. The values for the unit cell sizes and angles from a geometry optimised molecular structure and its underlying HOPG symmetry axes were compared with those obtained from the corresponding drift-corrected STM image. This comparison acted as a test of the validity of the calculation results.

5.3 Self-assembly of freebase thymine-functionalised porphyrins

In this section, the self-assembly of tetra-TP on its own at the interface between the TCB/THF solvent mixture and the HOPG substrate will be discussed first. After this, further investigations that demonstrate the ability of tetra-TP arrays to co-assemble with either PA or melamine and form bi-component networks will be introduced.

5.3.1 Tetra-TP on its own

Efforts were made to self-assemble mono-TP at the TCB-HOPG interface. However, no

molecular structure was ever captured during STM scans of the mono-TP. The reason for this lack of observed structure could be related to the smaller number of hydrogen bonds that a mono-TP molecule is capable of forming in comparison to the tetra-TP molecule. In addition, the presence of the non-planar tertiary butyl groups on the mono-TP molecule will lead to it having a far weaker adsorption interaction with the HOPG surface. In the case of tetra-TP, some undissolved particulate material was observed in solution even for the diluted tetra-TP solutions used in the project. When the tetra-TP solution deposited into the liquid cell was heated, it is believed that more of the tetra-TP was driven into solution increasing the concentration. On cooling, the additional tetra-TP that had been dissolved by heating then precipitated out of the solution. These additional tetra-TP molecules would then adsorb on the surface and form the self-assembled structures.

Morphology of tetra-TP self-assembled networks

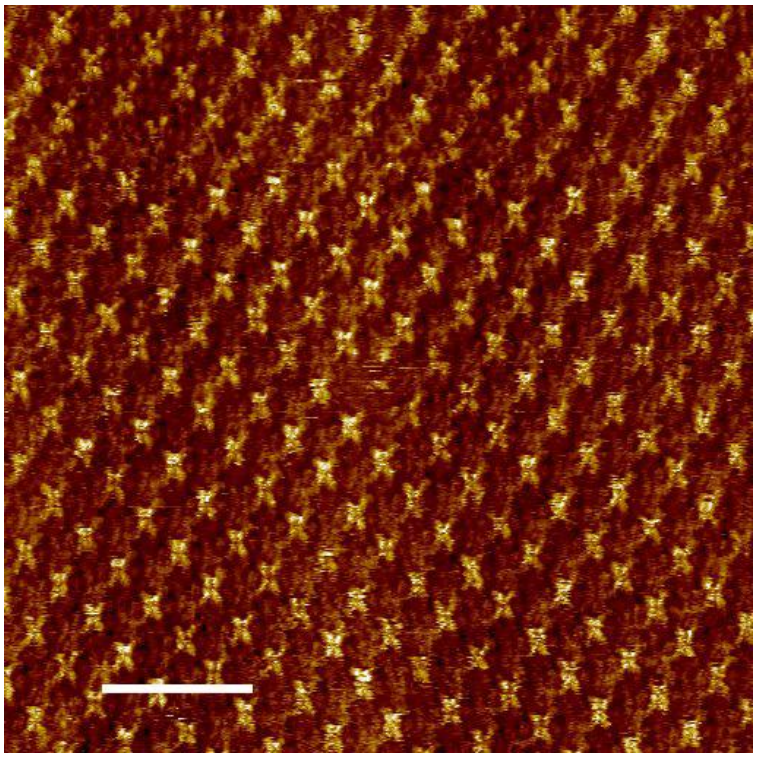

Figure 5.8. STM image of a 2D tetra-TP (0.031 mg/ml) mono-component network self-assembled at the interface between HOPG and TCB/THF mixture (9:1). STM scanning conditions: V_s = - 0.5 V; I_t = 0.015 nA. Image size: 100 nm. Scale bar: 20 nm.

Figure 5.8 is a 100 nm × 100 nm STM image showing the formation of an extended tetra-TP network with domain size larger than 100 nm. When deposited on HOPG, the mono-component tetra-TP forms a 2D self-assembled network that is part of the *p*2 plane symmetry group. Each cross-shaped bright feature in the STM image corresponds to a tetra-TP molecule. The tetra-TP molecules adsorb in a planar fashion with the porphyrin cores aligned parallel with the underlying HOPG surface.

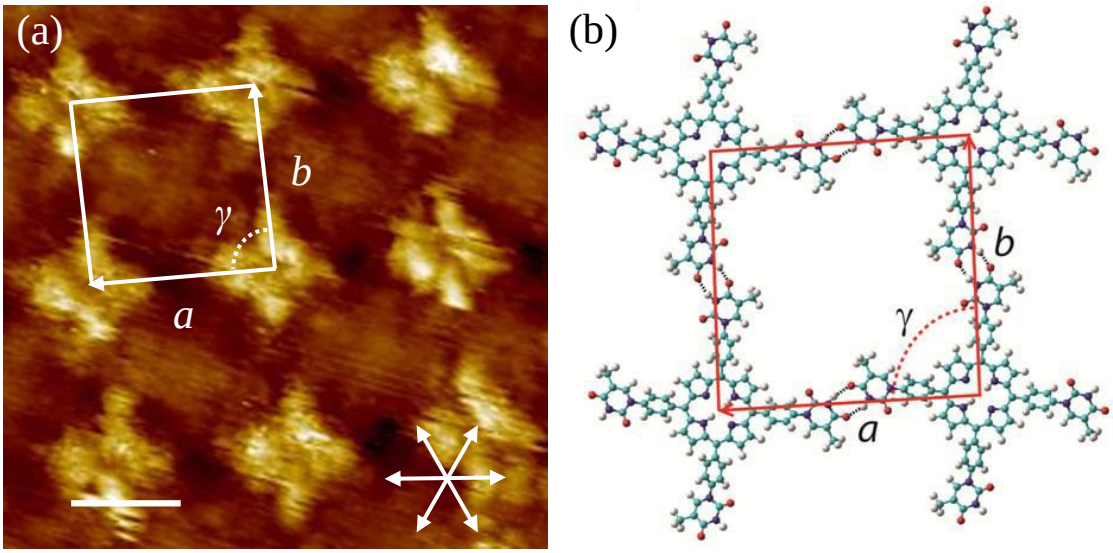

Figure 5.9. (a) Drift-corrected STM image of the 2D self-assembly of mono-component tetra-TP networks, the unit cell marked in white. White arrows at bottom right corner indicate the main symmetry axes of the underlying HOPG surface. STM imaging conditions: V_s = - 0.53 V; I_t = 0.012 nA. Image size: 8 nm. Scale bar: 1.6 nm. (b) Molecular model from a geometry optimised MM simulation of the mono-component tetra-TP network.

Analysis of drift-corrected STM images for the tetra-TP network, for example the high resolution STM image shown in Figure 5.9 (a), provided a quantitative measurement of the lattice parameters of the 2D unit cell, and the alignment of the unit cell with respect to the underlying HOPG lattice. The values were obtained by taking an average from more than three measurements on different drift-corrected STM images. Associated error values for the unit cell dimensions and angle were obtained by calculating the standard deviations of the sets of multiple measurements. By taking measurements from a series drift-corrected STM images of the tetra-TP

monocomponent structure, the unit cell lattice parameters were determined to be a = 25.9 ± 0.5 Å, b = 25.2 ± 0.6 Å and γ = 91 ± 1 °. The angles that the unit cell structure makes with respect to its underlying graphite symmetry axes were measured to be α = (6 ± 3) ° and β = (25 ± 3) °.

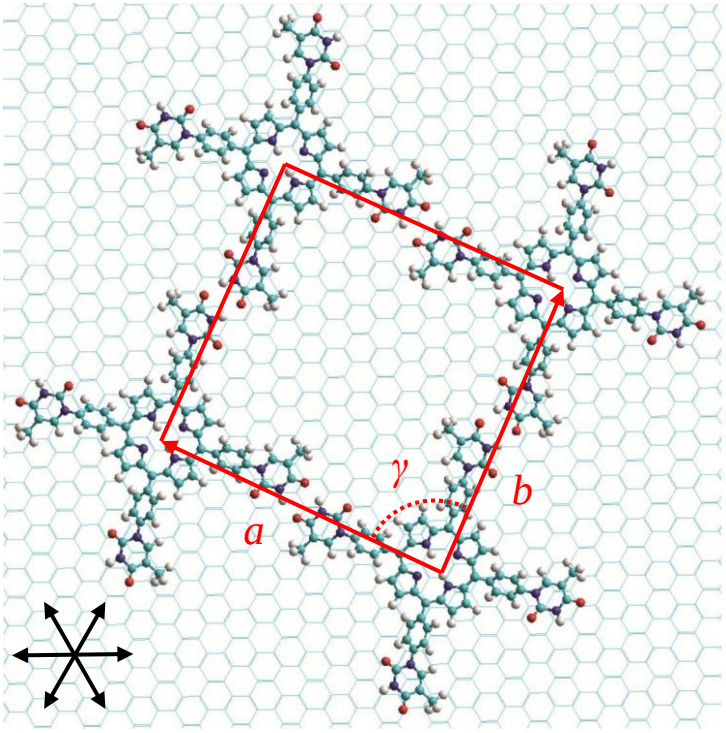

Figure 5.10. MM simulated tetra-TP structure overlaying a fixed graphene sheet after geometry optimisation.

MM simulations were employed as a complementary method to STM by calculating a geometry optimised molecular model for the self-assembled structure. In the MM simulations a unit cell of the tetra-TP unit structure was placed above a fixed graphene sheet (Figure 5.10). Figure 5.9 (b) presents the geometry optimised MM model for a unit cell of the tetra-TP network. The unit cell parameters of the tetra-TP structure obtained from the MM calculations were a = 26.0 Å, b = 25.9 Å and γ = 91 °. The unit cell vectors made angles of α = 4.7 ° and β = 24.3 ° with the underlying HOPG symmetry axes. These unit cell values were in good agreement with those obtained from the drift-corrected STM images. Therefore, this molecular model was chosen as a valid representation of the 2D tetra-TP network. As can be seen from this model, the

formation of the tetra-TP structure is driven by hydrogen bonding between the thymine groups on adjacent tetra-TP molecules. The thymine-thymine hydrogen bonding mode is slightly different but still similar to the bonding arrangement observed between mono-TP molecules in 3D crystals [193] and between thymine molecules self-assembled in 2D at the interface between HOPG and 1-octanol [183].

Adsorption-induced chirality of tetra-TP

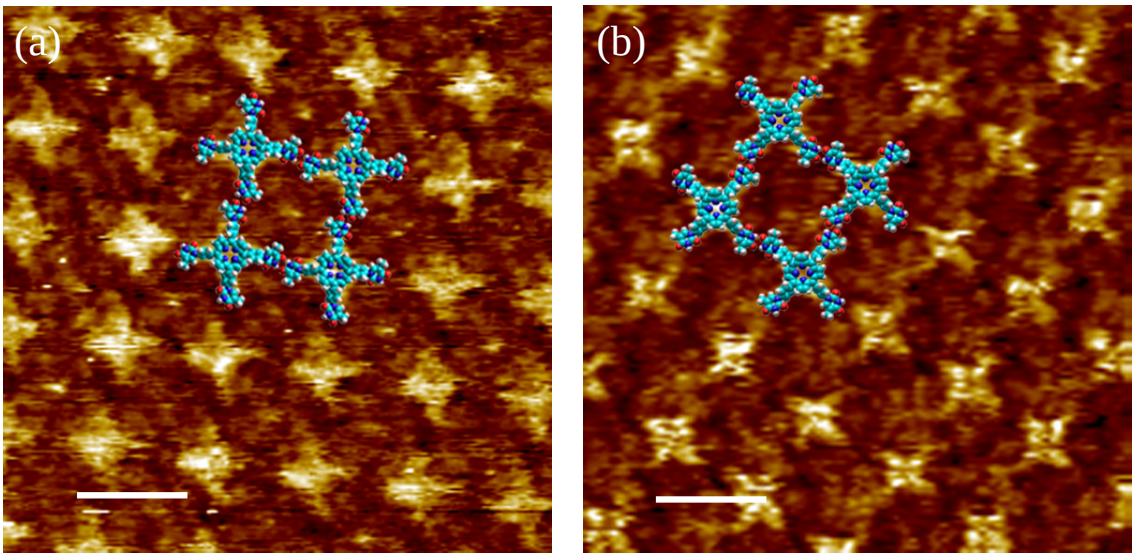

Figure 5.11. Drift-corrected STM images and molecular models showing mirror-image domains of the tetra-TP network (0.031 mg/ml). Both image sizes: 13.5 nm. Both scale bars: 2.7 nm. STM imaging parameters: (a) V_s = - 1.3 V, I_t = 0.02 nA; (b) V_s = - 0.5 V; I_t = 0.015 nA.

In some of the high resolution STM images, mirror-image domains of the tetra-TP networks were visible (see Figure 5.11). These two chiral arrangements of the tetra-TP structure could be observed at different locations on the same surface. The chiral tetra-TP structures result from the existence of the two possible orientations that the asymmetric thymine groups can adopt upon adsorption onto a HOPG surface. In each of the homochiral domains in Figure 5.11, tetra-TP molecules adopt a single handedness. As the two chiral domains both have a four-fold symmetry, all of the four thymine groups in individual tetra-TP molecule exhibit the same orientation with respect to the porphyrin macrocycle. In solution, it is believed that the four thymine groups in a

tetra-TP are able to rotate freely. Following adsorption onto the HOPG surface, the prochiral tetra-TP becomes chiral adopting either a right-handed or a left-handed configuration. The adsorption-induced chirality phenomenon has been observed in many other supramolecular self-assembled patterns formed by molecules at liquid-solid interfaces [200, 201].

5.3.2 Tetra-TP and PA

Morphology of tetra-TP and PA bi-component structure

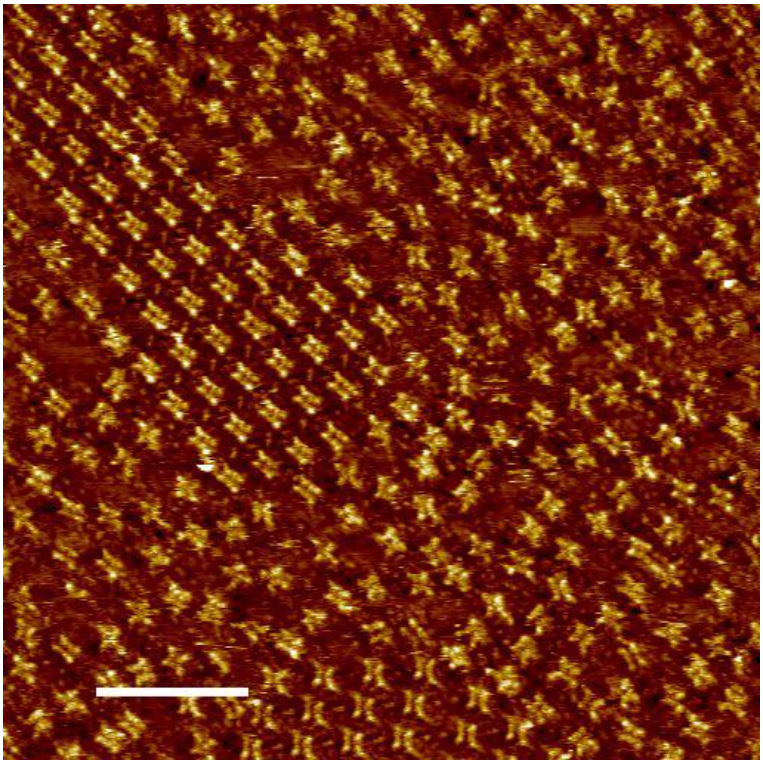

Figure 5.12. STM image of a 2D molecular network formed by the self-assembly of tetra-TP (0.031 mg/ml) and PA (0.089 mg/ml) at the liquid-solid interface. Scale bar is 14 nm. STM imaging conditions: V_s = - 0.5 V, I_t = 0.02 nA.

Figure 5.12 shows an STM image of the self-assembled structure formed by tetra-TP and PA at the solvent/HOPG interface. In this molecular network tetra-TP and PA co-crystallise into ordered bi-component structures surrounded by disordered regions

(see Figure 5.12). The domain size of the bi-component structures can be quantified by taking the square root of the surface area occupied by an ordered domain. In order to measure the average domain size of the ordered regions, the average value and standard deviation of five domain sizes collected from different locations on the same surface were calculated. As a result, the average domain size of the ordered regions formed under this set of conditions was determined to be 19 ± 7 nm. The ordered regions were observed in all of the STM images collected on this surface. The percentage of the surface covered with the disordered regions was analysed from three STM images collected from different locations of the same surface. The average percentage coverage of the disordered regions was estimated to be 83.1 % ± 5.5 %. No repeating structural motif can be seen in the disordered regions.

In order to illustrate the exact bonding mode between tetra-TP and 9-propyladenine in the ordered co-crystal, drift-corrected high resolution STM images were collected to determine the unit cell dimensions of the bi-component 2D self-assembled pattern. MM simulations were then conducted to interpret the molecular morphology observed from the STM images using a same method as described for the tetra-TP mono-component system. Unit cell values from the different possible molecular models were compared with the experimentally measured data for the purpose of validating a calculated structure.

Figure 5.13 (a) is a high resolution, drift-corrected STM image showing the unit cell structure of the ordered tetra-TP and PA co-crystal. By analysing more than three different STM images of this quality, unit cell parameters for the 2D network were measured to be a = (25.4 ± 0.7) Å, b = (22.2 ± 0.9) Å, and γ = (83.0 ± 2.0) °. The angles that the unit cell vectors make with respect to the underlying HOPG symmetry axes were determined to be α = (4.4 ± 1.2) °, and β = (26.9 ± 2.1) °.

MM calculations performed with no repeat boundary conditions were carried out to optimise the geometry of the ordered tetra-TP and PA structure on an underlying fixed graphene sheet (Figure 5.14). Figure 5.13 (b) presents the MM calculated unit cell of the co-crystal which has dimensions that are in good agreement with those measured directly from the drift-corrected STM images: a = 26.0 Å; b = 21.5 Å; γ = 85.7 °. The

angles that the unit cell vectors make with the underlying graphite symmetry axes were measured to be α = 4.7 °, and β = 30.0 °. The calculated model can be used to illustrate the various hydrogen bonding modes that exist in the tetra-TP and PA co-crystal structure presented in Figure 5.13 (a).

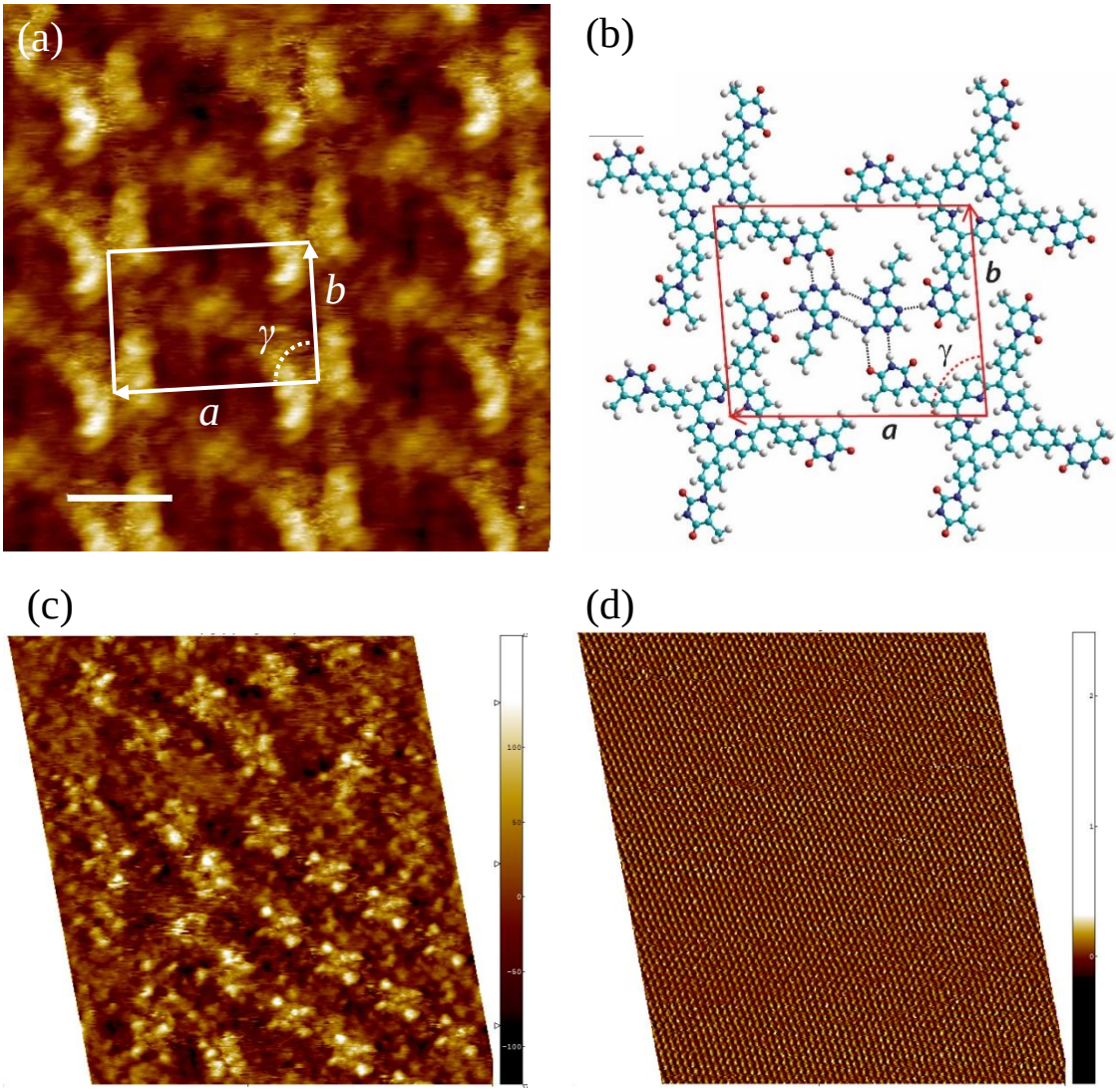

Figure 5.13. (a) Drift-corrected STM image of the tetra-TP and PA co-crystal structure. Scale bar: 1.6 nm. (b) Geometry optimised molecular model and unit cell (marked in red) for the 2D network. (c)-(d) A pair of STM images used for drift-correction showing the bi-component molecular network and the underlying HOPG surface respectively. STM imaging conditions: (a) V_s = - 0.55 V, I_t = 0.012 nA; (b) V_s = - 0.5 V, I_t = 0.02 nA; (c) V_s = - 0.05 V, I_t = 1 nA.

As can be seen from the molecular model shown in Figure 5.14, the two PA molecules are linked to each other by a hydrogen bond dimer. Each PA molecule is

linked to the two adjacent tetra-TP molecules by three hydrogen bonds. The hydrogen bonding dimer between the two PA molecules is consistent with the bonding scheme observed in self-assembled adenine structures on a HOPG surface from DFT calculations [183]. The three hydrogen bonds formed between the PA and two surrounding tetra-TP molecules consist of a hydrogen bond dimer that adopts a Watson-Crick adenine-thymine base pair type interaction [175] and a single -NH ••• N hydrogen bond.

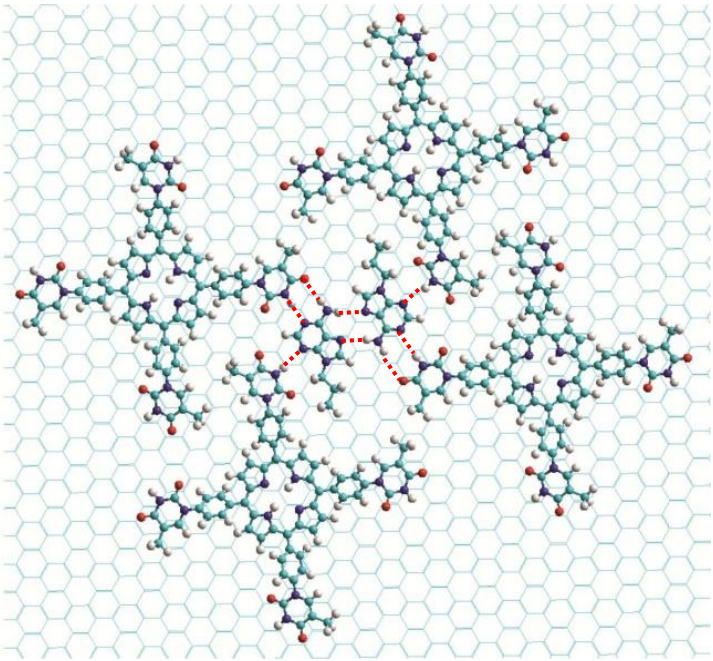

Figure 5.14. MM simulated molecular model for the tetra-TP and PA co-crystal with the fixed underlying graphene lattice. Red, dashed lines: hydrogen bonding.

Due to the adsorption-induced chirality of asymmetric thymine groups, the growth of mirror image domains has also been observed for the tetra-TP and PA bi-component system. Figure 5.15 presents an STM image showing the formation of two homochiral domains with opposite chirality for the tetra-TP and PA co-crystal. In each of the highly ordered domains all four of the thymine groups for each individual tetra-TP molecule adopt the same orientation with respect to the porphyrin macrocycle either clockwise or anti-clockwise. The two adsorption-induced enantiomers of the prochiral tetra-TP molecule lead to the observation of the two mirror-image domains of the tetra-TP and

PA bi-component self-assembled structure.

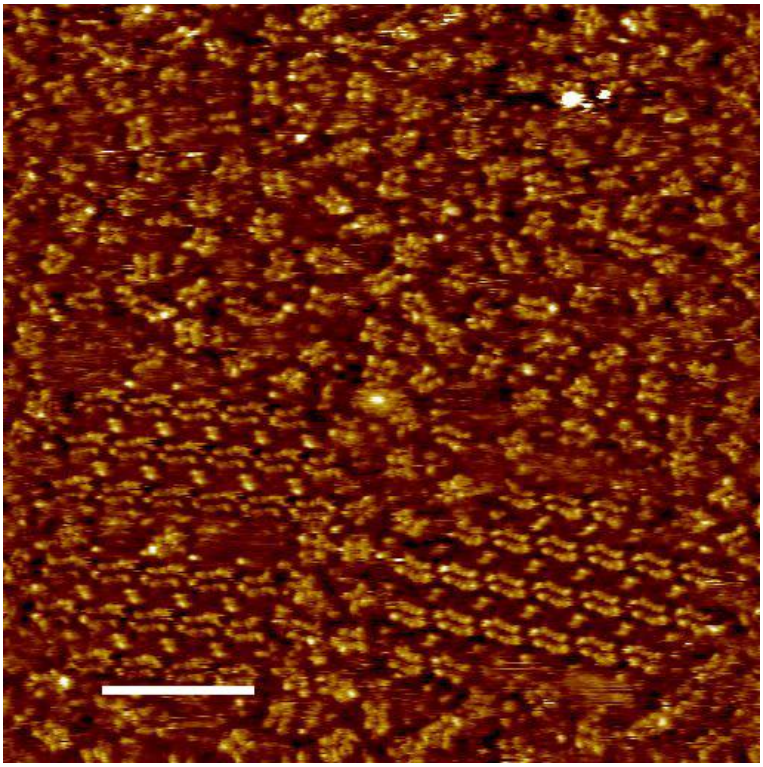

Figure 5.15. STM image of a bi-component network formed by tetra-TP (0.10 mg/ml) and PA (0.040 mg/ml) that shows the growth of mirror-image domains. Image size: 50 nm. Scale bar: 10 nm. STM imaging conditions: V_s = - 0.55 V; I_t = 0.015 nA.

Concentration and molar ratio dependency of the bi-component self-assembly

Efforts have been devoted to understanding the way the bi-component networks form, and to increasing the areas of the ordered bi-component structures. STM investigations were carried out to study the influence that the overall concentration and molar ratio of tetra-TP and PA had on the morphology of the bi-component self-assembled networks. Networks were formed using a range of mixtures of tetra-TP and PA with different molar ratio values and concentrations. These structures were then imaged using STM.

Figure 5.16 demonstrates four example STM images collected for tetra-TP and PA self-assembled networks prepared under different conditions. By comparing the network morphology in these STM images, it is observed that the formation and quality of the

ordered tetra-TP and PA co-crystal network is related to the overall concentration and molar ratio of the two molecular components in solution.

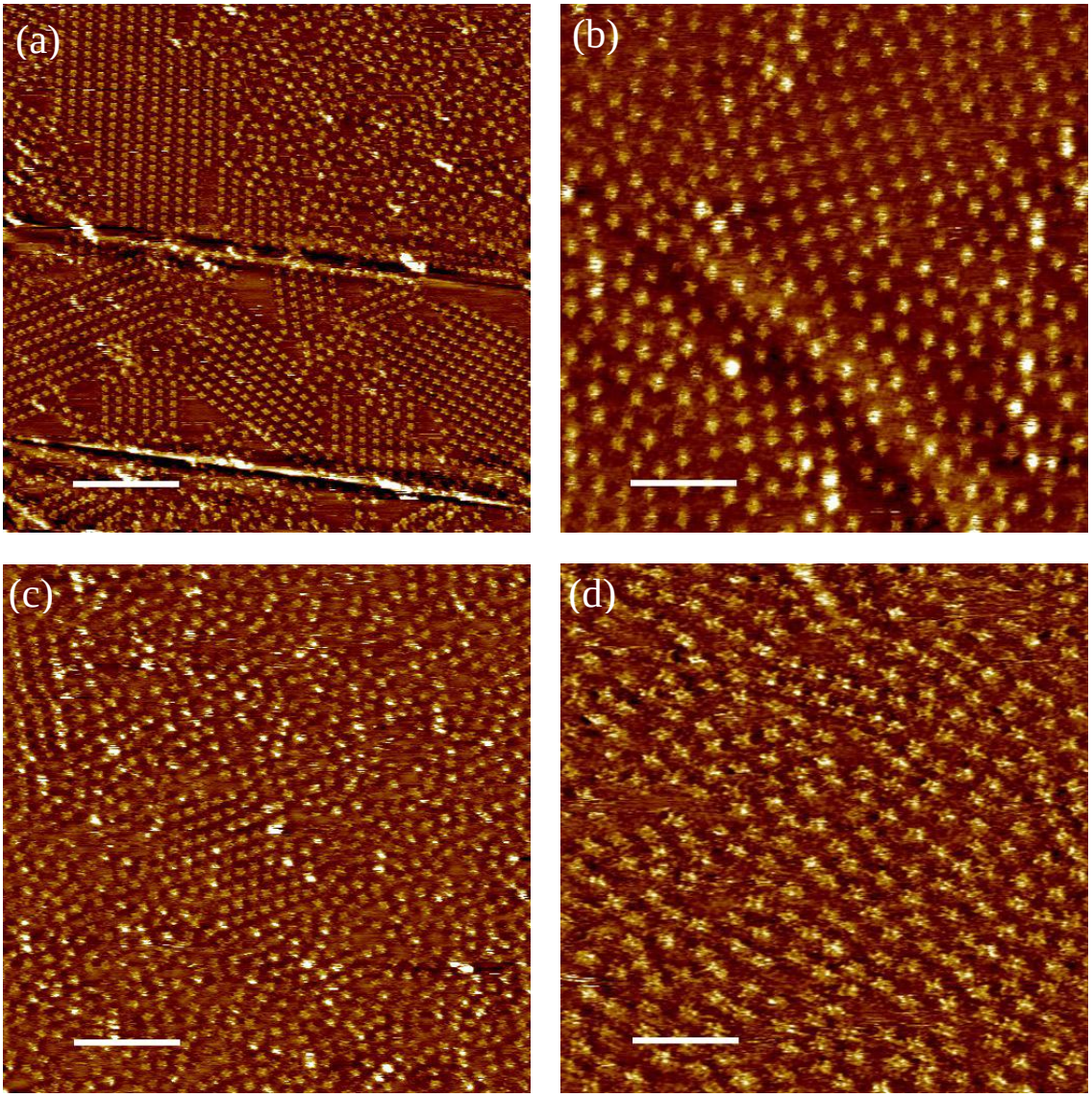

Figure 5.16. STM images showing the morphology of tetra-TP and PA networks formed at different overall concentrations and molar ratios of the two components. (a) Molar ratio between tetra-TP (0.015 mg/ml) and PA (0.044 mg/ml) is 1:16. (b) Molar ratio between tetra-TP (0.034 mg/ml) and PA (1.6×10^{-3} mg/ml) is 4:1. (c) Molar ratio between tetra-TP (0.020 mg/ml) and PA (0.22 mg/ml) is 1:64. (d) Molar ratio between tetra-TP (5.6×10^{-3} mg/ml) and PA (0.38 mg/ml) is 1:383. STM imaging conditions: (a) V_s = - 0.5 V, I_t = 0.02 nA; (b) V_s = - 0.55 V, I_t = 0.02 nA; (c) V_s = - 0.5 V, I_t = 0.02 nA; (d) V_s = - 0.5 V, I_t = 0.03 nA. Scale bars: (a) 30 nm; (b) 11 nm; (c) 20 nm; (d) 11 nm.

The same quantitative analysis method that was used to analyse the STM image

shown in Figure 5,12 was applied to study the structural order of bi-component networks formed by tetra-TP and PA under different conditions. The results of the quantitative analysis for the STM images presented in Figure 5.16 are listed in Table 5.1.

STM image	Mixture of tetra-TP and PA (mg/ml)	Molar ratio of tetra-TP to PA	Composition of ordered areas	% coverage of ordered areas	Domain size of ordered areas (nm)
Figure 5.12	Tetra-TP: 0.031 PA: 0.089	1:16	Bi-component	(16.9 ± 5.5) %	19 ± 7
Figure 5.16 (a)	Tetra-TP: 0.015 PA: 0.044	1:16	Bi-component	(24.2 ± 16.2) %	39 ± 14
Figure 5.16 (b)	Tetra-TP: 0.034 PA: 1.6×10^{-3}	4:1	Mono-component	(5.3 ± 4.4) %	19 ± 5
Figure 5.16 (c)	Tetra-TP: 0.020 PA: 0.22	1:64	Bi-component	(7.4 ± 2.3) %	16 ± 7
Figure 5.16 (d)	Tetra-TP: 5.6×10^{-3} PA: 0.38	1:383	Bi-component	(1.4 ± 0.8) %	9 ± 1

Table 5.1. Summary of results for the quantitative analysis of the bi-component networks formed by tetra-TP and PA under different sets of conditions.

In comparison with the network demonstrated in Figure 5.12, Figure 5.16 (a) maintains the same tetra-TP to PA molar ratio (1:16) but the concentrations of tetra-TP and PA are both decreased by half. At this molar ratio, the lower overall concentration leads to the growth of the tetra-TP and PA co-crystal with larger domain sizes, and lower coverage of disordered regions. This could be related to reduced kinetic trapping of the adsorbed tetra-TP molecules. As discussed previously, the additional tetra-TP molecules that are dissolved during the heating stage would precipitate on the HOPG surface when the sample is cooled. At the lower overall concentration, the kinetic

trapping effect is reduced leading to the growth of larger ordered domains compared with the network shown in Figure 5.12.

In Figure 5.16 (b), the concentration of tetra-TP is the same is in Figure 5.12. However, the molar ratio of tetra-TP to PA has been increased to 4:1 by lowering the concentration of PA. In this case, the highly ordered regions change from the tetra-TP and PA co-crystal to the tetra-TP mono-component self-assembled network surrounded by disordered regions.

When the amount of PA is increased to a high level, for example in Figure 5.16 (c), the ordered bi-component structures interspersed within the disordered regions display much smaller domain sizes as compared with Figure 5.16 (a).

In Figure 5.16 (d), the molar ratio of PA to tetra-TP is further increased (1:383) by lowering the concentration of tetra-TP. The large excess of PA molecules in comparison to tetra-TP results in the favourable growth of disordered regions at the expense of the ordered bi-component co-crystal.

The above results demonstrate that the formation of the self-assembled tetra-TP and PA co-crystal is strongly related to the overall concentration and molar ratio of the molecular species. The concentration and molar ratio dependency suggests the significance of kinetic effects in the surface-based self-assembly of tetra-TP and PA. the low solubility of tetra-TP molecules in the mixture of THF and TCB means that it is difficult for the adsorbed tetra-TP on HOPG to desorb back into the solution. As a result, the adsorbed tetra-TP and PA molecules are kinetically trapped on the HOPG surface. Consequently, the re-organisation of the molecular system becomes more difficult and the formation of ordered structures is reduced.

5.3.3 Tetra-TP and melamine

Molecular recognition between the diimide group of thymine derivatives and the diaminopyridine group of melamine has previously been explored as a route to build up a variety of self-assembled 2D nano-architectures. Example molecular systems include: 3D assemblies of melamine and thymine functionalised nanoparticles for the visual

detection of tiny amounts of melamine in raw milk [202]; and 2D porous self-assembled networks for guest adsorption under either UHV conditions [2] or at liquid-solid interfaces [203]. Figure 5.17 illustrates the triple hydrogen bonding scheme that can be observed between melamine and thymine derivatives.

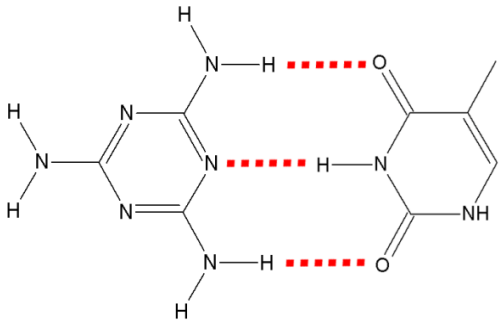

Figure 5.17. Chemical structure of melamine and its non-covalent interaction with thymine via three hydrogen bonds. Hydrogen bonds are marked by dashed red lines.

Melamine molecules were added to tetra-TP networks as linkers to form bi-component 2D self-assembled networks driven by the above complementary hydrogen bonding between melamine and thymine.

Figure 5.18 (a) presents an STM image with a scan size of 150 nm which shows the formation of a tetra-TP and melamine bi-component network at the interface between HOPG and DMSO-TCB. Some defects of the network are discernible at this scale, for example: vacancies corresponding to missing tetra-TP; and dislocations at domain boundaries (Figure 5.18 (b)). The large bright features visible in the image are probably due to 3D aggregates of undissolved molecules (Figure 5.18 (c). the leakage current caused by using DMSO as a solvent rather than THF or TCB meant that STM tips imaging in DMSO needed to be brought closer to the surface by applying a lower voltage and selecting a higher set-point tunnel current. Under these imaging conditions, a larger current flows between the tip and the surface. Thus, the relative influence of the leakage current resulting from the DMSO in the solvent mxiture can be reduced.

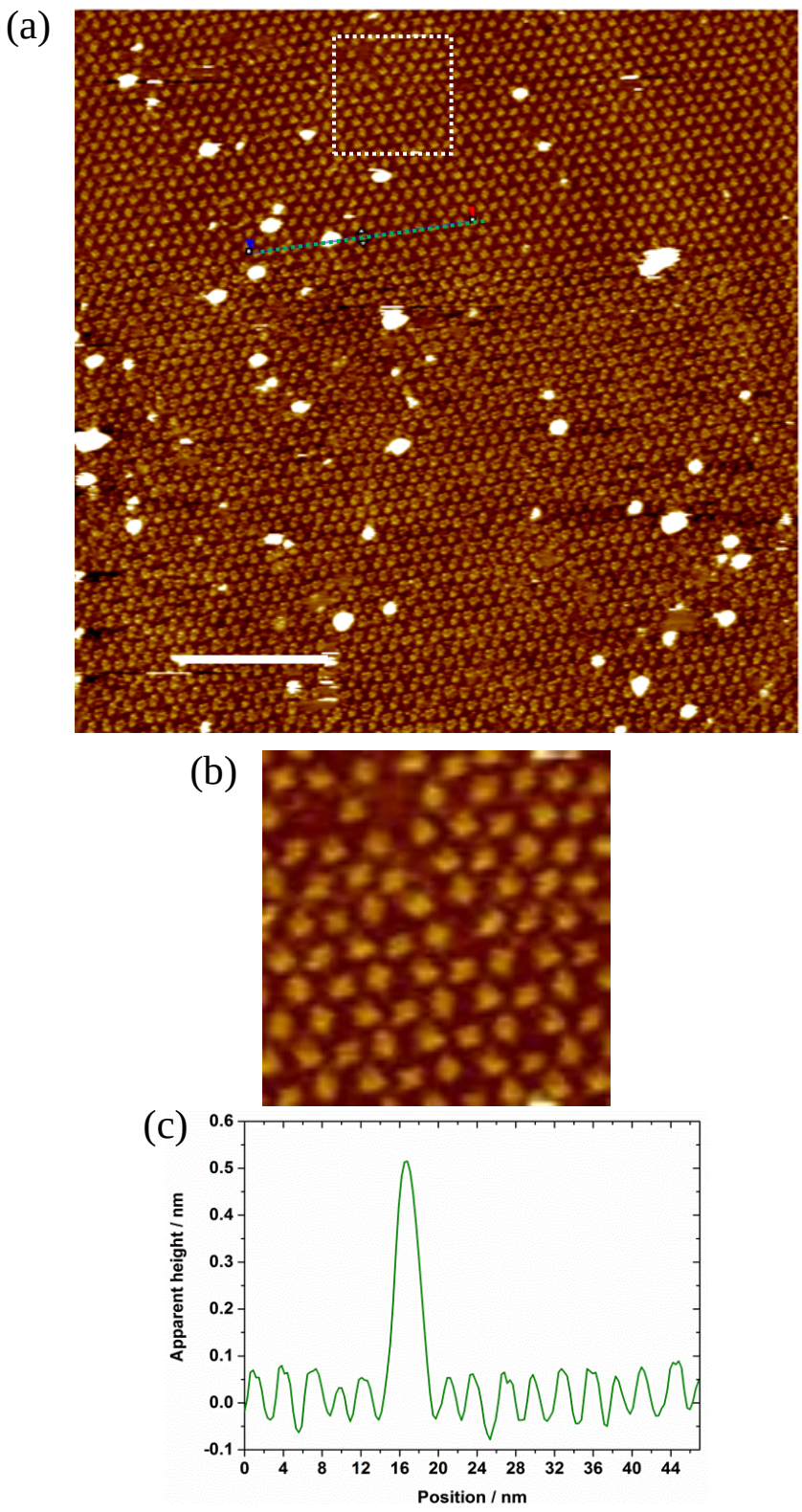

Figure 5.18. (a) STM image of a self-assembled network formed by tetra-TP (5.0×10^{-3} mg/ml) and melamine (0.050 mg/ml) at the liquid-solid interface. STM imaging conditions: V_s = - 0.45 V, I_t = 0.03 nA. Image size: 150 nm. Scale bar: 30 nm. (b) Magnified STM image of the region marked by the dashed, white square in (a). (c) Line profile showing the apparent height of one of the bright features in (a).

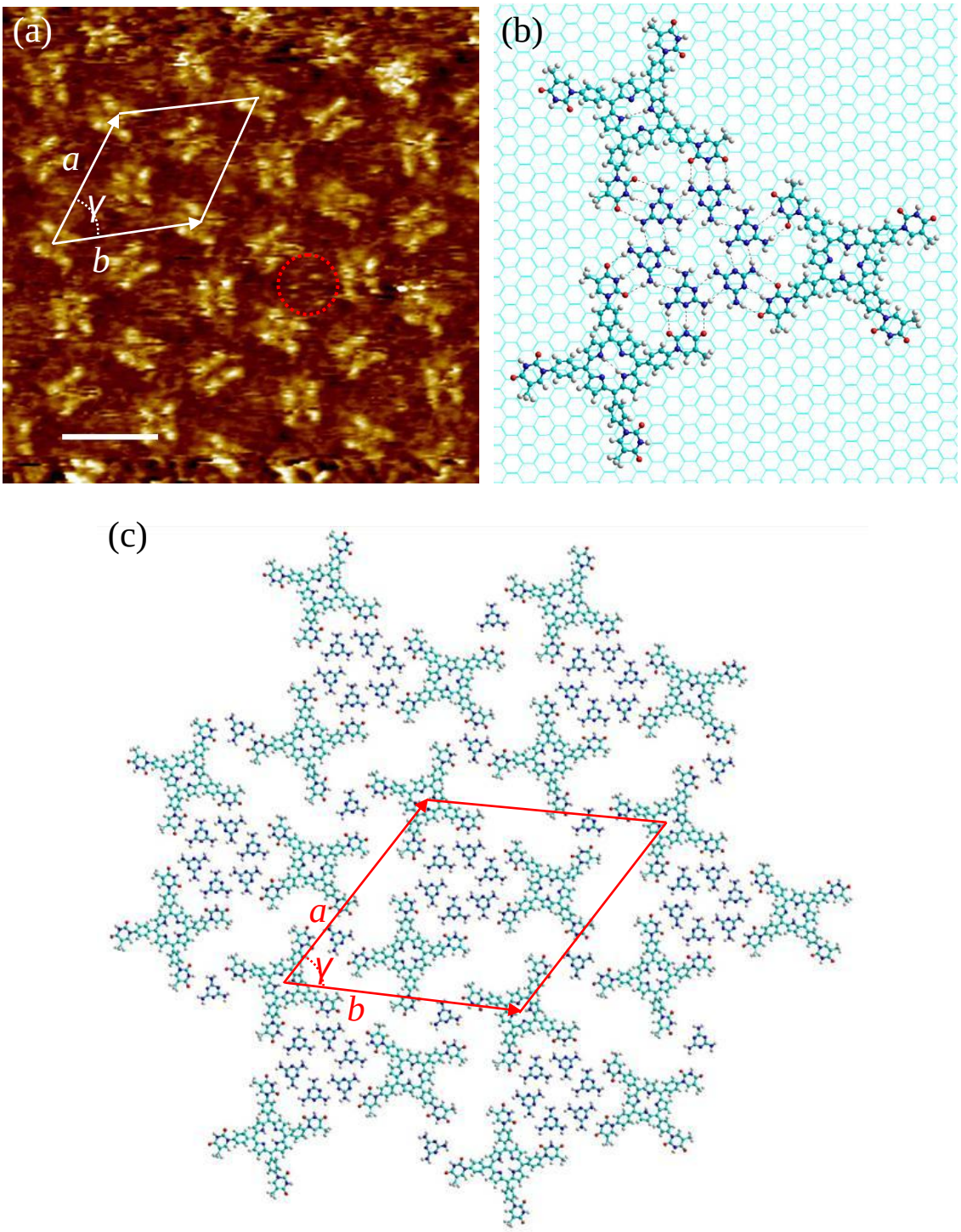

Figure 5.19. (a) High resolution, drift-corrected STM images of the tetra-TP (2.4×10^{-4} mg/ml) and melamine (0.090 mg/ml) network at the liquid-solid interface between HOPG and DMSO/TCB. The unit cell for the tetra-TP and melamine structure is marked in white. STM imaging conditions: V_s = - 0.5 V, I_t = 0.02 nA. Image size: 15 nm. Scale bar: 3 nm. (b) Geometry optimised MM simulations of six melamine molecules surrounded by three tetra-TP molecules with an underlying fixed graphene layer. (c) MM simulated molecular model for an extended region of the tetra-TP and melamine network. The unit cell of the network is marked in red.

Higher magnification STM images were collected to determine the exact structure of the bi-component tetra-TP and melamine self-assembled network and to measure its unit cell dimensions. Figure 5.19 (a) shows a high resolution, drift-corrected STM image on a HOPG surface covered with the tetra-TP and melamine network. From this image we can see that the tetra-TP molecules adopt three orientations with respect to the underlying surface. Each of the tetra-TP molecules has its central axis making an angle of 120 ° with that of adjacent tetra-TP molecules. Using multiple measurements from different regions of this STM image the lattice parameters of the network were determined to be a = (4.4 ± 0.4) nm; b = (4.7 ± 0.5) nm; γ = 58 ± 2 °. As can be seen from the STM image, some of the larger pores in the structure are not empty, for example the red, dashed ring marked in Figure 5.19 (a). In this molecular system, these pores are highly likely to hold a ring of six melamine molecules leading to an increasing number of hydrogen bonds. The reason for this STM image interpretation will be discussed later in this section.

Based on the morphology and dimensions of the tetra-TP and melamine network illustrated in STM images, tentative molecular models were built for the assembled structure using MM simulations. Due to the calculation limit of the computer used to run the HyperChem package, only one unit structure formed by the ring of six melamine molecules surrounded by three tetra-TP molecules was geometrically optimised with a fixed underlying graphene sheet taken into consideration (See Figure 5.19 (b). Figure 5.19 (c) is a tentative MM calculated model for the tetra-TP and melamine network with all of its larger pores filled by the six-melamine rings. The unit cell parameters for the tetra-TP and melamine network based on these simulations were calculated to be a = 5.0 nm; b = 5.2 nm; γ = 60 °, in good agreement with the experimentally measured values.

More high resolution STM images were collected to verify the molecular model shown in Figure 5.19 (c). Figure 5.20 shows an STM image in which the individual melamine molecules that act as linkages between tetra-TP molecules can be resolved. From the molecular model for one of the melamine junctions (Figure 5.20 (c)), each of the tetra-TP molecules has an achiral arrangement and the four thymine groups of a single tetra-TP adopt two different orientations.

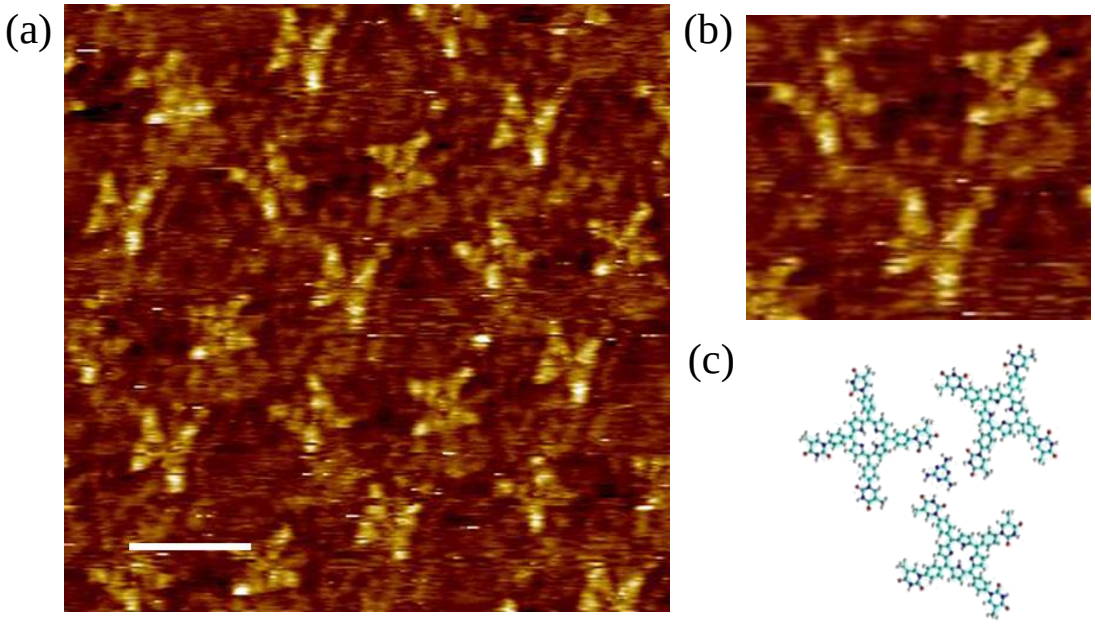

Figure 5.20. STM image of the tetra-TP (2.4×10^{-4} mg/ml) and melamine (0.090 mg/ml) network allowing the identification of the individual melamine linkers. STM imaging conditions: V_s = - 0.55 V, I_t = 0.015 nA. Image size: 12.5 nm. Scale bar: 2.5 nm. (b) Magnified STM image showing a melamine linking its adjacent tetra-TP molecules by three melamine-thymine hydrogen bond trimers. (c) Corresponding molecular structure of the melamine-linked junction.

Melamine molecules adsorbed in the larger pores of the tetra-TP and melamine network were visible in some of the STM images, for example, in Figure 5.21 (a). Details of the melamine assemblies within the pores as guest molecules can be seen from Figure 5.21 (b). We suggest that six melamine molecules form a hexagonal arrangement appearing as three bright spots in the STM images for two reasons. Firstly, the unit cell dimensions of the model match those of the STM images. The stabilisation and geometrical size of the hexagonal melamine self-assembled structure have also been verified using DFT simulations [204]. Secondly, the hexagonal arrangement of six melamine molecules is a commonly observed structural motif in other 2D self-assembled systems containing melamine [205-207]. Moreover, the three-spot STM feature for the porous melamine structure self-assembled at the liquid-solid interface is similar to a previous observation of melamine ad-layers adsorbed at the air-HOPG interface after solvent evaporation (Figure 5.22) [208]. Figure 5.21 (c) shows a molecular model built for the melamine assemblies in the pore formed by three tetra-TP

molecules with different orientations of their central axis. The guest-host structure is stabilised by six hydrogen bonding dimers between adjacent melamine molecules taking opposite directions and six pairs of thymine-melamine hydrogen bonding trimers.

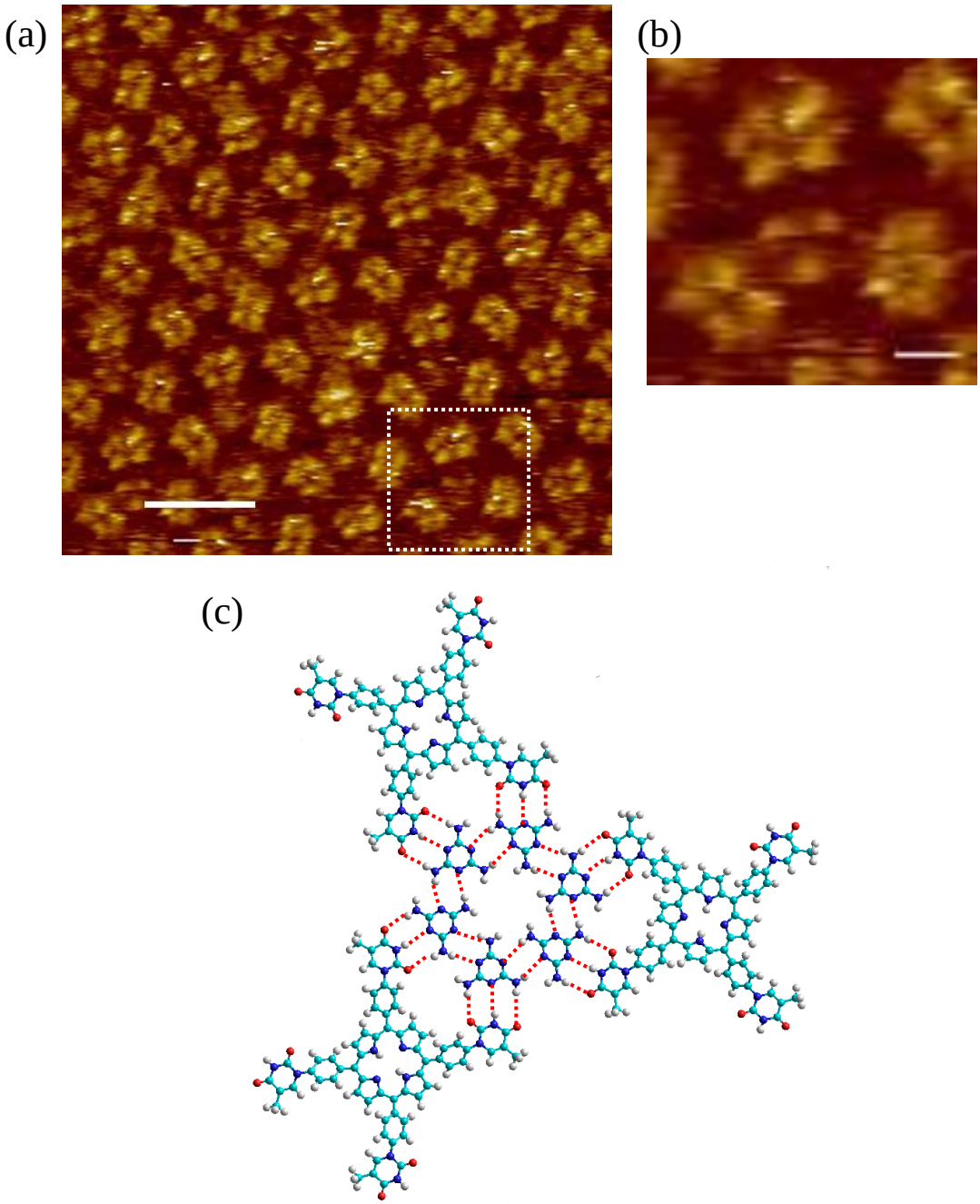

Figure 5.21. (a) STM image of the tetra-TP (2.4×10^{-4} mg/ml) and melamine (0.090 mg/ml) network showing the melamine rings. STM scanning parameters: V_s = - 0.55 V, I_t = 0.015 nA. Image size: 22 nm. Scale bar: 4.4 nm. (b) Magnified STM image of melamine adsorbed in a large pore formed by three tetra-TP molecules. (c) Corresponding molecular model of the nanostructure observed in (b). Dashed, red lines represent individual hydrogen bonds.

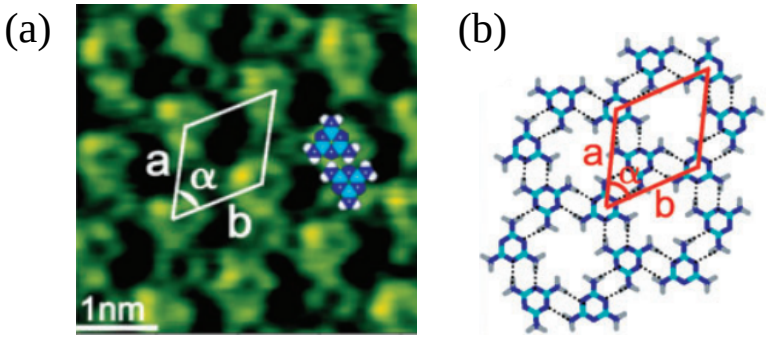

Figure 5.22. (a) STM image of 2D melamine self-assembly at the air HOPG interface. (b) Corresponding molecular model. From reference [208].

The concentrations and molar ratios of tetra-TP and melamine were adjusted in an attempt to explore other possible self-assembled structures and gain control over the previously described ordered network. However, no other co-assembled structure was observed to form between tetra-TP and melamine. Interestingly, tetra-TP on its own cannot adsorb from the mixed solvent of DMSO and TCB onto HOPG to form the mono-component network. Melamine molecules play an important role in the adsorption of tetra-TP at the interface between HOPG and the solvent mixture of DMSO and TCB. Further investigations on intermolecular interactions between tetra-TP, melamine and solvent molecules are required to determine the reasons why tetra-TP behaves in a different way at the interface between HOPG and DMSO/TCB.

5.4 Self-assembly of Zn-tetra-TP

The inclusion of zinc within the core of the thymine functionalised porphyrin opens up several possibilities for building tuneable functional porphyrin assemblies at liquid-solid interfaces controlled by metal-ligand coordination interactions [209-211]. In this section, the results of STM investigations into the self-assembly of Zn-tetra-TP related molecular systems will be discussed.

5.4.1 Zn-tetra-TP on its own

The STM image shown in Figure 5.23 (a) shows a Zn-tetra-TP mono-component

network self-assembled at the liquid-solid interface. Compared with the tetra-TP network formed using a similar molar concentration (Figure 5.8), the Zn-tetra-TP network has a lower coverage which was determined to be (80.0 ± 6.7) % by calculating the average and standard deviation of four sets of data.

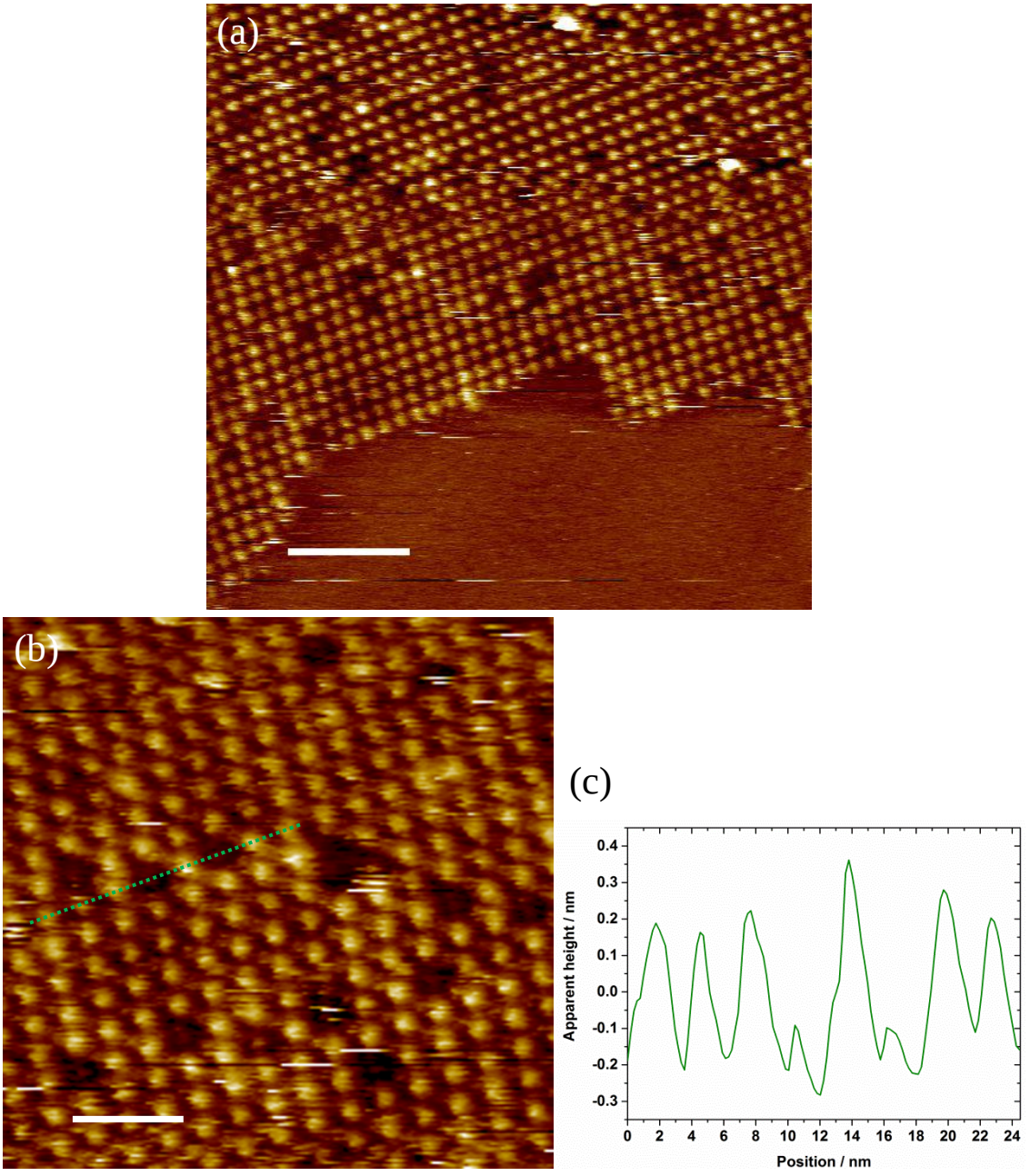

Figure 5.23. (a) STM image of the Zn-tetra-TP (0.028 mg/ml) network self-assembled at the interface between HOPG and THF/TCB. Image size: 100 nm. Scale bar: 20 nm. STM scanning conditions: V_s = - 0.5 V, I_t = 0.02 nA. (b) Magnified STM image showing detailed structure of the Zn-tetra-TP network. Image size: 45 nm. Scale bar: 9 nm. STM scanning conditions: V_s = - 0.5 V, I_t = 0.03 nA. (c) Line profile showing the height of different porphyrin species.

The reduced coverage of Zn-tetra-TP mono-component is most probably related to its higher solubility in the mixture of THF and TCB (1:9). As discussed previously in section 5.3.1, undissolved tetra-TP particulates were present in THF/TCB solutions at concentrations as low as 0.03 mg/ml. However, no undissolved particulates were visible for Zn-tetra-TP at the same concentration. Similar to the tetra-TP network, the Zn-tetra-TP network is also weakly stabilised and proved difficult to image consistently using STM.

More details concerning the structure of the Zn-tetra-TP network are revealed by the higher magnification STM image presented in Figure 5.23 (b). Each Zn-tetra-TP molecule appears as a bright feature in the image [212, 213]. The symmetrical cruciform shape of the porphyrin molecules that was previously observed for the tetra-TP network is not observed. However, the P2 plane symmetry of the porphyrin lattice is still clearly resolved in the STM images. On first inspection, some Zn-tetra-TP molecules appear to be missing from the 2D network leaving vacancies in the structure. However, some of the holes within the network are not empty, but seem to be filled by another molecular species with a much darker contrast in the STM image corresponding to a lower topographic height. As illustrated in Figure 5.23 (c), line profiles can be taken to measure the heights of the different molecular features in the STM image. By calculating the average and standard deviation of multiple measurements the heights of the Zn-tetra-TP and darker molecular species were determined to be (0.32 ± 0.04) nm and (0.14 ± 0.05) nm respectively. This substitution impurity is highly likely to be freebase tetra-TP which was not converted to Zn-tetra-TP during the synthesis procedures for the porphyrin raw materials [214, 215]. If this is the case, the hydrogen bonding scheme between Zn-tetra-TP molecules should be identical as that for tetra-TP.

5.4.2 Zn-tetra-TP and freebase tetra-TP

In order to confirm the hypothesis that the features with different contrasts observed in Figure 5.23 correspond to freebase and Zn containing porphyrins, mixed solutions of tetra-TP and Zn-tetra-TP were used to form network structures. A mixed solution with a

1:4 molar ratio of tetra-TP and Zn-tetra-TP was used to form a molecular network at the interface between HOPG and THF/TCB.

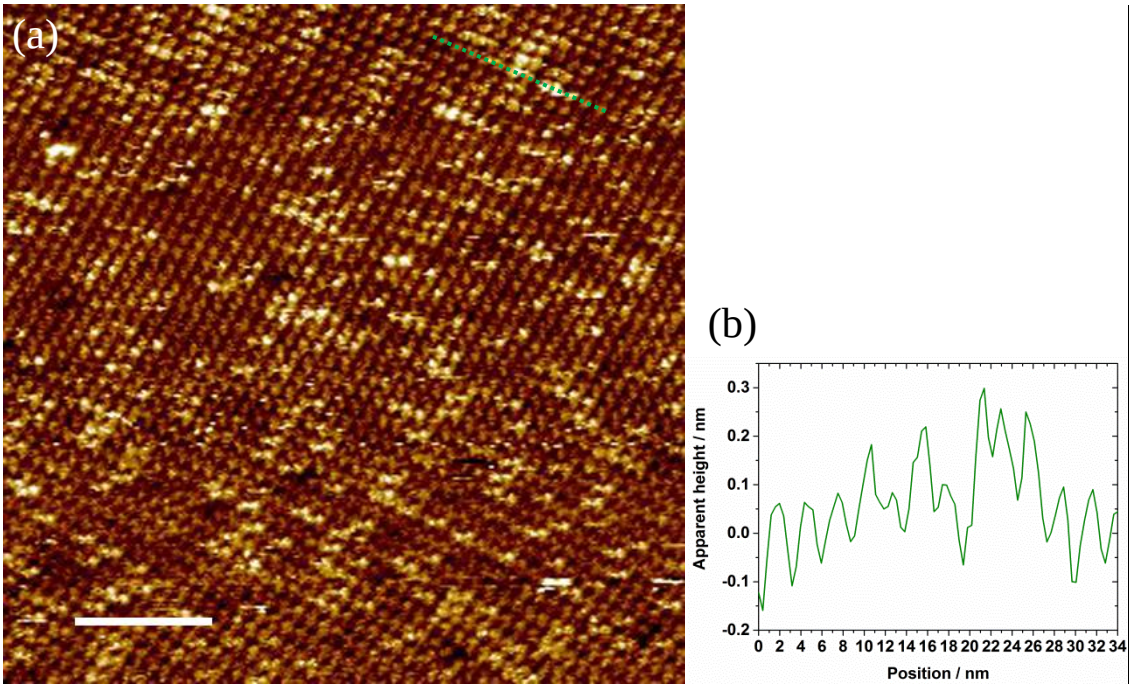

Figure 5.24. (a) STM image of the network formed using a mixture of Zn-tetra-TP (0.040 mg/ml) and freebase tetra-TP (0.010 mg/ml) at the liquid-solid interface. Image size: 115 nm. Scale bar: 23 nm. STM scanning conditions: V_s = - 0.65 V, I_t = 0.015 nA. (b) Line profile showing the heights of bright and dark porphyrin species.

The molecular network formed by the self-assembly of these two porphyrin species is presented in Figure 5.24 (a). The resulting 2D network shows a mixed composition of bright and dark contrast porphyrins distributed within a single domain of the tetra-TP square lattice. Therefore, the adsorption fashion and thymine-thymine hydrogen bonding recognition of Zn-tetra-TP should be exactly the same as those of tetra-TP. The result of the mixing experiment suggests an identical unit cell structure of the Zn-tetra-TP monocomponent network to that of the tetra-TP. By measuring surface areas covered with the bright and dark porphyrins in Figure 5.24 (a), the percentage of the bright and dark porphyrins were calculated to be 33.1 % and 66.9 %, respectively. As shown in Figure 5.24 (b), the heights of the bright and dark porphyrins were measured by taking line profiles. By calculating the average and standard deviation of

multiple measurements, the heights of the bright and dark porphyrins were determined to be (0.28 ± 0.04) nm and (0.15 ± 0.02) nm, respectively.

5.4.3 Zn-tetra-TP and PA

Figure 5.25 shows an STM image recorded for the self-assembled network formed by Zn-tetra-TP and 9-propyladenine (PA). In this STM image, the mixture of Zn-tetra-TP (0.040 mg/ml) and PA (0.043 mg/ml) in THF and TCB (1:9 in volume) was deposited onto a HOPG surface at room temperature. The two components self-assembled into a combination of highly ordered bi-component regions and disordered regions occupying the areas between ordered domains. For the STM image shown in Figure 5.25, the percentage of porphyrins within disordered regions was estimated to be 35.1 %. By calculating the average and standard deviation of eight domain size values collected from this STM image, the average domain size of the ordered areas was measured to be (23 ± 5) nm.

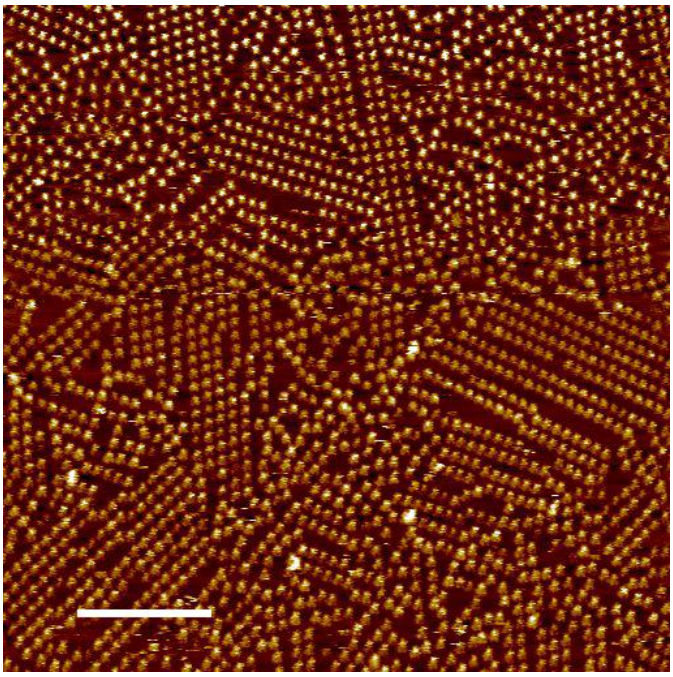

Figure 5.25. STM images recorded at room temperature for the Zn-tetra-TP (0.040 mg/ml) and PA (0.043 mg/ml) network deposited from a mixed solution onto a HOPG substrate without pre-heating. Imaging parameters: V_s = - 0.65 V, I_t = 0.015 nA. Image size: 150 nm. Scale bar: 30 nm.

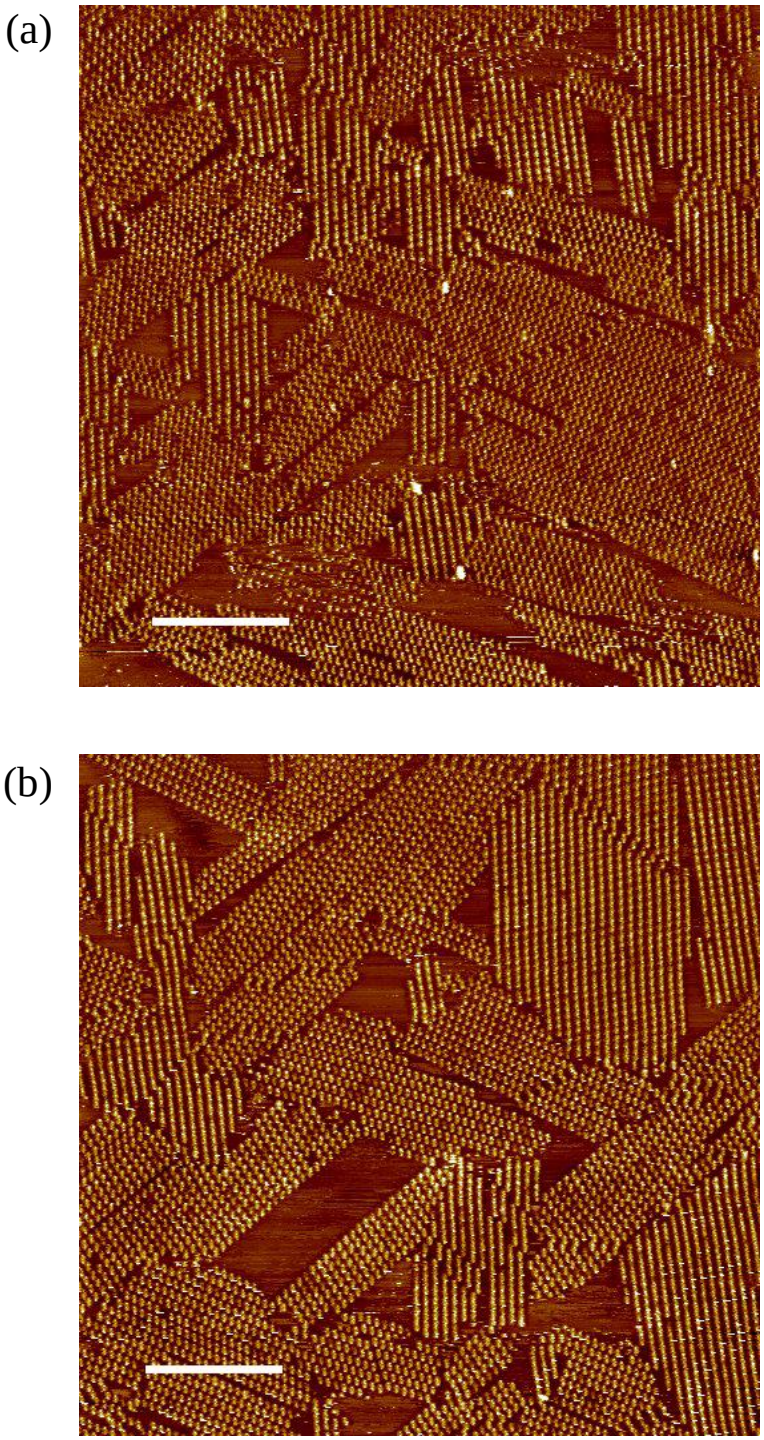

Figure 5.26. Typical STM images collected at sequentially elevated temperatures for the Zn-tetra-TP (0.040 mg/ml) and PA (2.2×10^{-4} mg/ml) co-assembled structures. (a) 50 ℃. (b) 60 ℃. STM imaging conditions are both: V_s = - 0.65 V, I_t = 0.015 nA. Both image sizes are 200 nm. Both scale bars are 40 nm.

In-situ STM investigations were carried out to study the morphology of the Zn-tetra-TP and PA co-assembled networks at elevated temperatures. First, an STM

sample was prepared using the previously described method used for the bi-component network. The STM sample was then heated up to 50 ℃, 60 ℃ and 70 ℃ in a step by step fashion. STM images were collected after each temperature increase. Less than 30 minutes were spent collecting STM images at each temperature in order to minimise the influence that solvent evaporation would have on the solution concentration.

Figure 5.26 (a) shows an STM image of the Zn-tetra-TP and PA network taken at 50 ℃. Highly ordered domains of the bi-component co-crystal structure were observed on the surface. Within the co-crystal domains, the two distinct contrasts for the porphyrin molecules was still visible. The average domain size of the ordered regions was measured to be (38 ± 14) nm by calculating the average and standard deviaiton of eight sets of data. A similar morphology of the Zn-tetra-TP and PA network was formed at 60 ℃ (Figure 5.26 (b)). The average domain size of the ordered bi-component networks was determined to be (36 ± 14) nm. This value shows no significant change compared with the network imaged at 50 ℃. When the STM sample was heated up to 70 ℃, no structure was observed in the STM images. Therefore, we assume that the network had decomposed and potentially the molecules had desorbed back into the solution. At temperatures above 60 ℃, the bi-component network was destroyed possibly due to a stronger preference for desorption of the molecular components or the disruption of the intermolecular hydrogen bonding.

5.5 Conclusions

Highly ordered and extended tetra-TP arrays with a square-shape unit cell have been prepared at the interface between HOPG and organic solvent mixtures. The formation of these structures was driven by thymine-thymine hydrogen bonds. The mono-component tetra-TP network can be disrupted by the addition of 9-propyladenine (PA) molecules into the molecular system. The addition of PA leads to the formation of a co-crystal of tetra-TP and PA stabilised by inter-adenine hydrogen bonding and Watson-Crick type [175] thymine-adenine interactions. The formation of the co-crystal structure depends strongly on the overall concentration and molar ratio of the two components, indicating

that kinetic effects play an important role in the self-assembly process. More diverse bi-component tetra-TP nanostructures can be built by including melamine. Directed by the triple hydrogen bonding interaction between melamine and thymine, tetra-TP and melamine self-assemble into bi-component nanostructures at the interface between HOPG and DMSO/TCB. In the tetra-TP-melamine network, melamine molecules not only link tetra-TP molecules stabilised by the triple melamine-thymine hydrogen bonding, but also self-assemble within the pores of the bi-component network as guest molecules.

Similar to the self-assembly behaviour of tetra-TP, Zn-tetra-TP can also form mono-component networks at the interface between HOPG and THF/TCB. Impurities in the Zn-tetra-TP raw material that consist of zinc free tetra-TP molecules lead to the formation of substitutional defects in the Zn-tetra-TP network.

PA can also be used to grow ordered co-crystal structures in combination with Zn-tetra-TP. Compared with tetra-TP, Zn-tetra-TP has the potential to construct more complex molecular structures at interfaces driven by the axial coordination interactions between the central zinc atom and suitable complex forming ligands such as pyridine.

5.6 Future work

The results obtained in this chapter demonstrate a novel strategy for the formation of highly ordered porphyrin arrays using the selective and directional hydrogen bonding interactions between DNA nucleobase functional groups. In addition to the thymine-adenine interactions studied here, other molecular recognition between DNA bases can be incorporated to prepare more complex surface-based self-assembled structures. In terms of organic synthesis, a variety of other DNA nucleobase functionalised molecules could be designed to generate more complex self-assembled molecular surface structures.

The observation of chiral domains within both the tetra-TP mono-component network and the tetra-TP and PA network opens the route for using these systems to study 2D chirality. More efforts can be put into controlling the chirality of these

self-assembled networks. For example, adding a chiral component to see if it leads to a preferred chiral arrangement.

The coordination of the central Zn atom of Zn-tetra-TP with a pyridine ligand creates opportunities to extend the self-assembly of mono-layers to bi-layers by binding other axial ligands leading to more applications for the porphyrin assembles. Since the Zn-tetra-TP mono-component network can be easily disrupted by STM imaging, more studies are required to form Zn-tetra-TP arrays with higher stability. A potential solution would be to attempt self-assembly of Zn-tetra-TP with a similar tetra adenine functionalised porphyrin species. The selective hydrogen bonding between thymine and adenine will open up the possibility of forming far more complex 2D arrangements. The increased structural complexity will result in more new properties of 2D self-assembled porphyrin structures for potential applications in catalysis, sensors and molecular electronics.

Chapter 6

On-surface synthesis and characterisation of mono-layer covalent-organic frameworks

The formation of surface-supported two-dimensional covalent organic frameworks (2D-COFs) via Schiff-base condensation reactions between either 5,10,15,20-meso-tetra(4-aminophenyl) porphyrin (TAPP) or 5,10,15,20-meso-tetra(4-aminophenyl) porphyrin Zn(II) (ZnTAPP) and benzene-1,4-dicarboxaldehyde (BDA) has been investigated. Through careful control of environmental conditions during growth, highly ordered 2D-COFs were synthesised on HOPG with domain sizes larger than 100 nm. The morphology of the porphyrin 2D-COFs was studied using a combination of STM and AFM. Additionally, XPS was employed as a complementary spectroscopic technique to SPM to reveal the chemical composition of the 2D-COFs. Our XPS results show the co-existence of conjugated imine and non-conjugated hemiaminal links between the porphyrins after Schiff-base condensation reactions. The chemical compositions of the links are closely related to the electronic properties of the 2D-COF. Our findings highlight the importance of investigating both the morphological and chemical structure of 2D-COFs utilising complementary experimental techniques.

6.1 Introduction

Due to the intrinsic weakness of noncovalent interactions in comparison to covalent bonds, 2D self-assembled molecular networks often have low levels of thermal and chemical stability. This instability can hinder the use of non-covalently stabilised molecular networks in technological applications. An effective solution to this problem is to link molecular components using covalent bonds. The concept of covalent-organic

frameworks (COFs), where molecular building blocks are linked by strong covalent bonds, was first reported by Côté and Yaghi *et al.* [68]. Their paper presented the synthesis of highly robust and thermally stable porous bulk 2D-COFs based on the dehydration reaction between diboronic acid and hexahydroxy triphenylene. These bulk 2D-COFs consist of 2D covalently stabilised layers stacked on top of each other with non-covalent interactions between the different layers. With the decrease in material dimensions from bulk to 2D, surface-based covalently bonded networks have evolved into an active area of research. The interest in surface-based 2D-COFs has arisen as a result of the stability of covalent bonds and the diversity of synthetic monomers that are available [216]. The most commonly used reaction schemes to grow long-range ordered 2D-COFs on solid surfaces are boronic acid and Schiff-base condensation reactions. These poly-condensation reactions are reversible and thus can be modulated by thermodynamic equilibrium conditions.

To address the current challenge of growing high-quality 2D-COFs over large surface areas, the growth of porphyrin 2D-COFs via an amine-aldehyde condensation reaction on a HOPG surface has been investigated. The morphology and chemical properties of the resulting 2D-COF materials were then characterised using a combination of STM, AFM and XPS. In this chapter, experimental results on two molecular systems are presented. Firstly, 2D-COFs were formed on HOPG via Schiff-base condensation reactions between freebase TAPP and BDA. Secondly, a zinc-containing amine functionalised porphyrin, ZnTAPP, was used as a molecular building block to grow 2D-COFs also using BDA as a linking molecule.

6.2 Experimental methods

6.2.1 Synthetic route

In this section, the reaction scheme designed to activate the Schiff-base condensation reactions between the amine groups on TAPP (Figure 6.1 (a)) or ZnTAPP (Figure 6.1 (b)), and the aldehyde groups on BDA (Figure 6.1 (c)) is presented.

The porphyrin molecules, TAPP and ZnTAPP, were synthesised as part of a collaboration with Hugo Bronstein's group at UCL. In the synthetic scheme for TAPP, freebase tetra(4-nitrophenyl)porphyrin was initially synthesised via the cyclotetramerisation of pyrrole and *p*-nitrobenzaldehyde [217]. The nitro groups were then reduced to amines by adopting a method previously described in the literature [218]. Freebase TAPP was metallated with zinc to produce ZnTAPP [219]. Other chemicals, benzene-1,4-dicarboxaldehyde (BDA), copper sulphate ($CuSO_4 \cdot 5H_2O$), toluene (anhydrous, 99.8 %), chloroform (anhydrous, > 99%) and 1,2,4-trichlorobenzene (anhydrous, > 99%), were purchased commercially from Sigma-Aldrich and used in the experiments directly without any further purification. The substrates, highly-oriented pyrolytic graphite (HOPG) (12 mm × 12 mm, grade-ZYB) were purchased from Bruker. The components in the reaction vessel (Figure 6.2) including the 15 mL glass tube, PTFE screw cap and CAPFE O-ring seal were ordered from ACE Glass Inc.

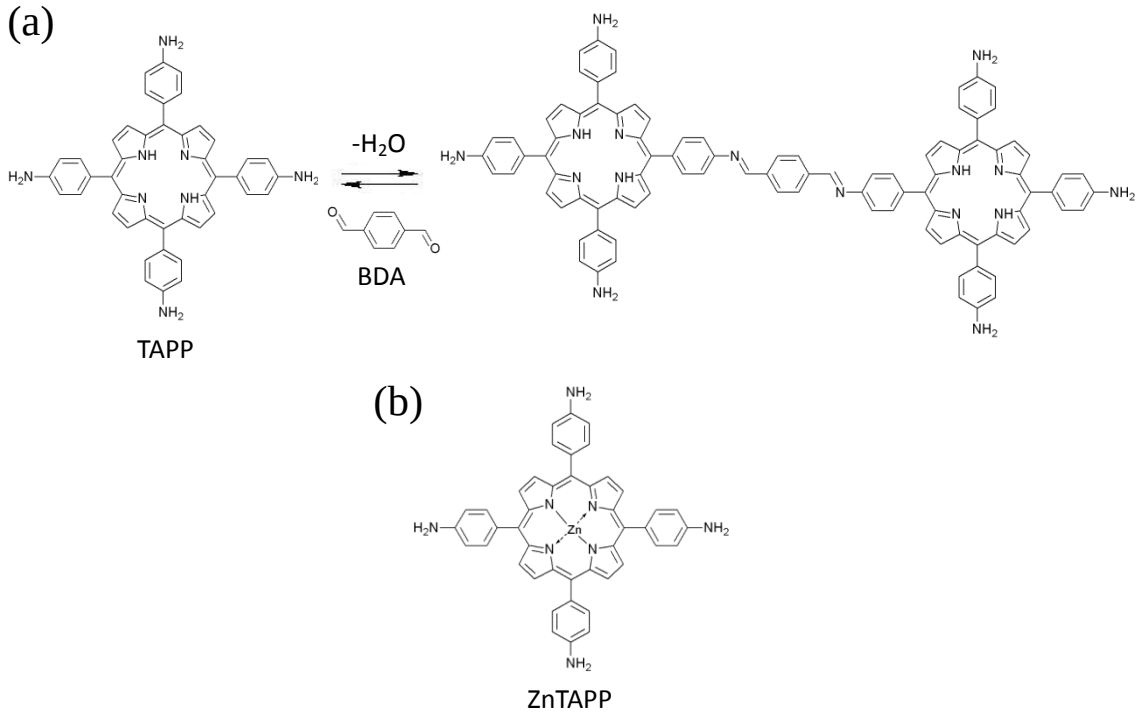

Figure 6.1. (a) Molecular structures of TAPP and BDA. Schiff-base condensation reaction between BDA and TAPP for the synthesis of 2D-COFs. (b) Molecular structure of ZnTAPP.

The glass tube shown in Figure 6.2 was used as a reaction vessel for the fabrication

of porphyrin 2D-COFs. For the purpose of promoting reversibility of the Schiff-base condensation reaction, a small amount of copper(II) sulphate pentahydrate ($CuSO_4 \cdot 5H_2O$) was added in the tube as an equilibrium regulator [64]. One of the precursor molecules, TAPP (or ZnTAPP), was deposited from toluene solutions onto a freshly cleaved HOPG surface in small quantities (0.1 –1.0 μg). After evaporation of the toluene, the HOPG substrate with deposited TAPP (or ZnTAPP) was loaded into the reaction vessel. The other reactant, BDA, was placed onto the inside wall of the reaction vessel either as solid or by drop deposition from a solution using a volatile solvent such as toluene or chloroform. The sealed reaction vessel was then heated slowly to a high temperature at 120 ℃ – 150 ℃ using a laboratory oven. The sample was kept at the elevated temperature for between 2 and 24 hours. At these high temperatures, the BDA (melting point: 114 ℃ – 116 ℃) vaporises within the sealed reaction vessel.

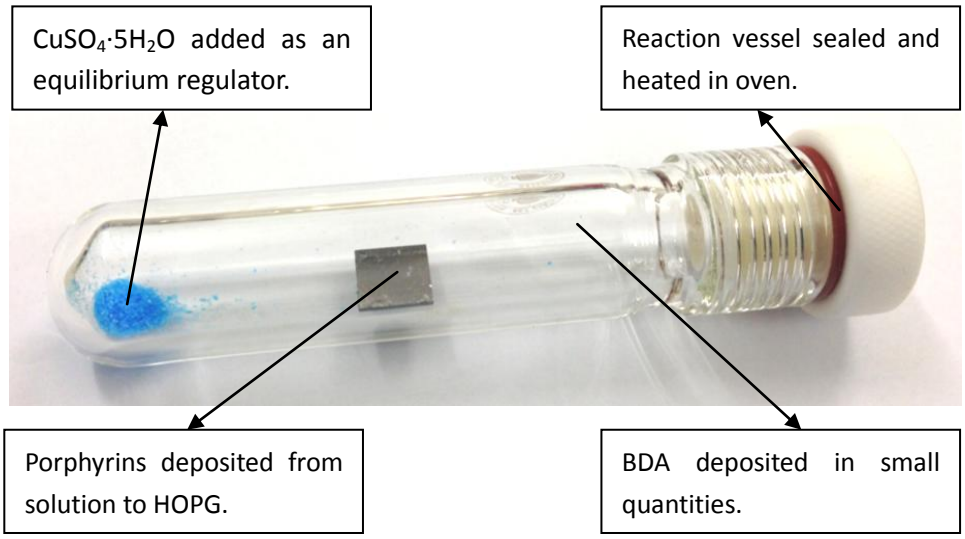

Figure 6.2. The glass tube used as the reaction vessel for the formation of porphyrin 2D-COF at the vapor-solid interface.

As can be seen from Figure 6.3, the BDA molecules present in the vapour phase react with the porphyrin molecules on the solid surface forming 2D-COF structures. After the glass tube was removed from the oven, its cap was opened immediately. The HOPG piece was taken out of the tube promptly to avoid water condensation on the surface. The sample was then allowed to cool down naturally prior to characterisation experiments.

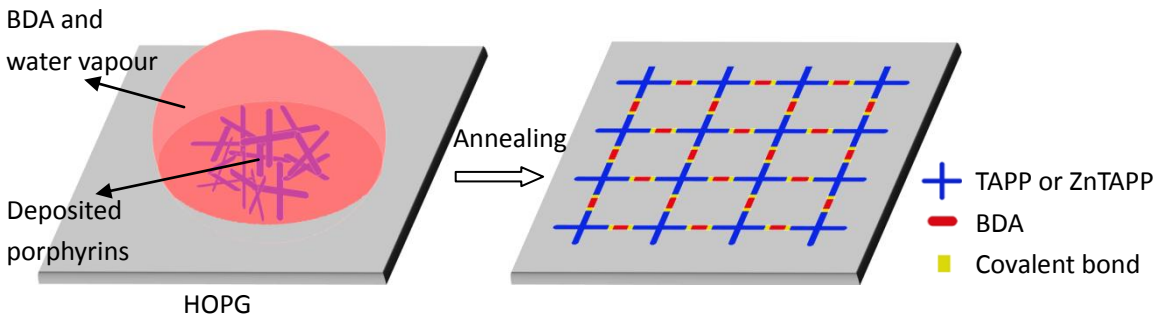

Figure 6.3. Schematic diagram showing the growth of highly ordered porphyrin 2D-COFs at the interface between the BDA vapour and the HOPG surface with deposited TAPP or ZnTAPP.

6.2.2 Morphology characterisation

The molecular scale morphology of the porphyrin 2D-COFs was investigated using STM operating under ambient conditions. All STM imaging of the 2D-COF structures was carried out using a PicoSPM (Agilent) system operating in constant-current mode at ambient conditions. For some of the STM images, a drop of 1-phenyloctane was deposited on HOPG to improve the resolution of the STM imaging. Several of the high-resolution STM images were drift-corrected by using the lattice parameters of the underlying HOPG as a reference.

The morphology of the drop deposited porphyrin films and resulting 2D-COFs was examined at micrometer scales using Multimode8 (Bruker) and Cypher (Asylum Research) AFM systems. SCANASYST-AIR AFM cantilevers (Bruker) were used for all the AFM images collected on Bruker Multimode 8 AFM in PeakForce Tapping mode. These cantilevers were silicon tips on nitride levers with a force constant of 0.4 N/m and a resonant frequency of 70 kHz.

Apart from drift-corrected STM images, all STM and AFM images presented in this Chapter have undergone no further imaging processing other than flattening.

6.2.3 Chemical structure characterisation

In order to study the chemical changes induced by 2D-COF formation, XPS measurements were first performed on HOPG surfaces with unreacted TAPP (or

ZnTAPP) films that had not undergone the 2D-COF growth process. These measurements could then be directly compared to XPS measurements taken from 2D-COF samples in order to study the chemical changes brought about by the covalent network formation.

A Thermo Scientific K-Alpha instrument equipped with a monochromatic Al Kα X-ray source (1486.6 eV) was used to perform the XPS characterisation. In order to avoid charge accumulation on the surfaces, a low-energy argon-ion gun (< 10 eV) was switched on during the acquisition of all XPS scans presented in the project. The TAPP 2D-COF samples were transferred to UHV following 2D-COF formation. The TAPP control samples were loaded into UHV directly without undergoing any heating steps. The samples were made as close to to the date of XPS analysis as possible. If any waiting between sample fabrication and XPS analysis was required, the samples were stored inside a lab desicator to avoid exposure to moisture. For each of the TAPP control and 2D-COFs samples, XPS signals were collected over binding energy regions associated with the C1s, O1s and N1s core levels. Survey scans were also acquired to give an overview of possible photoelectron emission from other species present on the surface. Multiple XPS scans were carried out for several different samples for each type of sample composition in order to ensure the reproducibility and consistency of the XPS peak shapes and binding energies. STM was used to confirm the formation of 2D-COF structures before sending samples for XPS scans. After XPS analysis, STM experiments on the samples were carried out to confirm that the structures were not destroyed by the measuring process. Based on results from a large number of STM and XPS experiments on 2D-COFs, it is found that good quality XPS spectra could be obtained only when highly ordered 2D-COFs were observed via STM to grow over extended areas on the HOPG surface.

CasaXPS software was utilised to analyse the XPS data. A Shirley background was fitted to the area of interest for each XPS spectrum. The XPS peaks identified in the spectra were fitted with Gaussian-Lorentzian peak shapes. For all the XPS spectra, the binding energy positions of C1s peaks were consistently at 284.7 ± 0.1 eV which is often used as a reference when comparing binding energies with values in literature.

This also means that direct comparisons of binding energy values between our samples without further correction are feasible. Various constraints (position and full width at half maximum) were applied to the XPS peaks during the fitting process. Detailed information of the starting positions for the constraints will be discussed in the experimental results chapter.

6.3 TAPP COFs

6.3.1 Morphology studies

In this section, three aspects on the morphology studies of the formation of the 2D-COFs will be discussed in detail. They include: the morphological structure of the 2D-COFs; experimental conditions during the growth of the 2D-COFs; and the relationship between the homogeneity of the porphyrin films prepared by drop deposition and the quality of the resulting TAPP/BDA 2D-COFs.

The STM and AFM results of the morphology studies illustrate the optimum experimental parameters for the growth of high-quality TAPP/BDA 2D-COFs. These conditions include: the temperature to activate the amine-aldehyde reactions; the concentration of the molecular components; the purity of porphyrins deposited on surfaces and the partial pressure of water released by $CuSO_4 \cdot 5H_2O$ on heating. The homogeneity of the porphyrin films formed by drop deposition from solution has been demonstrated to be closely related to the quality of the 2D-COFs after the growth process.

Morphological structure of the 2D-COFs

STM images of TAPP/BDA 2D-COFs grown using TAPP films that were drop deposited from toluene solutions display a structure with a *p*4 symmetry. Figure 6.4 (a) and (b) present two STM images of TAPP/BDA 2D-COFs with scan sizes of 150 nm and 250 nm, respectively. The highly ordered TAPP 2D-COF structures display domain

sizes in excess of 100 nm and almost complete coverage of the HOPG surface. Under ambient conditions, other attempts have been made to grow identical surface-supported TAPP/BDA 2D-COFs either at solid-liquid interfaces [73] or by depositing both reactants onto the substrate [76]. Compared with structures previously reported in literature, the domain sizes observed for the TAPP/BDA 2D-COFs presented here that have been grown at the vapour-solid interface are larger than 100 nm for the first time.

The detailed structure of the TAPP 2D-COFs is revealed by the high-resolution STM image shown in Figure 6.4 (c). This STM image has undergone drift-correction by using the lattice parameters of the underlying HOPG substrate. The cruciform-shaped bright features in the image, one of which is highlighted using a white, dashed circle in Figure 6.4 (c), correspond to the conjugated porphyrin cores of TAPP. Ten sets of unit cell parameters were taken from the dirft-corrected STM image presented in Figure 6.4 (c). The average of the ten measurements were used as the measured values. The associated errors of the measured values were obtained by calculating the standard deviations of the ten sets of data. As a result, the unit cell parameters of TAPP/BDA 2D-COF were determined to be $a = b = 2.6 \pm 0.2$ nm and $\gamma = 89 \pm 3$ °.

S. Lei *et al.* have carried out DFT simulations of TAPP/BDA 2D-COF structures [76]. In their DFT simulations, a primitive cell with 110 atoms was calculated and the the surface was included. The distance between TAPP molecules linked together by BDA via Schiff-base condensation reactions was calculated to be 2.6 ± 0.1 nm. This DFT calculation acts as a theoretical support for the experimental measurement of TAPP/BDA 2D-COFs conducted by M. Kunitake *et al.* using *in situ* STM scanning at the liquid-solid interface [73]. In comparison, the unit cell values determined for the TAPP/BDA 2D-COFs presented here, which were grown at the solid-vapour interface are in good agreement with those previously reported. The close match between the dimensions of the DFT simulated 2D-COFs and our experimentally measured structures is strong evidence supporting the formation of covalent bonds between TAPP and BDA.

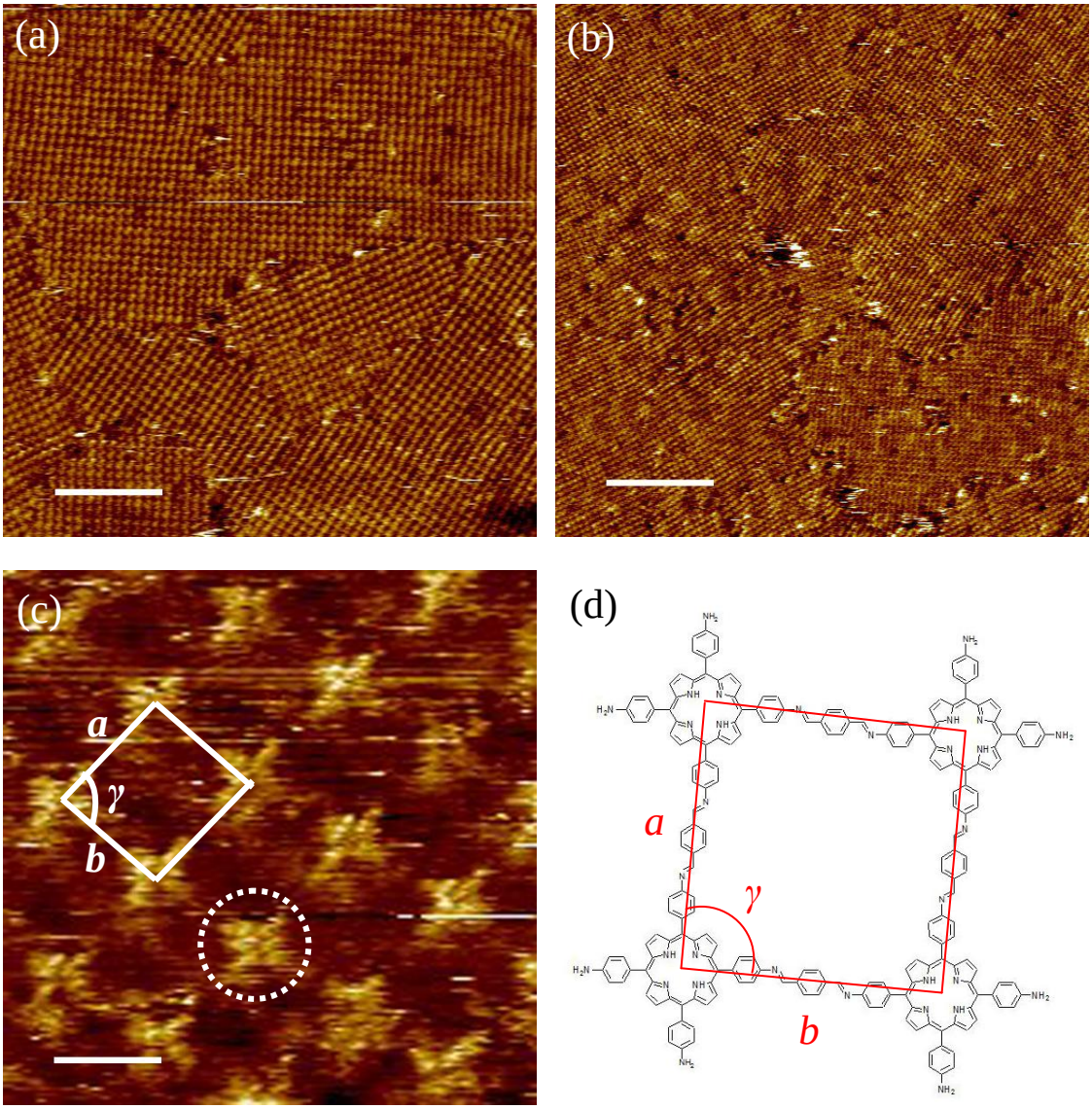

Figure 6.4. STM images and schematic representation of TAPP/BDA 2D-COFs. (a)-(b) Large-scale STM images. Growth conditions: 0.15 g of $CuSO_4 \cdot 5H_2O$; ~ 1 mg of BDA as solid; 20 µl of 0.2 mg/ml TAPP in toluene (saturated); 2 hours at 150 ℃. Imaging parametres are both V_s = -0.55 V, I_t = 20 pA. Image sizes: (a) 150 nm (scale bar: 30 nm); (b) 250 nm (scale bar: 50 nm). (c) Drift-corrected STM image with a porphyrin core marked in a white, dashed circle. Imaging parameters: V_s = -0.3 V, I_t = 5 pA. Image size: 10 nm (scale bar: 2 nm). (d) Schematic diagram of the unit cell of TAPP/BDA 2D-COF structures with a *p*4 symmetry.

Figure 6.4 (d) shows a schematic diagram of a unit cell of the TAPP/BDA 2D-COF in which all imine linkages adopt a *trans*-conformation. Due to the structural flexibility of the aldehyde groups of BDA, the resulting imine linkages can lie either at the same side (*cis*-conformation) or the opposite side (*trans*-conformation) with respect to the

molecular axis between two adjacent porphyrin cores (see Figure 6.5). The *trans*-conformation of imine linkages has been demonstrated to be more energetically favourable than the *cis*-conformation [76]. In real experimental systems, the less stable *cis*-conformation could exist due to kinetic trapping [220]. Direct observations of *trans*- and *cis*-conformation are achievable from STM images, where the four lobes of a TAPP molecule are visible. For the STM images collected in this work, the two conformations of the TAPP/BDA 2D-COFs are not discernible directly. Since highly ordered unit cells are observed within each domain, the imine linkages could not adopt a mixture of the two conformations in each unit cell. Under the condition that the TAPP/BDA 2D-COFs exhibit long-range order, the orientation of the covalent imine linkages shown in Figure 6.4 (d) is proposed.

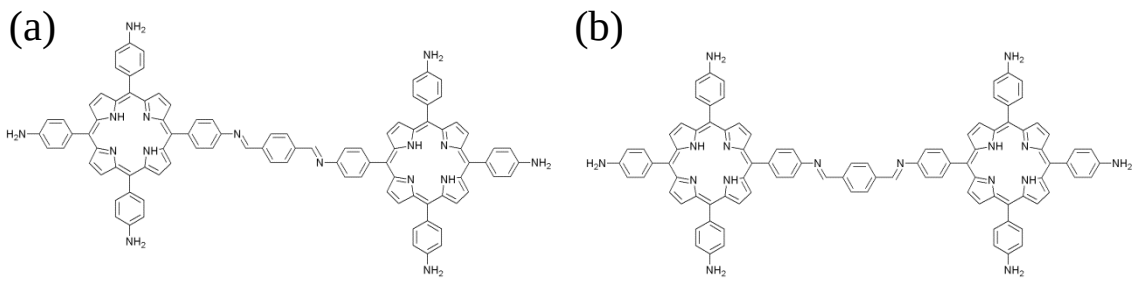

Figure 6.5. Schematic diagrams of the two possible conformations of the imine linkages between TAPP and BDA. (a) *Trans*-conformation. (b) *Cis*-conformation.

Multi-layered structure of the 2D-COFs

In some areas of the HOPG surfaces covered by TAPP/BDA 2D-COFs, multi-layered structures of the covalently bonded porphyrin sheets are observed by STM. Figure 6.5 (a)-(d) are four STM images showing the growth of multi-layers or bi-layers of TAPP/BDA 2D-COFs on HOPG. The multi-layer 2D-COFs appear as brighter sheets in the STM images compared with the mono-layer regions. The multi-layer regions are recorded as areas of higher features, because the STM tip moves vertically away from the surface to maintain the set-point tunnel current.

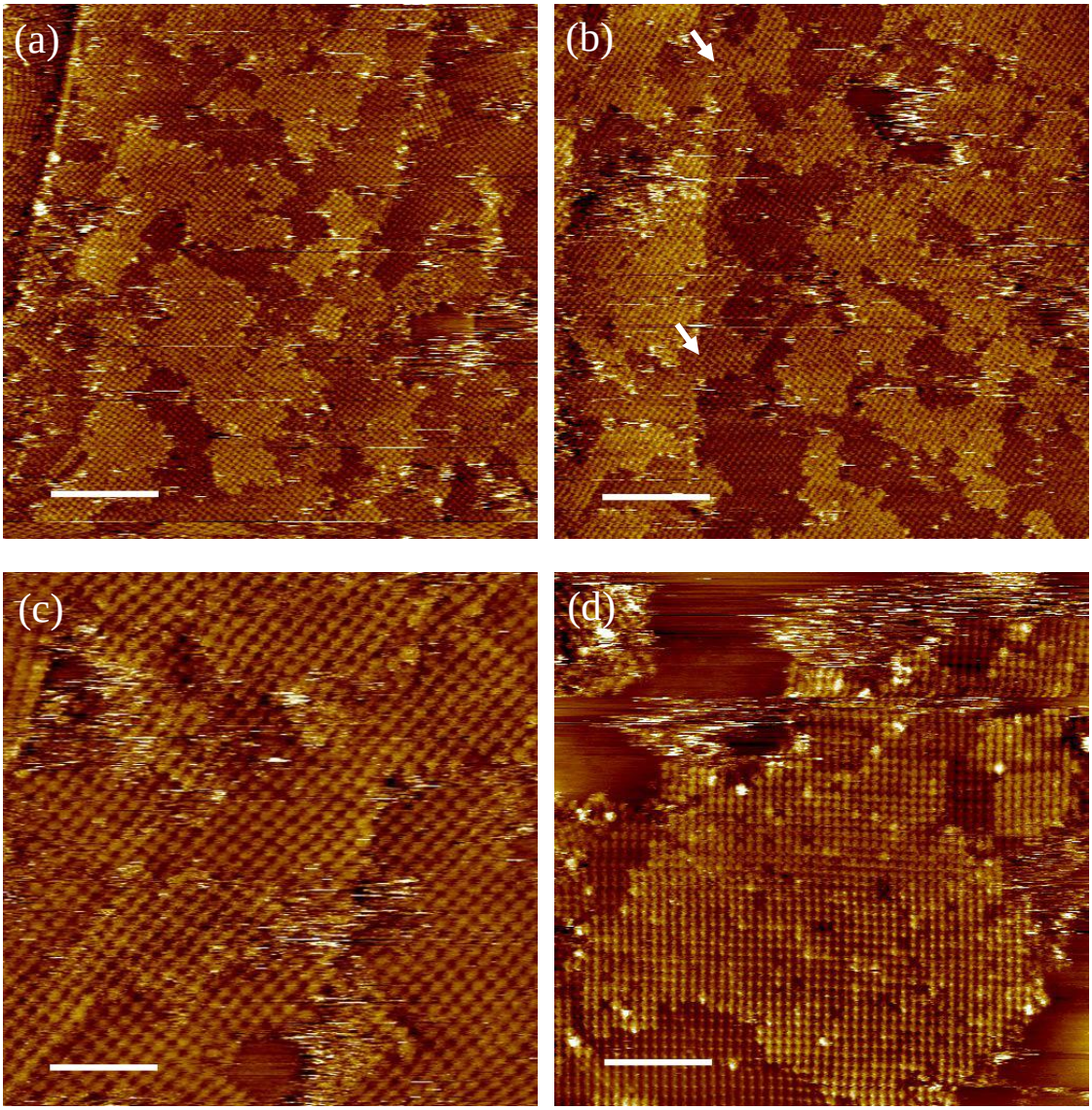

Figure 6.6. STM images showing the growth of bi-layer 2D-COFs on HOPG. (a)-(c) Sample fabrication parameters: 0.15 g of $CuSO_4 \cdot 5H_2O$; 0.09 mg of BDA; 10 μl of 0.004 mg/ml TAPP in toluene; heating at 150 ℃ for 3 hours. All STM images were collected under the condition: V_s = -0.85 V, I_t = 8 pA. Image sizes (a)-(b) 250 nm (scale bars: 50 nm); (c) 95 nm (scale bar: 19 nm). (d) Sample preparation conditions: 0.15 g of $CuSO_4 \cdot 5H_2O$; ~ 1 mg of BDA as solid; 28 μl of 0.2 mg/ml TAPP in toluene (saturated); 2 hours at 150 ℃. STM scanning parameters: V_s = -0.6 V, I_t = 10 pA. Image size: 150 nm (scale bar: 30 nm).

The highly ordered multi-layered or bi-layered structures can grow across HOPG step edges, as indicated by the white arrows in Figure 6.6 (b). The domain sizes of upper layers in the multi-layered structures can be in excess of 100 nm.

In some zoomed-in STM images, Figure 6.6 (d) for example, the porphyrin sheets

in upper layers are observed to be commensurate with the 2D-COF layers underneath. As illustrated in Figure 6.7, the porphyrin cores in upper layers are sitting directly above those in layers below. The revelation of accurate structures of multi-layer TAPP 2D-COFs has significant implications for the application of 2D-COFs as templates for guest adsorption and as components in electronic devices. The varying depth of pores in multi-layered TAPP/BDA 2D-COFs would change the adsorption energy of guest molecules on the surface. The electronic structure of the bi-layer 2D-COFs may also be different from that of the mono-layer due to inter-layer coupling interactions,

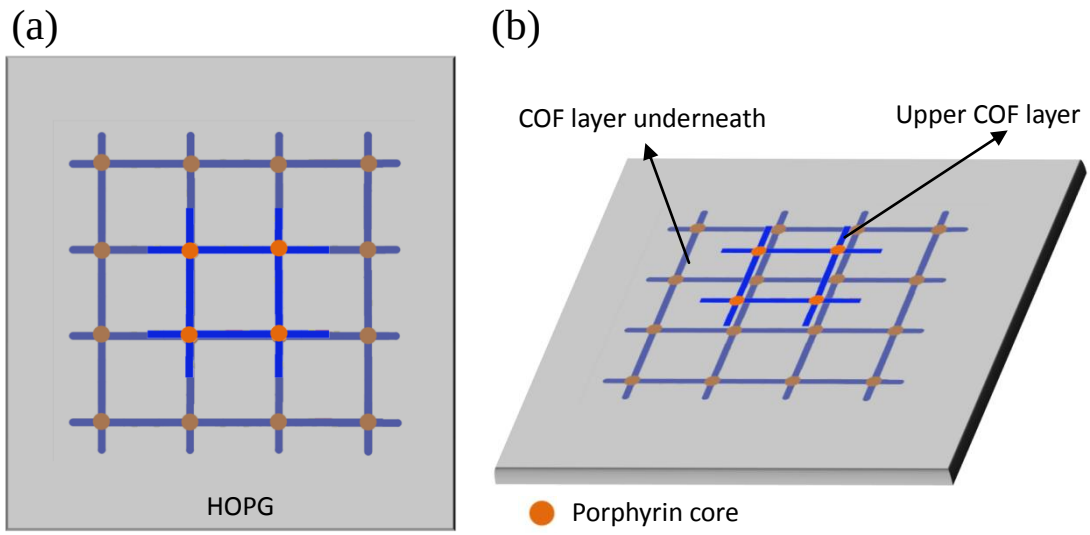

Figure 6.7. Schematic illustrations of the multi-layer growth of TAPP/BDA 2D-COFs on a HOPG surface. (a) Top view. (b) 3D view.

Figure 6.8 shows an example line profile taken across the edge of a bi-layer structure to determine the apparent thickness of mono-layer and bi-layer TAPP/BDA 2D-COFs in STM images. For the mono-layers or bi-layers, repeated measurements were taken from 6 different line profiles from 3 different STM images (two line profiles in each image). In each of the line profiles, 3 - 5 height values for porphyrin cores were acquired. An average of the height values was taken as the result of the individual line profile. Using this analysis method, 6 measured heights were collected for the bi-layers or mono-layers. The final measured height of the bi-layers or mono-layers was the average value calculated from the 6 measurements. The error associated with the

measured height was the standard deviations of the 6 measurements. Consequently, the apparent height of single-layer TAPP/BDA 2D-COFs was measured to be 0.7 ± 0.2 nm. The apparent height of bilayer TAPP/BDA 2D-COFs was determined to be 1.0 ± 0.4 nm.

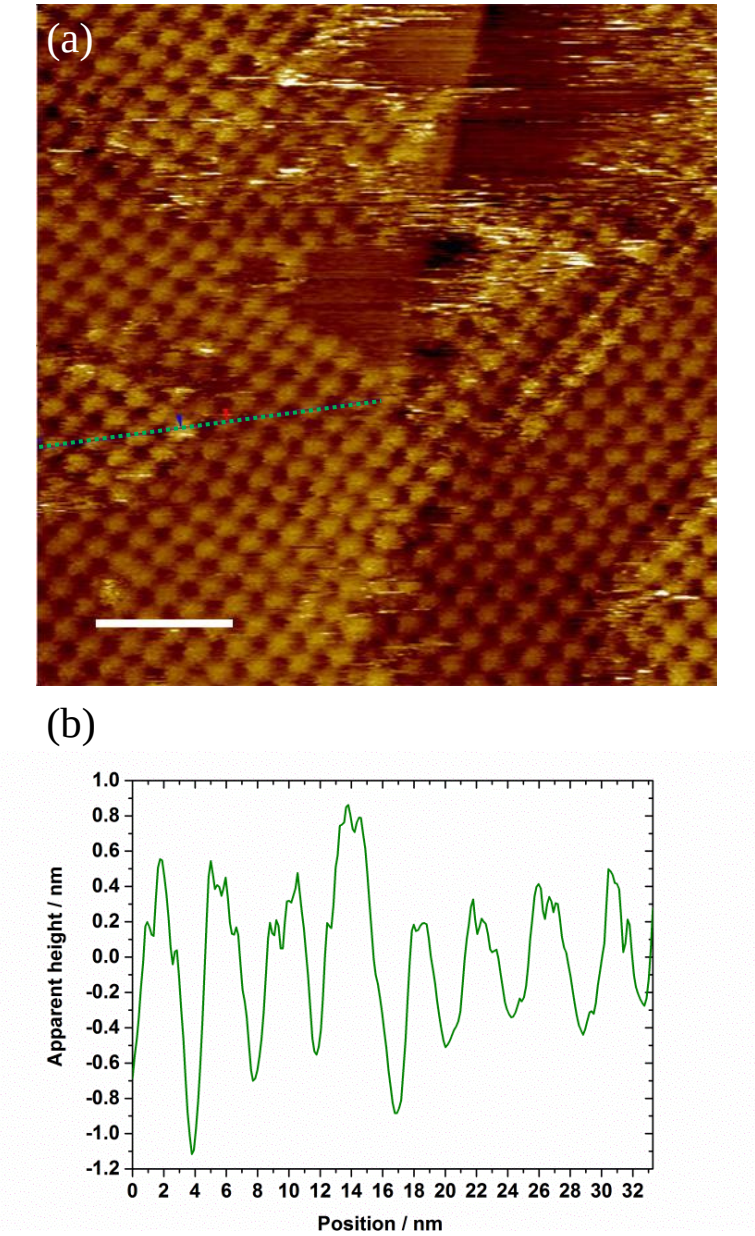

Figure 6.8. High-resolution STM image and its height profile (solid, blue line) that demonstrate the formation of bi-layers on the 2D-COFs. (a) An STM image showing the growth of bi-layers. Sample preparation conditions: 0.15 g of $CuSO_4 \cdot 5H_2O$; 0.09 mg of BDA; 10 µl of 0.004 mg/ml TAPP in toluene; 3 hours at 150 ℃. STM scanning parameters are V_s = -0.85 V, I_t = 8 pA. Image size is 65 nm (scale bar: 13 nm). (b) Line profile taken through the edge of the bi-layer TAPP/BDA COF structure (corresponding to the green, dashed line in (a)).

Growth conditions

In this section, three growth factors that have a substantial influence on the morphology of the porphyrin 2D-COFs will be discussed. These factors include the amount of $CuSO_4\ 5H_2O$ added to regulate the equilibrium of the Schiff-base condensation reaction and the concentration and purity of TAPP/toluene solutions drop deposited onto the HOPG surface.

$CuSO_4\ 5H_2O$ was added to the glass reaction vessel (Figure 6.2) as an equilibrium regulator. When heated, $CuSO_4\ 5H_2O$ undergoes a dehydration process releasing water [221]. An increase in the number of water molecules in the vapour above the HOPG surface shifts the equilibrium of the Schiff-base condensation reaction towards the reactants. This increase in the reversibility of the Schiff-base condensation reaction helps to eliminate defects in the growing 2D-COFs and leads to the formation of highly ordered structures. The amount of $CuSO_4\ 5H_2O$ has been found to have an effect on the morphology of resulting TAPP/BDA 2D-COF structures.

Figure 6.9 (a) - (c) presents three typical STM images of the porphyrin 2D-COFs synthesised with different amounts of $CuSO_4\ 5H_2O$. When all other growth conditions were identical, 0.1 g, 0.15 g, 0.25g of $CuSO_4\ 5H_2O$ were added into three 15 ml pressure tubes, respectively. Even though the amount of $CuSO_4\ 5H_2O$ was varied over a relatively small range, the morphology and degree of order of the TAPP 2D-COFs changed significantly.

With 0.15 g of $CuSO_4\ 5H_2O$, good-quality TAPP/BDA 2D-COFs were formed with few unreacted TAPP molecules trapped between domain boundaries (see Figure 6.9 (b)).

On increasing the amount of $CuSO_4\ 5H_2O$ to 0.25 g, the coverage and domain sizes of the TAPP 2D-COFs decreases drastically (Figure 6.9 (c)). As all other fabrication conditions are identical to the cases of 0.1 g and 0.15 g of $CuSO_4\ 5H_2O$, the change in morphology is likely to be caused by the excessive amount of water released by the $CuSO_4\ 5H_2O$. The increase in water pressure at the vapour-solid interface drives the equilibrium of the Schiff-base condensation reactions towards the unreacted

components hindering the synthesis of highly ordered TAPP/BDA 2D-COF structures.

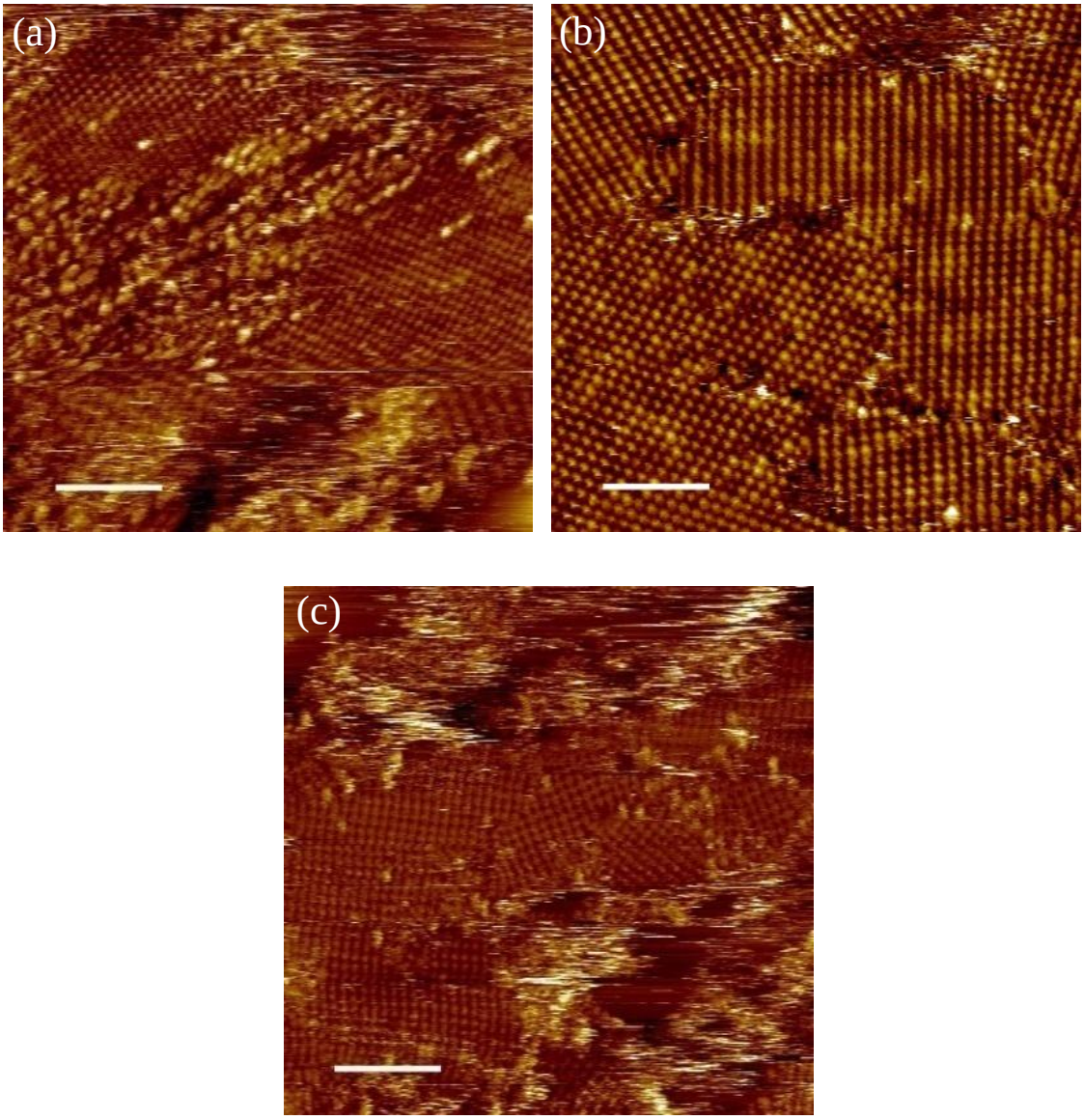

Figure 6.9. STM images of freebase TAPP COF structures fabricated with various amounts of copper sulphate. (a) 0.1 g of $CuSO_4$ $5H_2O$. Scale bar: 30 nm. (b) 0.15 g of $CuSO_4$ $5H_2O$. Scale bar: 20 nm. (c) 0.25 g of $CuSO_4$ $5H_2O$. Scale bar: 30 nm. Scanning conditions: (a) V_s = -0.6 V; I_t = 0.013 nA. (b) V_s = -0.6 V; I_t = 0.015 nA. (c) V_s = -0.85 V; I_t = 0.01 nA.

When decreasing the amount of $CuSO_4$ $5H_2O$ from 0.15 g to 0.1 g, a significant change in the structural order of the porphyrin 2D-COFs occurs. As can be seen in Figure 6.9 (a), a large amount of disordered structure between domain boundaries is observed appearing as higher features on the surface. These disordered regions are

likely to be unreacted or partially reacted TAPP molecules kinetically trapped between domains during the formation of the TAPP 2D-COFs. In contrast to the case of 0.25 g of $CuSO_4\ 5H_2O$, the stacking of porphyrin molecules between domain boundaries demonstrates an insufficient reversibility of the Schiff-base reaction under the condition of 0.1 g of $CuSO_4\ 5H_2O$. This lack of reversibility prevents defect removal from the growing 2D-COF. Another difference between the morphology of the 2D-COFs synthesised using 0.1 g and 0.25 g of $CuSO_4\ 5H_2O$ exists at the edges of the 2D-COFs. The results of adding 0.1 g of $CuSO_4\ 5H_2O$ show less obstacle to the imine growth as no disordered structure was observed at the edges between the 2D-COFs and bare HOPG.

From the various different quantities of $CuSO_4\ 5H_2O$ tested, the water vapour pressure released by heating 0.15 g of $CuSO_4\ 5H_2O$ at 120 ℃ - 150 ℃ (the most commonly used temperature ranges in this project) has proven to be the optimal condition for the 15 mL glass reaction vessel in terms of the quality of resulting TAPP/BDA 2D-COFs.

Careful control over the concentration of TAPP/toluene solutions is required to grow good-quality mono-layer TAPP/BDA 2D-COFs on HOPG. Deposition of highly concentrated TAPP/toluene solutions is more likely to lead to the growth of multi-layer TAPP/BDA 2D-COFs as presented previously. When lowering the concentration of TAPP/toluene solutions deposited on HOPG, mono-layer porphyrin 2D-COFs can form on HOPG with large domain sizes in excess of 100 nm over extended areas. In Figure 6.10, two STM images (Figure 6.10 (a) and (b)) are presented as experimental evidence for the growth of mono-layer TAPP/BDA 2D-COFs when depositing TAPP molecules from diluted toluene solutions. The average size of the ordered TAPP 2D-COF was calculated by quantitative analysis. Fifteen ordered domains of the 2D-COF were selected from three STM images scanned on the surfaces presented in Figure 6.10. The area of each of the domains was measured directly from the STM image. The square root of the domain area was then taken to represent the size of the domain. The average value and standard deviation of the fifteen measurements were calculated. Consequently, the average domain size of the TAPP 2D-COF was determined to be 70 ± 35 nm. In the

range of 3 - 15 hours, the length of time that the samples are annealed showed no measurable impact on the domain size or quality of TAPP/BDA 2D-COFs.

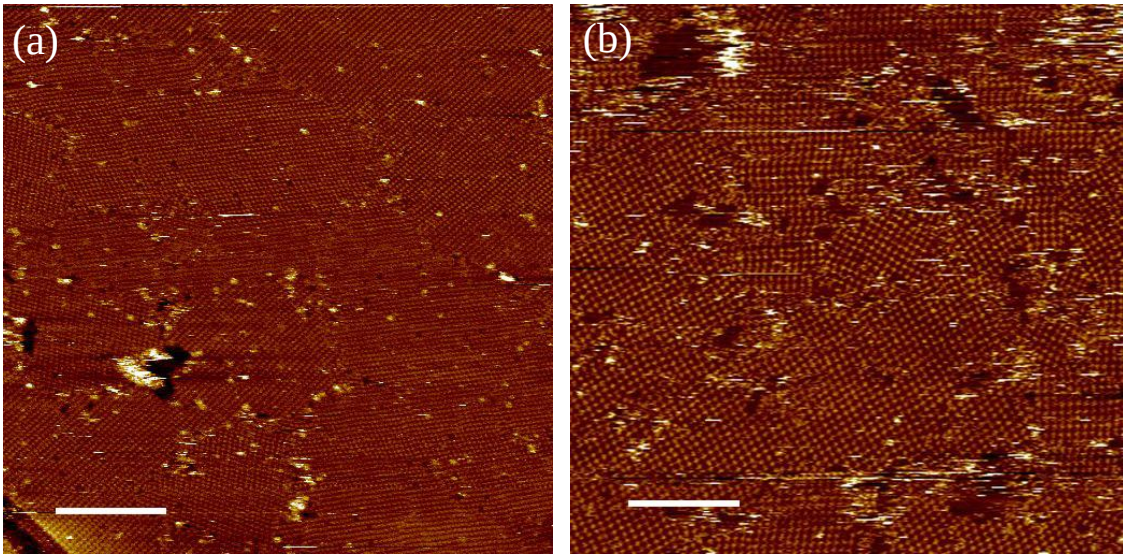

Figure 6.10. STM images that show the formation of single-layer TAPP/BDA 2D-COFs by depositing TAPP from a toluene solution on HOPG. (a) 2D-COFs synthesis conditions: 0.15 g of $CuSO_4 \cdot 5H_2O$; 0.05 mg of BDA; 5 μL of 0.0065 mg/ml TAPP in toluene; 14 hours at 120 ℃. STM scanning parameters: V_s = -0.85 V, I_t = 3 pA. Image size: 300 nm (scale bar: 60 nm). (b) 2D-COFs fabrication conditions: 0.15 g of $CuSO_4 \cdot 5H_2O$; 0.05 mg of BDA; 5 μl of 0.002 mg/ml TAPP in toluene; 3 hours at 120 ℃. STM scanning conditions:V_s = -0.85 V, I_t = 10 pA. Image size: 200 nm (scale bar: 40 nm).

In order to maintain the reproducibility and quality of TAPP/BDA 2D-COF growth, the presence of any contamination on the HOPG surfaces should be minimised at all times. Possible sources of contamination include: the raw materials provided by our collaborators in synthetic chemistry; the volatile organic solvents used to dissolve precursors deposited on HOPG; and the experimental tools employed to make up and deposit the solutions. In addition to their influence on the structural quality of 2D-COFs as observed via STM, the presence of contamination can be detected using complementary methods. For example, XPS and NMR are both commonly used to identify contaminants in raw materials.

The introduction of contamination to the HOPG surface can lead to the formation of poor quality 2D-COF structures or even prevent 2D-COF formation altogether. The

reason for this is probably that the contamination prevents the facile diffusion of the TAPP molecules across the surface and thereby prevents the 2D-COF layer from forming.

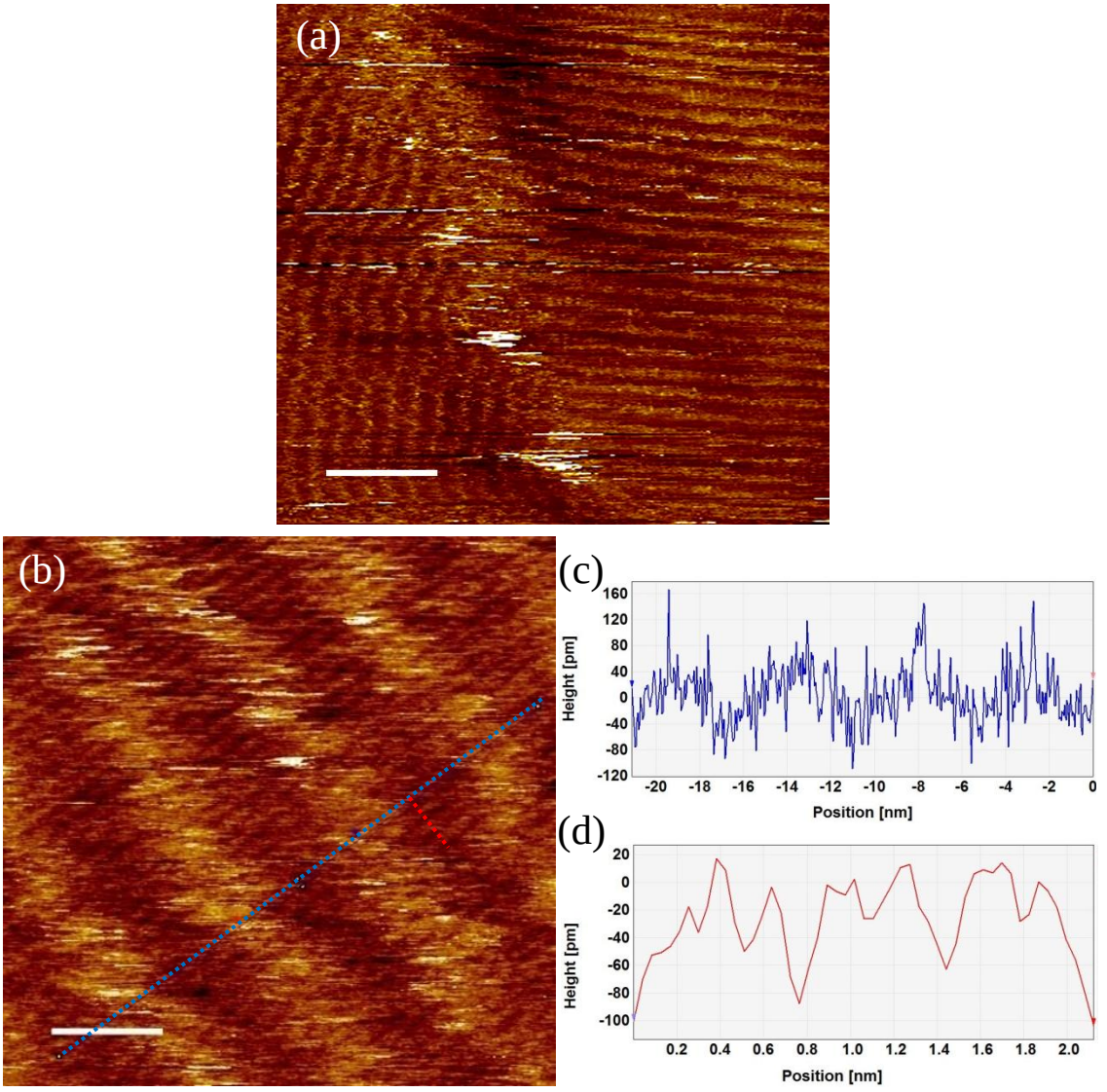

Figure 6.11. (a) STM image of the network formed fo by contaminants following 2D-COFs growth. STM scanning parameters: V_s = -0.85 V, I_t = 10 pA. Image size: 95 nm (scale bar: 19 nm). (b) Enlarged STM image of the contamination with line profiles taken through the periodic 1D network (blue and red dashed lines). Imaging parameters: V_s = -0.65 V, I_t = 10 pA. Image size: 19.6 nm (scale bar: 3.9 nm). (c) Height profile corresponding to the blue dashed line in (b) (d) Height profile corresponding to the red dashed line in (b)..

Figure 6.11 (a) shows a striped feature imaged by STM that was commonly observed for a contaminated HOPG surface. In Figure 6.11 (b), a line profile marked in

blue is taken through the periodic 1D bright features. Based on five measurements on this image, the distance between two adjacent bright 1D linear rows was measured to be 5.3 ± 0.1 nm (Figure 6.11 (c)). The associated error was obtained by calculating the standard deviation of the five measurements.

In addition to measuring the spacing between the bright rows, the much smaller spacing between the rows at right angles to these was measured as illustrated by the line profile marked in red in Figure 6.11 (b). Using the same data acquisiton and processing method, the distance between two adjacent dark rows was determined to be 0.6 ± 0.1 nm (Figure 6.11 (d)).

If the linear structure in Figure 6.11 (a) and (b) was seen to cover the HOPG surface, the coverage of the porphyrin 2D-COFs was extremely low. In this case, ordered TAPP/BDA 2D-COF structures were hardly ever imaged during STM scans. The formation of this linear network appears to prevent the growth of the 2D-COF by occupying the surface, and preventing the TAPP molecules from diffusing.

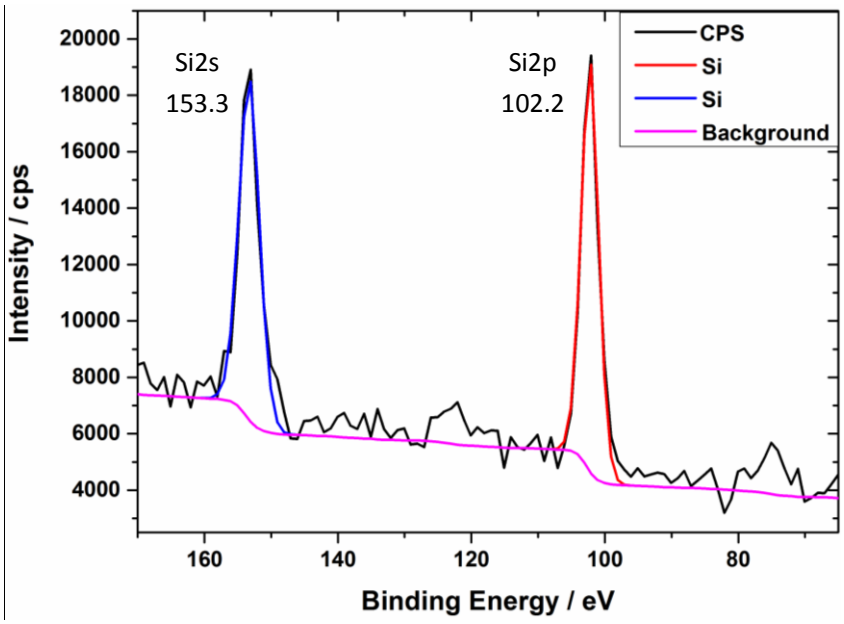

Figure 6.12. XPS spectrum showing Si contamination in the unreacted TAPP control sample.

In order to identify the contamination, AFM and XPS investigations were performed. The chemical composition of the contamination was probed by XPS

characterisation. XPS signals were collected on a dry TAPP film deposited from a TAPP/toluene solution (10 µl, 0.07 mg/ml) made using disposable needles. Figure 6.12 shows a XPS spectrum extracted from a survey scan of the unreacted TAPP control sample (C1s peak: 284.7 eV). By referring to literature values, the two binding energy peaks at 102.2 eV and 153.3 eV are designated to Si2p and Si2s photoemission lines, respectively [222, 223]. Considering all the materials deposited onto the HOPG surface, the contamination is most likely to result from polydimethylsiloxane (PDMS) thin coatings on disposable needles used to make up TAPP/toluene solutions. Such XPS peaks within this binding energy range were no longer detected when disposable syringes and hypodermic needles were replaced by glass pipettes in the preparation of the TAPP solutions. Meanwhile, the formation of highly ordered TAPP/BDA 2D-COFs could be observed consistently via STM imaging.

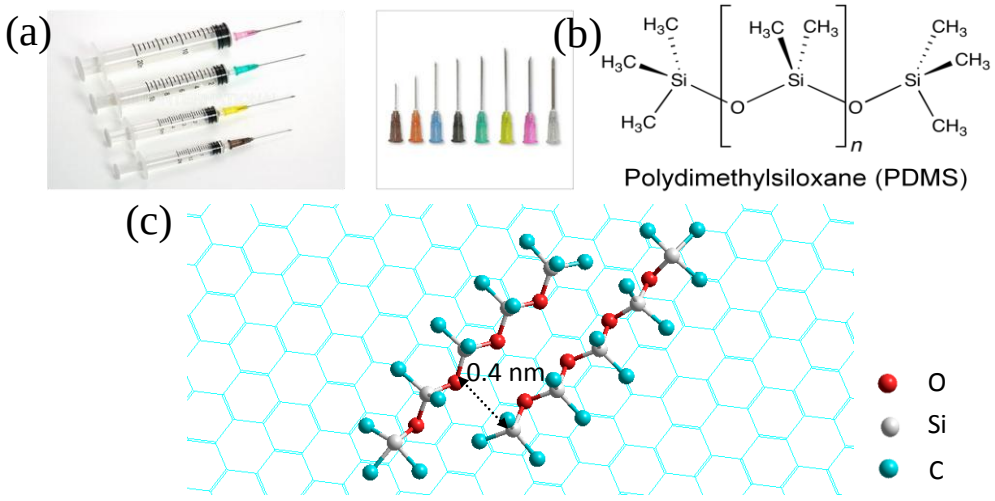

Figure 6.13. (a) Plastic syringes and disposable medical needles previously used to make solutions. (b) Molecular structure of PDMS which is commonly coated as a thin film onto the surface of disposable hypodermic needles. (C) HyperChem simulation of PDMS on HOPG.

Figure 6.13 (b) shows the chemical formula of PDMS, which is a linear silicon-based polymer with *n* repeating monomer units $(–SiO(CH_3)_2-)_n$ and terminated with trimethylsiloxy units. PDMS, also referred as silicone fluid, has a wide range of applications in the pharmaceutical industry such as: lubricants for glass cartridges in disposable syringes [224]; coatings on rubber cap components; and foam or gas

remover for the reconstitution of powder drugs [225]. Most disposable needles for medical uses are coated with PDMS thin films outside their stainless steel tubes (Figure 6.13 (a)). The thin PDMS coatings help to increase lubricity of the needles to ensure a smooth motion of liquids during injection [226]. However, PDMS exhibits a poor compatibility with the organic solvents used in our project. When in contact with toluene or TCB, PDMS swells to a substantial degree, and uncross-linked oligomers PDMS are extracted into the solvent [227]. A HyperChem simulation has been carried out to calculate the distance between two adjacent PDMS (n = 3) chains (Figure 6.13 (c)). In this simulation, a fixed graphene sheet was added below the PDMS chains. The initial distance between the graphene sheet and the PDMS chains was set as 0.35 nm. The MM+ force field was chosen to optimise the geometry of the PDMS chains on the graphene sheet. The distance between the two PDMS chains was determined to be 0.4 nm, which is in agreement with the value measured from the STM image in Figure 6.11 (b).

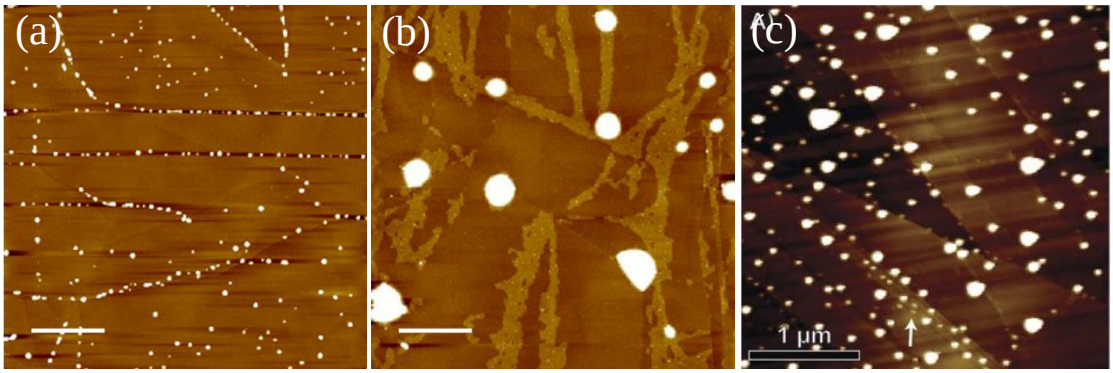

Figure 6.14. (a) AFM scan of an unreacted TAPP control sample. The deposited TAPP/toluene solution was made using disposable needles (10 µl, 0.0065 mg/ml). Image size: 7 µm. Scale bar: 1.4 µm. (b) AFM image of TAPP/BDA 2D-COFs grown using a template in (a). Image size: 5 µm. Scale bar: 1 µm. (c) AFM image showing contamination-induced nanobubble-like objects at the water-HOPG interface [228].

In addition to XPS analysis, AFM analysis of the contaminated samples display features that are consistent with previously reported PDMS contaminated samples [228]. Figure 6.14 is a comparison between AFM images collected on unreacted TAPP films (Figure 6.14 (a)) and TAPP/BDA 2D-COFs (Figure 6.14 (b)) and an exemple AFM

image reported in literature of a PDMS contaminated HOPG sample (Figure 6.14 (c)). The presence of PDMS as a source of contamination has been raised as an issue by scientists working in the surface nanobubble community [228]. Figure 6.14 (c) is an AFM image taken at the interface between HOPG and degassed water. The bright nanobubble-like objects remained unchanged under the degassing environment suggesting they cannot be attributed to real gaseous cavities adsorbing on the HOPG surface. Based on further investigations on all the materials used in their experiments, R.P. Berkelaar *et al.* pointed out that the nanobubble-like features were actually caused by PDMS contamination. The PDMS was introduced to the water when using disposable syringe needles to drop cast solutions onto graphite surfaces. According to this finding, it is highly likely the bright bubble-like features observed in Figure 6.14 (a) and (b) also consist of PDMS contamination from the similar disposable needles that were initially used in our experimental procedure.

All the findings above indicate that any possible contamination sources should be carefully controlled throughout the 2D-COF sample preparation process. If possible, contamination should also be removed from the raw materiasl before the growth stage in 2D-COF fabrication. Following identification of PDMS as a contamination source, only glass volumetric flasks and glass pipettes were used in further experiments on 2D-COFs growth.

Homogeneity of porphyrin films prior to 2D-COF growth

The homogeneity of porphyrin films deposited by drop casting has been found to be closely related to the morphology of the resulting 2D-COFs. This relationship was investigated in detail using Multimode8 AFM operating in PeakForce Tapping mode. The morphology of HOPG surfaces after drop deposition of 10 μl of TAPP/toluene solutions with a range of concentrations were imaged at a micrometer scale. Subsequently, AFM imaging was performed on TAPP/BDA 2D-COFs grown using these TAPP control samples as templates. The growth of highly ordered TAPP/BDA 2D-COF structures on HOPG surfaces was confirmed using STM followed by AFM

characterisations. AFM images were collected from samples made using TAPP in toluene solutions at three concentrations: 0.065 mg/ml, 0.016 mg/ml. and 0.008 mg/ml.

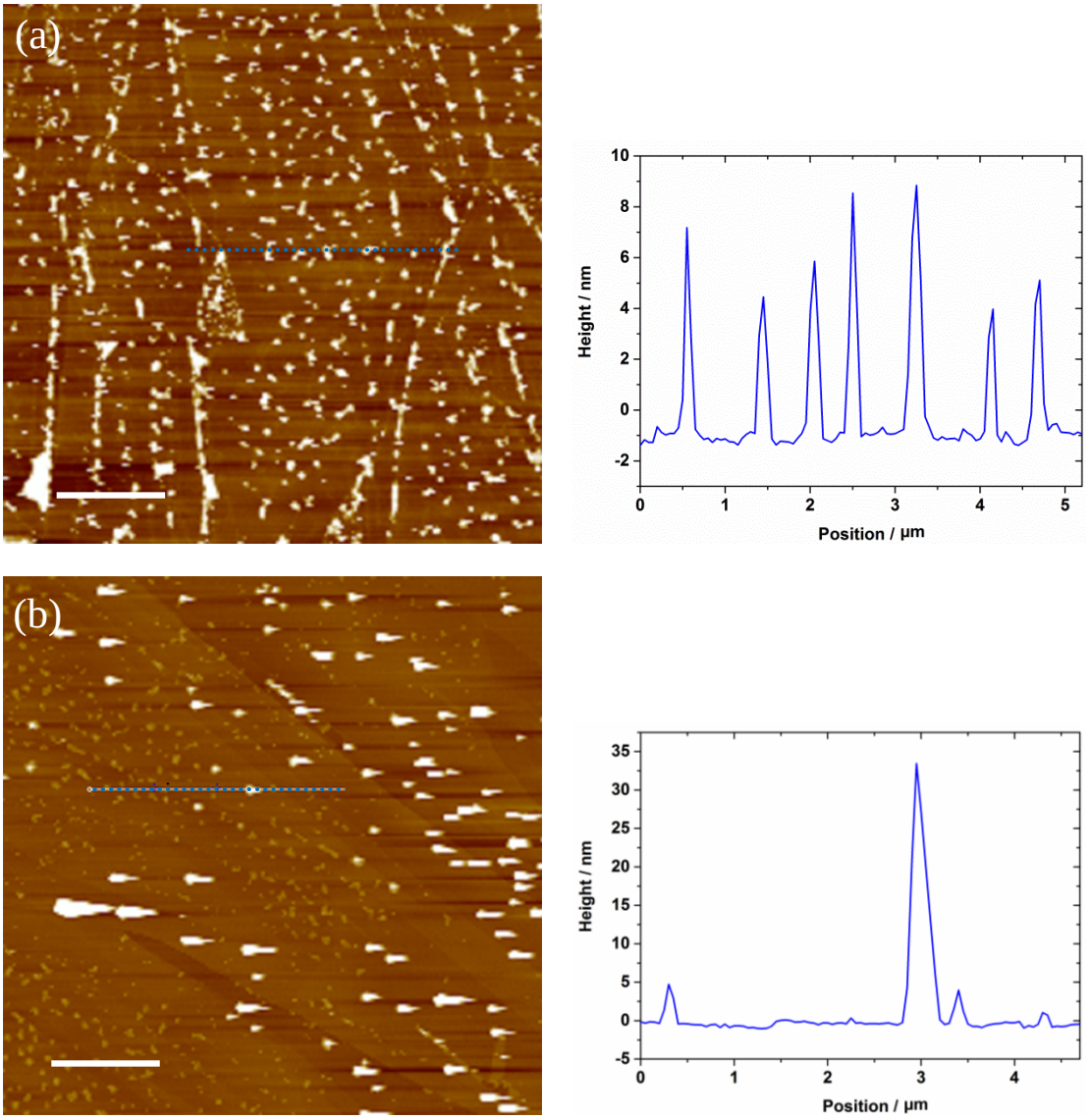

Figure 6.15. (a) AFM image of the HOPG surface with unreacted TAPP film made by drop deposition of 10 µl of a 0.065 mg/ml toluene solution. (b) AFM image of the HOPG surface with TAPP/BDA 2D-COF grown using the TAPP template shown in (a). Line profiles are taken from (a) and (b) respectively to illustrate the height of 3D islands. Sample preparation conditions: 0.15 g of $CuSO_4 \cdot 5H_2O$; 0.06 mg of BDA; 10 µl of 0.065 mg/ml TAPP in toluene; 15 hours at 130 ℃. Size of both images are 10 µm with 2 µm scale bars.

When TAPP molecules are deposited from 10 µl of a 0.065 mg/ml toluene solution, the morphology of porphyrin films formed on HOPG after toluene evaporation is

illustrated in Figure 6.15 (a). TAPP molecules exist as 3D aggregates forming an inhomogeneous film on the surface. As can be seen from Figure 6.15 (a), the distribution of the TAPP aggregates is driven by the presence of step edges of the HOPG surface. Step edges provide natural nucleation points for the aggregation of TAPP molecules during the drying of the TAPP/toluene film. Twenty measurements on the heights of the 3D aggregates were carried out from the AFM image in Figure 6.15 (a). The average and standard deviation of these measured heights were taken to represent the height distribution of the 3D aggregates. Using this data collection and analysis method, the height of the 3D TAPP aggregates was determined to be 8.6 ± 3.0 nm.

As can be seen from Figure 6.15 (b), the morphology of the TAPP 2D-COFs grown from a template shown in Figure 6.15 (a) is also highly inhomogenous. A line profile taken through the 3D aggregates in the AFM image shows the height of the bright features after the 2D-COF growth process at the elevated temperature. The sample after the 2D-COF growth appear to have two distinct heights of features. Some are lower features of 4 – 10 nm in height and some are higher features of 30 – 40 nm in height. Both of these features could be 3D porphyrin aggregates formed during the annealing process. When heated, some TAPP molecules in the 3D aggregates shown in Figure 6.15 (a) starts to move. If individual TAPP molecules diffuse along the HOPG surface, they may form mono-layer 2D-COFs by reacting with BDA in the vapour phase. The coalescence of 3D TAPP aggregates diffusing on the surface may result in even larger aggregates. In order to increase the degree of chemical conversion for unreacted TAPP molecules, attempts have been made to re-anneal the surface with 2D-COFs strcutrues in an atmosphere of BDA vapour at 130 ℃ for 3h. Even in this case, the higher bright features corresponding to the 3D TAPP aggregates were observed again using AFM.

Decreasing the amount of TAPP intitally deposited on HOPG to 10 μl of a 0.016 mg/ml TAPP/toluene solution drastically changes the morphology of the unreacted porphyrin films. After toluene evaporation the TAPP films consist of more flat areas with far fewer 3D aggregates as shown in Figure 6.16 (a). Similar to the situation at the higher concentration of 0.065 mg/ml, the 3D aggregates could not be removed

completely from the surface by initiating the 2D-COF growth. Figure 6.16 (b) shows part of the HOPG surface after performing 2D-COF growth from the template presented in Figure 6.16 (a). In this case, a significant aggregation can be observed following 2D-COF growth. In contrast to the few aggregates present prior to 2D-COF growth, a number of 3D aggregates form on the HOPG surface after annealing.

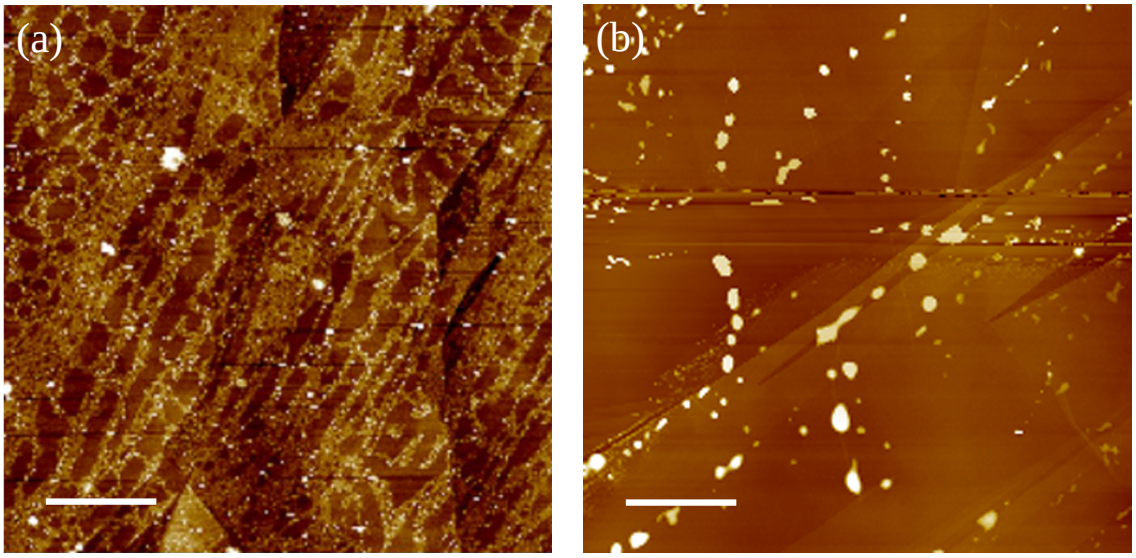

Figure 6.16. Example AFM images of TAPP films on HOPG before and after the Schiff-base condensation reaction using 10 µl of a 0.016 mg/ml toluene solution. (a) Unreacted TAPP film following solvent evaporation. (b) 2D-COFs and 3D TAPP aggregates after 2D-COF growth. Sample preparation conditions: 0.15 g of $CuSO_4 \cdot 5H_2O$; 0.06 mg of BDA; 10 µl of 0.016 mg/ml TAPP in toluene; 15 hours at 130 ℃. Both image sizes: 10 µm; scale bars: 2 µm.

As the concentration of TAPP dissolved in toluene solutions was further lowered to 0.008 mg/ml, the morphology of unreacted TAPP films following toluene evaporation changes to a more homogeneous morphology with a cellular network structure, as shown in Figure 6.17 (a). The homogeneous distribution of TAPP molecules when deposited from the low concentration of 0.008 mg/ml toluene solutions can be confirmed from the line profile in Figure 6.17 (b). The height of the TAPP films can be measured from the AFM image by taking line profiles through the TAPP domains. Five line profiles were taken on the AFM image shown in Figure 6.17 (a) to obtain twenty height values. The average and standard deviation of these twenty height values were

calculated to represent the height of the TAPP film. As a result, the height of the unreacted TAPP film deposited on the HOPG surface was determined to be 0.7 ± 0.1 nm, identical to the height of the TAPP 2D-COF measured using STM. Similar cellular network-like morphologies have been observed in other systems formed by deposition of nano-materials from volatile organic solvents onto solid surfaces, e.g., deposition of thiol-passivated colloidal Au nanoparticles from toluene onto Si(111) substrates via spin coating [229]. Cellular networks are an out-of-equilibrium structure that forms because of rapid solvent evaporation and the subsequent kinetic trapping of the material following removal of the solvent [230].

The morphology of the initial cellular patterns formed by TAPP following rapid toluene evaporation plays an important role in determining the morphology of the 2D-COFs grown using the TAPP films as templates. Figure 6.17 (c) is an AFM image of a HOPG surface on which TAPP/BDA 2D-COF structures were grown following the formation of unreacted TAPP films presented in Figure 6.17 (a). The majority of the HOPG surface is covered by TAPP 2D-COFs which appear as the higher features in the AFM image. In Figure 6.17 (d), a zoomed-in AFM image was taken on the surface shown in Figure 6.17 (c) to provide more details of the 2D-COF structures. As can be seen in Figure 6.17 (e), a line profile taken on this area (marked in a blue, dashed line) is shown to illustrate the height of the flat TAPP/BDA 2D-COFs .

The quality of the TAPP/BDA 2D-COFs shown in Figure 6.17 (c) and (d) was evaluated by measuring the heights values and surface area of the 2D-COFs. Nine line profiles were taken from the AFM image in Figure 6.17 (d) to acquire twenty height values. The average and standard deviation of these twenty height values were calculated to represent the height of the 2D-COFs on the HOPG surface and its associated error value. Using this data analysis method, the average height of the 2D-COF films was determined to be 0.4 ± 0.1 nm. Regarding the surface area covered by the 2D-COF, a quantitative analysis was carried out on the AFM image in Figure 6.17 (d). In this AFM image (area: 9 μm^2), the total surface areas covered by the 2D-COF structures were measured to be 7.5 μm^2 using the SPIP software. The percentage of the surface area covered by the 2D-COF structures reaches approximately

83 %.

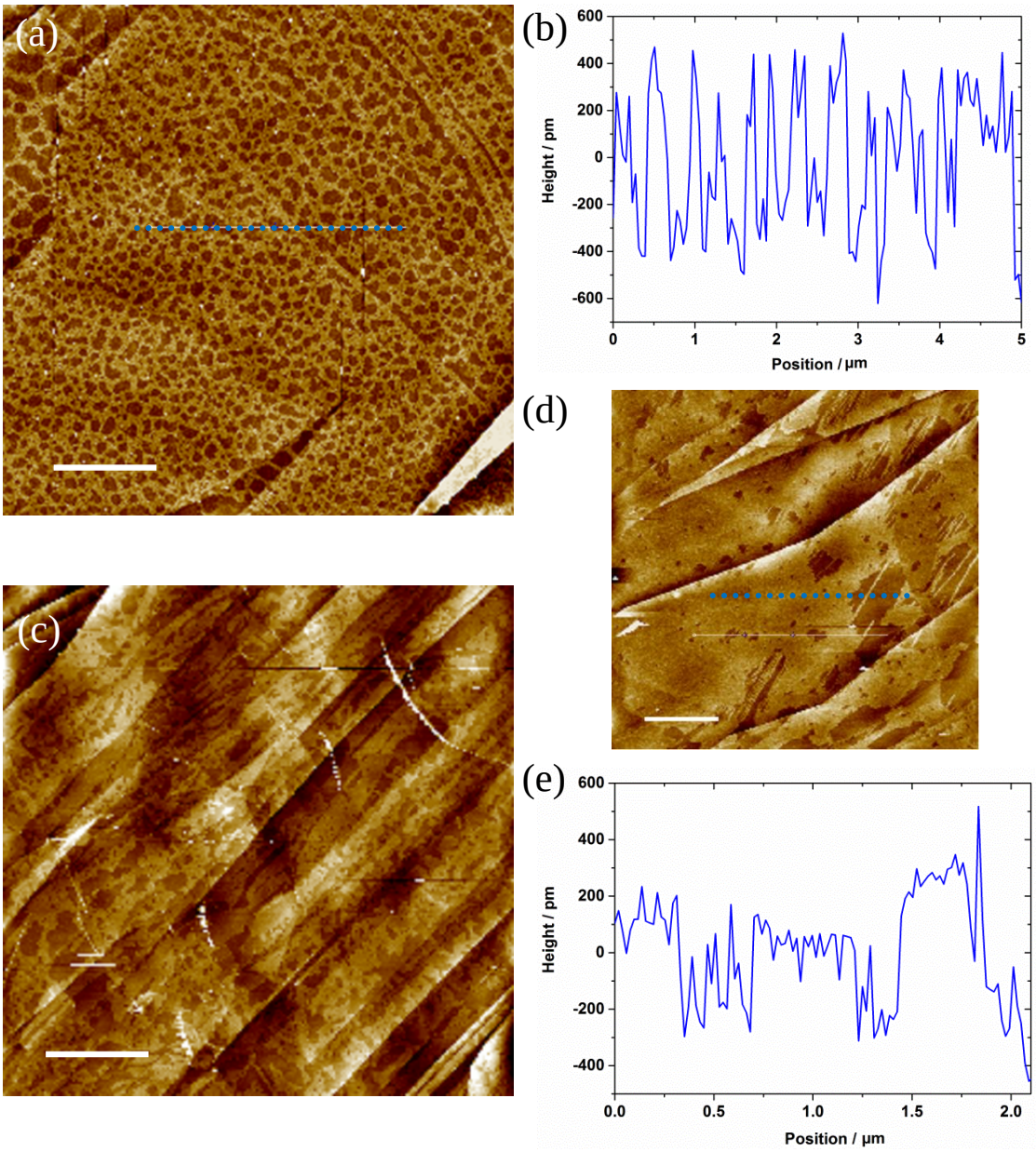

Figure 6.17. AFM images of HOPG surfaces with unreacted TAPP films and TAPP 2D-COF layers by depositing 10 µl TAPP/toluene solutions with a concentration of 0.008 mg/ml. (a) Cellular networks formed by unreacted TAPP following toluene evaporation. (b) Line profile through the cellular network in (a) (marked in blue, dashed line). (c) HOPG surface after TAPP 2D-COF growth. Sample preparation conditions: 0.15 g of $CuSO_4 \cdot 5H_2O$; 0.06 mg of BDA; 10 µl of 0.008 mg/ml TAPP in toluene; 15 hours at 130 ℃. (d) Zoomed in AFM image on the surface shown in (c). (e) Line profile taken through TAPP 2D-COF networks in (d) (marked in blue, dashed line). Scale bars in (a) and (c): 2 µm. Scale bar in (d): 0.8 µm

Ultra-high resolution AFM studies

The Cypher AFM produced by Asylum Research has a proven ability to produce molecular scale resolution of 2D supramolecular structures [141, 231, 232]. This technique has been employed to image highly ordered TAPP/BDA 2D-COFs grown on HOPG surfaces.

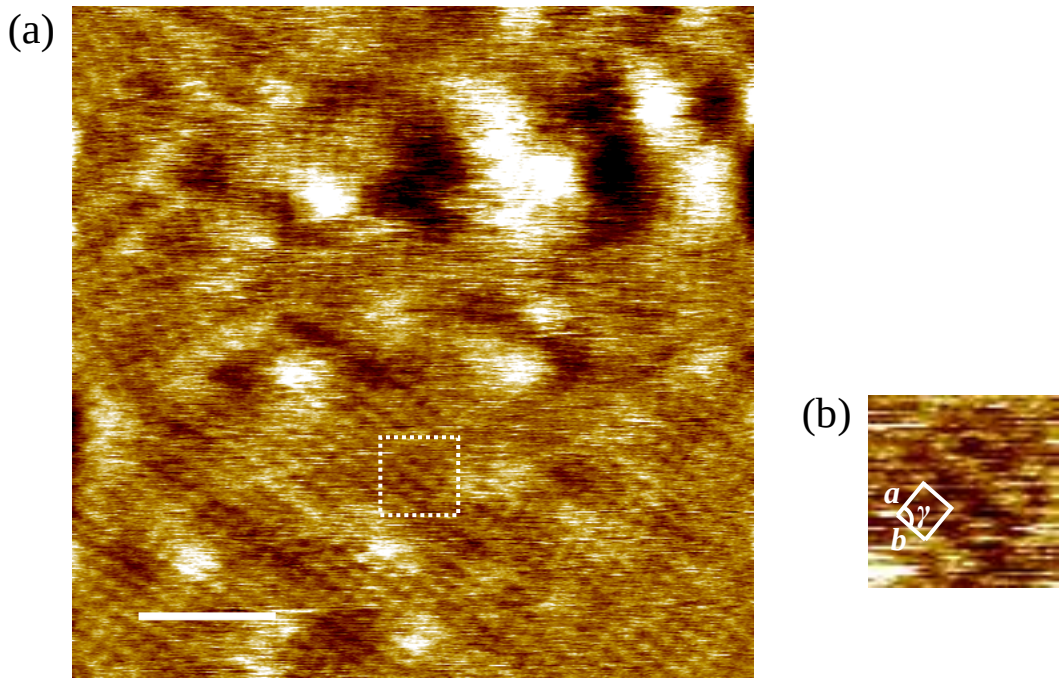

Figure 6.18. (a) Cypher AFM image of TAPP/BDA 2D-COFs grown on HOPG. Image size: 100 nm. Scale bar: 20 nm. Sample preparation conditions: 0.15 g of $CuSO_4 \cdot 5H_2O$; 0.06 mg of BDA; 10 µl of 0.065 mg/ml TAPP in toluene; 3 hours at 130 ℃. (b) Enlarged AFM image of the ordered area marked in a white, dashed square area in (a). Image size: 10 nm.

All AFM imaging on a Cypher AFM system was carried out by scientists from the School of Physics and Astronomy at the University of Nottingham. Figure 6.18 - 6.20 present a series of Cypher AFM images collected on a HOPG surface which was covered by TAPP/BDA 2D-COFs. In Figure 6.18 (a), the molecular structure of square-shaped porphyrins was resolved by the Cypher AFM. This imaging resolution is comparable to that of an ambient STM system. As illustrated in Figure 6.18 (b), the unit cell dimensions of TAPP/BDA 2D-COF can be measured from the high-resolution AFM

image. Under the condition of no drift-correction, ten sets of unit cell dimensions were collected from the AFM image in Figure 6.18 (a). The average values and standard deviations of these ten sets of data were analysed to determine the unit cell dimensions of TAPP/BDA 2D-COF. As of result of this data acquisition and analysis, the unit cell dimensions of TAPP/BDA 2D-COF were determined to be $a = b = 2.6 \pm 0.2$ nm and $\gamma = 87 \pm 3°$. The results obtained in the Cypher AFM measurement are in excellent agreement with the values measured from the drift-corrected STM image shown in Figure 6.4 (c).

In Figure 6.19 (a), 3D aggregates and multi-layered growth of the TAPP 2D-COFs were both identified. A line profile was taken through one of the 3D aggregates to show the height of this 3D aggregate feature (Figure 6.19 (b)). As marked in a red, dashed line in Figure 6.19 (a), the height of the multi-layer TAPP 2D-COFs can also be measured from the AFM image.

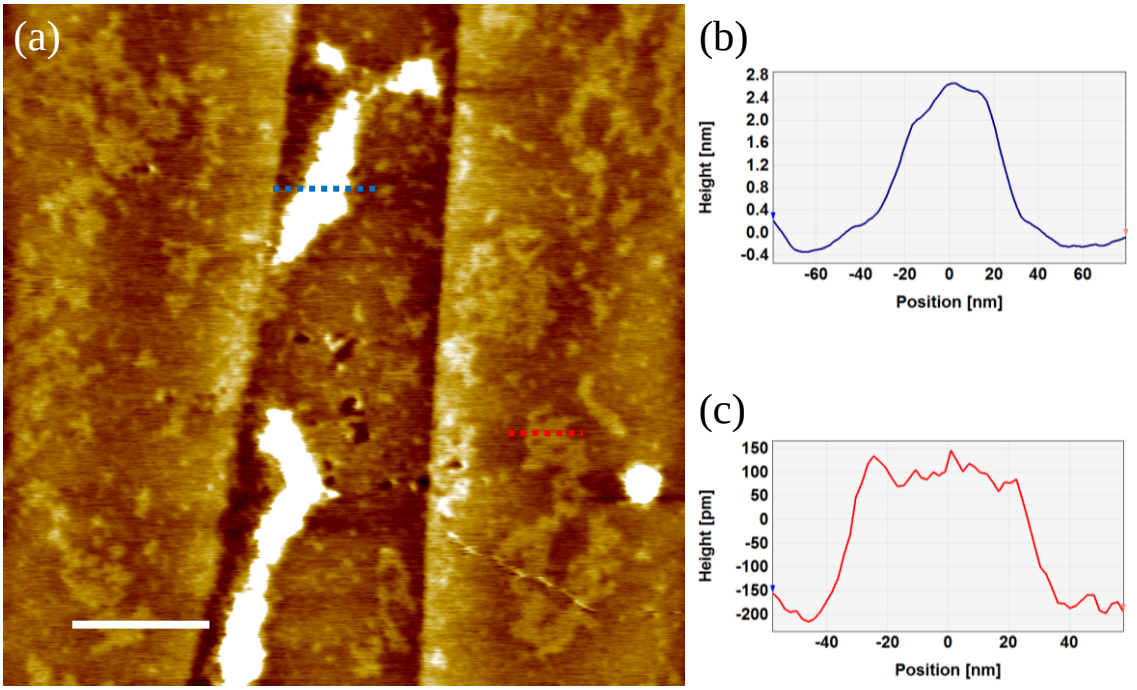

Figure 6.19. (a) Cypher AFM image on a HOPG surface covered with a TAPP/BDA 2D-COF. Image size: 1 µm. Scale bar: 200 nm. (b) Line profile through the 3D aggregate feature in (a) (marked by a blue, dashed line). (c) Line profile thought the multi-layered structure in (a) (marked by a red, dashed line).

AFM images with larger scan sizes were taken on the surface to obtain more information about the 3D aggregate features and multi-layer TAPP 2D-COF regions. Figure 6.20 (a) presents a 5 μm × 5 μm AFM image on the same sample. In order to measure the average height of the 3D aggregate features, twenty height values were collected from different parts of the image. The average value and standard deviation of these twenty measured heights were calculated. As a result, the average height of the 3D aggregate features was determined to be 3.5 ± 1.0 nm. Compared with the AFM observation in Figure 6.15 (b), this size is smaller than the higher 3D aggregates, but similar to the lower features. This difference in morphology may be related to the length of annealing time. In the previous case, the sample was annealed at 130 ℃ for 15 h, instead of 3 h. The long heating times may enhance the coalescence of 3D aggregates.

The average height and its associated error of the multi-layer regions of 2D-COF were obtained by measuring twenty height values from Figure 6.20 (a). By calculating the average and standard deviation of the twenty measurements, the height of the multi-layer structures was determined to be 0.4 ± 0.1 nm, which is good agreement with the height of the mono-layer TAPP 2D-COF measured using the Multimode AFM. From Figure 6.20 (a), the percentage surface coverage of the mono- and bi-layer 2D-COF regions was measured using the SPIP software. The surface area covered with the bi-layer 2D-COF was measured to be 5.4 μm^2 in total. Thus, approximately 20 % of the HOPG surface was covered with bi-layer 2D-COF.

From the AFM image shown in Figure 6.20 (a), it can be seen that the bi-layer 2D-COFs regions (highlighted by red overlays) were grown in areas far away from the 3D aggregates instead of being focussed around them. This raises questions about the structure and composition of the 3D assemblies on the surface. The high coverage of the TAPP 2D-COFs on HOPG is further demonstrated by the AFM image in Figure 6.20 (b). The imaging ability of Cypher AFM to resolve both individual molecular structures and larger scale features of the TAPP 2D-COFs illustrates the possibility to grow porphyrin 2D-COFs on non-conductive surfaces which are not applicable to STM imaging. A range of insulating or semi-conducting substrates, such as boron nitride, can potentially be used for supporting 2D-COF growth.

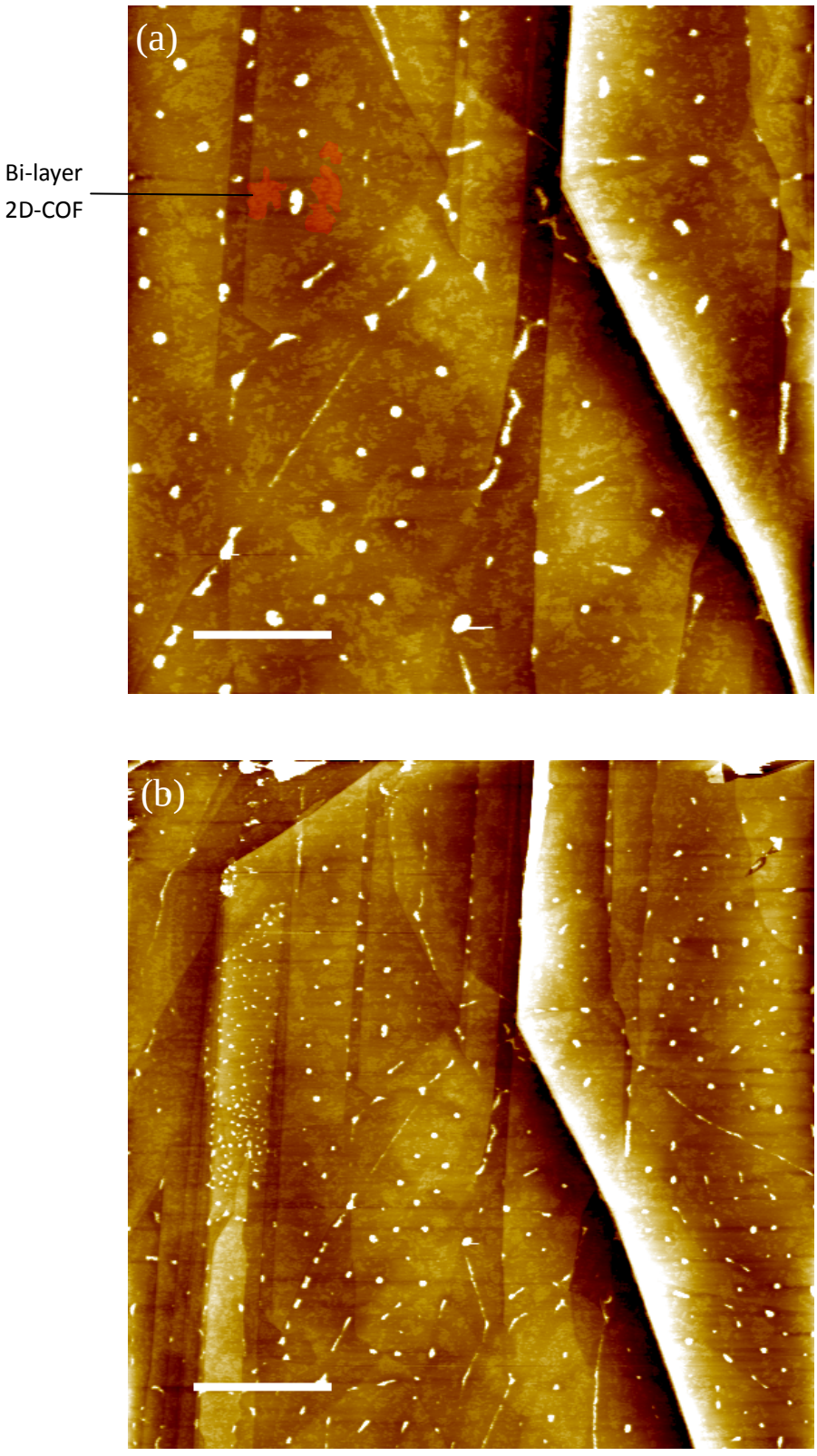

Figure 6.20. Cypher AFM images of a HOPG surface covered with TAPP/BDA 2D-COFs. (a) Red overlays added to highlight bi-layer regions of 2D-COF. Image size: 5 μm. Scale bar: 1 μm. (b) Image size: 10 μm. Scale bar: 2 μm.

Deposition of unreacted TAPP films by spin coating

The AFM results above demonstrate that the morphology of TAPP 2D-COFs depends on the morphology of the drop-cast TAPP films prior to activating the Schiff-base condensation reaction. With this in mind, some efforts were made to deposit unreacted TAPP onto the HOPG surface by spin coating. To prepare such samples, a 10 µl droplet of TAPP dissolved in toluene was deposited onto a freshly cleaved 1.2 cm × 1.2 cm HOPG surface using a glass pipette and spin-coated at 2000 r.p.m. for 1 minute. AFM images in Figure 6.21, Figure 6.22 and Figure 6.23 present the morphology of porphyrin films produced by spin coating using 10 µl TAPP/toluene solutions at concentrations of 0.065 mg/ml, 0.033 mg/ml and 0.016 mg/ml, respectively.

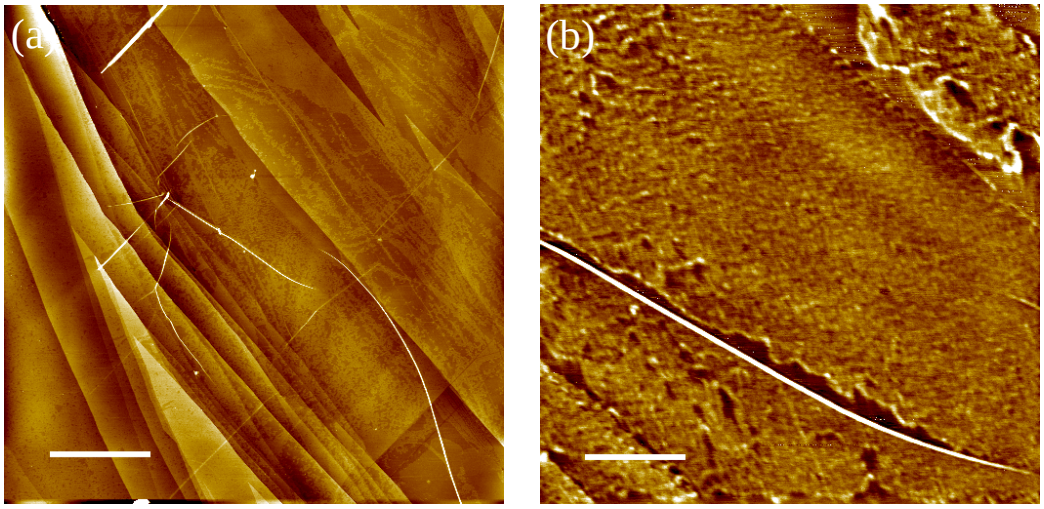

Figure 6.21. PeakForce Tapping mode AFM images of HOPG surfaces spin coated with 10 µl of 0.065 mg/ml TAPP/toluene solutions. (a) Image size: 10 µm. Scale bar: 2 µm. (b) Image size: 2 µm. Scale bar: 0.4 µm.

In Figure 6.23 (b), the heights of the 3D bright features can be measured by taking line profiles. In order to analyse the height of these features, twenty height values were collected from the AFM image in Figure 6.23 (b). The average and standard deviation of these twenty measured values were then calculated to determine the average height and its assciated error. By adopting this data acquisition and analysis method, the average height of the 3D aggregate features was determined to be 0.7 ± 0.2 nm, which is

comparable to the thickness of the unreacted TAPP films formed via drop deposition of 10 µl, 0.008 mg/ml of TAPP/toluene solutions onto the HOPG surface (Figure 6.17 (a)).

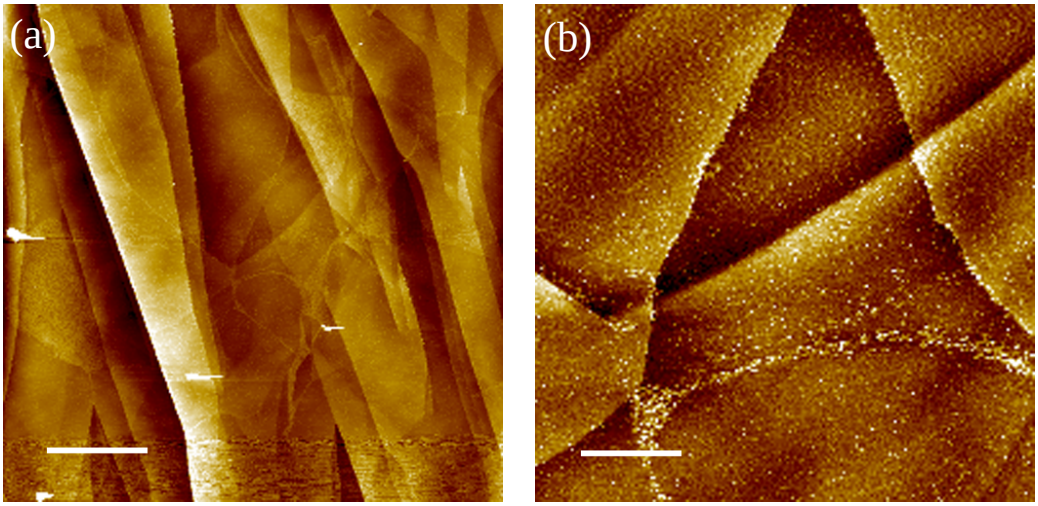

Figure 6.22. AFM images of HOPG surfaces after the deposition of 10 µl of 0.033 mg/ml TAPP/toluene solutions by spin coating. (a) Large-scale AFM scan. Image size: 10 µm. Scale bar: 2 µm. (b) Enlarged AFM scan. Image size: 1.5 µm. Scale bar: 0.3 µm.

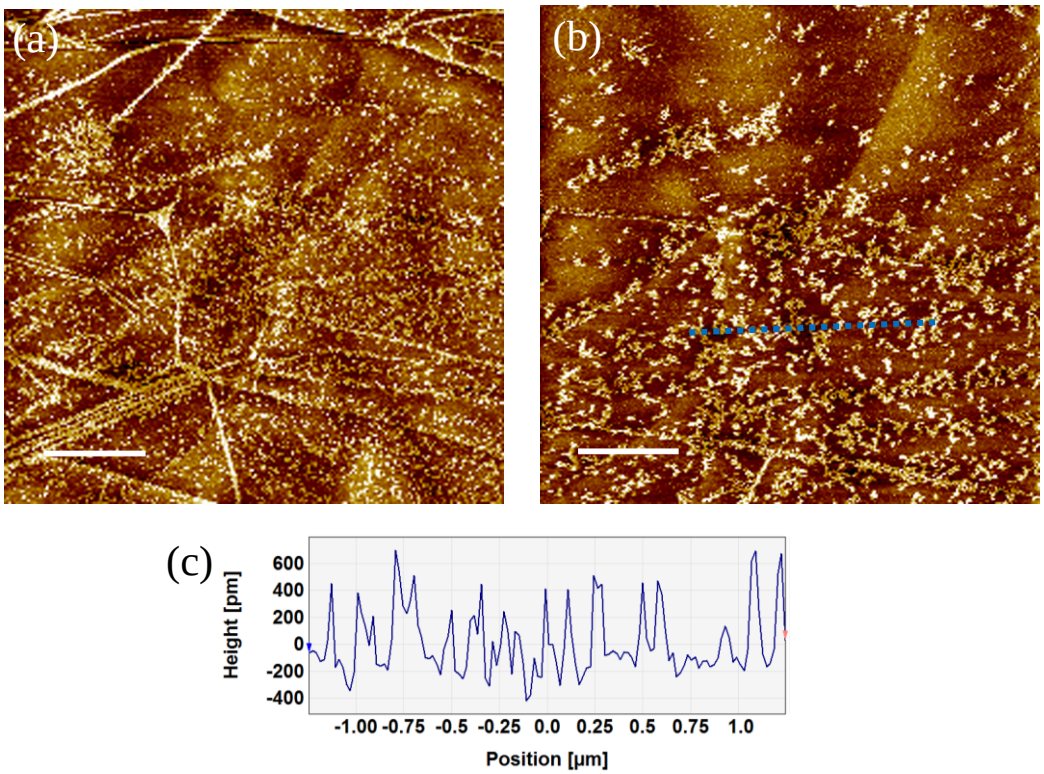

Figure 6.23. AFM images of HOPG surfaces spin coated with 10 µl of 0.016 mg/ml TAPP/toluene solutions. (a) Image size: 10 µm. Scale bar: 2 µm. (b) Image size: 5 µm. Scale bar: 1 µm. With a line profile taken throught the higher features.

In comparison with the quality of TAPP films obtained by drop deposition, spin coating leads to a much more homogeneous distribution of materials across the HOPG surface. These AFM studies provide some preliminary results for further research on the fabrication of high-quality 2D-COFs by adopting novel experimental methods to deposit unreacted TAPP onto solid surfaces.

6.3.2 Chemical structure of TAPP/BDA 2D-COFs

In addition to morphology studies via STM and AFM, the chemical structure of the bonds formed between TAPP molecules and BDA linkers via Schiff-base condensation reactions was investigated using XPS. In comparison with XPS measurements on unreacted TAPP films, the chemical changes following covalent bonds formation between TAPP and BDA can be revealed.

Blank HOPG control sample

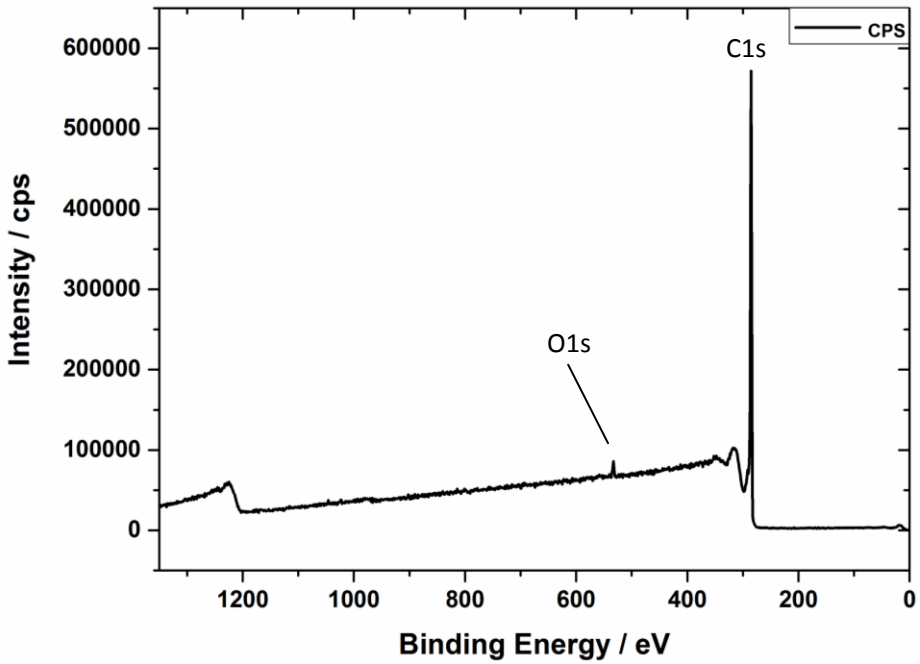

Figure 6.24. XPS survey scan of the blank HOPG control sample.

In order to investigate the influence of the underlying HOPG surface, XPS spectra were collected on a new, freshly cleaved HOPG sample. Figure 6.24 shows the survey scan of the blank control HOPG surface. In this XPS spectrum, two distinct peaks can be observed in the binding energy regions of C1s and O1s.

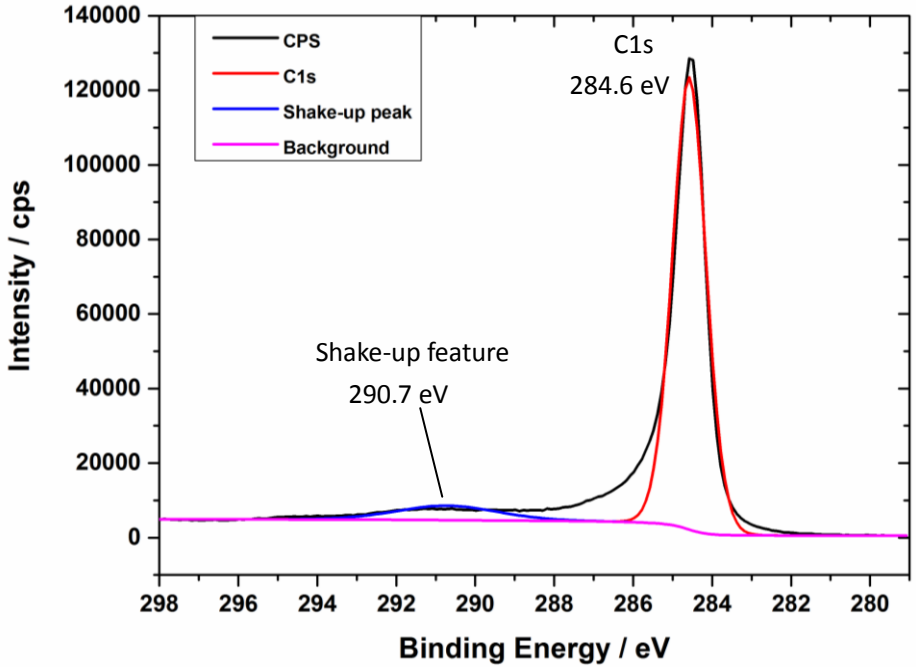

Figure 6.25. C1s XPS spectrum of the blank HOPG control sample.

Figure 6.25 shows a C1s XPS spectrum collected for the blank HOPG control sample. Compared with previous XPS studies of HOPG reported in literature [233-235], this assymetric C1s spectrum is a standard line shape for the C1s region of a HOPG surface. A Gaussian/Lorentzian peak at 284.6 ± 0.1 eV was fitted for the main peak of this spectrum. This peak value is in good agreement with the expected binding energy for the sp^2 carbons of HOPG [235]. The associated error value of 0.1 eV was determined based on the data acquisiton accuracy of the XPS machine. A broad shake-up peak was fitted at 290.7 ± 0.1 eV, the presence of which is due to the π-π^* transition of the aromatic HOPG surface. The full width at half maximum (FWHM) of the fitted C1s peak is 1.0 ± 0.1 eV.

In contrast to the C1s spectrum, the presence of oxygen species on the cleaved

HOPG surface as demonstrated by the O1s spectrum is less straightforward to interpret. Despite a large volume of published fitting results, the identification of single oxygen peaks from an O1s XPS spectrum is controversial [236]. Figure 6.26 presents the O1s spectrum for the blank control HOPG sample. The oxygen peak in the spectrum indicates the existence of oxygen species on the HOPG surface. During the cleavage process, more step edges are introduced to the HOPG surface [237]. The surface defects may act as reaction sites for carbon and O_2/H_2O in air. The O1s spectrum was deconvoluted using a two-component fitting model in literature [238]. The two oxygen peaks at 533.9 ± 0.1 eV and 532.3 ± 0.1 eV were assigned to oxygens in –COOH and –C=O/C-OH, respectively [239].

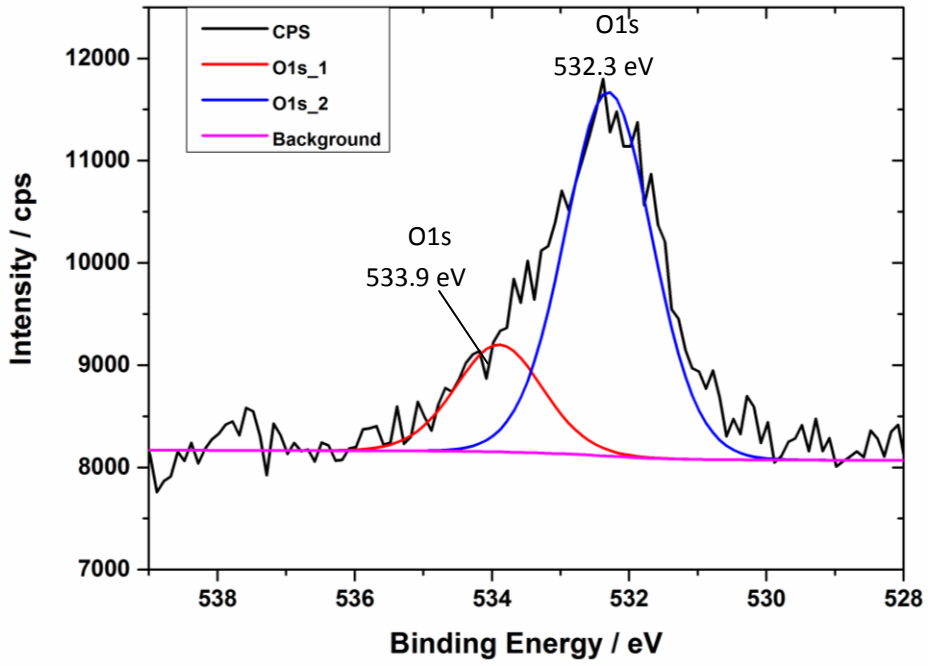

Figure 6.26. O1s XPS spectrum of the blank HOPG control sample.

Unreacted TAPP control sample

The unreacted TAPP control sample for the XPS investigations was made by depositing 10 µl of a 0.065 mg/ml TAPP/toluene solution onto a freshly cleaved HOPG surface. The sample was loaded into the UHV chamber of the XPS machine immediately following toluene evaporation.

Figure 6.27 is a C1s XPS spectrum collected for the unreacted TAPP films supported by HOPG underneath. Compared with Figure 6.25, this C1s XPS spectrum is also a standard line shape for the C1s region of a HOPG surface. A Gaussian/Lorentzian peak at 284.7 ±0.1 eV was fitted for the main peak of this spectrum (FWHM: 1.0 ±0.1 eV). In the XPS data analysis, the the C1s peak position was used as a check to ensure the other peak positions were consistent. The C1s peaks on all of the samples obtained for XPS measurements always fall at the same position. Due to the abundant existence of carbon in the HOPG substrate and TAPP, the C1s peak is not a suitable peak for studying the chemical structure of the 2D-COFs.

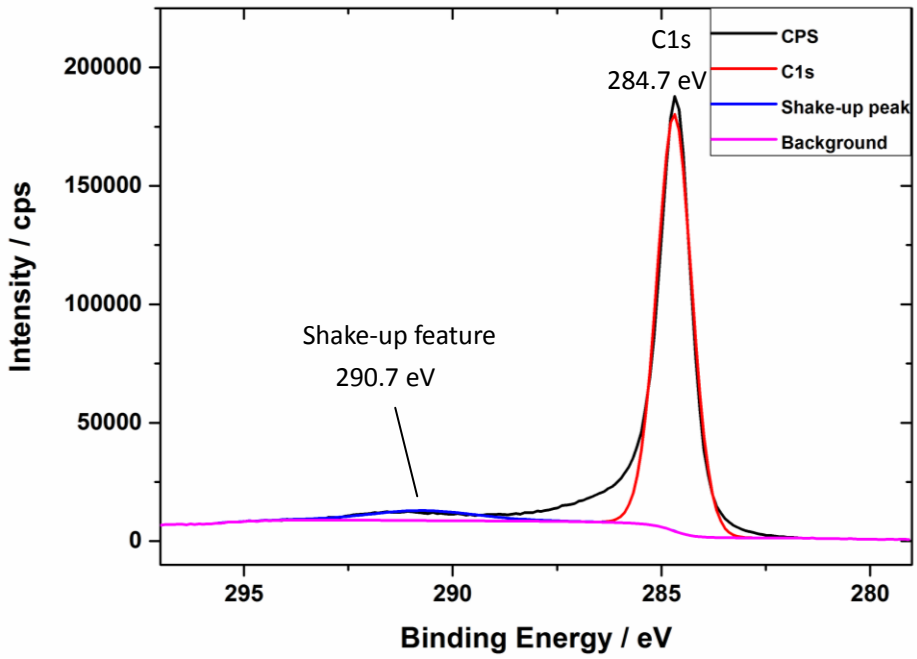

Figure 6.27. C1s XPS spectrum on unreacted TAPP control sample. A Gaussian/Lorentzian peak has been fitted for the spectrum at 284.7 ±0.1 eV.

Figure 6.28 (a) shows a comparison between the background-subtracted O1s XPS spectra of the unreacted TAPP control and the blank HOPG control sample. Compared with the XPS spectrum of the blank HOPG, the O1s XPS spectrum of the TAPP control sample exhibited a slight decrease in intensity. Following the deposition of TAPP from the toluene solution, most step edges on the HOPG surface were covered with 3D TAPP aggregates (Figure 6.15 (a)). The aggregation of unreacted TAPP along step edges

would reduce the amount of reactions sites that were in exposure with O_2 and H_2O in air. The decrease in reaction probability for carbon on the HOPG surface and O_2/H_2O in air would arise a decrease in the intensity of O1s signals detected by XPS.

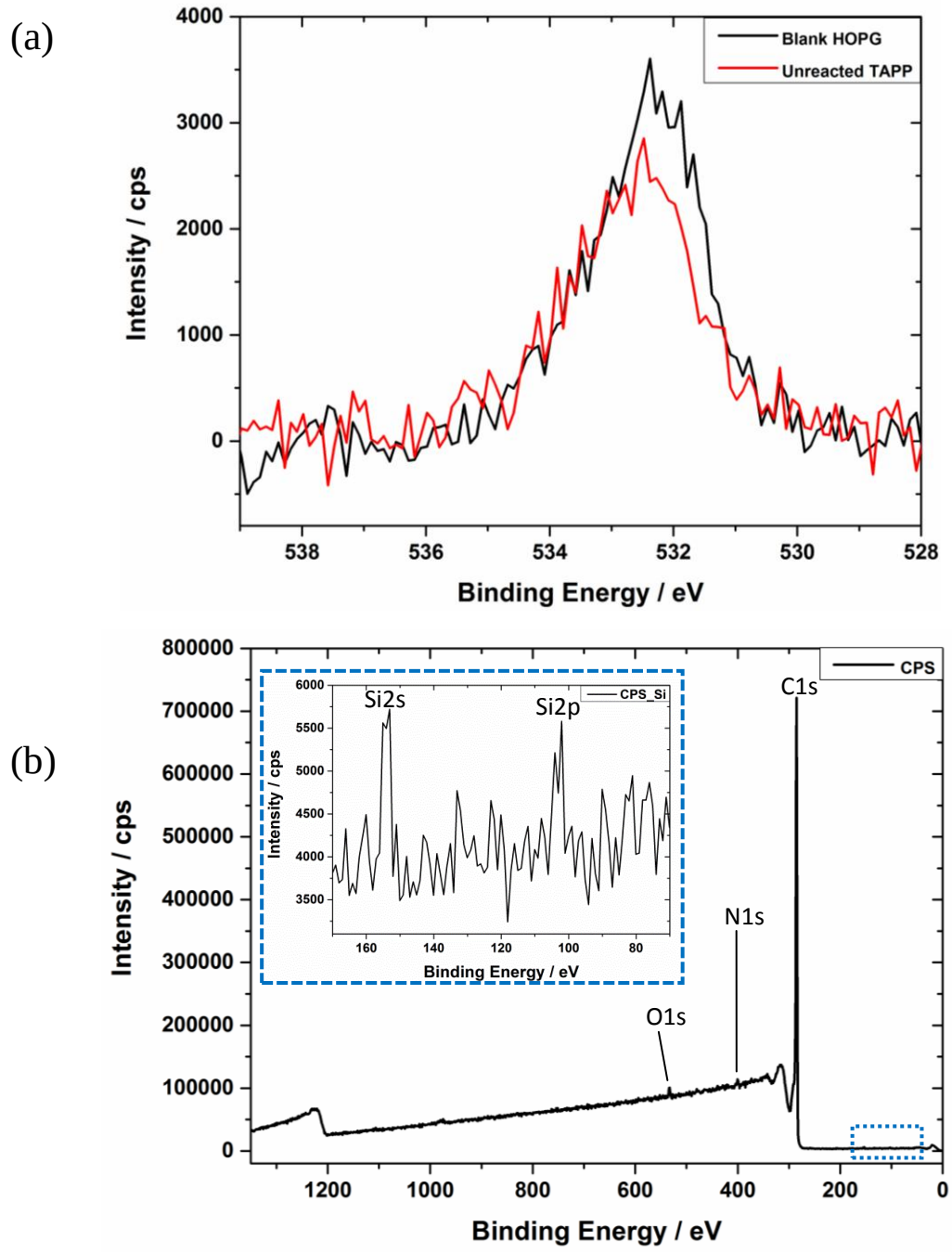

Figure 6.28. (a) O1s XPS spectra for unreacted TAPP control and freashly cleaved HOPG samples after background subtraction. (b) Survey scan for unreacted TAPP control sample. Insert: XPS spectrum in the binding energy range of 170 – 70 eV (highlighted by blue, dashed squares).

The existence of a very small amount of silicon species present on the TAPP control sample can be proved from the survey scan in the binding energy range of 70 – 170 eV [222], as presented in the insert of Figure 6.28 (b). The silicon contamination was likely to be caused by previous PDMS contamination left on the surface. Thus, the oxygen in PDMS (Binding energy: 532.3 eV [240, 241]) probably had a minor contribution to the oxygen signal of unreacted TAPP in Figure 6.28 (a).

Nitrogen species	Chemical formula	Binding energy in literature (eV)
Amine on phenyl ring	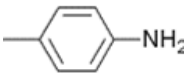	~ 399.4[242, 243]
Protonated nitrogen inside porphyrin core	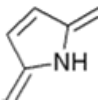	~ 399.7[244, 245]
Non-protonated nitrogen inside porphyrin core	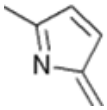	~ 397.7[244, 245]
Satellite peak	----	401 - 402[244, 246]

Table 6.1. XPS binding energy values of nitrogen species for TAPP according to reports in literature.

N1s XPS spectra were used to study the chemical composition of the unreacted TAPP and the chemical nature of the bonds formed between porphyrins via Schiff-base condensation reactions. For a TAPP molecule, the chemical structure of which is shown in Figure 6.1 (a), there are three distinct nitrogen species: nitrogens in amine groups on the outer phenyl rings: protonated nitrogens inside the porphyrin core; and non-protonated nitrogens inside the porphyrin core. The binding energy positions for these nitrogen species reported in literature are given in Table 6.1. The C1s peak values of these reported measurements were used to check the consistency of the measured peak positions.

In addition to the N1s peaks expected for the unreacted TAPP control sample, an additional satellite peak was also observed based on the molecular structure of TAPP. This satellite peak is commonly observed in the binding energy range 401 – 402 eV in N1s XPS spectra of porphyrins [244, 246]. The satellite feature results from electron interactions within the aromatic porphyrin core [247].

When performing peak fitting for the N1s peak spectra, the positions of the three nitrogen peaks listed in Table 6.2 were restrained to be ± 0.3 eV either side of the positions recorded in literature. A wider set of constraints were adopted for the satellite peak due to the greater uncertainty associated with the shake-up transition of electrons. The starting position of the satellite peak was set to be 402 ± 0.5 eV. The FWHM obtained by fitting to the intense C1s carbon peak was 1.0 eV. This value was used as a standard for other XPS scans [246]. Therefore, restraints set for the FWHMs of the XPS peaks were set to be between 0.8 and 1.2 eV excluding the satellite peak. The restraint for the FWHM of the satellite peak was set to be between 1 and 2 eV.

When fitting peaks to a N1s XPS spectrum, the number of peaks to fit is decided according to the number of nitrogen species existing in the molecular system. In the case of fitting the N1s spectrum collected from unreacted TAPP films, three peaks are expected to be required corresponding to the three nitrogen species as the discussed in Table 6.2. Additionally, a broad satellite peak should be added at around 402 eV.

For most complex XPS spectra with multiple different species there a large number of mathematically valid fits that are possible. However, only fits to the data that make physical sense given the expected molecular structure of the sample should be considered. For the unreacted TAPP control sample, three criteria were used to assess the validity of a possible fit to the N1s XPS spectra. Firstly, the percentage of the total fit area assigned to the area of the satellite peak should be 5% – 15% [244, 246, 248]. Secondly, the combined area of the protonated and non-protonated nitrogens in the porphyrin cores should make up half of the remaining fit area once the area of the satellite peak has been subtracted. Thirdly, the area of the peak associated with the protonated nitrogen in the porphyrin core should be larger than the peak associated with the non-protonated nitrogen in the porphyrin core. According to previous XPS studies of

porphyrins, the ratio between the areas of these two nitrogen species should be between 1.2 and 1.5 [244, 249]. The difference in areas is related to the higher electronegativity of the protonated nitrogen compared with the non-protonated nitrogen.

Figure 6.29 shows the N1s XPS spectrum collected for the unreacted TAPP control sample. This N1s spectrum is an average taken from two identical N1s scans acquired for the TAPP control sample. Based on the fitting criteria described above, a satellite peak (marked in green) and three nitrogen peaks were fitted for the N1s XPS spectrum using Gaussian-Lorentzian functions.

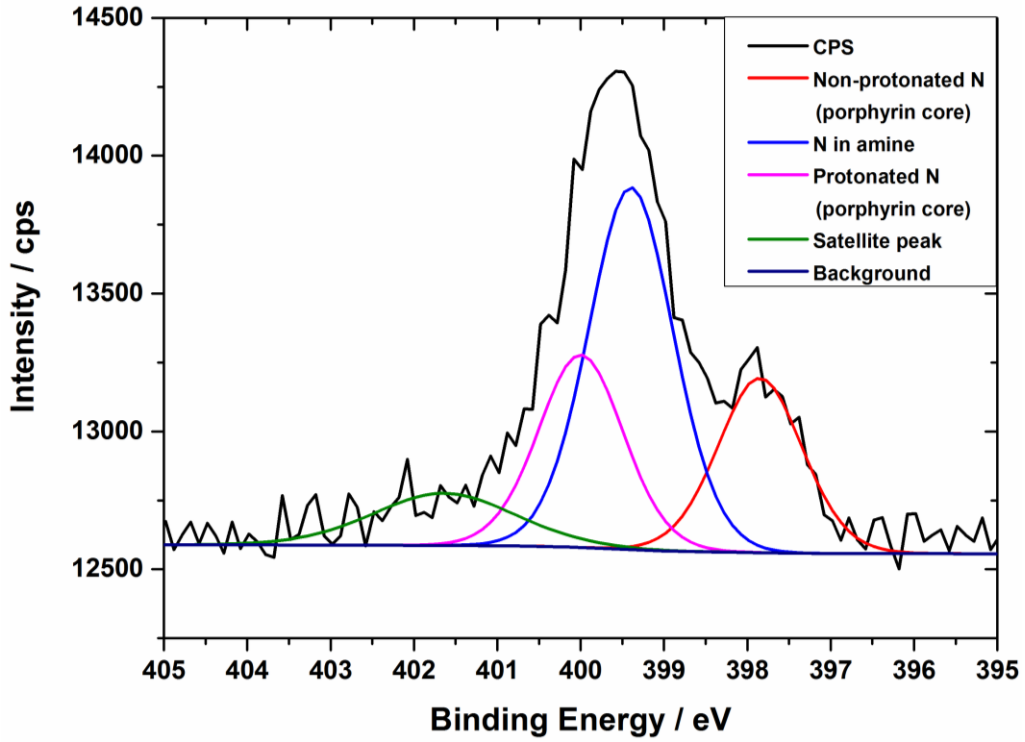

Figure 6.29. N1s XPS spectrum for unreacted TAPP on HOPG substrate. The black curve represents the raw data collected in the XPS experiments. The four peaks in green, pink, blue and red (from left to right) are the nitrogen peaks with Gaussian-Lorentzian line-shapes which were fitted into the raw data based on the fitting criteria set for the TAPP control sample.

The binding energy positions associated with these nitrogen peaks are summarised in Table 6.3. The percentage contributions of the peak areas corresponding to the three nitrogen species of TAPP were calculated under the condition that the contribution of the satellite peak was first removed from the total area of the fitted peaks. The peak

areas of amine nitrogen is 47.2 %, which is nearly half of the total amount of nitrogen species. The peak separation of the protonated and non-protonated nitrogens is 2.2 ± 0.1 eV, which is in good agreement with the previously published values listed in Table 6.2. The percentage peak areas for the protonated and non-protonated nitrogens in the porphyrin cores are 29 % and 23.8 %, respectively. By comparing this data with that collected from N1s XPS spectra of the TAPP/BDA 2D-COFs, more information about the formation of covalent bonds between TAPP and BDA can be acquired.

Peaks in XPS spectrum	Nitrogen species	Chemical formula	Binding energy in experiment (± 0.1 eV)	Percentage of total fit area
—	Amine on phenyl ring	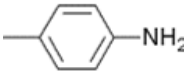	399.4	47.2 %
—	Protonated nitrogen inside porphyrin core	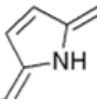	400.0	29.0 %
—	Non-protonated nitrogen inside porphyrin core	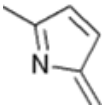	397.8	23.8 %
—	Satellite peak	----	401.6	----

Table 6.2. Experimentally measured binding energy values for the four nitrogen peaks in the peak fitting of the N1s spectrum of the TAPP control sample shown in Figure 6.29. Percentage contributions to the total fit area for the peaks associated with the three nitrogen species present in unreacted TAPP are also given. The area of the satellite peak has been removed from the total fit area prior to calculating the percentage contributions of the other nitrogen species.

TAPP/BDA 2D-COFs sample

The TAPP/BDA 2D-COFs sample was prepared by adopting the synthetic method introduced in section 6.2.1. The 2D-COF sample was grown from an unreacted TAPP sample formed by drop depositing 10 µl of TAPP/toluene solution with a concentration

of 0.065 mg/ml only onto a freshly cleaved HOPG substrate.

Using the CasaXPS software package, Gaussian-Lorentzian line-shape peaks were used to model all the XPS spectra recorded on the TAPP/BDA 2D-COF sample. Figure 6.30 shows the C1s XPS spectrum which has been fitted with one peak at 284.7 ± 0.1 eV. This is consistent with the C1s binding energy from the TAPP control sample. Thus, no further correction is needed when comparing N1s binding energies between the TAPP control sample and the TAPP/BDA 2D-COFs.

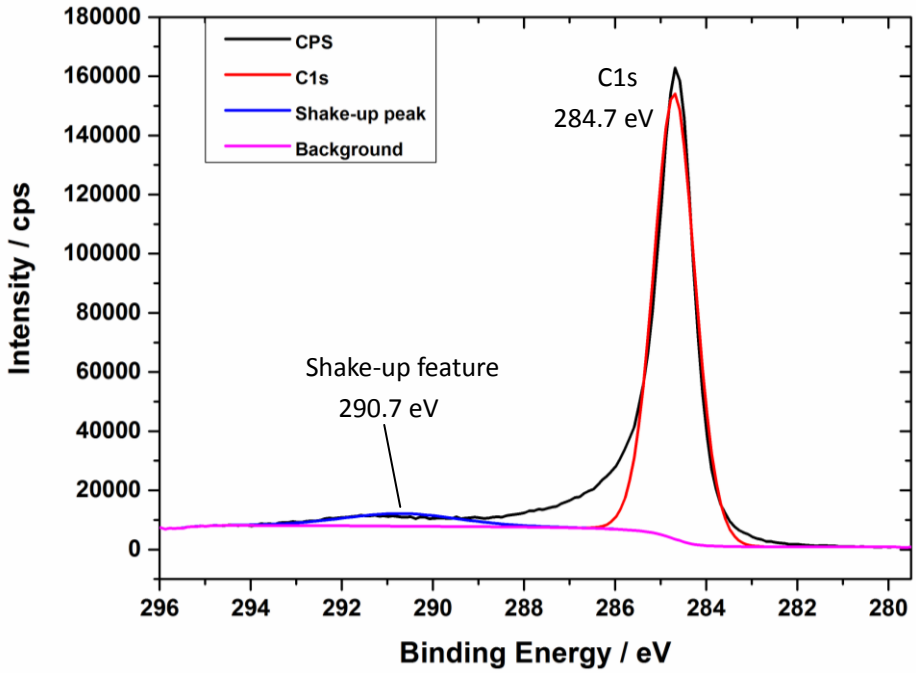

Figure 6.30. C1s XPS spectrum on TAPP/BDA 2D-COFs.

Similar to the XPS data recorded for the unreacted TAPP control sample, a strong O1s signal was detected as can be seen in Figure 6.31 (a). In comparison to the O1s XPS spectrum acquired for the TAPP control sample, the O1s signal for the TAPP 2D-COF sample exhibits an increase in intensity and higher binding energy components. The increase in the O1s signals could result from the enhanced reactivity of the HOPG surface in the reaction vessel at the elevated temperatures used for 2D-COF growth. The increased O1s signal could also be related to the adsorption of BDA on the HOPG surface. A number of unknown oxygen components, in particular water and excess BDA,

may exist in the system rendering the O1s XPS peak fitting ambiguous [236]. From the survey scan shown in Figure 6.31 (b), the TAPP/BDA 2D-COFs system was free from silicon contamination

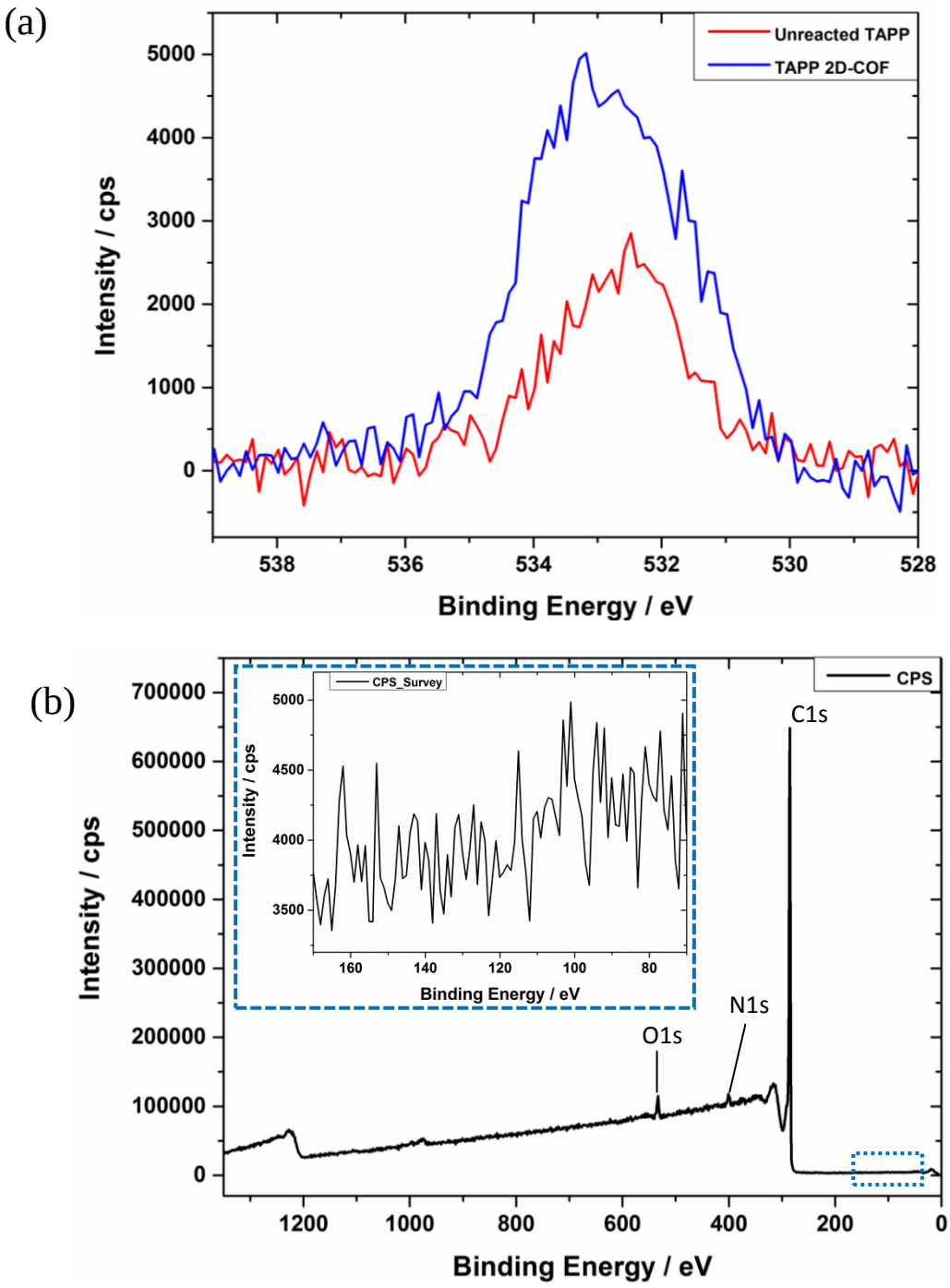

Figure 6.31. (a) O1s XPS spectra for TAPP 2D-COF and unreacted TAPP control samples following background subtraction. (b) Survey scan for TAPP 2D-COF sample. Insert: XPS spectrum in the binding energy range of 170 – 70 eV (highlighted by blue, dashed squares). .

When fitting the N1s spectrum for the TAPP/BDA 2D-COF sample, the criteria associated with the nitrogen species in the porphyrin core that were set for the TAPP control sample remain unchanged. A proportion of the amine groups on the phenyl rings will be involved in the Schiff-base condensation reaction between TAPP and BDA. Thus, the precentage contribution related to the peak areas of the amine groups is expected to decrease following the formation of TAPP/BDA 2D-COFs. The restraints set for the starting positions and FWHMs of the 2D-COFs sample were the same as those for the unreacted TAPP. New peaks are expected to occur due to the covalent reaction. At least one of these peaks is likely to be associated with imine nitrogens formed by the standard Schiff-base condensation reaction between TAPP and BDA. The N1s binding energy of imine groups is observed from literacture to be around 398.5 eV [243, 250].

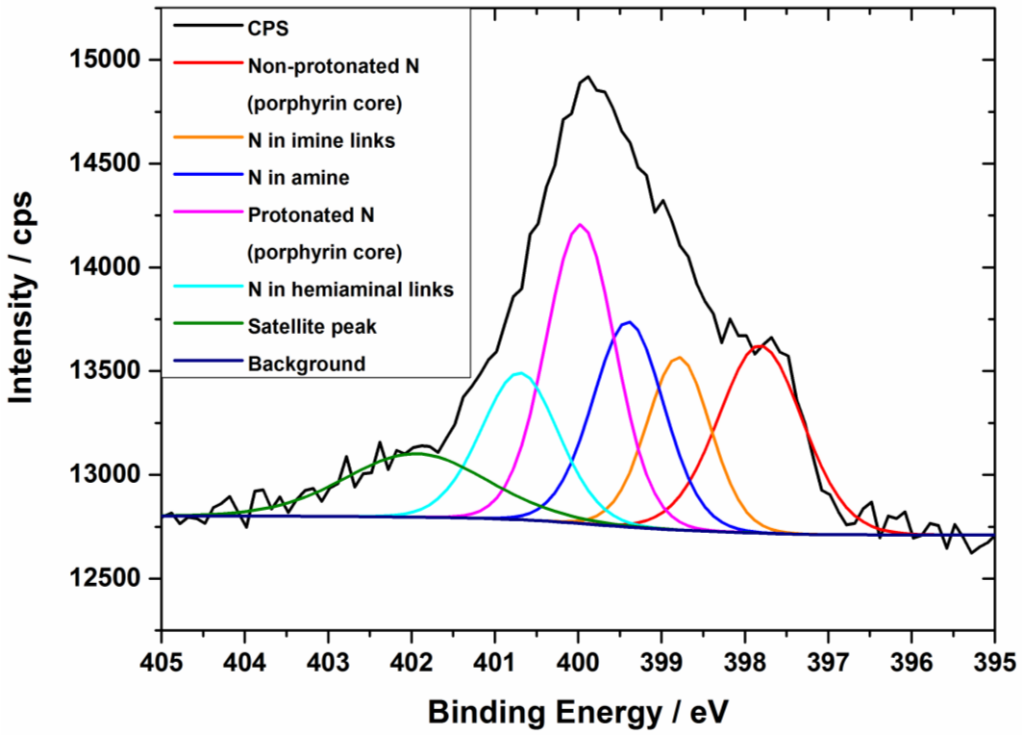

Figure 6.32. N1s XPS spectrum for TAPP/BDA 2D-COFs on HOPG. The black curve represents the raw data collected in the XPS experiments. Six peaks with Gaussian-Lorentzian shapes were used to model the XPS spectrum including one satallite peak and five N1s peaks.

Figure 6.32 is the N1s XPS spectrum of the TAPP 2D-COFs sample with peaks

modelled using Gaussian-Lorentzian functions. This N1s spectrum is an average taken from two N1s scans acquired at different locations on the TAPP/BDA 2D-COF sample. Compared with the N1s spectrum collected for the TAPP control sample (see Figure 6.29), two new peaks associated with the Schiff-base condensation reaction are present: one at 398.8 ± 0.1 eV; and the other one at 400.7 ± 0.1 eV. The peak at 398.8 eV is associated with the formation of imine links (Figure 6.33 (a)) via a complete condensation reaction between the amine groups of TAPP and the aldehyde groups of BDA. The peak at 400.7 eV is consistent with the binding energy recorded for similar hemiaminal links as reported by Di Giovannantonio *et al.* [243]. In their recent XPS study, the hemiaminal state was identified in a 1D-COF structure formed via a Schiff-base condensation reaction at the liquid-solid interface. As illustrated in Figure 6.33 (b), the hemiaminal structure is a recognised intermediate state in the Schiff-base condensation reaction. Apart from the observed formation on a solid surface [243], intermediate states existing in Schiff-base condensation reactions have only been detected in solution using other experimental techniques, such as Raman Spectroscopy [251], mass spectroscopy [252] and nuclear magnetic resonance [253].

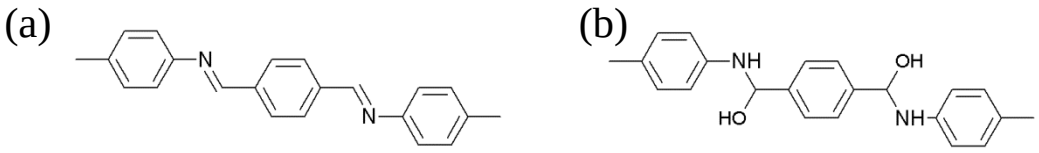

Figure 6.33. Schematic diagrams of the covalent bonds formed between TAPP and BDA via the Schiff-base condensation reactions. (a) Imine links. (b) Hemiaminal links.

The results of peak fitting for the N1s XPS spectrum of the TAPP 2D-COFs is summarised in Table 6.3. Apart from the contribution from the satellite peak, the percentage that the unreacted amine groups make up in the total nitrogen species is 18.6 %. This means there still exists a large number of unreacted amine groups present at the surface after the TAPP/BDA 2D-COF growth. This is despite there being a large excess of BDA loaded into the glass reaction vessel. While there is a lack of direct experimental proof, one possibility is that these unreacted amines exist within the 3D

aggregates imaged by AFM on HOPG, as shown in Figure 6.15 (b). As TAPP molecules tend to stack into 3D structures, the vapourised BDA molecules may not be able to reach the amine groups inside the 3D aggregates, preventing the condensation reaction from occuring.

Peaks in XPS spectrum	Nitrogen species	Chemical formula	Binding energy in experiment (±0.1 eV)	Percentage of total fit area
—	Amine on phenyl ring	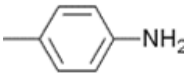	399.5	18.6 %
—	Protonated nitrogen inside porphyrin core	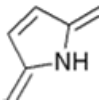	400.0	30 %
—	Non-protonated nitrogen inside porphyrin core	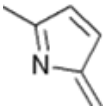	397.8	19.4 %
—	Nitrogen in imine links	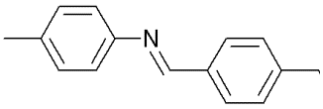	398.8	18.6 %
—	Nitrogen in hemiaminal links	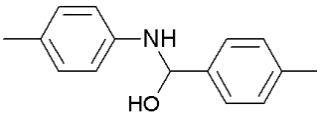	400.7	13.4 %
—	Satellite peak	----	401.9	----

Table 6.3. Summary of the binding energy values measured by XPS experiments corresponding to the chemical states of different nitrogen species in the TAPP/BDA 2D-COFs. Percentage contributions of the five N1s peaks to the total fit area. These percentage contributions were calculated after the area of the satellite peak had been removed from the total fit area.

The percentages of imine and hemiaminal groups in the linkages between TAPP and BDA are 18.6 % and 13.4 %, respectively. The high proportion of hemiaminal groups is likely to be related to the presence of significant amount of water vapour

during the 2D-COFs growth. The presence of water in the reaction vessel is favourable to the formation of hemiaminal groups in terms of the equilibrium position of the condensation reaction. In the experimental method used, the cap of the reaction vessel was opened and the sample removed immediately after taking the vessel out of the oven. My belief is that this rapid quenching of the sample led to the chemical composition of the 2D-COF being fixed at the composition that was present during the growth process. Some variation in the percentage contribution of the hemiaminal composition was observed for TAPP/BDA 2D-COF samples prepared using exactly the same growth parameters. Thus, the ratio of imine to hemiaminal in the resulting 2D-COFs was not exactly consistent between different samples grown using the same conditions. This demonstrates that the chemical structure of the covalent links in the 2D-COFs depends very delicately on the growth conditions.

The influence that the amount of $CuSO_4$ $5H_2O$ added to the reaction vessels has on the chemical composition of the TAPP 2D-COFs was investigated. Five samples were parepared using the standard synthetic parameters (10 μl of 0.06 mg/ml TAPP/toluene solution, 0.064 mg of BDA, and heating at 130 ℃ for 15 hours) but with varying amounts of $CuSO_4$ $5H_2O$ (0.00 g, 0.05 g, 0.10 g, 0.15 g, and 0.20 g). Figures 6.34 - 6.38 present the N1s XPS spectra collected for these five TAPP 2D-COF samples. The N1s spectra were all fitted using the six-component model introduced for the N1s spectrum shown in Figure 6.32. The percentage contributions of the five nitrogen species existing in the TAPP 2D-COFs are summarised in Table 6.4.

As can be seen from Table 6.4, the percentage contributions from the protonated and non-protonated nitrogen species inside the porphyrin cores show no significant change across the five samples. Given that these nitrogen species play no role in the Schiff-base condensation reaction this is as expected. However, a drastic increase in the ratio of imine (36 %) to hemiaminal (3 %) is observed when no $CuSO_4$ $5H_2O$ was added during the 2D-COF growth. With the inclusion of $CuSO_4$ $5H_2O$ (0.05 to 0.20 g), the percentage contributions from the imine nitrogen species decreased to between 12 % - 25 %. The corresponding contributions from the hemiaminal nitrogen species increased to between 15 % - 18 %. These results indicate that the water molecules

released by the $CuSO_4$ $5H_2O$ has a significant influence on the chemical composition of the resulting 2D-COF. The presence of water during 2D-COF growth biases the equilibrium position of the Schiff-base condensation reaction towards the formation of hemiaminal groups.

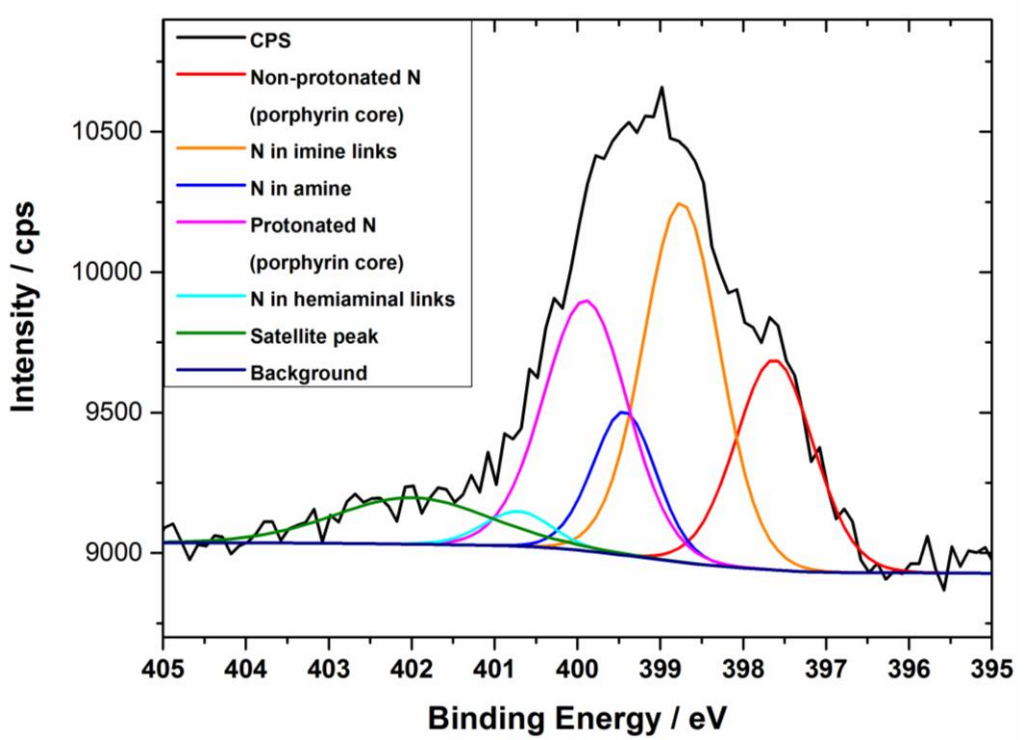

Figure 6.34. N1s XPS spectrum for TAPP/BDA 2D-COFs on HOPG. $CuSO_4$ $5H_2O$: 0.00 g.

The chemical nature of the links formed between molecular components plays a crucial role in determining the electronic properties of 2D-COF materials. To interpret the precise composition of the links, more complementary techniques are needed to probe both the chemical structure and the morphology of 2D-COFs. In the future, more efforts will be focussed on coverting hemiaminal links to imine links by adjusting growth conditions, particularly by the presence of water. Other more advanced spectroscopic methods are required to provide more evidence for the existence of hemiaminal groups, and hopefully to confirm the location of the hemiaminal groups within the 2D-COF layers.

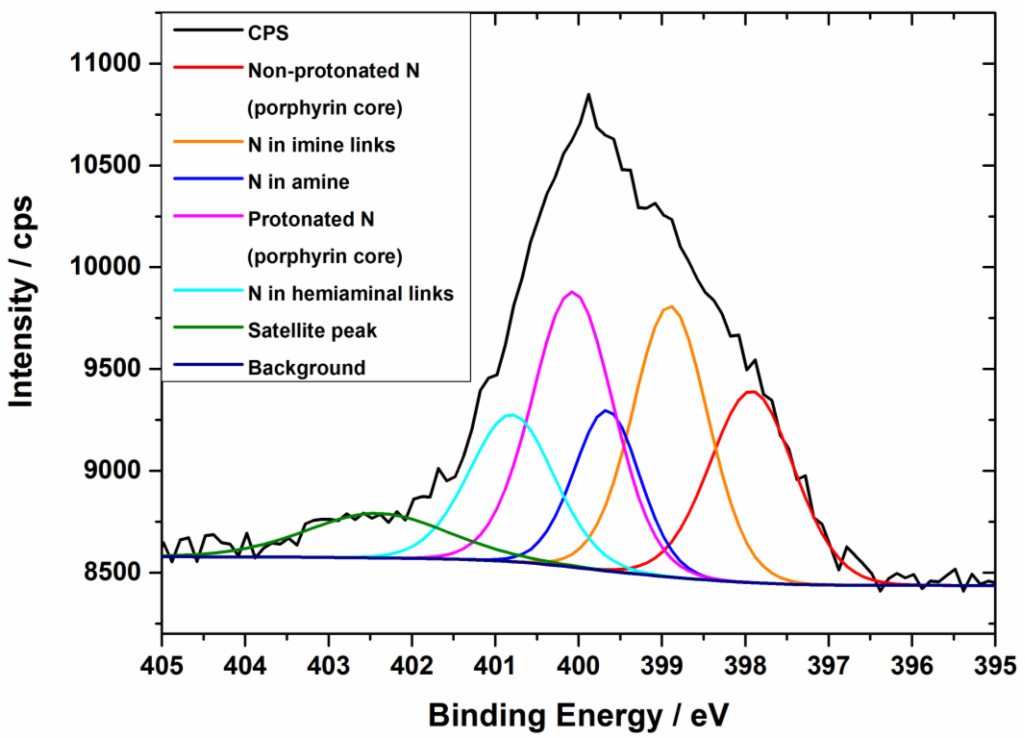

Figure 6.35. N1s XPS spectrum for TAPP/BDA 2D-COFs on HOPG. $CuSO_4$ $5H_2O$: 0.05 g.

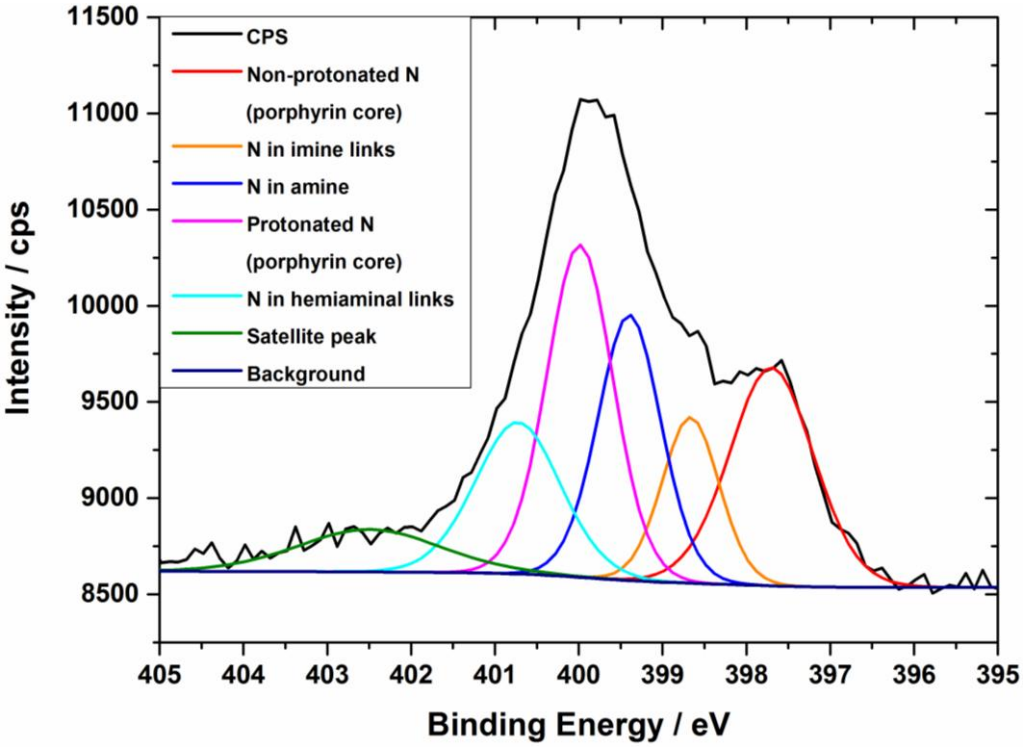

Figure 6.36. N1s XPS spectrum for TAPP/BDA 2D-COFs on HOPG. $CuSO_4$ $5H_2O$: 0.10 g.

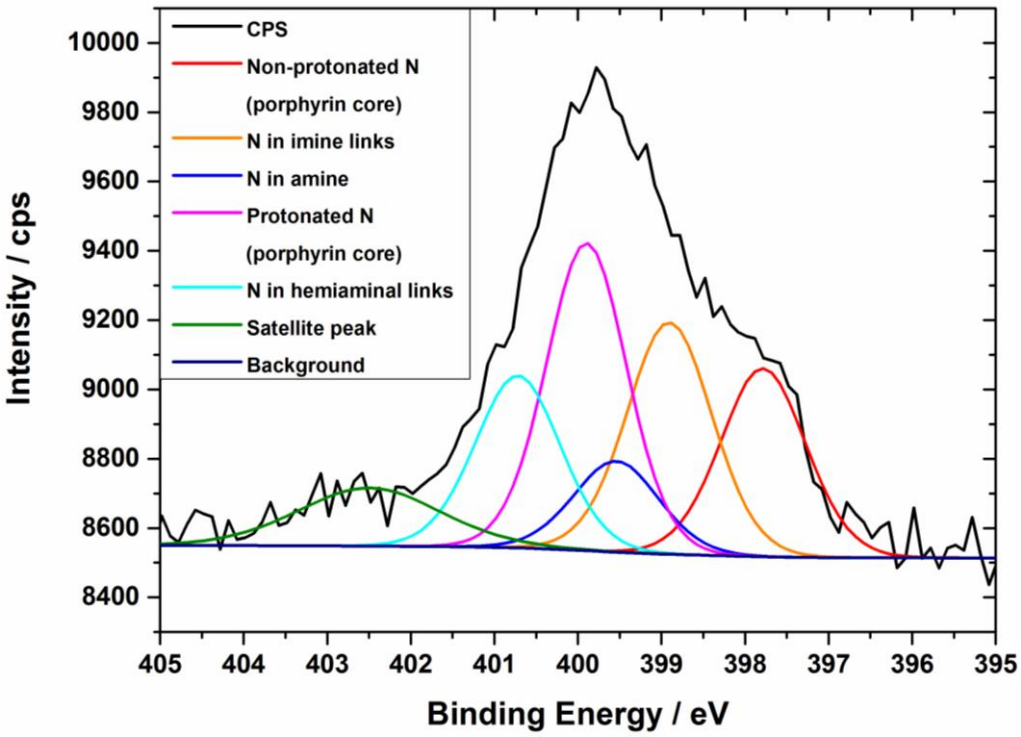

Figure 6.37. N1s XPS spectrum for TAPP/BDA 2D-COFs on HOPG. $CuSO_4$ $5H_2O$: 0.15 g.

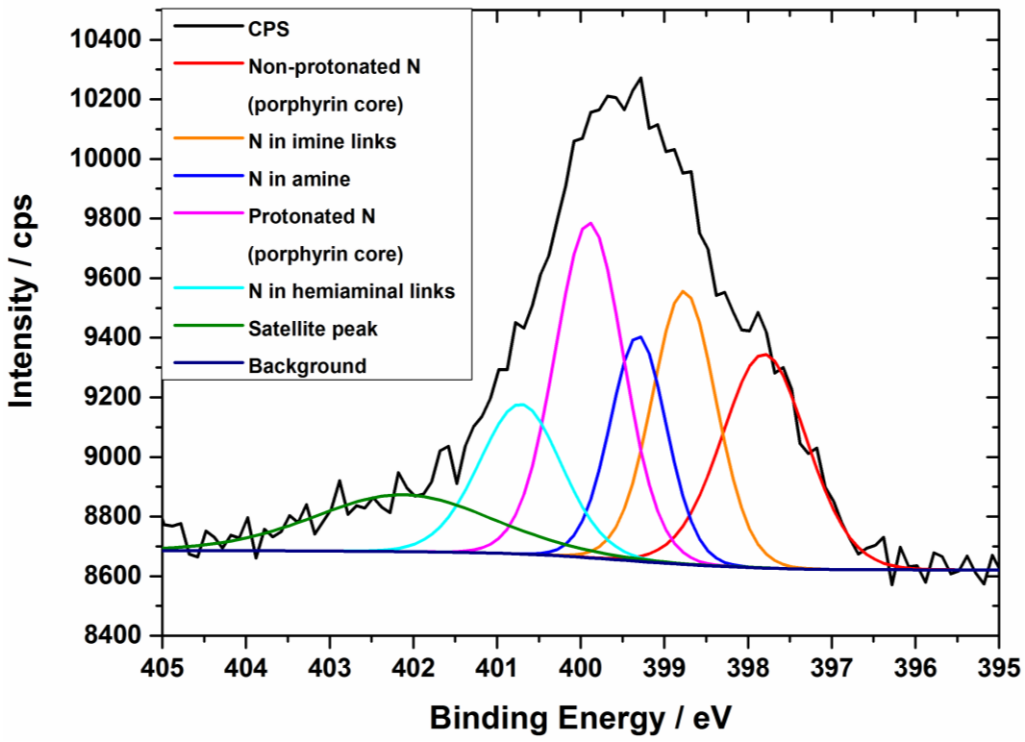

Figure 6.38. N1s XPS spectrum for TAPP/BDA 2D-COFs on HOPG. $CuSO_4$ $5H_2O$: 0.20 g.

Peaks in XPS spectrum	Nitrogen species	Amount of $CuSO_4$ $5H_2O$				
		0.00 g	0.05 g	0.10 g	0.15 g	0.20 g
	Amine on phenyl ring	12 %	13 %	21 %	9 %	15 %
	Protonated nitrogen inside porphyrin core	28 %	27 %	28 %	30 %	27 %
	Non-protonated nitrogen inside porphyrin core	22 %	20 %	23 %	19 %	22 %
	Nitrogen in imine links	36 %	25 %	12 %	24 %	21 %
	Nitrogen in hemiaminal links	3 %	15 %	16 %	18 %	15 %

Table 6.4. Summary of the percentage contributions to the total fit area from the five nitrogen species present in the TAPP 2D-COF samples grown with different amounts of $CuSO_4$ $5H_2O$. For each of the samples, the area of the corresponding satellite peak has been removed from the total fitted area prior to calculating the percentage contributions.

6.4 ZnTAPP COFs

In this section, experimental results on the formation of 2D-COFs via Schiff-base condensation reactions between BDA and a metal-containing tetra-amine-porphyrin, 5,10,15,20-tetrakis-(4-aminophenyl)porphyrin-Zinc(II) (ZnTAPP) (Figure 6.1), are discussed. Both STM and AFM were employed to study the morphology of ZnTAPP/BDA 2D-COFs. The chemical nature of the covalent bonds formed beween ZnTAPP and BDA were studied using XPS.

6.4.1 Morphology studies of ZnTAPP/BDA 2D-COFs

STM studies

Ordered ZnTAPP/BDA 2D-COF structures can be formed on HOPG by depositing ZnTAPP from either toluene or 1,2,4-trichlorobenzene (TCB) solutions.

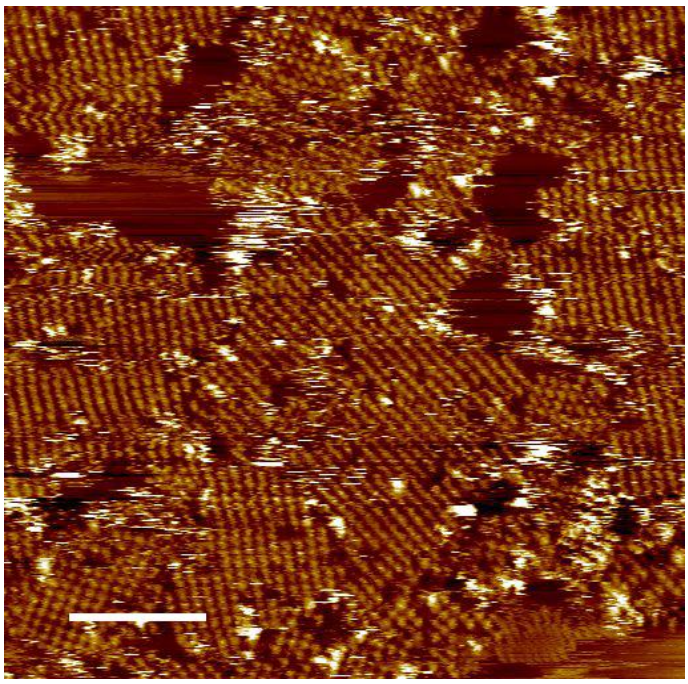

Figure 6.39. STM image of ZnTAPP/BDA 2D-COFs grown by depositing ZnTAPP from TCB. Sample fabrication conditions: 0.15 g of $CuSO_4 \cdot 5H_2O$; ~ 1 mg of BDA as solid; 20 μl of 0.1 mg/ml ZnTAPP in TCB; heating at 150 ℃ for 2 hours. STM scanning parameters: V_s = -0.55 V, I_t = 12 pA. Prior to STM imaging a drop of 1-phenyloctane was deposited on the surface to improve imaging resolution. Image size: 150 nm. Scale bar: 30 nm.

Figure 6.39 is an STM image showing the growth of the ZnTAPP 2D-COFs. The ZnTAPP molecules were dissolved in TCB and then deposited onto a freshly cleaved HOPG surface and the TCB allowed to evaporate. The HOPG substrate covered with an unreacted ZnTAPP film was then loaded into a reaction vessel. Quantitative analysis was carried out for this STM image using the same method adopted for the STM image shown in Figure 6.10. Surface coverages were measured from four STM images

collected at different locations of the ZnTAPP/BDA 2D-COF sample. By taking the average and standard deviation of the results from these four measurements, the average surface coverage of the ZnTAPP/BDA 2D-COF on the HOPG surface was determined to be 83 % ± 4 %. To measure the average domain size of the ZnTAPP 2D-COF, ten domain size values were collected from the four STM images. From the calculation of the average and standard deviation of these ten measured values, the average domain size of the ZnTAPP 2D-COF was determined to be 44 ± 16 nm.

The growth of ZnTAPP/BDA 2D-COFs was also observed by utilising an unreacted ZnTAPP thin film deposited from toluene solutions. Figure 6.40 shows two STM images of the ZnTAPP 2D-COFs formed under this condition. The surface coverage of the ZnTAPP 2D-COF determined from the STM image shown in Figure 6.40 (a) was 87 %. The average domain size of the 2D-COFs in this STM image was determined by collecting five domain size values and then calculating their average and standard deviation. As a result, the domain size of the ZnTAPP 2D-COFs shown in Figure 6.40 (a) was measured to be 35 ± 6 nm. For the growth condition presented in Figure 6.40 (b), three STM images collected at different locations of the same sample were used in the 2D-COF quality analysis. By taking the average and standard deviation of the surface coverage values from these three STM images, the average surface coverage of the 2D-COFs was determined to be 90 ± 3 %. In order to measure the average domain size, ten domain size values were collected from the three STM images. By calculating the average and standard deviation of these ten measured values, the average domain size of the ZnTAPP 2D-COFs presented in Figure 6.40 (b) was determined to be 49 ± 18 nm. Compared with the freebase TAPP 2D-COFs, the domain sizes of the ZnTAPP 2D-COFs are significantly smaller. We suggest that this possibly results from the lower solubility of ZnTAPP in toluene. ZnTAPP molecules show a stronger tendency to self-aggregate than freebase TAPP. Thus, newly prepared ZnTAPP/toluene solutions should be used to ensure a more reproducible ZnTAPP 2D-COFs growth.

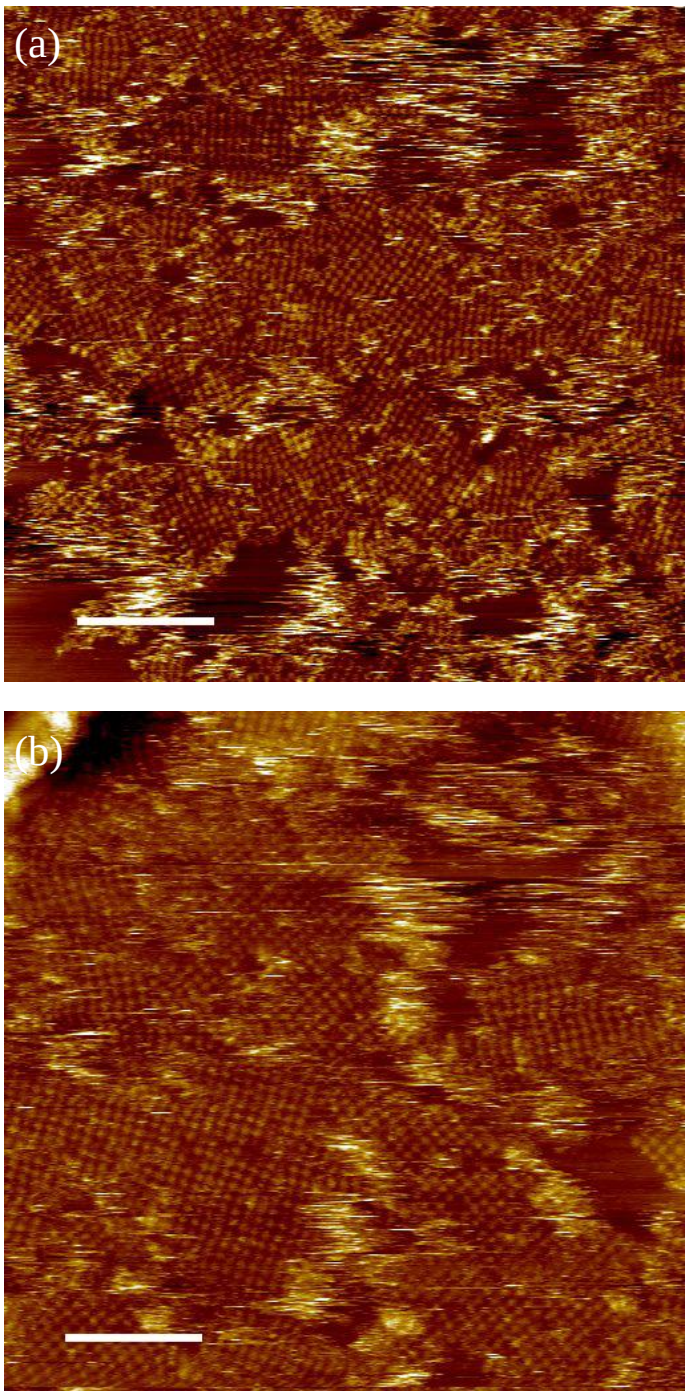

Figure 6.40. STM images of ZnTAPP/BDA 2D-COFs prepared by depositing ZnTAPP from toluene solutions. 2D-COF growth conditions: (a) $CuSO_4$ $5H_2O$: 0.15 g; ZnTAPP: 20 μl, 0.005 mg/ml; BDA: ~ 1 mg in solid; Heating: 120 ℃, 3 h. (b) $CuSO_4$ $5H_2O$: 0.15 g; ZnTAPP: 10 μl, 0.009 mg/ml; BDA: ~ 1 mg in solid; Heating: 120 ℃, 15 h.STM imaging parameters: (a) V_s = -0.85 V; I_t = 0.008 nA. Image size: 200 nm. Scale bar: 40 nm. (b) V_s = -1 V; I_t = 0.01 nA. Image size: 150 nm. Scale bar: 30 nm.

Unit cell parameters of the ZnTAPP 2D-COFs were determined from high

resolution STM images that had been drift-corrected using the underlying HOPG lattice (see Figure 6.41 (a)). Figure 6.41 (b) shows a pair of drift-corrected STM images for the measurement of the unit cell dimensions of the ZnTAPP 2D-COFs. The zinc-containing porphyrin 2D-COFs exhibit indentical unit cell dimensions to that of their freebase counterparts within the accuracy of the STM measurement. The unit cell lattice values were measured to be $a = b = 2.6 \pm 0.2$ nm and $\gamma = 89 \pm 3°$. The average and associated error values were determined by calculating the average and standard deviation of five sets of data collected from Figure 6.41 (a) and (b).

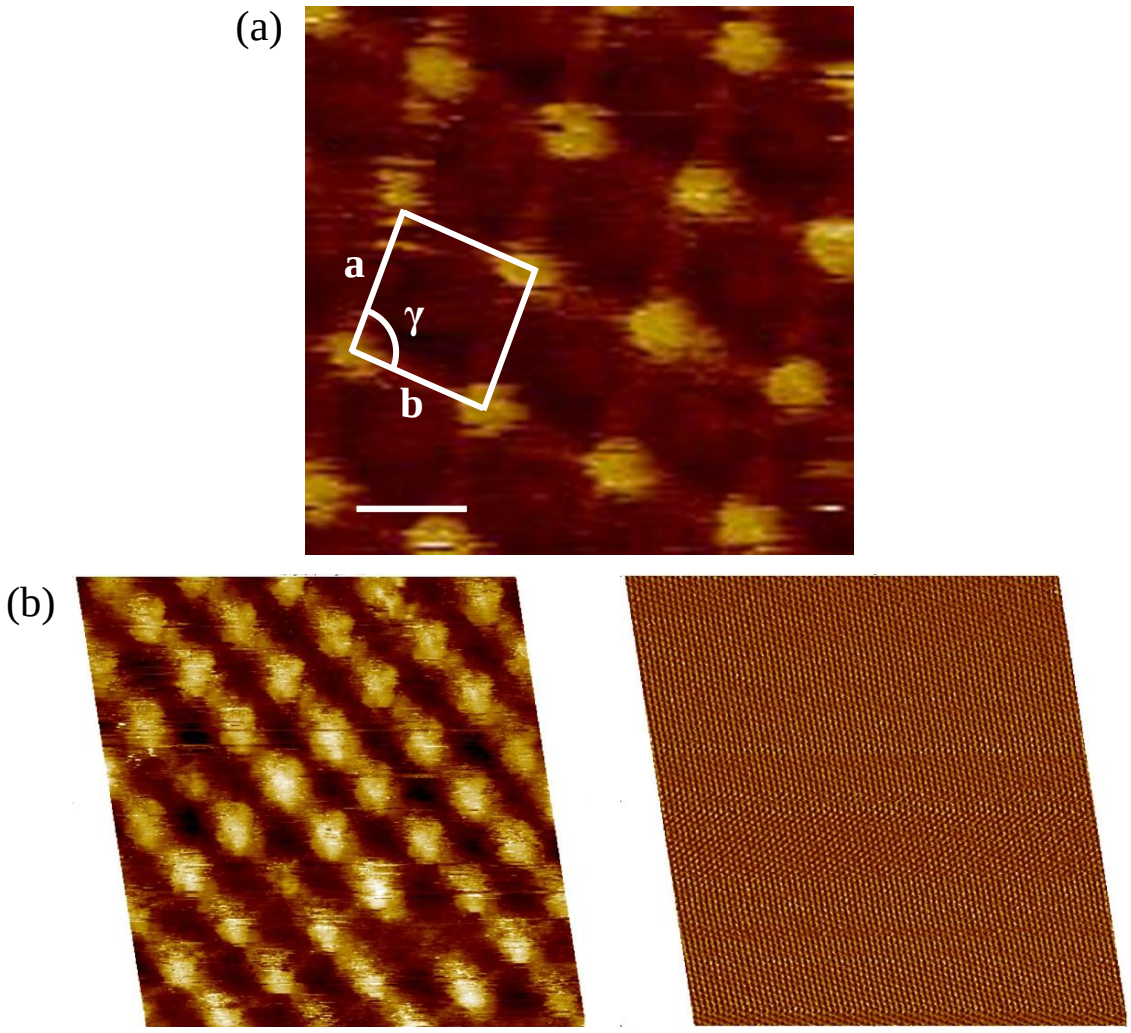

Figure 6.41. (a) Drift-corrected STM image of ZnTAPP/BDA 2D-COFs. Image size: 10 nm. Scale bar: 2 nm. STM scanning parameters: V_s = -0.5 V; I_t = 0.015 nA. (b) A pair of drift-corrected STM images of the ZnTAPP 2D-COFs stucture (left) and underlying HOPG lattice (right). STM imaging conditions: left: V_s = -0.55 V; I_t = 0.015 nA; right V_s = -0.02 V; I_t = 1 nA.

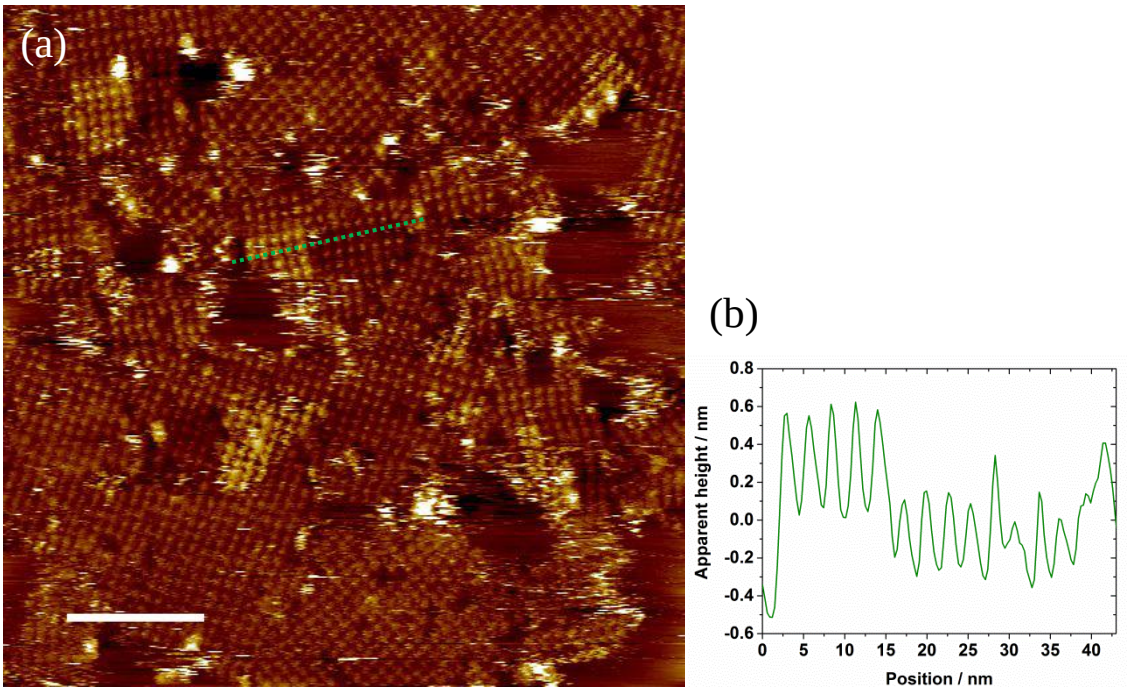

Figure 6.42. (a) STM image of ZnTAPP/BDA 2D-COFs demonstrating the formation of bi-layer 2D-COF structures. Sample preparation parameters: 0.15 g of $CuSO_4 \cdot 5H_2O$; 20 μl, 0.1 mg/ml. ZnTAPP in TCB; ~ 1 mg of BDA in solid; heating at 150 ℃ for 2h. STM imaging conditions: V_s = -0.55 V; I_t = 0.015 nA. (b) Line profile measuring the apparent heights of the bi-layer and mono-layer 2D-COFs.

In some STM images, for example, Figure 6.42 (a), the growth of bi-layer ZnTAPP 2D-COFs was observed. To measure the apparent heights of the bi-layer and mono-layer 2D-COFs, multiple line profiles (Figure 6.42 (b)) were taken to collect ten height values for each of the structures from the STM image shown in Figure 6.42 (a). The average and standard deviation of the ten height values were calculated to determine the average height and associated error of the bi-layer / mono-layer. As a result, the height of the bi-layer and mono-layer ZnTAPP/BDA 2D-COFs were measured to be 0.8 ± 0.2 nm and 0.4 ± 0.1 nm, respectively. The percentage of the bi-layer ZnTAPP 2D-COFs was much lower than that of the bi-layer TAPP 2D-COFs. This probably results from the lower diffusion ability of the Zn containing porphyrin molecules on the underlying ZnTAPP 2D-COFs.

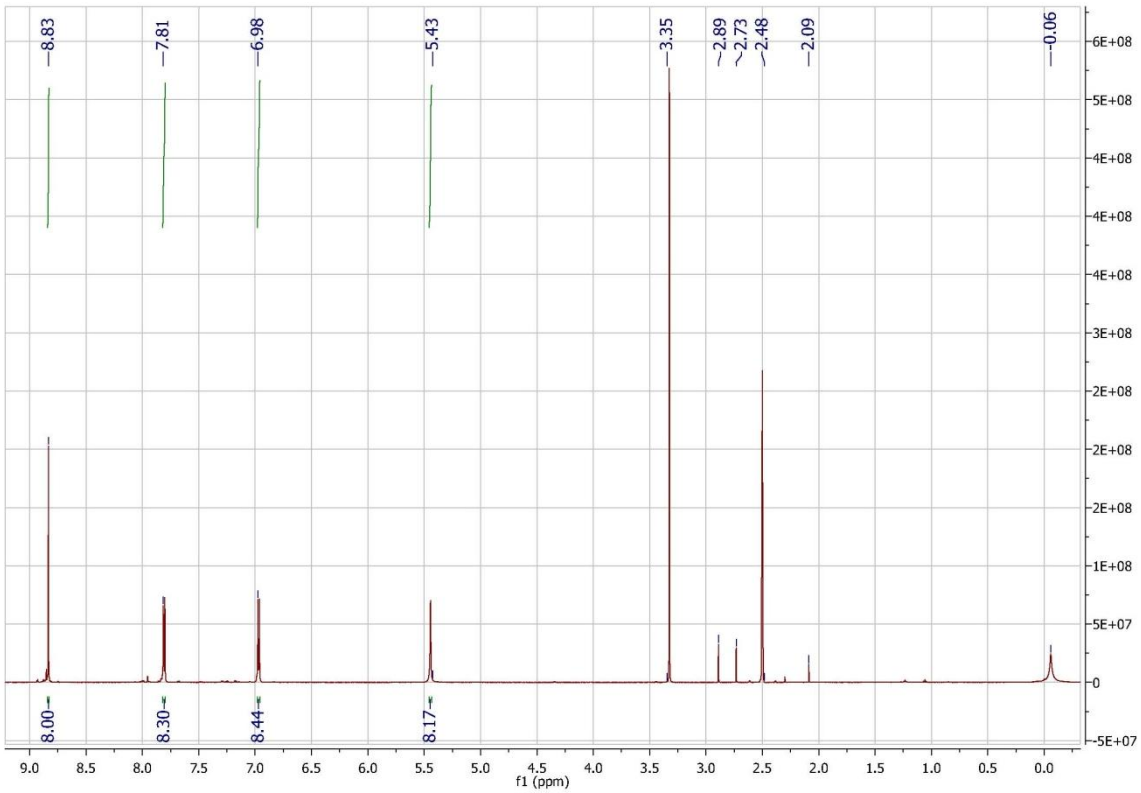

Figure 6.43. NMR spectrum of ZnTAPP run in deuterated DMSO.

The growth processes for the ZnTAPP 2D-COFs have so far not been reproducible. This is possibly related to the low purity of the ZnTAPP raw materials. Contamination present in the raw Zn-TAPP material may act as obstacles to the diffusion of ZnTAPP on the HOPG surface and prevent the formation of high quality 2D-COFs with large doamin sizes. Even after the use of the disposable syringe needles was stopped, significant silicon XPS signals could still be detected in the ZnTAPP molecular systems. From a synthetic point of view, the main source of silicon contamination would be from vacuum grease used to seal glassware joints. This source of contamination has been further confirmed by performing NMR analysis on the ZnTAPP powder used for 2D-COFs growth. Figure 6.43 presents the NMR spectrum of the ZnTAPP run in deuterated DMSO (collected by Niall Goodeal). The peak at – 0.06 corresponds to silicon grease. Therefore, efforts to synthesis ultra-pure porphyrin raw materials will play an important role in the future successful growth of ordered 2D-COF structures on surfaces.

During the synthesis of the ZnTAPP raw materials, more efforts need to be put into improving the purity of ZnTAPP by removing all silicon related contamination. Then the 2D-COFs growth conditions, such as temperature and the amounts of precursors, should be adjusted carefully to increase the coverage and domain sizes of the ZnTAPP 2D-COFs. Other volatile organic solvents in which ZnTAPP has a better solubility than toluene could also be investigated for the deposition of ZnTAPP.

AFM studies

The morphology of unreacted ZnTAPP films drop deposited onto HOPG from toluene solutions and the morphology ZnTAPP/BDA 2D-COFs grown from these deposited films were studied using Bruker Multimode8 AFM. As with TAPP 2D-COF samples, the homogeneity of the unreacted ZnTAPP films plays a significant role in determining the quality of the resulting 2D-COFs grown from them. STM and AFM measurements were performed on the samples after the 2D-COF growth process.

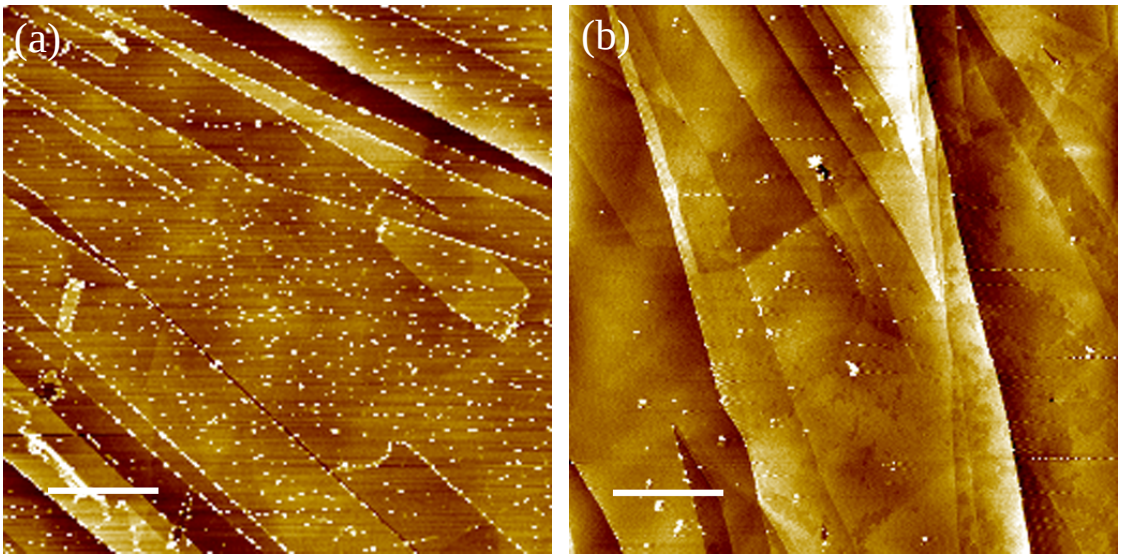

Figure 6.44. PeakForce tapping mode AFM images of HOPG surfaces with: (a) unreacted ZnTAPP by drop depositing 10 μl of 0.09 mg/ml toluene solutions; and (b) ZnTAPP 2D-COF grown on a template in (a). ZnTAPP/BDA 2D-COF growth conditions: 0.15 g of $CuSO_4$ $5H_2O$, 0.064 mg of BDA, 10 μl of 0.09 mg/ml ZnTAPP in toluene solutions, heating at 130 ℃ for 15 hours. Both image sizes: 10 μm. Both scale bars: 2 μm.

Figure 6.44 (a) shows the distribution of ZnTAPP on the HOPG surface following drop deposition of 10 µl of a 0.09 mg/ml ZnTAPP/toluene solution. ZnTAPP molecules exist as the bright 3D aggregates which locate along the step edges and on the terraces of the HOPG surface. By taking multiple line profiles through the 3D assemblies, the average height of the ZnTAPP aggregates was determined to be 5.0 ± 2.0 nm. The AFM image in Figure 6.44 (b) presents the ZnTAPP 2D-COF structures grown from the unreacted ZnTAPP film shown in Figure 6.44 (a). The sample was annealed at 130 ℃ for 15 hours with water and BDA in the vapour phase. The 2D-COF exhibits a high level of homogeneity as can been seen from the AFM scan in Figure 6.44 (b).

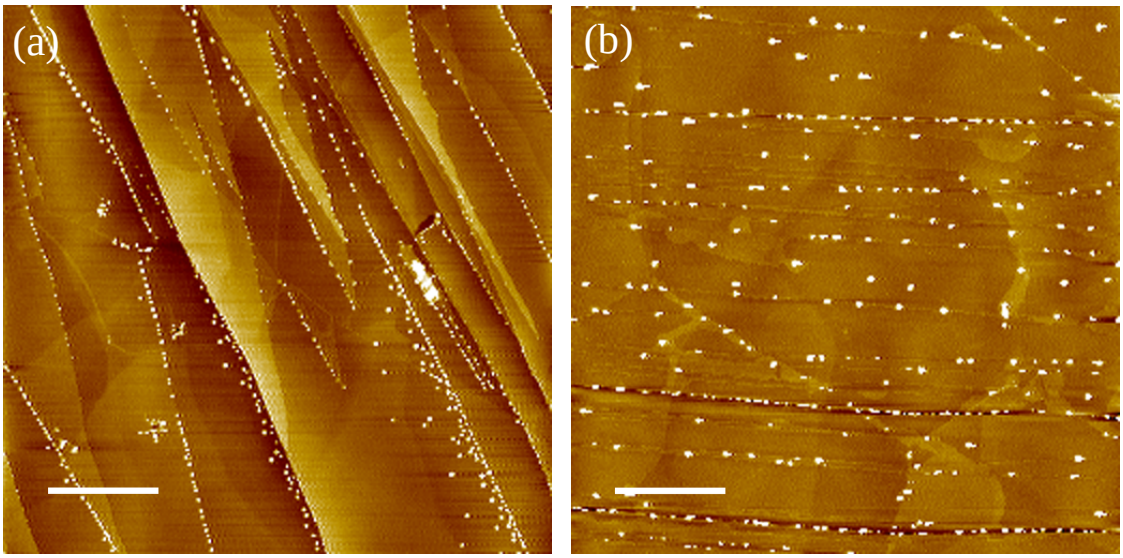

Figure 6.45. AFM images of HOPG surfaces with: (a) unreacted ZnTAPP by drop deposition of 5 µl of 0.005 mg/ml toluene solutions; and (b) ZnTAPP 2D-COFs grown using the template shown in (a). ZnTAPP/BDA 2D-COF growth conditions: 0.15 g of $CuSO_4$ $5H_2O$, 0.053 mg of BDA, 5 µl of 0.005 mg/ml ZnTAPP in toluene solutions, heating at 120 ℃ for 1 h 30 min. Both image sizes: 10 µm. Both scale bars: 2 µm.

If the amount of ZnTAPP drop deposited on HOPG is decreased to 5 µl of 0.005 mg/ml ZnTAPP/toluene solutions, the ZnTAPP molecules still exist as 3D aggregates with a preference to stack along the step edges as can been seen from the AFM image in Figure 6.45 (a). ZnTAPP 2D-COFs were grown on this unreacted ZnTAPP film by heating the substrate at 120 ℃ for 1.5 hours. The coverage of the ZnTAPP 2D-COF

formed via the Schiff-base condensation reaction was smaller compared with the result presented in Figure 6.44 (b). This difference is probably related to the differences in annealing temperature and time between the two experiments. The higher annealing temperature and longer time used in the case presented in Figure 6.44 would be more favourable for the growth of the ZnTAPP 2D-COFs by increasing the diffusion ability of ZnTAPP molecules on the HOPG surface. Apart from the annealing conditions, the decrease in the coverage of 2D-COFs in Figure 6.45 (b) could also be related to a lower amount of nucleation sites resulting from the decrease in the number of the 3D aggregates compared with the case shown in Figure 6.44.

6.4.2 Chemical structure of ZnTAPP/BDA 2D-COFs

The chemical nature of the covalent bonds formed between ZnTAPP and BDA via the Schiff-base condensation reaction was probed using XPS. While two different nitrogen species are present in a freebase porphyrin core [254], only a single nitrogen peak is detected in a metalloporphyrin core [255]. Details on the XPS experiments and criteria for XPS peak fitting can be found in sections 6.2.3 and 6.3.2. In a similar fashion to TAPP molecular system, nitrogen XPS signals were used to investigate the covalent bonding beween ZnTAPP and BDA.

Unreacted ZnTAPP control sample

ZnTAPP control samples were made by drop depositing 10 µl of a ZnTAPP/toluene solution with a concentration of 0.027 mg/ml. The sample was loaded into the XPS machine following complete evaporation of the solvent and without any further heating steps.

Figure 6.46 presents a series of XPS spectra for the ZnTAPP control sample, including: C1s, O1s, Zn2p signals and a survey scan of the full binding energy range. These XPS spectra were not used to analyse the chemical environment of the bonding formed after the Schiff-base condensation reactions, however, they do provide an

overview of the elemental species present in the system.

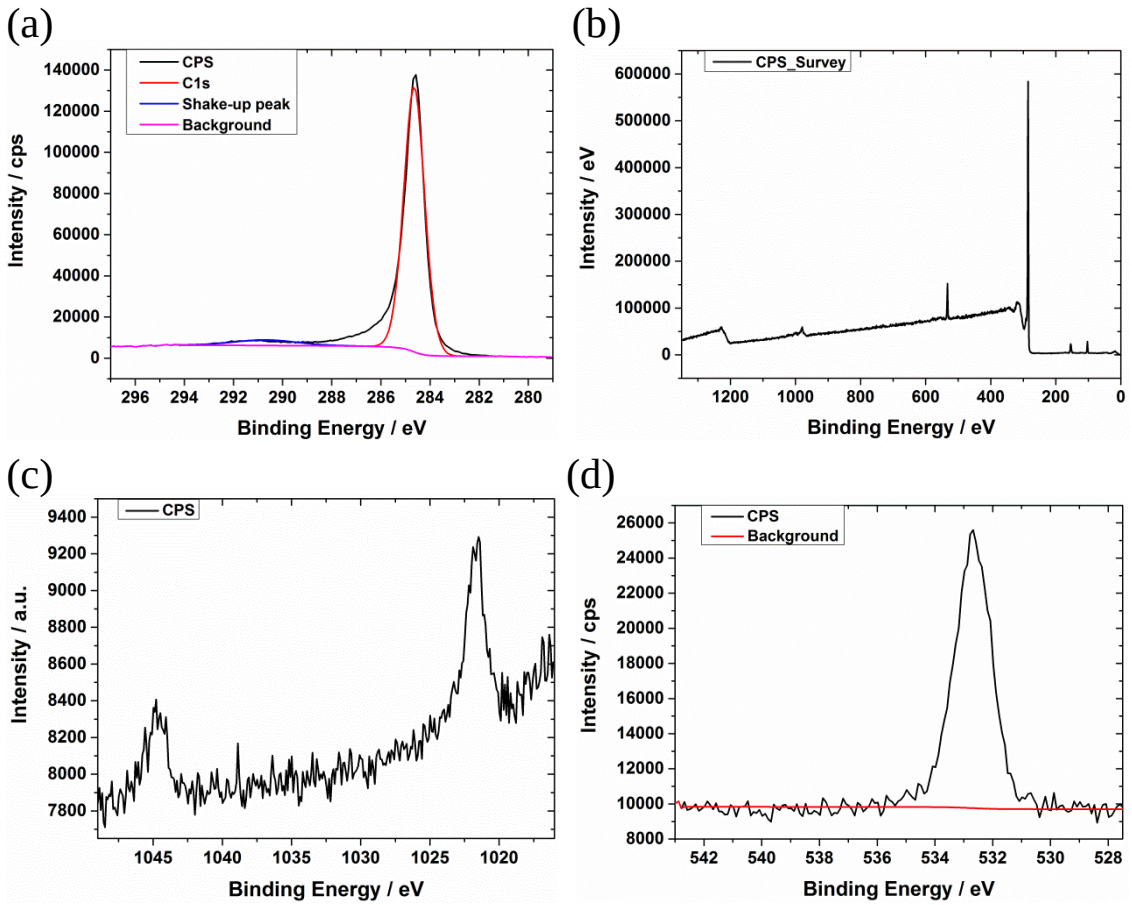

Figure 6.46. XPS spectra for the unreacted ZnTAPP control sample. (a) C1s XPS region with a Gaussian-Lorentzian peak at 284.6 ± 0.1 eV fitted to the spectrum; (b) survey scan; (c) Zn2p; and (d) O1s.

Figure 6.47 is an N1s XPS spectrum collected from an unreacted ZnTAPP control sample. This spectrum is an average taken from two areas on the same ZnTAPP control sample. Three nitrogen peaks are expected from this spectrum, including: one satellite peak; one nitrogen peak corresponding to the amine groups on the outer phenyl rings; and one nitrogen peak associated with the nitrogens coordinated to the central zinc atom in the porphyrin core. According to previous reports in literature, the binding energy of the nitrogen coordinated to the central zinc atom is 398.5 ± 0.3 eV [244, 247, 249]. The starting positions for the satellite peak and the nitrogen peak associated with unreacted amines were set to be 402 ± 0.5 eV and 399.5 ± 0.3 eV. The restraints for the FWHMs

of the peaks were the same as those used for fitting the XPS data for the freebase TAPP molecular system.

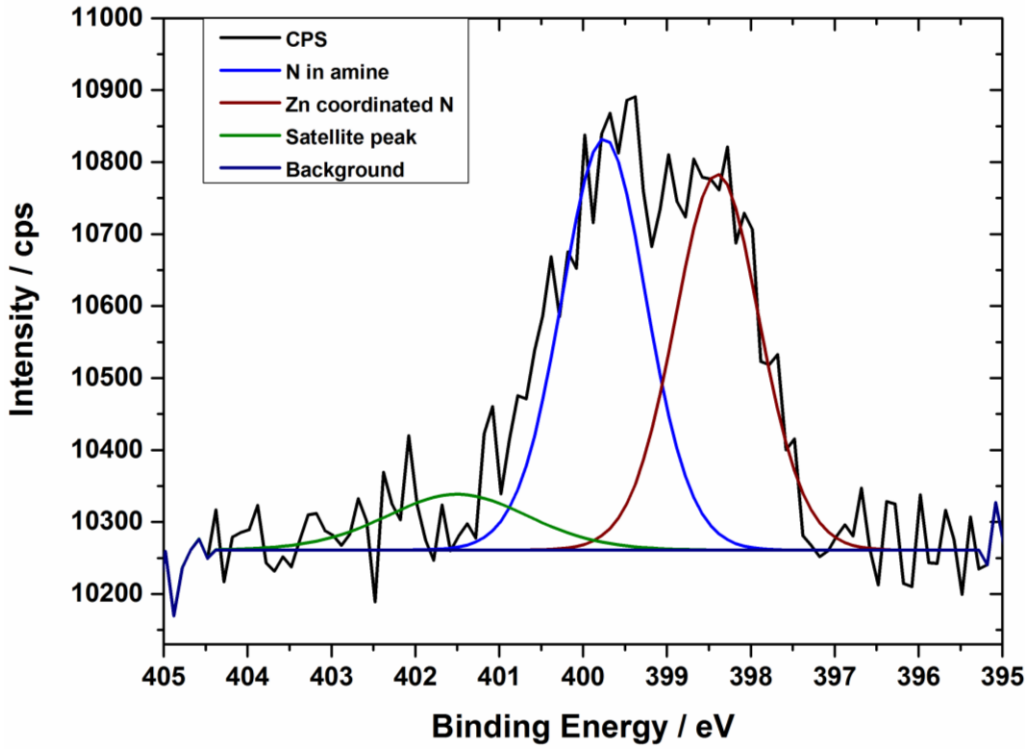

Figure 6.47. N1s XPS spectrum for the unreacted ZnTAPP control sample.

Peaks in XPS spectrum	Nitrogen species	Chemical formula	Binding energy in experiment (±0.1 eV)	Percentage of total fit area
—	Amine on phenyl ring	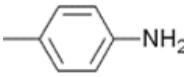	399.8	51.4 %
—	Nitrogen coordinated to zinc inside porphyrin core	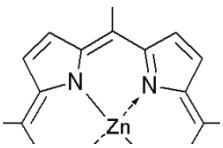	398.4	48.6 %
—	Satellite peak	----	401.5	----

Table 6.5. Summary of binding energies and percentage contributions of N1s peaks from the N1s spectrum of unreacted ZnTAPP.

Detailed information about the peak fitting to the N1s XPS spectrum in Figure 6.46 is summarised in Table 6.5. The percentage contribution of the two different nitrogen species in the ZnTAPP control sample to the total fit area was calculated after the area of the satellite peak was removed from the total fit area. The percentage contributions associated with the amine and zinc coordinated nitrogen were calculated to be 51.4 % and 48.6 %, respectively. The percentage contribution of the nitrogen species to the total fitted area is roughly equal, in good agreement with the expected the molecular structure of the unreacted ZnTAPP sample.

ZnTAPP /BDA 2D-COFs

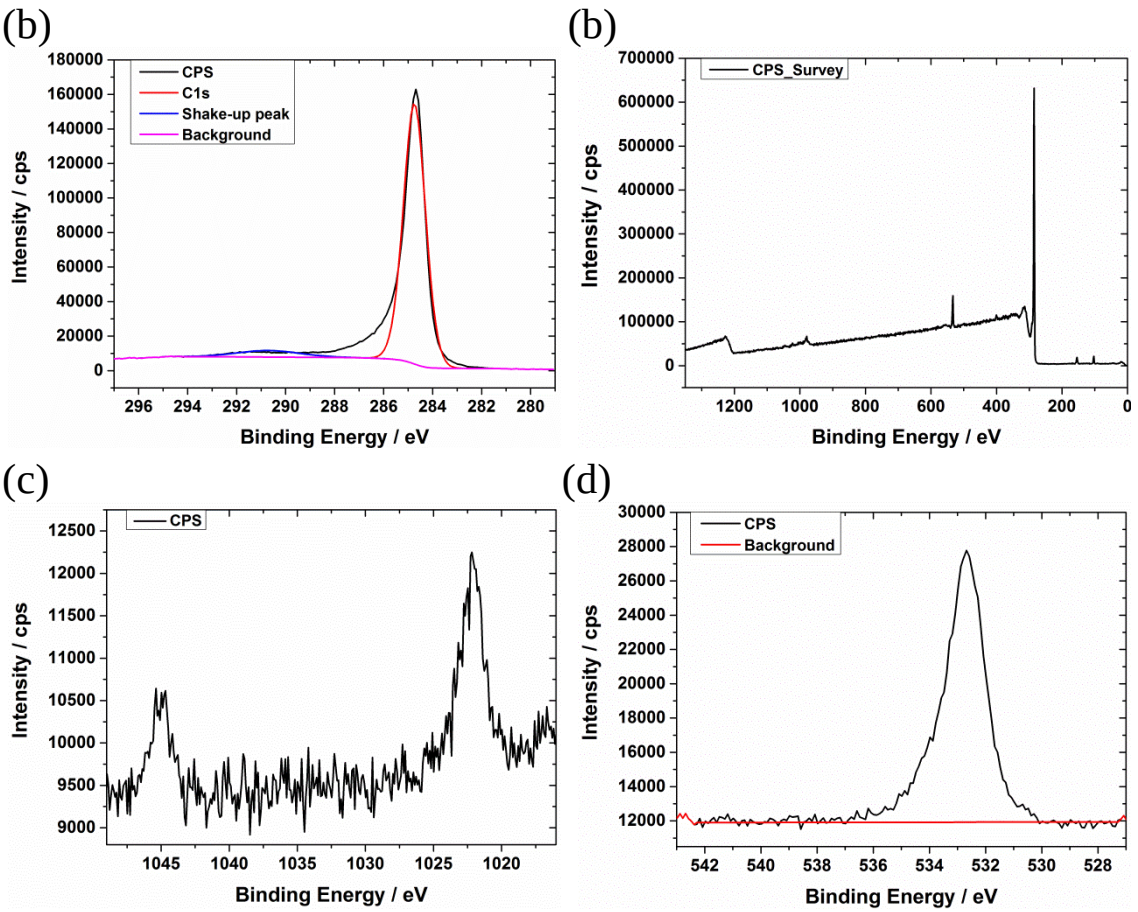

Figure 6.48. XPS spectra for the ZnTAPP/BDA 2D-COFs sample. (a) C1s, the binding energy of the main peak: 284.7 ± 0.1 eV; (b) survey scan; (c) Zn2p; and (d) O1s.

The growth conditions for the ZnTAPP/BDA 2D-COFs used in the XPS

investigation were as follows: 0.15 g of $CuSO_4 \cdot 5H_2O$; 10 μL of 0.09 mg/ml ZnTAPP/toluene solutions; 0.064 mg of BDA; heating at 130 ℃ for 15 hours. STM and AFM imaging was conducted on this sample to ensure the formation of the highly ordered ZnTAPP 2D-COFs over extended areas prior to XPS analysis.

Figure 6.48 presents C1s, Zn2p, O1s and survey scan XPS spectra on the ZnTAPP/BDA 2D-COFs sample. As the binding energy of the C1s peak is 284.7 ± 0.1 eV, the XPS spectra collected for the ZnTAPP 2D-COF can be compared with those for the unreacted ZnTAPP without further correction.

Figure 6.49 is an averaged, fitted N1s spectrum collected for the ZnTAPP/BDA 2D-COFs sample. Apart from the satellite peak, three nitrogen peaks were fitted for this spectrum. The binding energy of the N1s peaks for nitrogen coordinated to Zn and for nitrogen in an imine group are so similar that their individual contributions to the XPS spectrum cannot be separated [243]. The N1s peak located at the binding energy of 400.6 eV corresponds to hemiaminal links formed between ZnTAPP and BDA.

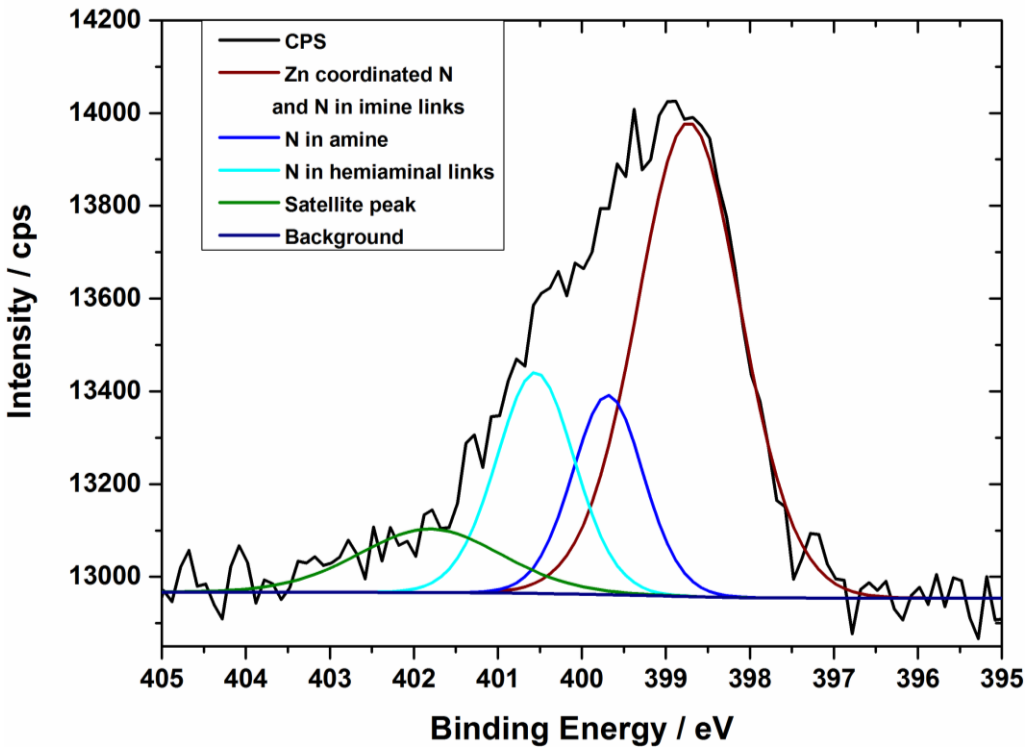

Figure 6.49. N1s XPS spectrum for the ZnTAPP/BDA 2D-COF sample.

The results of peak fitting for the N1s XPS spectrum of the ZnTAPP 2D-COFs are summarised in Table 6.6. In comparison to the N1s spectrum of unreacted ZnTAPP, the intensity of the peak associated with unreacted amine groups decreases significantly from 51.4 % to 17.6 % as the amine groups covert into imine and hemiaminal links. The percentage contribution of the nitrogen coordinated with zinc is assumed to be constant before and after 2D-COF growth as these atoms are not involved in the Schiff-base condensation reaction. The percentage contribution of the imine nitrogens is expected to be zero prior to the reaction taking place and is therefore estimated to increase to 12.4 % after the formation of the 2D-COF.

Peaks in XPS spectrum	Nitrogen species	Chemical formula	Binding energy in experiment (±0.1 eV)	Percentage of total fit area
—	Amine on phenyl ring	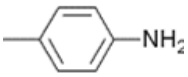	399.7	17.6 %
—	Nitrogen coordinated to zinc inside porphyrin core & Nitrogen in imine links	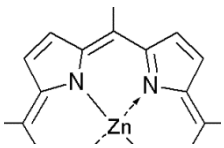 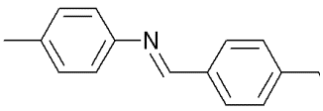	398.7	61.0 %
—	Nitrogen in hemiaminal links	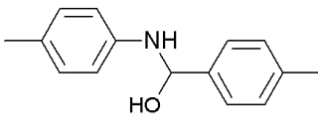	400.6	21.4 %
—	Satellite peak	----	401.8	----

Table 6.6. Peak fitting and interpretation of N1s XPS spectrum for ZnTAPP/BDA 2D-COF.

Compared with the TAPP/BDA 2D-COF, the covalent bonds formed between ZnTAPP and BDA exhibit a higher hemiaminal to imine ratio in the XPS N1s spectrum

shown in Figure 6.49. This is possibly related to the influence of the zinc atoms within porphyrin cores. However, this could also be related simply to statistical fluctuation in the amount of imine and hemiaminal linkages. Further experiments that investigate a larger number of samples are required in order to demostrate a clear correlation between the presence of zinc and the hemiaminal to imine ratio.

6.5 Conclusions

In conclusion, highly ordered 2D-COFs were grown on HOPG substrates using the Schiff-base condensation reaction between either 5,10,15,20-meso-tetra(4-aminophenyl) porphyrin (TAPP) or 5,10,15,20-meso-tetra(4-aminophenyl) porphyrin Zn(II) (Zn-TAPP) and benzene-1,4-dicarboxaldehyde (BDA). Through using the facile synthetic method described in the thesis, the domain sizes of the TAPP 2D-COFs formed can be larger than 100 nm by adjusting the experimental parameters. These parameters include: the amount of porphyrin components deposited on the HOPG surface; the pressure of water vapour released by copper sulphate; annealing temperature; and annealing time. In order to ensure the consistency and reproducibility of 2D-COFs growth processes, the supporting surfaces, solvents and the raw molecular materials should be free from contamination. Highly purified raw materials and contamination-free solution preparation schemes are required for a successful 2D-COF preparation process.

The exact morphological structures of the porphyrin/BDA 2D-COFs were determined using a combination of STM and AFM. The homogeneity of unreacted porphyrin films drop deposited onto surfaces is closely related to the structural quality and the domain size of the resulting 2D-COFs. in addition to mono-layer 2D-COFs, multi-layer porphyrin 2D-COFs grown on HOPG were also identified.

The chemical composition of the covalent bonds formed between the amine functionalised porphyrins and BDA was demonstrated by XPS to consist of a mixture of imine and hemiaminal groups. These variations in the chemical composition of the 2D-COFs were not discernible by SPM techniques. The water vapour released by $CuSO_4$ $5H_2O$ influences not only the morphology and structural order of 2D-COFs, but

also modifies the chemical composition of the bonds formed following the Schiff-base condensation reaction.

The above results relating to the growth, morphology and chemical composition of 2D-COFs will play a key role in advancing studies towards the design, and controllable growth of novel 2D-COF materials with tuneable stuctures and functional properties.

6.6 Future work

In the future, investigations are suggested in three major aspects: novel growth schemes for 2D-COF materials; improvements in the morphology of porphyrin 2D-COFs; and deeper insights into the chemical composition of Schiff-base 2D-COFs and how this is influenced by environmental conditions during growth.

In our study, AFM imaging has been conducted on HOPG surfaces covered with unreacted porphyrin films and grown 2D-COFs. The initial distribution of porphyrins on the HOPG surface following deposition has been found to play a major role in determining the quality of the resulting 2D-COFs. Therefore, it would be interesting to try and deposit porphyrin molecules onto surfaces using different depsition processes. These might include: thermal evaporation under UHV; and spin coating. Compared with drop deposition, spin coating would help produce a more homogeneous unreacted porphyrin film in preparation for 2D-COF growth. The ability of the Cypher AFM system to resolve the molecular structure of porphyrins in 2D-COFs also opens the possibility of using insulating or semi-conducting surfaces to grow 2D-COFs.

Based on previous studies of the morphology of 2D-COFs, more research can be conducted around the growth of multi-layer 2D-COFs and the composition of the 3D aggregates left on the surface after the growth process. More specifically, additional experiments need to be carried out in order to reveal how porphyrins in the upper layers of multi-layer structures stack on top of those in lower layers. Further experiments are also needed to discover the exact chemical composition of the 3D aggregates.

In terms of the chemical composition of the 2D-COFs, other complementary spectroscopic techniques are needed to resolve the formation of imine and hemiaminal

groups. One such technique with the ability to combine the spatial resolution of SPM with the chemical specificity of optical spectroscopy is tip-enhanced Raman Spectroscopy (TERS). Some experiments have been performed in an attempt to tune the ratio between imine and hemiaminal groups. Additionally, several other reaction conditions to grow the TAPP 2D-COFs have been investigated to convert more of the hemiaminal linkages into imine linkages. However, no persuasive results have yet been obtained. The numerous potential applications of porous porphyrin 2D-COFs make research into guest adsorption, post-synthesis functionalisation and chemical strengthening of the bonds formed via Schiff-base condensation reactions promising areas of study. One particular example that merit further study is an attempt to chemically modify the 2D-COF structure by reducing imine links to secondary amine links. Such a chemical modification could be attempted by exposing the gwon 2D-COF to a typical reducing agent such as sodium borohydride. Reduction of the imine linkages to secondary amine links would produce a 2D-COF structure with a greatly enhaned resistance to decomposition by hydrolysis, an important step to making the 2D-COF structures more widely applicable.

Chapter 7

Summary and future work

The synthesis and characterisation of two-dimensional (2D) organic molecular networks are in the interdisciplinary fields of surface physics and chemistry, molecular nanocience and 2D materials. These 2D molecular networks have potential applications in molecular electronics, chemical catalysis and sensors. The formation of highly ordered 2D molecular networks can be realised either by a non-covalent supramolecular self-assembly approach or by covalent on-surface synthesis of 2D covalent-organic frameworks (2D-COFs).

This PhD thesis has focused on studies of 2D self-assembled molecular networks and 2D-COFs grown on HOPG substrates. Three distinct molecular systems have been investigated using scanning probe microscopy (SPM), X-ray photoelectron spectroscopy (XPS) and molecular mechanics (MM) simulations. These results demonstrate the numerous factors that influence the formation of hydrogen bond stabilised 2D self-assembled molecular networks. Moving from non-covalent molecular networks to 2D-COFs, the results presented in this thesis demonstrate the pivotal importance of using coupled chemical and structural analysis to investigate how the chemical composition of 2D-COFs can be tuned by controlling the growth environment.

In chapter 4, the self-assembly of a tetra-carboxylic acid derivative, 5,5´-(anthracene-2,6-diyl) diisophthalic acid (ATC) was investigated at a liquid-solid interface. ATC molecules self-assemble into extended 2D molecular networks at the interface between heptanoic acid and HOPG. Three distinct self-assembled molecular arrangements were observed for ATC including: porous Kagomé, parallel and close-packed structures. Concentration variation experiments showed that the observed morphology of ATC 2D self-assembled networks exhibit a concentration dependency. The Kagomé structure dominates at the low concentrations, while the parallel and

close-packed structures dominate at higher concentrations. The co-assembly of ATC with a guest molecule, coronene, leads to the formation of a bi-component Kagomé structure. The chirality of the Kagomé structure was identified using STM images of the central anthracene backbone of the ATC molecule. This chirality arises from the prochiral nature of ATC which can adopt one of two different enantiomers upon adsorption to the HOPG surface. These results illustrate the possibility to utilise the self-assembly of ATC to gain a systematic understanding of morphology and chirality control over interfacial self-assembled molecular networks.

In chapter 5, the surface-based self-assembly behaviour of thymine functionalised porphyrins, including tetra-(phenylthymine)porphyrin (tetra-TP) and its metallated derivative, tetra-(phenylthymine)porphyrin-Zn(Ⅱ) (Zn-tetra-TP) was investigated. These molecules formed highly ordered 2D porphyrin arrays stabilised by thymine-thymine hydrogen bonding when deposited at a liquid-solid interface. In addition to mono-component porphyrin networks, both thymine functionalised porphyrins are also observed to co-crystallise with 9-propyladenine (PA) molecules to form an ordered bi-component molecular network. Freebase tetra-TP has also been shown to form a bi-component network with melamine. The formation of these homo-molecular and hetero-molecular networks demonstrate a novel strategy for the assembly of highly ordered porphyrin arrays on surfaces by utilising selective hydrogen bonding interactions between DNA nucleobase pairs.

Chapter 6 discussed the synthesis of highly ordered porphyrin 2D-COFs at the vapour-solid interface. Schiff-base condensation reactions between either 5,10,15,20-meso-tetra(4-aminophenyl) porphyrin (TAPP) or 5,10,15,20-meso-tetra(4-aminophenyl) porphyrin Zn(II) (Zn-TAPP) and benzene-1,4-dicarboxaldehyde (BDA) were used as a facile synthetic route to 2D-COF formation. The results presented here demonstrate the importance that the molecular system is free from any contamination in order to ensure the consistent growth of the 2D-COF layers. According to the results of AFM invesitgations, the morphology of the resulting 2D-COFs are closely related to the homogeneity of the deposited porphyrin films on the HOPG surface prior to 2D-COF growth. In addition to these morphological

studies, the chemical nature of the covalent bonds fromed between the amine functionalised porphyrins and BDA has been revealed to consist of both conjugated imine and non-conjugated hemiaminal bonds. This chemical composition is linked to the environmental conditions under which the 2D-COFs were synthesised. Our results highlight the importance of utilising complementary experimental tools to study both the morphology and chemical composition of 2D-COF materials.

In the future, more investigations are needed for each of these molecular systems. The interfacial self-assembly of ATC shows a dependency on the concentration of solutions deposited onto HOPG surfaces. In orded to illustrate exactly how self-assembled structures of ATC change with concentration, a more detailed range of concentration experiments is required to be carried out. As the ATC solutions were deposited on HOPG substrates at room temperature, kinetic effects will have a significant influence on the morpholgy of the resulting ATC network. The role that kinetic effects play in the self-assembly process of ATC needs to be further investigated by adding annealing and cooling steps to the network preparation. This temperature change would remove or minimise kinetic effects, and thus, promote the formation of self-assembled structures with minimum Gibbs free energy. Therefore, the 2D self-assembly of prochiral of ATC would be controlled by changing concentration and temperature. The results from these experiments would reveal new knowledge about the thermodynamic and kinetic factors that influence carboxylic acid drived 2D self-assembly. This would contribute to utilising ATC as another model molecular system to study guest adsorption and chirality selection for 2D self-assembly that occurs at the liquid-solid interfaces.

In comparison to carboxylic acid groups, the flexible and selective hydrogen bonding between DNA nucleobases has the potential to drive the self-assembly of 2D molecular networks with more structural diversity. This increase in complexity of possible morphological structures would offer a wider range of 2D molecular networks to explore the functional properties and performance in real applications. The study of the 2D self-assembly of the thymine functionalised porphyrins is expected to be expanded to include porphyrin molecules functionalised with other DNA nucleobases

such as adenine. The observation of chrial domains for the tetra-TP mono-component network and the tetra-TP and PA bi-component network suggests the possibility of controlling the chirality of these self-assembled structures. One possibility for achieving this chiral control would be the inclusion of a small quantity of an additional chiral component. This approach is similar to the *sergeants and soldiers* approach utilised by K.-H. Ernst *et al.* [256]. The self-assembly of Zn-tetra-TP can be potentially extended from mono-layers to bi-layers directed by the axial coodination bonding between pyridine and the central Zn atom. In order to form stable 2D Zn porphyrin arrays, the self-assembly of Zn-tetra-TP with a similar tetra adenine functionalised porphyrin species are suggested to be studied.

Of the three different molecular systems investigated in the thesis the porphyrin 2D-COFs offer the most potential for development and future applications. The additional chemical and environmental stability offered by covalent bonding makes 2D-COFs good candidates for numerous applications ranging from catalysis to molecular electronics. In relation to the fabrication of 2D-COFs, future work will be carried out to optimise the growth procedure, with a particular focus on improving the structural quality and domain size of the 2D-COFs. One of this first steps towards improving the structural quality of the 2D-COFs is to gain more control over the homogeneity of the initial porphyrin layer deposited on the surface prior to 2D-COF growth. Spin coating is a widely used industrial deposition technique that may be used as an alternative method to produce homogeneous porphyrin films. By increasing the structural quality and domain size of the 2D-COF materials, it is hoped that new materials properties inherent to the 2D materials that are linked to the level of structural order will start to emerge. In particular, the conjugated nature of imine bonds suggests the possibility of using 2D-COF fabrication methods to form new, fully conjugated 2D materials. Conjugation over large areas in these 2D materials will open up the possibility of using the 2D-COF layers as components in electronic devices such as sensors of field-effect transistors [257, 258].

One aspect that will be of fundamental interest is the formation of an electronic band structure for these 2D materials. As the size of ordered 2D-COF domains increases

then fully conjugated 2D-COF layers will start to develop a delocalised valence band structure that reflects the chemical composition and structural order of the material. Planned future collaborations include the use of experimental techniques that will allow us to probe the band structure of 2D materials with nanometre resolution. One such experimental tool is nanoscale angle resolved photoemission spectroscopy (Nano-ARPES) at the SOLEIL synchrotron in France [259]. Nano-ARPES measurements of the porphyrin 2D-COFs would help us to determine if the materials are conjugated and if so to what extent. Knowledge of the extent of the 2D-COF conjugation is particularly important for the future application of 2D-COFs. The XPS results presented in chapter 6 have shown that the Schiff-base condensation reaction produced a mixture conjugated imine and non-conjugated hemiaminal linkages between molecules. The ability to study the nanoscale electronic properties of the 2D-COFs may help to clarify where the imine and hemiaminal links reside within the 2D-COF structure and what influence this has on the material's electronic properties.

In addition to observing a mixture imine and hemiaminal linkages in the porphyrin 2D-COFs, the results in chapter 6 also demonstrated that the ratio of these two types of linkages can be influenced by the environmental conditions used during growth, particulary by the amount of water vapour present With this in mind, further studies are required to investigate exactly how different environmental conditions influence the composition and structural quality of the 2D-COFs: e.g. humidity, pressure, atmospheric composition and temperature. Developing a reproducible fabrication scheme that allows a more precise control over the chemical composition of the Schiff-base 2D-COFs is an important step for investigating how this composition influences the physical properties of 2D-COFs. This understanding of the link between structural and chemical composition and physical properties is pivotal for the future development of 2D-COFs for technological applications.

All of the 2D-COF layers investigated in this thesis were grown on HOPG substrates. The choice of HOPG as a supporting substrate is largely based on its inert nature, ease of preparation and high conductivity. These properties make HOPG an indeal substrate both for growing ordered 2D molecular networks and for investigating

their structure of these networks with SPM. However, the use of a conductive substrate leads to several limitations in the properties and further analysis of 2D-COFs. One major limitation being that a conductive supporting substrate prevents 2D-COFs being used for electronic device fabrication. Recent developments in high resolution ambient AFM have made it possible to extend molecular resolution SPM investigations of 2D-COFs to insulator and semiconductor surfaces. In particular, the growth of 2D-COF layers on transparent substrates would allow the optical properties of 2D-COF layers to be more easily investigated. There are close structural and chemical similarities between the porphyrins used in 2D-COF fabrication and the optically active bio-components in photosynthesis: e.g. chlorophyll [260]. Being able to grow ordered and possibly even complex porphyrin 2D-COF layers on transparent non-conductive substrates would make possible a wide array of optical spectroscopy experiments to study light induced energy transfer and charge separation in 2D molecular layers. Combining such experiments with the fine control over 2D-COF chemical and structural composition discussed above could open up new directions of research into optically functional 2D molecular nanostructures.

In the experiments presented here, multi-layer porphyrin 2D-COFs were observed to grow. However, the detailed stacking relationship between the top and bottom layers of the 2F-COFs have not yet been fully revealed. Additional experiments are needed to be carried out in order to illustrate how porphyrins in the upper layers of multi-layer structures stack on top of those in lower layers.

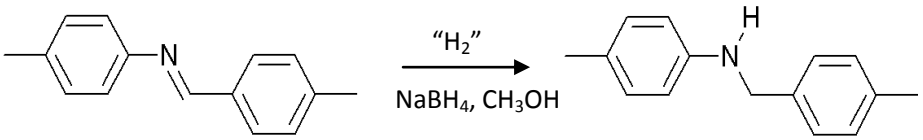

Figure 7.1. Schematic illustration showing the irreversible reduction of an imine linkage to a secondary amine linkage.

Finally, a significant area that warrants further investigation is the post growth chemical modification of porphyrin 2D-COF layers. One key example of this approach

would be the reduction of imine groups to secondary amines (Figure 7.1). This chemical conversion would produce covalent linkages between porphyrin molecules that are far more robust and in particular resilient to decomposition by hydrolysis. Another important approach to the modification of 2D-COF structures is the use of component moleucles that produce 2D-COFs decorated with functional groups which could then be used for further modification. An example of this is the use of dialdehyde linker molecules with diol functional groups (Figure 7.2). Once incorporated into a porphyin 2D-COF of the same morphology as presented in chapter 6, a suitably chosen molecule would leave the diol functional groups pointing into the pores of the 2D-COF network. These functional groups could then be used as reactive sites to attach other molecular species via the reaction between diol and boronic acid. This approach would provide a controllable way of adding functionality to the 2D-COF layers. This type of step by step molecular approach to the growth of complex 2D materials would open up a vast array of possibilities for the design and application of functional molecular nanostructures.

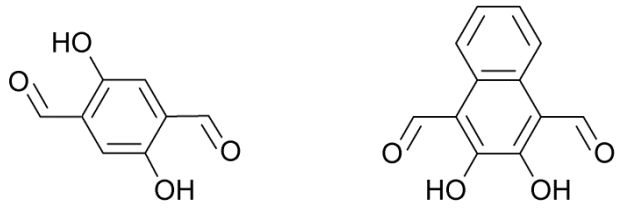

Figure 7.2 The molecular structure of newly designed dialdehyde linker molecules with diol functional groups for the synthesis of porphyrin 2D-COFs.

Bibliography

1. He, Y., T. Ye, M. Su, C. Zhang, A.E. Ribbe, W. Jiang, and C. Mao, Hierarchical self-assembly of DNA into symmetric supramolecular polyhedra. *Nature*, **2008**. 452(7184): p. 198-201.
2. Theobald, J.A., N.S. Oxtoby, M.A. Phillips, N.R. Champness, and P.H. Beton, Controlling molecular deposition and layer structure with supramolecular surface assemblies. *Nature*, **2003**. 424(6952): p. 1029-1031.
3. Madueno, R., M.T. Räsänen, C. Silien, and M. Buck, Functionalizing hydrogen-bonded surface networks with self-assembled monolayers. *Nature*, **2008**. 454(7204): p. 618-621.
4. Wei, X., W. Tong, V. Fidler, and M.B. Zimmt, Reactive capture of gold nanoparticles by strongly physisorbed monolayers on graphite. *Journal of colloid and interface science*, **2012**. 387(1): p. 221-227.
5. Richard, C., F. Balavoine, P. Schultz, T.W. Ebbesen, and C. Mioskowski, Supramolecular self-assembly of lipid derivatives on carbon nanotubes. *Science*, **2003**. 300(5620): p. 775-778.
6. Resendiz, M.J., J.C. Noveron, H. Disteldorf, S. Fischer, and P.J. Stang, A self-assembled supramolecular optical sensor for Ni (II), Cd (II), and Cr (III). *Organic letters*, **2004**. 6(5): p. 651-653.
7. dos Santos, C.M., A.J. Harte, S.J. Quinn, and T. Gunnlaugsson, Recent developments in the field of supramolecular lanthanide luminescent sensors and self-assemblies. *Coordination Chemistry Reviews*, **2008**. 252(23): p. 2512-2527.
8. Davis, J.T. and G.P. Spada, Supramolecular architectures generated by self-assembly of guanosine derivatives. *Chemical Society Reviews*, **2007**. 36(2): p. 296-313.
9. Lackinger, M. and W.M. Heckl, Carboxylic acids: Versatile building blocks and mediators for two-dimensional supramolecular self-assembly. *Langmuir*, **2009**. 25(19): p. 11307-11321.

10. Barth, J.V., G. Costantini, and K. Kern, Engineering atomic and molecular nanostructures at surfaces. *Nature*, **2005**. 437(7059): p. 671-679.

11. Mazur, U. and K.W. Hipps, Kinetic and thermodynamic processes of organic species at the solution-solid interface: the view through an STM. *Chemical Communications*, **2015**. 51(23): p. 4737-4749.

12. Voorhees, P.W., The theory of Ostwald ripening. *J. Stat. Phys.*, **1985**. 38(1-2): p. 231-252.

13. Gutzler, R., L. Cardenas, and F. Rosei, Kinetics and thermodynamics in surface-confined molecular self-assembly. *Chemical Science*, **2011**. 2(12): p. 2290-2300.

14. Wang, Y., M. Lingenfelder, S. Fabris, G. Fratesi, R. Ferrando, T. Classen, K. Kern, and G. Costantini, Programming Hierarchical Supramolecular Nanostructures by Molecular Design. *The Journal of Physical Chemistry C*, **2013**. 117(7): p. 3440-3445.

15. Rest, C., R. Kandanelli, and G. Fernández, Strategies to create hierarchical self-assembled structures via cooperative non-covalent interactions. *Chemical Society Reviews*, **2015**. 44(8): p. 2543-2572.

16. Neuheuser, T., B.A. Hess, C. Reutel, and E. Weber, Ab initio calculations of supramolecular recognition modes. Cyclic versus noncyclic hydrogen bonding in the formic acid/formamide system. *The Journal of Physical Chemistry*, **1994**. 98(26): p. 6459-6467.

17. Wang, C.-S., Y. Zhang, K. Gao, and Z.-Z. Yang, A new scheme for determining the intramolecular seven-membered ring NH... O= C hydrogen-bonding energies of glycine and alanine peptides. *The Journal of chemical physics*, **2005**. 123(2): p. 24307-24307.

18. Desiraju, G.R. and T. Steiner, *The weak hydrogen bond*. 1999, Oxford: Oxford University Press. 12-13.

19. Feyereisen, M.W., D. Feller, and D.A. Dixon, Hydrogen bond energy of the water dimer. *The Journal of Physical Chemistry*, **1996**. 100(8): p. 2993-2997.

20. Leiserowitz, L., Molecular packing modes. Carboxylic acids. *Acta*

Crystallographica Section B: Structural Crystallography and Crystal Chemistry, **1976**. 32(3): p. 775-802.

21. Lackinger, M., S. Griessl, W.M. Heckl, M. Hietschold, and G.W. Flynn, Self-Assembly of Trimesic Acid at the Liquid-Solid Interface a Study of Solvent-Induced Polymorphism. *Langmuir*, **2005**. 21(11): p. 4984-4988.
22. Yokoyama, S., T. Hirose, and K. Matsuda, Phototriggered formation and disappearance of surface-confined self-assembly composed of photochromic 2-thienyl-type diarylethene: a cooperative model at the liquid/solid interface. *Chemical Communications*, **2014**. 50(45): p. 5964-5966.
23. Ciesielski, A., M. El Garah, S. Masiero, and P. Samorì, Self‐assembly of Natural and Unnatural Nucleobases at Surfaces and Interfaces. *Small*, **2016**. 12(1): p. 83-95.
24. Bléger, D., A. Bocheux, D. Kreher, F. Mathevet, A.-J. Attias, G. Metgé, L. Douillard, C. Fiorini-Debuisschert, and F. Charra, An optimized alkyl chain-based binding motif for 2D self-assembly: a comprehensive crystallographic approach. *Nanoscale*, **2013**. 5(4): p. 1452-1455.
25. Gellman, A.J. and K.R. Paserba, Kinetics and Mechanism of Oligomer Desorption from Surfaces: n-Alkanes on Graphite. *The Journal of Physical Chemistry B*, **2002**. 106(51): p. 13231-13241.
26. Yin, S., C. Wang, X. Qiu, B. Xu, and C. Bai, Theoretical study of the effects of intermolecular interactions in self‐assembled long‐chain alkanes adsorbed on graphite surface. *Surf. Interface Anal.*, **2001**. 32(1): p. 248-252.
27. Grimme, S., Do special noncovalent π–π stacking interactions really exist? *Angew. Chem. Int. Ed.*, **2008**. 47(18): p. 3430-3434.
28. Mena‐Osteritz, E. and P. Bäuerle, Complexation of C60 on a cyclothiophene monolayer template. *Advanced Materials*, **2006**. 18(4): p. 447-451.
29. Claessens, C.G. and J.F. Stoddart, Review commentary–interactions in self-assembly. *J. Phys. Org. Chem.*, **1997**. 10: p. 254-272.
30. Zhu, J., Z. Dong, S. Lei, L. Cao, B. Yang, W. Li, Y. Zhang, J. Liu, and J. Shen, Design of Aromatic Helical Polymers for STM Visualization: Imaging of Single

and Double Helices with a Pattern of π–π Stacking. *Angew. Chem.*, **2015**. 127(10): p. 3140-3144.

31. Balandina, T., K. Tahara, N. Sändig, M.O. Blunt, J. Adisoejoso, S. Lei, F. Zerbetto, Y. Tobe, and S. De Feyter, Role of Substrate in Directing the Self-Assembly of Multicomponent Supramolecular Networks at the Liquid–Solid Interface. *ACS nano*, **2012**. 6(9): p. 8381-8389.
32. Park, K.-W., J. Adisoejoso, J. Plas, J. Hong, K. Müllen, and S. De Feyter, Self-Assembly Behavior of Alkylated Isophthalic Acids Revisited: Concentration in Control and Guest-Induced Phase Transformation. *Langmuir*, **2014**. 30(50): p. 15206-15211.
33. El Garah, M., A. Dianat, A. Cadeddu, R. Gutierrez, M. Cecchini, T.R. Cook, A. Ciesielski, P.J. Stang, G. Cuniberti, and P. Samorì, Atomically Precise Prediction of 2D Self‐Assembly of Weakly Bonded Nanostructures: STM Insight into Concentration‐Dependent Architectures. *Small*, **2016**. 12(3): p. 343-350.
34. Adisoejoso, J., K. Tahara, S. Lei, P. Szabelski, W. Rzysko, K. Inukai, M.O. Blunt, Y. Tobe, and S. De Feyter, One building block, two different nanoporous self-assembled monolayers: a combined STM and Monte Carlo study. *ACS nano*, **2011**. 6(1): p. 897-903.
35. Lei, S., K. Tahara, F.C. De Schryver, M. Van der Auweraer, Y. Tobe, and S. De Feyter, One Building Block, Two Different Supramolecular Surface‐Confined Patterns: Concentration in Control at the Solid–Liquid Interface. *Angew. Chem.*, **2008**. 120(16): p. 3006-3010.
36. Ikeda, T., M. Asakawa, K. Miyake, M. Goto, and T. Shimizu, Scanning tunneling microscopy observation of self-assembled monolayers of strapped porphyrins. *Langmuir*, **2008**. 24(22): p. 12877-12882.
37. Xu, L., X. Miao, B. Zha, and W. Deng, Self-Assembly Polymorphism: Solvent-Responsive Two-Dimensional Morphologies of 2,7-Ditridecyloxy-9-fluorenone by Scanning Tunneling Microscopy. *The Journal of Physical Chemistry C*, **2012**. 116(30): p. 16014-16022.
38. Sirtl, T., W. Song, G. Eder, S. Neogi, M. Schmittel, W.M. Heckl, and M.

Lackinger, Solvent-Dependent Stabilization of Metastable Monolayer Polymorphs at the Liquid–Solid Interface. *ACS Nano*, **2013**. 7(8): p. 6711-6718.

39. Gutzler, R., T. Sirtl, J.r.F. Dienstmaier, K. Mahata, W.M. Heckl, M. Schmittel, and M. Lackinger, Reversible Phase Transitions in Self-Assembled Monolayers at the Liquid− Solid Interface: Temperature-Controlled Opening and Closing of Nanopores. *Journal of the American Chemical Society*, **2010**. 132(14): p. 5084-5090.
40. Marie, C., F. Silly, L. Tortech, K. Müllen, and D. Fichou, Tuning the packing density of 2D supramolecular self-assemblies at the solid− liquid interface using variable temperature. *ACS nano*, **2010**. 4(3): p. 1288-1292.
41. Bhattarai, A., U. Mazur, and K. Hipps, A single molecule level study of the temperature-dependent kinetics for the formation of metal porphyrin monolayers on Au (111) from solution. *Journal of the American Chemical Society*, **2014**. 136(5): p. 2142-2148.
42. Griessl, S.J., M. Lackinger, F. Jamitzky, T. Markert, M. Hietschold, and W.M. Heckl, Incorporation and manipulation of coronene in an organic template structure. *Langmuir*, **2004**. 20(21): p. 9403-9407.
43. Schull, G., L. Douillard, C. Fiorini-Debuisschert, F. Charra, F. Mathevet, D. Kreher, and A.-J. Attias, Single-molecule dynamics in a self-assembled 2D molecular sieve. *Nano letters*, **2006**. 6(7): p. 1360-1363.
44. Lei, S., M. Surin, K. Tahara, J. Adisoejoso, R. Lazzaroni, Y. Tobe, and S.D. Feyter, Programmable hierarchical three-component 2D assembly at a liquid− solid interface: Recognition, selection, and transformation. *Nano letters*, **2008**. 8(8): p. 2541-2546.
45. Adisoejoso, J., K. Tahara, S. Okuhata, S. Lei, Y. Tobe, and S. De Feyter, Two‐Dimensional Crystal Engineering: A Four‐Component Architecture at a Liquid–Solid Interface. *Angew. Chem.*, **2009**. 121(40): p. 7489-7493.
46. Xiao, W., P. Ruffieux, K. Aït-Mansour, O. Gröning, K. Palotas, W.A. Hofer, P. Gröning, and R. Fasel, Formation of a Regular Fullerene Nanochain Lattice. *The Journal of Physical Chemistry B*, **2006**. 110(43): p. 21394-21398.

47. Wei, Y. and J.E. Reutt-Robey, Directed organization of C70 kagome lattice by titanyl phthalocyanine monolayer template. *Journal of the American Chemical Society*, **2011**. 133(39): p. 15232-15235.

48. Wang, Y., R. Yamachika, A. Wachowiak, M. Grobis, K. Khoo, D.-H. Lee, S.G. Louie, and M. Crommie, Novel Orientational Ordering and Reentrant Metallicity in K x C 60 Monolayers for 3≤ x≤ 5. *Physical review letters*, **2007**. 99(8): p. 086402.

49. Li, M., K. Deng, S.B. Lei, Y.L. Yang, T.S. Wang, Y.T. Shen, C.R. Wang, Q.D. Zeng, and C. Wang, Site‐Selective Fabrication of Two‐Dimensional Fullerene Arrays by Using a Supramolecular Template at the Liquid‐Solid Interface. *Angew. Chem.*, **2008**. 120(35): p. 6819-6823.

50. den Boer, D., G.D. Han, and T.M. Swager, Templating Fullerenes by Domain Boundaries of a Nanoporous Network. *Langmuir*, **2014**. 30(3): p. 762-767.

51. Blunt, M., X. Lin, M. del Carmen Gimenez-Lopez, M. Schröder, N.R. Champness, and P.H. Beton, Directing two-dimensional molecular crystallization using guest templates. *Chemical Communications*, **2008**(20): p. 2304-2306.

52. Blunt, M.O., J.C. Russell, M. del Carmen Gimenez-Lopez, N. Taleb, X. Lin, M. Schröder, N.R. Champness, and P.H. Beton, Guest-induced growth of a surface-based supramolecular bilayer. *Nature chemistry*, **2011**. 3(1): p. 74-78.

53. McFadden, C.F., P.S. Cremer, and A.J. Gellman, Adsorption of chiral alcohols on "chiral" metal surfaces. *Langmuir*, **1996**. 12(10): p. 2483-2487.

54. Ahmadi, A., G. Attard, J. Feliu, and A. Rodes, Surface reactivity at "chiral" platinum surfaces. *Langmuir*, **1999**. 15(7): p. 2420-2424.

55. Sun, K., T.N. Shao, J.L. Xie, M. Lan, H.K. Yuan, Z.H. Xiong, J.Z. Wang, Y. Liu, and Q.K. Xue, Chiral pinwheel clusters lacking local point chirality. *small*, **2012**. 8(13): p. 2078-2082.

56. Ernst, K.H., Molecular chirality at surfaces. *physica status solidi (b)*, **2012**. 249(11): p. 2057-2088.

57. Wei, Y., K. Kannappan, G.W. Flynn, and M.B. Zimmt, Scanning tunneling

microscopy of prochiral anthracene derivatives on graphite: chain length effects on monolayer morphology. *Journal of the American Chemical Society*, **2004**. 126(16): p. 5318-5322.

58. Katsonis, N., E. Lacaze, and B.L. Feringa, Molecular chirality at fluid/solid interfaces: expression of asymmetry in self-organised monolayers. *Journal of Materials Chemistry*, **2008**. 18(18): p. 2065-2073.
59. Blunt, M.O., J.C. Russell, N.R. Champness, and P.H. Beton, Templating molecular adsorption using a covalent organic framework. *Chemical Communications*, **2010**. 46(38): p. 7157-7159.
60. Grill, L., M. Dyer, L. Lafferentz, M. Persson, M.V. Peters, and S. Hecht, Nano-architectures by covalent assembly of molecular building blocks. *Nature nanotechnology*, **2007**. 2(11): p. 687-691.
61. Wen, J., D. Luo, L. Cheng, K. Zhao, and H. Ma, Electronic Structure Properties of Two-Dimensional π-Conjugated Polymers. *Macromolecules*, **2016**. 49(4): p. 1305-1312.
62. Adjizian, J.-J., P. Briddon, B. Humbert, J.-L. Duvail, P. Wagner, C. Adda, and C. Ewels, Dirac Cones in two-dimensional conjugated polymer networks. *Nature communications*, **2014**. 5.
63. Kissel, P., R. Erni, W.B. Schweizer, M.D. Rossell, B.T. King, T. Bauer, S. Götzinger, A.D. Schlüter, and J. Sakamoto, A two-dimensional polymer prepared by organic synthesis. *Nature chemistry*, **2012**. 4(4): p. 287-291.
64. Liu, X.-H., C.-Z. Guan, S.-Y. Ding, W. Wang, H.-J. Yan, D. Wang, and L.-J. Wan, On-surface synthesis of single-layered two-dimensional covalent organic frameworks via solid–vapor interface reactions. *Journal of the American Chemical Society*, **2013**. 135(28): p. 10470-10474.
65. Yaghi, O.M., M. O'Keeffe, N.W. Ockwig, H.K. Chae, M. Eddaoudi, and J. Kim, Reticular synthesis and the design of new materials. *Nature*, **2003**. 423(6941): p. 705-714.
66. Russell, J.C., M.O. Blunt, J.M. Garfitt, D.J. Scurr, M. Alexander, N.R. Champness, and P.H. Beton, Dimerization of Tri(4-bromophenyl)benzene by

Aryl−Aryl Coupling from Solution on a Gold Surface. *Journal of the American Chemical Society*, **2011**. 133(12): p. 4220-4223.

67. Eder, G., E.F. Smith, I. Cebula, W.M. Heckl, P.H. Beton, and M. Lackinger, Solution Preparation of Two-Dimensional Covalently Linked Networks by Polymerization of 1,3,5-Tri(4-iodophenyl)benzene on Au(111). *ACS Nano*, **2013**. 7(4): p. 3014-3021.
68. Cote, A.P., A.I. Benin, N.W. Ockwig, M. O'Keeffe, A.J. Matzger, and O.M. Yaghi, Porous, crystalline, covalent organic frameworks. *Science*, **2005**. 310(5751): p. 1166-1170.
69. Zwaneveld, N.A.A., R. Pawlak, M. Abel, D. Catalin, D. Gigmes, D. Bertin, and L. Porte, Organized Formation of 2D Extended Covalent Organic Frameworks at Surfaces. *Journal of the American Chemical Society*, **2008**. 130(21): p. 6678-6679.
70. Dienstmaier, J.r.F., A.M. Gigler, A.J. Goetz, P. Knochel, T. Bein, A. Lyapin, S. Reichlmaier, W.M. Heckl, and M. Lackinger, Synthesis of well-ordered COF monolayers: surface growth of nanocrystalline precursors versus direct on-surface polycondensation. *ACS nano*, **2011**. 5(12): p. 9737-9745.
71. Guan, C.-Z., D. Wang, and L.-J. Wan, Construction and repair of highly ordered 2D covalent networks by chemical equilibrium regulation. *Chemical Communications*, **2012**. 48(24): p. 2943-2945.
72. Weigelt, S., C. Busse, C. Bombis, M.M. Knudsen, K.V. Gothelf, T. Strunskus, C. Wöll, M. Dahlbom, B. Hammer, and E. Lægsgaard, Covalent interlinking of an aldehyde and an amine on a Au (111) surface in ultrahigh vacuum. *Angew. Chem.*, **2007**. 119(48): p. 9387-9390.
73. Tanoue, R., R. Higuchi, N. Enoki, Y. Miyasato, S. Uemura, N. Kimizuka, A.Z. Stieg, J.K. Gimzewski, and M. Kunitake, Thermodynamically Controlled Self-Assembly of Covalent Nanoarchitectures in Aqueous Solution. *ACS Nano*, **2011**. 5(5): p. 3923-3929.
74. Xu, L., X. Zhou, W.Q. Tian, T. Gao, Y.F. Zhang, S. Lei, and Z.F. Liu, Surface‐Confined Single‐Layer Covalent Organic Framework on

Single‐Layer Graphene Grown on Copper Foil. *Angew. Chem. Int. Ed.*, **2014**. 53(36): p. 9564-9568.

75. Xu, L., X. Zhou, Y. Yu, W.Q. Tian, J. Ma, and S. Lei, Surface-confined crystalline two-dimensional covalent organic frameworks via on-surface schiff-base coupling. *ACS nano*, **2013**. 7(9): p. 8066-8073.
76. Sun, X., L. Fan, X. Zhou, W.Q. Tian, Z. Guo, Z. Li, X. Li, and S. Lei, Surface confined synthesis of porphyrin containing two-dimensional polymers: the effect of rigidity and preferential adsorption of building blocks. *Chemical Communications*, **2015**. 51(27): p. 5864-5867.
77. Hu, Y., N. Goodeal, Y. Chen, A.M. Ganose, R.G. Palgrave, H. Bronstein, and M.O. Blunt, Probing the chemical structure of monolayer covalent-organic frameworks grown via Schiff-base condensation reactions. *Chemical Communications*, **2016**. 52(64): p. 9941-9944.
78. Dong, W.-L., S.-Y. Li, J.-Y. Yue, C. Wang, D. Wang, and L.-J. Wan, Fabrication of bilayer tetrathiafulvalene integrated surface covalent organic frameworks. *Physical Chemistry Chemical Physics*, **2016**. 18(26): p. 17356-17359.
79. Yue, J.-Y., X.-H. Liu, B. Sun, and D. Wang, The on-surface synthesis of imine-based covalent organic frameworks with non-aromatic linkage. *Chemical Communications*, **2015**. 51(76): p. 14318-14321.
80. Xu, L., L. Cao, Z. Guo, Z. Zha, and S. Lei, Side-functionalized two-dimensional polymers synthesized via on-surface Schiff-base coupling. *Chemical Communications*, **2015**. 51(41): p. 8664-8667.
81. Liu, X.-H., J.-Y. Yue, Y.-P. Mo, Y. Yao, C. Zeng, T. Chen, H.-J. Yan, Z.-H. Wang, D. Wang, and L.-J. Wan, Surface Host–Guest Supramolecular Assemblies on Porphyrin-Based Covalent Organic Grids. *The Journal of Physical Chemistry C*, **2016**.
82. Cui, D., J. MacLeod, M. Ebrahimi, D. Perepichka, and F. Rosei, Solution and air stable host/guest architectures from a single layer covalent organic framework. *Chemical Communications*, **2015**. 51(92): p. 16510-16513.
83. Zha, Z., L. Xu, Z. Wang, X. Li, Q. Pan, P. Hu, and S. Lei, 3D Graphene

Functionalized by Covalent Organic Framework Thin Film as Capacitive Electrode in Alkaline Media. *ACS applied materials & interfaces*, **2015**. 7(32): p. 17837-17843.

84. Binnig, G., H. Rohrer, C. Gerber, and E. Weibel, Surface studies by scanning tunneling microscopy. *Physical review letters*, **1982**. 49(1): p. 57.
85. Tománek, D., S.G. Louie, H.J. Mamin, D.W. Abraham, R.E. Thomson, E. Ganz, and J. Clarke, Theory and observation of highly asymmetric atomic structure in scanning-tunneling-microscopy images of graphite. *Physical Review B*, **1987**. 35(14): p. 7790.
86. Binnig, G. and H. Rohrer, Scanning tunneling microscopy—from birth to adolescence. *Rev. Mod. Phys.*, **1987**. 59(3): p. 615.
87. Salkola, M., A. Balatsky, and D. Scalapino, Theory of scanning tunneling microscopy probe of impurity states in a d-wave superconductor. *Physical review letters*, **1996**. 77(9): p. 1841.
88. Wiesendanger, R., *Scanning Probe Microscopy and Spectroscopy: Methods and Applications*. 1994, Cambridge: Cambridge University Press.
89. Chen, C.J., *Introduction to Scanning Tunneling Microscopy (Second Edition)*. 2008: Oxford University Press.
90. Bowker, M. and P.R. Davies, *Scanning Tunneling Microscopy in Surface Science, Nanoscience and Catalysis*. 2010, Wiley-VCH.
91. Tersoff, J. and D. Hamann, Theory and application for the scanning tunneling microscope. *Physical review letters*, **1983**. 50(25): p. 1998.
92. Tersoff, J. and D.R. Hamann, Theory of the scanning tunneling microscope. *Physical Review B*, **1985**. 31(2): p. 805-813.
93. Lang, N.D., Vacuum tunneling current from an adsorbed atom. *Physical Review Letters*, **1985**. 55(2): p. 230-233.
94. Lang, N.D., Theory of Single-Atom Imaging in the Scanning Tunneling Microscope. *Physical Review Letters*, **1986**. 56(11): p. 1164-1167.
95. Lang, N.D., Spectroscopy of single atoms in the scanning tunneling microscope. *Physical Review B*, **1986**. 34(8): p. 5947-5950.

96. *Scanning Tunneling Microscopy and Spectroscopy: Theory, Techniques, and Applications*, ed. D.A. Bonnell. 1993, New York: VCH Publisher, Inc.

97. Chen, C.J., Origin of atomic resolution on metal surfaces in scanning tunneling microscopy. *Physical Review Letters*, **1990**. 65(4): p. 448-451.

98. Fermi, E., Golden Rule. *Nucl. Phys.*, **1950**.

99. Bardeen, J., Tunnelling from a many-particle point of view. *Physical Review Letters*, **1961**. 6(2): p. 57.

100. Spong, J., H. Mizes, L. LaComb Jr, M. Dovek, J. Frommer, and J. Foster, Contrast mechanism for resolving organic molecules with tunnelling microscopy. *Nature*, **1989**. 338(6211): p. 137-139.

101. Miura, A., Z. Chen, H. Uji-i, S. De Feyter, M. Zdanowska, P. Jonkheijm, A.P. Schenning, E. Meijer, F. Würthner, and F.C. De Schryver, Bias-dependent visualization of electron donor (D) and electron acceptor (A) moieties in a chiral DAD triad molecule. *Journal of the American Chemical Society*, **2003**. 125(49): p. 14968-14969.

102. Lackinger, M., T. Müller, T. Gopakumar, F. Müller, M. Hietschold, and G.W. Flynn, Tunneling voltage polarity dependent submolecular contrast of naphthalocyanine on graphite. A STM study of close-packed monolayers under ultrahigh-vacuum conditions. *The Journal of Physical Chemistry B*, **2004**. 108(7): p. 2279-2284.

103. Fisher, A. and P. Blöchl, Adsorption and scanning-tunneling-microscope imaging of benzene on graphite and MoS 2. *Physical review letters*, **1993**. 70(21): p. 3263.

104. Hla, S.-W., Scanning tunneling microscopy single atom/molecule manipulation and its application to nanoscience and technology. *Journal of Vacuum Science & Technology B*, **2005**. 23(4): p. 1351-1360.

105. Gimzewski, J.K. and C. Joachim, Nanoscale science of single molecules using local probes. *Science*, **1999**. 283(5408): p. 1683-1688.

106. Eigler, D.M. and E.K. Schweizer, Positioning single atoms with a scanning tunnelling microscope. *Nature*, **1990**. 344(6266): p. 524-526.

107. Hla, S.-W., L. Bartels, G. Meyer, and K.-H. Rieder, Inducing All Steps of a Chemical Reaction with the Scanning Tunneling Microscope Tip: Towards Single Molecule Engineering. *Physical Review Letters*, **2000**. 85(13): p. 2777-2780.

108. Hulsken, B., R. Van Hameren, J.W. Gerritsen, T. Khoury, P. Thordarson, M.J. Crossley, A.E. Rowan, R.J. Nolte, J.A. Elemans, and S. Speller, Real-time single-molecule imaging of oxidation catalysis at a liquid–solid interface. *Nature nanotechnology*, **2007**. 2(5): p. 285-289.

109. Samorí, P., K. Müllen, and J.P. Rabe, Molecular‐Scale Tracking of the Self‐Healing of Polycrystalline Monolayers at the Solid–Liquid Interface. *Advanced Materials*, **2004**. 16(19): p. 1761-1765.

110. Griessl, S.J.H., M. Lackinger, F. Jamitzky, T. Markert, M. Hietschold, and W.M. Heckl, Room-Temperature Scanning Tunneling Microscopy Manipulation of Single C60 Molecules at the Liquid−Solid Interface: Playing Nanosoccer. *The Journal of Physical Chemistry B*, **2004**. 108(31): p. 11556-11560.

111. Surin, M., P. Samorì, A. Jouaiti, N. Kyritsakas, and M.W. Hosseini, Molecular tectonics on surfaces: Bottom‐up fabrication of 1D coordination networks that form 1D and 2D arrays on graphite. *Angew. Chem. Int. Ed.*, **2007**. 46(1‐2): p. 245-249.

112. El Garah, M., A. Ciesielski, N. Marets, V. Bulach, M.W. Hosseini, and P. Samorì, Molecular tectonics based nanopatterning of interfaces with 2D metal–organic frameworks (MOFs). *Chemical Communications*, **2014**. 50(82): p. 12250-12253.

113. Piot, L., R.M. Meudtner, T. El Malah, S. Hecht, and P. Samorì, Modulating Large‐Area Self‐Assembly at the Solid–Liquid Interface by pH‐Mediated Conformational Switching. *Chemistry–A European Journal*, **2009**. 15(19): p. 4788-4792.

114. Plas, J., O. Ivasenko, N. Martsinovich, M. Lackinger, and S. De Feyter, Nanopatterning of a covalent organic framework host–guest system. *Chemical Communications*, **2016**. 52(1): p. 68-71.

115. Nirmalraj, P., D. Thompson, A. Molina-Ontoria, M. Sousa, N. Martín, B.

Gotsmann, and H. Riel, Nanoelectrical analysis of single molecules and atomic-scale materials at the solid/liquid interface. *Nature materials*, **2014**. 13(10): p. 947-953.

116. *Agilent Technologies 5500 Scanning Probe Microscope: User's Guide*. Agilent Technologies.
117. *HOPG*. [cited 2016 7 June]; Available from: http://nanoprobes.aist-nt.com/apps/HOPG%20info.htm.
118. Tatar, R. and S. Rabii, Electronic properties of graphite: A unified theoretical study. *Physical Review B*, **1982**. 25(6): p. 4126.
119. So, A., U. Hvid, M. Mortensen, and K. Mo, Preparation of platinum/iridium scanning probe microscopy tips. *Rev. Sci. Instrum.*, **1999**. 70(7): p. 3059-3067.
120. Rogers, B., J. Shapter, W. Skinner, and K. Gascoigne, A method for production of cheap, reliable pt–ir tips. *Rev. Sci. Instrum.*, **2000**. 71(4): p. 1702-1705.
121. González, C., E. Abad, Y. Dappe, and J. Cuevas, Theoretical study of carbon-based tips for scanning tunnelling microscopy. *Nanotechnology*, **2016**. 27(10): p. 105201.
122. Grushko, V., O. Lübben, A. Chaika, N. Novikov, E. Mitskevich, A. Chepugov, O. Lysenko, B. Murphy, S. Krasnikov, and I. Shvets, Atomically resolved STM imaging with a diamond tip: simulation and experiment. *Nanotechnology*, **2013**. 25(2): p. 025706.
123. Ohmori, T., L. Nagahara, K. Hashimoto, and A. Fujishima, Characterization of carbon material as a scanning tunneling microscopy tip for insitu electrochemical studies. *Rev. Sci. Instrum.*, **1994**. 65(2): p. 404-406.
124. Castellanos-Gomez, A., N. Agraït, and G. Rubio-Bollinger, Carbon fibre tips for scanning probe microscopy based on quartz tuning fork force sensors. *Nanotechnology*, **2010**. 21(14): p. 145702.
125. Van de Walle, G., J. Gerritsen, H. Van Kempen, and P. Wyder, High‐stability scanning tunneling microscope. *Rev. Sci. Instrum.*, **1985**. 56(8): p. 1573-1576.
126. Simpson, A. and W. Wolfs, Thermal expansion and piezoelectric response of PZT Channel 5800 for use in low‐temperature scanning tunneling microscope

designs. *Rev. Sci. Instrum.*, **1987**. 58(11): p. 2193-2195.

127. Pohl, D.W., Some design criteria in scanning tunneling microscopy. *IBM J. Res. Dev.*, **1986**. 30(4): p. 417-427.

128. Yurov, V.Y. and A. Klimov, Scanning tunneling microscope calibration and reconstruction of real image: Drift and slope elimination. *Rev. Sci. Instrum.*, **1994**. 65(5): p. 1551-1557.

129. Kawakatsu, H., Y. Hoshi, T. Higuchi, and H. Kitano, Crystalline lattice for metrological applications and positioning control by a dual tunneling‐unit scanning tunneling microscope. *Journal of Vacuum Science & Technology B*, **1991**. 9(2): p. 651-654.

130. Van de Leemput, L., P. Rongen, B. Timmerman, and H. Van Kempen, Calibration and characterization of piezoelectric elements as used in scanning tunneling microscopy. *Rev. Sci. Instrum.*, **1991**. 62(4): p. 989-992.

131. Libioulle, L., A. Ronda, M. Taborelli, and J. Gilles, Deformations and nonlinearity in scanning tunneling microscope images. *Journal of Vacuum Science & Technology B*, **1991**. 9(2): p. 655-658.

132. Horcas, I., R. Fernández, J. Gomez-Rodriguez, J. Colchero, J. Gómez-Herrero, and A. Baro, WSXM: a software for scanning probe microscopy and a tool for nanotechnology. *Rev. Sci. Instrum.*, **2007**. 78(1): p. 013705.

133. Binnig, G., C.F. Quate, and C. Gerber, Atomic force microscope. *Physical review letters*, **1986**. 56(9): p. 930.

134. *Atomic Force Microscopy*. [cited 2016 8 June]; Available from: http://www.nanoscience.de/HTML/methods/afm.html.

135. Gross, L., F. Mohn, N. Moll, P. Liljeroth, and G. Meyer, The chemical structure of a molecule resolved by atomic force microscopy. *Science*, **2009**. 325(5944): p. 1110-1114.

136. Albrecht, T., P. Grütter, D. Horne, and D. Rugar, Frequency modulation detection using high‐Q cantilevers for enhanced force microscope sensitivity. *J. Appl. Phys.*, **1991**. 69(2): p. 668-673.

137. Gross, L., Recent advances in submolecular resolution with scanning probe

microscopy. *Nature chemistry*, **2011**. 3(4): p. 273-278.

138. Zhang, J., P. Chen, B. Yuan, W. Ji, Z. Cheng, and X. Qiu, Real-space identification of intermolecular bonding with atomic force microscopy. *Science*, **2013**. 342(6158): p. 611-614.

139. Kawai, S., A. Sadeghi, F. Xu, L. Peng, A. Orita, J. Otera, S. Goedecker, and E. Meyer, Extended Halogen Bonding between Fully Fluorinated Aromatic Molecules. *ACS Nano*, **2015**. 9(3): p. 2574-2583.

140. de Oteyza, D.G., P. Gorman, Y.-C. Chen, S. Wickenburg, A. Riss, D.J. Mowbray, G. Etkin, Z. Pedramrazi, H.-Z. Tsai, A. Rubio, M.F. Crommie, and F.R. Fischer, Direct Imaging of Covalent Bond Structure in Single-Molecule Chemical Reactions. *Science*, **2013**. 340(6139): p. 1434-1437.

141. Korolkov, V.V., S.A. Svatek, S. Allen, C.J. Roberts, S.J. Tendler, T. Taniguchi, K. Watanabe, N.R. Champness, and P.H. Beton, Bimolecular porous supramolecular networks deposited from solution on layered materials: graphite, boron nitride and molybdenum disulphide. *Chemical Communications*, **2014**. 50(64): p. 8882-8885.

142. Korolkov, V.V., S. Allen, C.J. Roberts, and S.J.B. Tendler, Green Chemistry Approach to Surface Decoration: Trimesic Acid Self-Assembly on HOPG. *The Journal of Physical Chemistry C*, **2012**. 116(21): p. 11519-11525.

143. Korolkov, V.V., N. Mullin, S. Allen, C.J. Roberts, J.K. Hobbs, and S.J.B. Tendler, The structure and formation of hydrogen-bonded molecular networks on Au(111) surfaces revealed by scanning tunnelling and torsional-tapping atomic force microscopy. *Physical Chemistry Chemical Physics*, **2012**. 14(45): p. 15909-15916.

144. *The Cypher™ Atomic Force Microscope*. [cited 2016 12 June]; Available from: http://www.asylumresearch.co.uk/Products/Cypher/CypherProduct.shtml#Introduction.

145. Stöckle, R.M., Y.D. Suh, V. Deckert, and R. Zenobi, Nanoscale chemical analysis by tip-enhanced Raman spectroscopy. *Chem. Phys. Lett.*, **2000**. 318(1):

p. 131-136.

146. Einstein, A., The photoelectric effect. *Ann. Phys*, **1905**. 17(132): p. 4.

147. *Key Features and Benefits of the K-Alpha+*. [cited 2016 13 June]; Available from: http://xpssimplified.com/kalpha_surface_analysis.php.

148. Hocquet, A. and M. Langgård, An evaluation of the MM+ force field. *Molecular modeling annual*, **1998**. 4(3): p. 94-112.

149. Wang, J., R.M. Wolf, J.W. Caldwell, P.A. Kollman, and D.A. Case, Development and testing of a general amber force field. *J. Comput. Chem.*, **2004**. 25(9): p. 1157-1174.

150. MacKerell, A.D., N. Banavali, and N. Foloppe, Development and current status of the CHARMM force field for nucleic acids. *Biopolymers*, **2000**. 56(4): p. 257-265.

151. Damm, W., A. Frontera, J. Tirado–Rives, and W.L. Jorgensen, OPLS all‐atom force field for carbohydrates. *J. Comput. Chem.*, **1997**. 18(16): p. 1955-1970.

152. *Force field (chemistry)* [cited 2016 16 June]; Available from: https://en.wikipedia.org/wiki/Force_field_(chemistry).

153. Barnard, R.A., A. Dutta, J.K. Schnobrich, C.N. Morrison, S. Ahn, and A.J. Matzger, Two‐Dimensional Crystals from Reduced Symmetry Analogues of Trimesic Acid. *Chemistry–A European Journal*, **2015**. 21(15): p. 5954-5961.

154. Ivasenko, O. and D.F. Perepichka, Mastering fundamentals of supramolecular design with carboxylic acids. Common lessons from X-ray crystallography and scanning tunneling microscopy. *Chemical Society Reviews*, **2011**. 40(1): p. 191-206.

155. Li, Z., B. Han, L.J. Wan, and T. Wandlowski, Supramolecular Nanostructures of 1,3,5-Benzene-tricarboxylic Acid at Electrified Au(111)/0.05 M H2SO4 Interfaces: An in Situ Scanning Tunneling Microscopy Study. *Langmuir*, **2005**. 21(15): p. 6915-6928.

156. Clair, S., S. Pons, A.P. Seitsonen, H. Brune, K. Kern, and J.V. Barth, STM Study of Terephthalic Acid Self-Assembly on Au(111): Hydrogen-Bonded Sheets on an Inhomogeneous Substrate. *The Journal of Physical Chemistry B*, **2004**.

108(38): p. 14585-14590.

157. De Marchi, F., D. Cui, J. Lipton-Duffin, C. Santato, J.M. MacLeod, and F. Rosei, Self-assembly of indole-2-carboxylic acid at graphite and gold surfaces. *The Journal of chemical physics*, **2015**. 142(10): p. 101923.

158. Lackinger, M., S. Griessl, T. Markert, F. Jamitzky, and W.M. Heckl, Self-assembly of benzene-dicarboxylic acid isomers at the liquid solid interface: Steric aspects of hydrogen bonding. *The Journal of Physical Chemistry B*, **2004**. 108(36): p. 13652-13655.

159. Schmitt, T., L. Hammer, and M.A. Schneider, Evidence for On-Site Carboxylation in the Self-Assembly of 4, 4′-Biphenyl Dicarboxylic Acid on Cu (111). *The Journal of Physical Chemistry C*, **2016**. 120(2): p. 1043-1048.

160. MacLeod, J.M., J.A. Lipton-Duffin, D. Cui, S. De Feyter, and F. Rosei, Substrate Effects in the Supramolecular Assembly of 1,3,5-Benzene Tricarboxylic Acid on Graphite and Graphene. *Langmuir*, **2015**. 31(25): p. 7016-7024.

161. MacLeod, J.M., Z. Ben Chaouch, D.F. Perepichka, and F. Rosei, Two-Dimensional Self-Assembly of a Symmetry-Reduced Tricarboxylic Acid. *Langmuir*, **2013**. 29(24): p. 7318-7324.

162. Aitchison, H., H. Lu, M. Zharnikov, and M. Buck, Monolayers of Biphenyl-3,4′,5-tricarboxylic Acid Formed on Cu and Ag from Solution. *The Journal of Physical Chemistry C*, **2015**. 119(25): p. 14114-14125.

163. Cebula, I., E.F. Smith, M.d.C. Gimenez-Lopez, S. Yang, M. Schröder, N.R. Champness, and P.H. Beton, Packing of isophthalate tetracarboxylic acids on Au (111): Rows and disordered herringbone structures. *The Journal of Physical Chemistry C*, **2013**. 117(36): p. 18381-18385.

164. Nguyen, D.C.Y., L. Smykalla, T.N.H. Nguyen, T. Rüffer, and M. Hietschold, Deposition Temperature-and Solvent-Dependent 2D Supramolecular Assemblies of Trimesic Acid at the Liquid-Graphite Interface Revealed by Scanning Tunneling Microscopy. *The Journal of Physical Chemistry C*, **2016**.

165. Zhou, H., H. Dang, J.-H. Yi, A. Nanci, A. Rochefort, and J.D. Wuest, Frustrated

2D Molecular Crystallization. *Journal of the American Chemical Society*, **2007**. 129(45): p. 13774-13775.

166. Blunt, M.O., J.C. Russell, M. del Carmen Giménez-López, J.P. Garrahan, X. Lin, M. Schröder, N.R. Champness, and P.H. Beton, Random tiling and topological defects in a two-dimensional molecular network. *Science*, **2008**. 322(5904): p. 1077-1081.

167. Zhang, S., J. Zhang, K. Deng, J. Xie, W. Duan, and Q. Zeng, Solution concentration controlled self-assembling structure with host-guest recognition at the liquid-solid interface. *Physical Chemistry Chemical Physics*, **2015**. 17(37): p. 24462-24467.

168. Yan, L., E.J. Bautista, and J.M. Seminario, Ab initio analysis of electron currents through benzene, naphthalene, and anthracene nanojunctions. *Nanotechnology*, **2007**. 18(48): p. 485701.

169. Cyr, D.M., B. Venkataraman, G.W. Flynn, A. Black, and G.M. Whitesides, Functional group identification in scanning tunneling microscopy of molecular adsorbates. *The Journal of Physical Chemistry*, **1996**. 100(32): p. 13747-13759.

170. Syôzi, I., Statistics of kagomé lattice. *理論物理学の進歩*, **1951**. 6(3): p. 306-308.

171. Mekata, M., Kagome: The story of the basketweave lattice. *Phys. Today*, **2003**. 56(2): p. 12.

172. Schlickum, U., R. Decker, F. Klappenberger, G. Zoppellaro, S. Klyatskaya, W. Auwarter, S. Neppl, K. Kern, H. Brune, and M. Ruben, Chiral kagomé lattice from simple ditopic molecular bricks. *Journal of the American Chemical Society*, **2008**. 130(35): p. 11778-11782.

173. Furukawa, S., H. Uji-i, K. Tahara, T. Ichikawa, M. Sonoda, F.C. De Schryver, Y. Tobe, and S. De Feyter, Molecular geometry directed kagomé and honeycomb networks: toward two-dimensional crystal engineering. *Journal of the American Chemical Society*, **2006**. 128(11): p. 3502-3503.

174. Shi, Z. and N. Lin, Porphyrin-based two-dimensional coordination Kagome lattice self-assembled on a Au (111) surface. *Journal of the American Chemical*

Society, **2009**. 131(15): p. 5376-5377.

175. Watson, J.D. and F.H. Crick, Molecular structure of nucleic acids. *Nature*, **1953**. 171(4356): p. 737-738.

176. Hoogsteen, K., The structure of crystals containing a hydrogen-bonded complex of 1-methylthymine and 9-methyladenine. *Acta crystallographica*, **1959**. 12(10): p. 822-823.

177. Sessler, J.L., C.M. Lawrence, and J. Jayawickramarajah, Molecular recognition via base-pairing. *Chemical Society Reviews*, **2007**. 36(2): p. 314-325.

178. Sivakova, S. and S.J. Rowan, Nucleobases as supramolecular motifs. *Chemical Society Reviews*, **2005**. 34(1): p. 9-21.

179. Papageorgiou, A.C., S. Fischer, J. Reichert, K. Diller, F. Blobner, F. Klappenberger, F. Allegretti, A.P. Seitsonen, and J.V. Barth, Chemical Transformations Drive Complex Self-Assembly of Uracil on Close-Packed Coinage Metal Surfaces. *ACS Nano*, **2012**. 6(3): p. 2477-2486.

180. Ciesielski, A., S. Haar, A. Bényei, G. Paragi, C.F. Guerra, F.M. Bickelhaupt, S. Masiero, J. Szolomájer, P. Samorì, G.P. Spada, and L. Kovács, Self-Assembly of N3-Substituted Xanthines in the Solid State and at the Solid–Liquid Interface. *Langmuir*, **2013**. 29(24): p. 7283-7290.

181. Ciesielski, A., S. Colella, L. Zalewski, B. Bruchmann, and P. Samorì, Nanopatterning the graphite surface with ordered macrocyclic or ribbon-like assemblies of isocytosine derivatives: an STM study. *CrystEngComm*, **2011**. 13(18): p. 5535-5537.

182. Liu, L., D. Xia, L.H. Klausen, and M. Dong, The self-assembled behavior of DNA bases on the interface. *International journal of molecular sciences*, **2014**. 15(2): p. 1901-1914.

183. Mamdouh, W., M. Dong, S. Xu, E. Rauls, and F. Besenbacher, Supramolecular nanopatterns self-assembled by adenine-thymine quartets at the liquid/solid interface. *Journal of the American Chemical Society*, **2006**. 128(40): p. 13305-13311.

184. Auwärter, W., D. Écija, F. Klappenberger, and J.V. Barth, Porphyrins at

interfaces. *Nature chemistry*, **2015**. 7(2): p. 105-120.

185. Gottfried, J.M., Surface chemistry of porphyrins and phthalocyanines. *Surf. Sci. Rep.*, **2015**. 70(3): p. 259-379.

186. Krasnikov, S.A., C.M. Doyle, N.N. Sergeeva, A.B. Preobrajenski, N.A. Vinogradov, Y.N. Sergeeva, A.A. Zakharov, M.O. Senge, and A.A. Cafolla, Formation of extended covalently bonded Ni porphyrin networks on the Au (111) surface. *Nano Research*, **2011**. 4(4): p. 376-384.

187. Lei, S., C. Wang, S. Yin, H. Wang, F. Xi, H. Liu, B. Xu, L. Wan, and C. Bai, Surface stabilized porphyrin and phthalocyanine two-dimensional network connected by hydrogen bonds. *The Journal of Physical Chemistry B*, **2001**. 105(44): p. 10838-10841.

188. Otsuki, J., E. Nagamine, T. Kondo, K. Iwasaki, M. Asakawa, and K. Miyake, Surface patterning with two-dimensional porphyrin supramolecular arrays. *Journal of the American Chemical Society*, **2005**. 127(29): p. 10400-10405.

189. Auwärter, W., A. Weber-Bargioni, A. Riemann, A. Schiffrin, O. Gröning, R. Fasel, and J. Barth, Self-assembly and conformation of tetrapyridyl-porphyrin molecules on Ag (111). *The Journal of chemical physics*, **2006**. 124(19): p. 194708.

190. Auwärter, W., F. Klappenberger, A. Weber-Bargioni, A. Schiffrin, T. Strunskus, C. Wöll, Y. Pennec, A. Riemann, and J.V. Barth, Conformational adaptation and selective adatom capturing of tetrapyridyl-porphyrin molecules on a copper (111) surface. *Journal of the American Chemical Society*, **2007**. 129(36): p. 11279-11285.

191. Yoshimoto, S., N. Yokoo, T. Fukuda, N. Kobayashi, and K. Itaya, Formation of highly ordered porphyrin adlayers induced by electrochemical potential modulation. *Chemical Communications*, **2006**(5): p. 500-502.

192. Yuan, Q., Y. Xing, and E. Borguet, An STM Study of the pH Dependent Redox Activity of a Two-Dimensional Hydrogen Bonding Porphyrin Network at an Electrochemical Interface. *Journal of the American Chemical Society*, **2010**. 132(14): p. 5054-5060.

193. Slater, A.G., Y. Hu, L. Yang, S.P. Argent, W. Lewis, M.O. Blunt, and N.R. Champness, Thymine functionalised porphyrins, synthesis and heteromolecular surface-based self-assembly. *Chemical Science*, **2015**. 6(2): p. 1562-1569.

194. Lai, S.-W., M.C. Chan, K.-K. Cheung, and C.-M. Che, Spectroscopic Properties of Luminescent Platinum (II) Complexes Containing 4, 4', 4"-Tri-tert-butyl-2, 2': 6', 2"-terpyridine (tBu3tpy). Crystal Structures of [Pt (tBu3tpy) Cl] ClO4 and [Pt (tBu3tpy){CH2C (O) Me}] ClO4. *Inorganic Chemistry*, **1999**. 38(19): p. 4262-4267.

195. Radivojevic, I., I. Likhtina, X. Shi, S. Singh, and C.M. Drain, Self-organized nanofibers and nanorods of porphyrins bearing hydrogen bonding motifs. *Chemical Communications*, **2010**. 46(10): p. 1643-1645.

196. Nowell, H., S.A. Barnett, K.E. Christensen, S.J. Teat, and D.R. Allan, I19, the small-molecule single-crystal diffraction beamline at Diamond Light Source. *Journal of synchrotron radiation*, **2012**. 19(3): p. 435-441.

197. Etter, M.C., Encoding and decoding hydrogen-bond patterns of organic compounds. *Accounts of Chemical Research*, **1990**. 23(4): p. 120-126.

198. Hoogsteen, K.R., The crystal and molecular structure of a hydrogen-bonded complex between 1-methylthymine and 9-methyladenine. *Acta Crystallographica*, **1963**. 16(9): p. 907-916.

199. Mohnani, S. and D. Bonifazi, Supramolecular architectures of porphyrins on surfaces: The structural evolution from 1D to 2D to 3D to devices. *Coordination Chemistry Reviews*, **2010**. 254(19): p. 2342-2362.

200. Elemans, J.A.A.W., I. De Cat, H. Xu, and S. De Feyter, Two-dimensional chirality at liquid-solid interfaces. *Chemical Society Reviews*, **2009**. 38(3): p. 722-736.

201. Écija, D., K. Seufert, D. Heim, W. Auwärter, C. Aurisicchio, C. Fabbro, D. Bonifazi, and J.V. Barth, Hierarchic Self-Assembly of Nanoporous Chiral Networks with Conformationally Flexible Porphyrins. *ACS Nano*, **2010**. 4(8): p. 4936-4942.

202. Ai, K., Y. Liu, and L. Lu, Hydrogen-bonding recognition-induced color change

of gold nanoparticles for visual detection of melamine in raw milk and infant formula. *Journal of the American Chemical Society*, **2009**. 131(27): p. 9496-9497.

203. Palma, C.-A., J. Bjork, M. Bonini, M.S. Dyer, A. Llanes-Pallas, D. Bonifazi, M. Persson, and P. Samorì, Tailoring bicomponent supramolecular nanoporous networks: phase segregation, polymorphism, and glasses at the solid− liquid interface. *Journal of the American Chemical Society*, **2009**. 131(36): p. 13062-13071.

204. Mura, M., N. Martsinovich, and L. Kantorovich, Theoretical study of melamine superstructures and their interaction with the Au (111) surface. *Nanotechnology*, **2008**. 19(46): p. 465704.

205. Silly, F., A.Q. Shaw, M.R. Castell, G.A.D. Briggs, M. Mura, N. Martsinovich, and L. Kantorovich, Melamine Structures on the Au(111) Surface. *The Journal of Physical Chemistry C*, **2008**. 112(30): p. 11476-11480.

206. Zhang, H.-M., Z.-X. Xie, L.-S. Long, H.-P. Zhong, W. Zhao, B.-W. Mao, X. Xu, and L.-S. Zheng, One-step preparation of large-scale self-assembled monolayers of cyanuric acid and melamine supramolecular species on Au (111) surfaces. *The Journal of Physical Chemistry C*, **2008**. 112(11): p. 4209-4218.

207. Xu, W., M. Dong, H. Gersen, E. Rauls, S. Vázquez‐Campos, M. Crego‐Calama, D.N. Reinhoudt, I. Stensgaard, E. Laegsgaard, and T.R. Linderoth, Cyanuric Acid and Melamine on Au (111): Structure and Energetics of Hydrogen‐Bonded Networks. *small*, **2007**. 3(5): p. 854-858.

208. Zhang, X., T. Chen, Q. Chen, L. Wang, and L.-J. Wan, Self-assembly and aggregation of melamine and melamine–uric/cyanuric acid investigated by STM and AFM on solid surfaces. *Physical Chemistry chemical physics*, **2009**. 11(35): p. 7708-7712.

209. Elemans, J.A., M.C. Lensen, J.W. Gerritsen, H. van Kempen, S. Speller, R.J. Nolte, and A.E. Rowan, Scanning probe studies of porphyrin assemblies and their supramolecular manipulation at a solid–liquid interface. *Advanced Materials*, **2003**. 15(24): p. 2070-2073.

210. Lensen, M.C., J.A. Elemans, S.J. van Dingenen, J.W. Gerritsen, S. Speller, A.E. Rowan, and R.J. Nolte, Giant Porphyrin Disks: Control of Their Self‐Assembly at Liquid–Solid Interfaces through Metal–Ligand Interactions. *Chemistry–A European Journal*, **2007**. 13(28): p. 7948-7956.

211. Yoshimoto, S., Y. Honda, O. Ito, and K. Itaya, Supramolecular Pattern of Fullerene on 2D Bimolecular "Chessboard" Consisting of Bottom-up Assembly of Porphyrin and Phthalocyanine Molecules. *Journal of the American Chemical Society*, **2008**. 130(3): p. 1085-1092.

212. Buchner, F., V. Schwald, K. Comanici, H.P. Steinrück, and H. Marbach, Microscopic Evidence of the Metalation of a Free‐Base Porphyrin Monolayer with Iron. *ChemPhysChem*, **2007**. 8(2): p. 241-243.

213. Visser, J., N. Katsonis, J. Vicario, and B.L. Feringa, Two-dimensional molecular patterning by surface-enhanced zn-porphyrin coordination. *Langmuir*, **2009**. 25(10): p. 5980-5985.

214. Lee, C.W., H.P. Lu, C.M. Lan, Y.L. Huang, Y.R. Liang, W.N. Yen, Y.C. Liu, Y.S. Lin, E.W.G. Diau, and C.Y. Yeh, Novel Zinc Porphyrin Sensitizers for Dye‐Sensitized Solar Cells: Synthesis and Spectral, Electrochemical, and Photovoltaic Properties. *Chemistry–A European Journal*, **2009**. 15(6): p. 1403-1412.

215. Wang, Q., W.M. Campbell, E.E. Bonfantani, K.W. Jolley, D.L. Officer, P.J. Walsh, K. Gordon, R. Humphry-Baker, M.K. Nazeeruddin, and M. Grätzel, Efficient light harvesting by using green Zn-porphyrin-sensitized nanocrystalline TiO2 films. *The Journal of Physical Chemistry B*, **2005**. 109(32): p. 15397-15409.

216. Liu, X.-H., C.-Z. Guan, D. Wang, and L.-J. Wan, Graphene-Like Single-Layered Covalent Organic Frameworks: Synthesis Strategies and Application Prospects. *Advanced Materials*, **2014**. 26(40): p. 6912-6920.

217. Ormond, A.B. and H.S. Freeman, Effects of substituents on the photophysical properties of symmetrical porphyrins. *Dyes and Pigments*, **2013**. 96(2): p. 440-448.

218. Semeikin, A., O. Koifman, and B. Berezin, Synthesis of tetraphenylporphins with active groups in the phenyl rings. 1. Preparation of tetrakis (4-aminophenyl) porphin. *Chemistry of Heterocyclic Compounds*, **1982**. 18(10): p. 1046-1047.

219. Yuasa, M., K. Oyaizu, A. Yamaguchi, and M. Kuwakado, Micellar Cobaltporphyrin Nanorods in Alcohols. *Journal of the American Chemical Society*, **2004**. 126(36): p. 11128-11129.

220. Schmitz, C.H., J. Ikonomov, and M. Sokolowski, Two-Dimensional Polyamide Networks with a Broad Pore Size Distribution on the Ag(111) Surface. *The Journal of Physical Chemistry C*, **2011**. 115(15): p. 7270-7278.

221. White, R.L., Variable temperature infrared study of copper sulfate pentahydrate dehydration. *Thermochim. Acta*, **2012**. 528: p. 58-62.

222. Alexander, M.R., R. Short, F. Jones, M. Stollenwerk, J. Zabold, and W. Michaeli, An X-ray photoelectron spectroscopic investigation into the chemical structure of deposits formed from hexamethyldisiloxane/oxygen plasmas. *Journal of materials science*, **1996**. 31(7): p. 1879-1885.

223. Vargo, T.G. and J.A. Gardella Jr, Development of Ti Kα x radiation for electron spectroscopy for chemical analysis of polymer surfaces. *Journal of Vacuum Science & Technology A*, **1989**. 7(3): p. 1733-1741.

224. Hopkins, G.H., *Silicone Oil Treatment of Vials*. 1980, Phoenixville, PA: Publication of the West Company.

225. Colas, A., J. Siang, and K. Ulman, *Silicones in Pharmaceutical Applications. Part 5: Siliconization of Parenteral Packaging Components* 2006, Midland(MI): Dow Corning Corporation.

226. Smith, E., M. Henley, E. Adams, A. DeMarco, J. Cronin, D. Wagenknecht, G. Battes, and M. Musolf, *J. of Parenteral Sc. and Tech., 42 (4S)*. 1988, technical report 12.

227. Lee, J.N., C. Park, and G.M. Whitesides, Solvent compatibility of poly (dimethylsiloxane)-based microfluidic devices. *Analytical chemistry*, **2003**. 75(23): p. 6544-6554.

228. Berkelaar, R.P., E. Dietrich, G.A.M. Kip, E.S. Kooij, H.J.W. Zandvliet, and D.

Lohse, Exposing nanobubble-like objects to a degassed environment. *Soft Matter*, **2014**. 10(27): p. 4947-4955.

229. Martin, C.P., M.O. Blunt, and P. Moriarty, Nanoparticle networks on silicon: Self-organized or disorganized? *Nano Letters*, **2004**. 4(12): p. 2389-2392.

230. Alhummiany, H., S. Jarvis, R.A. Woolley, A. Stannard, M. Blunt, and P. Moriarty, Dewetting of Au nanoparticle assemblies. *Journal of Materials Chemistry*, **2011**. 21(42): p. 16983-16989.

231. Page, A.J., A. Elbourne, R. Stefanovic, M.A. Addicoat, G.G. Warr, K. Voitchovsky, and R. Atkin, 3-Dimensional atomic scale structure of the ionic liquid-graphite interface elucidated by AM-AFM and quantum chemical simulations. *Nanoscale*, **2014**. 6(14): p. 8100-8106.

232. Korolkov, V.V., S.A. Svatek, A. Summerfield, J. Kerfoot, L. Yang, T. Taniguchi, K. Watanabe, N.R. Champness, N.A. Besley, and P.H. Beton, van der Waals-Induced Chromatic Shifts in Hydrogen-Bonded Two-Dimensional Porphyrin Arrays on Boron Nitride. *ACS Nano*, **2015**. 9(10): p. 10347-10355.

233. Mezzi, A. and S. Kaciulis, Surface investigation of carbon films: from diamond to graphite. *Surf. Interface Anal.*, **2010**. 42(6‐7): p. 1082-1084.

234. Kaciulis, S., Spectroscopy of carbon: from diamond to nitride films. *Surf. Interface Anal.*, **2012**. 44(8): p. 1155-1161.

235. Yang, D.-Q. and E. Sacher, Carbon 1s X-ray photoemission line shape analysis of highly oriented pyrolytic graphite: the influence of structural damage on peak asymmetry. *Langmuir*, **2006**. 22(3): p. 860-862.

236. Li, H., *Determination of Oxygen Functionality on Highly Oriented Pyrolytic Graphite (HOPG)*. 2012, Freien Universität Berlin: Berlin, Germany.

237. Pong, W.-T. and C. Durkan, A review and outlook for an anomaly of scanning tunnelling microscopy (STM): superlattices on graphite. *J. Phys. D: Appl. Phys.*, **2005**. 38(21): p. R329.

238. Zhang, G., D. Yang, and E. Sacher, X-ray Photoelectron Spectroscopic Analysis of Pt Nanoparticles on Highly Oriented Pyrolytic Graphite, Using Symmetric Component Line Shapes. *The Journal of Physical Chemistry C*, **2007**. 111(2): p.

565-570.

239. Yang, D.-Q. and E. Sacher, Platinum nanoparticle interaction with chemically modified highly oriented pyrolytic graphite surfaces. *Chem. Mater.*, **2006**. 18(7): p. 1811-1816.

240. Louette, P., F. Bodino, and J.-J. Pireaux, Poly (dimethyl siloxane)(PDMS) XPS reference core level and energy loss spectra. *Surf. Sci. Spectra*, **2005**. 12(1): p. 38-43.

241. Sharma, V., M. Dhayal, S. Shivaprasad, and S. Jain, Surface characterization of plasma-treated and PEG-grafted PDMS for micro fluidic applications. *Vacuum*, **2007**. 81(9): p. 1094-1100.

242. Gassman, P.G., A. Ghosh, and J. Almlof, Electronic effects of peripheral substituents in porphyrins: x-ray photoelectron spectroscopy and ab initio self-consistent field calculations. *Journal of the American Chemical Society*, **1992**. 114(25): p. 9990-10000.

243. Di Giovannantonio, M., T. Kosmala, B. Bonanni, G. Serrano, N. Zema, S. Turchini, D. Catone, K. Wandelt, D. Pasini, and G. Contini, Surface− Enhanced Polymerization via Schiff-Base Coupling at the Solid–Water Interface under pH Control. *The Journal of Physical Chemistry C*, **2015**. 119(33): p. 19228-19235.

244. Nemykin, V.N., P. Galloni, B. Floris, C.D. Barrett, R.G. Hadt, R.I. Subbotin, A.G. Marrani, R. Zanoni, and N.M. Loim, Metal-free and transition-metal tetraferrocenylporphyrins part 1: synthesis, characterization, electronic structure, and conformational flexibility of neutral compounds. *Dalton Transactions*, **2008**(32): p. 4233-4246.

245. Macquet, J., M. Millard, and T. Theophanides, X-ray photoelectron spectroscopy of porphyrins. *Journal of the American Chemical Society*, **1978**. 100(15): p. 4741-4746.

246. Niwa, Y., H. Kobayashi, and T. Tsuchiya, X‐ray photoelectron spectroscopy of tetraphenylporphin and phthalocyanine. *The Journal of Chemical Physics*, **1974**. 60(3): p. 799-807.

247. Karweik, D. and N. Winograd, Nitrogen charge distributions in free-base

porphyrins, metalloporphyrins, and their reduced analogs observed by X-ray photoelectron spectroscopy. *Inorganic Chemistry*, **1976**. 15(10): p. 2336-2342.

248. Muralidharan, S. and R. Hayes, Intense satellites in the N 1s x-ray photoelectron spectra of certain metalloporphyrins. *Journal of the American Chemical Society*, **1980**. 102(15): p. 5106-5107.

249. Sarno, D.M., L.J. Matienzo, and W.E. Jones, X-ray Photoelectron Spectroscopy as a Probe of Intermolecular Interactions in Porphyrin Polymer Thin Films. *Inorganic Chemistry*, **2001**. 40(24): p. 6308-6315.

250. Sun, X.L., L.X. Fan, Y.J. Yang, Z. Guo, W.Q. Tian, and S. Lei, Synthesis of One‐Dimensional Schiff Base Polymers that Contain an Oligothiophene Building Block on the Graphite Surface. *Chemistry–A European Journal*, **2015**. 21(18): p. 6898-6905.

251. Cooper, A., S.F. Dixon, M.A. Nutley, and J.L. Robb, Mechanism of retinal Schiff base formation and hydrolysis in relation to visual pigment photolysis and regeneration: resonance Raman spectroscopy of a tetrahedral carbinolamine intermediate and oxygen-18 labeling of retinal at the metarhodopsin stage in photoreceptor membranes. *Journal of the American Chemical Society*, **1987**. 109(24): p. 7254-7263.

252. Zhang, T., W. Zhou, W. Jin, Q. Jin, and H. Chen, Direct detection of aromatic amines and observation of intermediates of Schiff-base reactions by reactive desorption electrospray ionization mass spectrometry. *Microchemical Journal*, **2013**. 108: p. 18-23.

253. Upthagrove, A.L. and W.L. Nelson, Carbinolamines, imines, and oxazolidines from fluorinated propranolol analogs. 19F NMR and mass spectral characterization and evidence for formation as intermediates in cytochrome P450-catalyzed N-dealkylation. *Drug metabolism and disposition*, **2001**. 29(8): p. 1114-1122.

254. Zeller, M.V. and R.G. Hayes, X-ray photoelectron spectroscopic studies on the electronic structures of porphyrin and phthalocyanine compounds. *Journal of the American Chemical Society*, **1973**. 95(12): p. 3855-3860.

255. Karweik, D., N. Winograd, D.G. Davis, and K.M. Kadish, X-ray photoelectron spectroscopic studies of silver(III) octaethylporphyrin. *Journal of the American Chemical Society*, **1974**. 96(2): p. 591-592.

256. Parschau, M., S. Romer, and K.-H. Ernst, Induction of Homochirality in Achiral Enantiomorphous Monolayers. *Journal of the American Chemical Society*, **2004**. 126(47): p. 15398-15399.

257. Meric, I., M.Y. Han, A.F. Young, B. Ozyilmaz, P. Kim, and K.L. Shepard, Current saturation in zero-bandgap, top-gated graphene field-effect transistors. *Nature nanotechnology*, **2008**. 3(11): p. 654-659.

258. Xia, F., D.B. Farmer, Y.-m. Lin, and P. Avouris, Graphene field-effect transistors with high on/off current ratio and large transport band gap at room temperature. *Nano letters*, **2010**. 10(2): p. 715-718.

259. Avila, J., I. Razado, S. Lorcy, R. Fleurier, E. Pichonat, D. Vignaud, X. Wallart, and M.C. Asensio, Exploring electronic structure of one-atom thick polycrystalline graphene films: A nano angle resolved photoemission study. *Scientific reports*, **2013**. 3.

260. Krause, G. and E. Weis, Chlorophyll fluorescence and photosynthesis: the basics. *Annual review of plant biology*, **1991**. 42(1): p. 313-349.

List of abbreviations

1D One-dimensional

2D Two-dimensional

3D Three-dimensional

A Adenine

AFM Atomic Force Microscopy

AO Atomic orbital

ATC Anthracene tetra-carboxylic acid, 5, 5'-(anthracene-2,6-diyl) diisophthalic acid

BDA Benzene-1,4-dicarboxaldehyde

BDBA 1,4-benzenediboronic acid

BE Binding Energy

BPTC Biphenyl-3,3′,5,5′-tetra-carboxylic acid

BTB 1,3,5-tris(4-carboxyphenyl) benzene

CNT Carbon nanotube

CoOEP Cobalt(II) octaethylporphyrin

COF Covalent Organic Framework

COR Coronene

CPS counts per second

DBA Alkylated dehydrobenzo[12]annulene

DFT Density Functional Theory

DMSO Dimethyl sulfoxide

DNA Deoxyribonucleic acid

DOS Density of states

FWHM Full Width at Half Maximum

HBC Hexabenzocoronene

HOMO Highest occupied molecular orbital

HOPG Highly Oriented Pyrolytic Graphite

ISA Isophthalic acid

LDOS Local Density of States

LUMO lowest unoccupied molecular orbital

MM Molecular Mechanics

MO molecular orbital

NG Nanographene

NiOEP Nickel(II) octaethylporphyrin

NMR Nuclear Magnetic Resonance

NTC Napthylene tetra-carboxylic acid, 5,5′-naphthalene-2,6-diyldibenzene-1,3-dicarboxylic acid

PA 9-propyladenine

PDMS Polydimethylsiloxane

PFT PeakForce Tapping™

PTCDI Perylene tetracarboxylic di-imide

PTFE Polytetrafluoroethylene

QPTC quarterphenyl-3,3‴,5,5‴-tetra-carboxylic acid

QM Quantum mechanical

Sat Saturated solution

SEM Scanning Electron Microscopy

SPIP Scanning Probe Image Processor

SPM Scanning Probe Microscopy

STM Scanning Tunnelling Microscopy

STS Scanning Tunnelling Spectroscopy

T Thymine

TAPP 5,10,15,20-meso-tetra(4-aminophenyl) porphyrin

TBPB 1,3,5-tris(4-bromophenyl) benzene

TCB 1,2,4-trichlorobenzene

TEM Transmission electron microscopy

TERS Tip-enhanced Raman spectroscopy

Tetra-TP Tetra-(phenylthymine)porphyrin

THF Tetrahydrofuran

TMA Trimesic acid

TPTC Terphenyl-3,3″,5,5″-tetra-carboxylic acid

TSB35 1,3,5-tris[(E)-2-(3,5-didecyloxyphenyl)-ethenyl]- benzene

UHV Ultra-high vacuum

VB Valence band

WKB Wentzel-Kramers-Brillouin

XPS X-ray photoelectron Spectroscopy

XRD X-ray Diffraction

ZnTAPP 5,10,15,20-meso-tetra(4-aminophenyl) porphyrin Zn(II)

Zn-tetra-TP Tetra-(phenylthymine)porphyrin-Zn(Ⅱ)

List of figures

List of tables